

## REPORT DOCUMENTATION PAGE

Form Approved OMB NO. 0704-0188

The public reporting burden for this collection of information is estimated to average 1 hour per response, including the time for reviewing instructions, searching existing data sources, gathering and maintaining the data needed, and completing and reviewing the collection of information. Send comments regarding this burden estimate or any other aspect of this collection of information, including suggestions for reducing this burden, to Washington Headquarters Services, Directorate for Information Operations and Reports, 1215 Jefferson Davis Highway, Suite 1204, Arlington VA, 22202-4302. Respondents should be aware that notwithstanding any other provision of law, no person shall be subject to any penalty for failing to comply with a collection of information if it does not display a currently valid OMB control number.

**PLEASE DO NOT RETURN YOUR FORM TO THE ABOVE ADDRESS.**

1. REPORT DATE (DD-MM-YYYY) 12-02-2014	2. REPORT TYPE Final Report	3. DATES COVERED (From - To) 15-Feb-2011 - 14-Aug-2015		
4. TITLE AND SUBTITLE Rapid Assemblers for voxel-based VLSI robotics		5a. CONTRACT NUMBER W911NF-11-1-0093		
		5b. GRANT NUMBER		
		5c. PROGRAM ELEMENT NUMBER 0620BK		
6. AUTHORS Jonathan Hillar, Cheryl Perich, Steve Bernard, Rob MacCurdy, Fnu Apoorva, Hod Lipson		5d. PROJECT NUMBER		
		5e. TASK NUMBER		
		5f. WORK UNIT NUMBER		
7. PERFORMING ORGANIZATION NAMES AND ADDRESSES Cornell University Office of Sponsored Programs 373 Pine Tree Road Ithaca, NY 14850 -2820		8. PERFORMING ORGANIZATION REPORT NUMBER		
9. SPONSORING/MONITORING AGENCY NAME(S) AND ADDRESS (ES) U.S. Army Research Office P.O. Box 12211 Research Triangle Park, NC 27709-2211		10. SPONSOR/MONITOR'S ACRONYM(S) ARO		
		11. SPONSOR/MONITOR'S REPORT NUMBER(S) 59655-MS-DRP.5		
12. DISTRIBUTION AVAILABILITY STATEMENT Approved for Public Release; Distribution Unlimited				
13. SUPPLEMENTARY NOTES The views, opinions and/or findings contained in this report are those of the author(s) and should not be construed as an official Department of the Army position, policy or decision, unless so designated by other documentation.				
14. ABSTRACT The goal of this research is to develop scalable fabrication methods and design tools for assembling large scale robots out of billions of micro scale building blocks (voxels) arranged on a regular 3D lattice. Traditionally, robotic systems are constructed of custom-designed and fabricated components with arbitrary geometric and functional interfaces. The arbitrary nature of such integrations makes it difficult to design, simulate and fabricate complex 3D machines, as well as to repair, adapt and recycle existing machines, and to perform rigorous design automation. In contrast, electronic systems have reached very large scale integration (VLSI) levels through consistent definition of				
15. SUBJECT TERMS Digital Manufacturing, 3D printing, VLSI, Rapid Assembler, Electrophoresis, Electrowetting, Electroadhesion, VoxCAD, Robotics, Lego Electronics, CUDA based Physics Simulator				
16. SECURITY CLASSIFICATION OF: a. REPORT UU b. ABSTRACT UU c. THIS PAGE UU		17. LIMITATION OF ABSTRACT UU	15. NUMBER OF PAGES	19a. NAME OF RESPONSIBLE PERSON Hod Lipson
				19b. TELEPHONE NUMBER 607-255-1686

# **Report Title**

Rapid Assemblers for voxel-based VLSI robotics

## **ABSTRACT**

The goal of this research is to develop scalable fabrication methods and design tools for assembling large scale robots out of billions of micro scale building blocks (voxels) arranged on a regular 3D lattice. Traditionally, robotic systems are constructed of custom-designed and fabricated components with arbitrary geometric and functional interfaces. The arbitrary nature of such integrations makes it difficult to design, simulate and fabricate complex 3D

machines, as well as to repair, adapt and recycle existing machines, and to perform rigorous design automation. In contrast, electronic systems have reached very large scale integration (VLSI) levels through consistent definition of elementary building blocks, interfaces, and design rules. Biological systems, too, construct, repair, adapt and recycle large scale and complex 3D organisms by combining and recombining a relatively small repertoire of building blocks types - cell types, proteins types or amino acids types, depending on the scale of interest. In this proposal we envision a new robotics paradigm where machines are comprised of very large scale integration of billions of small scale building blocks (voxels). If each voxel has the size of about 300 microns, then the resulting assembly could look as smooth to the eye as a typical XGA LCD display - at about 85 Pixels Per Inch (PPI). The voxels will be self-aligning and interlocking, resulting in integrated and precise large scale integrations. Some voxels can be passive and very cheap, while others might be active sensors, actuators, computational and power components used more sparingly. The range of types of voxels available will define the range machines that can be fabricated.

---

**Enter List of papers submitted or published that acknowledge ARO support from the start of the project to the date of this printing. List the papers, including journal references, in the following categories:**

**(a) Papers published in peer-reviewed journals (N/A for none)**

Received      Paper

**TOTAL:**

**Number of Papers published in peer-reviewed journals:**

**(b) Papers published in non-peer-reviewed journals (N/A for none)**

Received      Paper

**TOTAL:**

**Number of Papers published in non peer-reviewed journals:**

**(c) Presentations**

[1] Cheryl A. Perich, Ashley Macner, Robert MacCurdy, Paul Steen, Hod Lipson, "Toward massively parallel manipulation of mm-scale components using elec-troosmotically controled drops", In Review

[2] Robert MacCurdy, Anthony McNicoll, and Hod Lipson, "Bitblox: A Printable Digital Material for Electromechanical Machines", In Review

**Number of Presentations:** 2.00

---

**Non Peer-Reviewed Conference Proceeding publications (other than abstracts):**

Received      Paper

**TOTAL:**

**Number of Non Peer-Reviewed Conference Proceeding publications (other than abstracts):**

---

**Peer-Reviewed Conference Proceeding publications (other than abstracts):**

Received      Paper

**TOTAL:**

**Number of Peer-Reviewed Conference Proceeding publications (other than abstracts):**

---

**(d) Manuscripts**

Received      Paper

02/10/2014 4.00 Jonathan D. Hiller, Joseph Miller, Hod Lipson. Microbricks for Three-Dimensional Reconfigurable Modular Microsystems,  
Journal of Microelectromechanical Systems (09 2011)

08/30/2013 2.00 Anthony McNicoll, Robert MacCurdy, Hod Lipson. Bitblox: A printable programmable digital material Parallel manipulation of mm-scale components using electroosmotically controlled droplet arrays  
,  
IN PREP (09 2013)

08/30/2013 3.00 Ashley Macner, Robert MacCurdy, Paul Steen , Cheryl Perich <sup>L</sup>, Hod Lipson <sup>L</sup>. Parallel manipulation of mm-scale components using electroosmotically controlled droplet arrays,  
IN PREP (09 2013)

**TOTAL:**      **3**

**Number of Manuscripts:****Books**ReceivedPaper**TOTAL:****Patents Submitted**

- [1] Fnu Apoorva, Robert MacCurdy, and Hod Lipson, "System and Methods for Electrowetting Based Pick and Place Assembly", Publication No WO2014014892 A2, Application No PCT/US2013/050650
- 
- [2] Fnu Apoorva and Hod Lipson, "Electroadhesion Based Rapid Assembler", Patent Application No- US61/790, 139.

**Patents Awarded****Awards****Graduate Students**

<u>NAME</u>	<u>PERCENT_SUPPORTED</u>	Discipline
Steve Bernard	0.32	
Rob MacCurdy	0.00	
Fnu Apoorva	0.84	
Jonathan Hillar	0.00	
Jonas Neubert	0.13	
<b>FTE Equivalent:</b>	<b>1.29</b>	
<b>Total Number:</b>	<b>5</b>	

**Names of Post Doctorates**

<u>NAME</u>	<u>PERCENT_SUPPORTED</u>
<b>FTE Equivalent:</b>	
<b>Total Number:</b>	

**Names of Faculty Supported**

<u>NAME</u>	<u>PERCENT_SUPPORTED</u>	National Academy Member
Hod Lipson	0.22	
<b>FTE Equivalent:</b>	<b>0.22</b>	
<b>Total Number:</b>	<b>1</b>	

## **Names of Under Graduate students supported**

<u>NAME</u>	<u>PERCENT_SUPPORTED</u>	Discipline
Anthony McNicoll	0.00	
Nick Perrotti	0.00	
Nick Chartrain	0.00	
<b>FTE Equivalent:</b>	<b>0.00</b>	
<b>Total Number:</b>	<b>3</b>	

### **Student Metrics**

This section only applies to graduating undergraduates supported by this agreement in this reporting period

The number of undergraduates funded by this agreement who graduated during this period: ..... 3.00

The number of undergraduates funded by this agreement who graduated during this period with a degree in science, mathematics, engineering, or technology fields:..... 3.00

The number of undergraduates funded by your agreement who graduated during this period and will continue to pursue a graduate or Ph.D. degree in science, mathematics, engineering, or technology fields:..... 1.00

Number of graduating undergraduates who achieved a 3.5 GPA to 4.0 (4.0 max scale):..... 0.00

Number of graduating undergraduates funded by a DoD funded Center of Excellence grant for Education, Research and Engineering:..... 0.00

The number of undergraduates funded by your agreement who graduated during this period and intend to work for the Department of Defense ..... 0.00

The number of undergraduates funded by your agreement who graduated during this period and will receive scholarships or fellowships for further studies in science, mathematics, engineering or technology fields:..... 1.00

## **Names of Personnel receiving masters degrees**

<u>NAME</u>
James Wang
Cheryl Perich
Jean Rouge
Jeff Ames
<b>Total Number:</b>
<b>4</b>

## **Names of personnel receiving PhDs**

<u>NAME</u>
Jonathan Hillar
Jonas Neubert
<b>Total Number:</b>
<b>2</b>

## **Names of other research staff**

<u>NAME</u>	<u>PERCENT_SUPPORTED</u>
<b>FTE Equivalent:</b>	
<b>Total Number:</b>	

## **Sub Contractors (DD882)**

## **Inventions (DD882)**

**Scientific Progress**

**Technology Transfer**

Final Report for

## Rapid Assemblers for voxel-based VLSI robotics

DARPA - MAXIMUM MOBILITY AND MANIPULATION (M3)

Cornell Creative Machines Lab - Hod Lipson

Performance Dates: February 1, 2011 – Aug 31, 2013

### *Task 1: Simulation*

#### Task overview and milestones

This task simulates the performance of a machine composed of large numbers of voxels. Both mechanical as well as electrical behavior were simulated. This task included an initial proof of concept demonstration of a simulated robot with 1000+ voxels. First we demonstrated two robots that used physically realizable linear actuation to crawl forward or backward: a snake-like robot and a multi-legged walker and built on that the evolving machines composed of heterogeneous voxels that can locomote. Following year we developed algorithms that can use high performance computing (HPC) environments to accelerate the computation of robots composed of both flexible and stiff materials. We used Comsol simulation suite to compare our simulator against several test designs in order to calibrate the simulation. This task was part of the design automation sub-goal, which allows a designer to specify goals, and the algorithm finds a morphology that satisfies those goals.

In first two quarters we demonstrated a CPU-based parallel simulator that utilized MPI (message passing interface), to coordinate the activities of several CPUs. Though this approach does work, we were not able to realize the speedup that we had hoped for. It appears that the overhead involved in MPI becomes excessive as the number of individual elements to be solved increases. The relaxation simulator fits into the class of embarrassingly parallel problems, and is well suited to a GPU machine, which has hundreds, if not thousands of simple compute engines, depending on the particular GPU used. This architecture is well suited to relaxation solvers, and we are currently deploying a solver with the NVIDIA CUDA platform. We are 6 weeks into the implementation, and do not have results to show yet, however the implementation appears straightforward, and example code has sped the process along. At last we built a preliminary simulator. We have made several version updates in the previous quarters that include performance increases, and important bug fixes that improve the fidelity and stability of this simulator. This simulator was used as the fitness evaluation engine for the progress reported in the Design Synthesis section below.

#### Technical Progress

We have designed a voxel-based simulator with a graphical user interface that we call VoxCad. With VoxCad, designers can build heterogeneous structures from a palette of user-defined materials. The current material properties that are supported allow voxels of different stiffness, mass, friction coefficient, and volumetric expansion to be defined. These parameters allow complex, actuated structures to be designed, and then simulated in a physically realistic way. Complex structural actuations can be achieved by controlling the magnitude and phase of each individual voxel's expansion. For example, simple walking robots can be built from a set of voxels whose volumetric expansions are -90, 0, and +90 degrees out of phase. The simple robot shown in Figure 1 illustrates the idea. At the start of each cycle the green voxels

are fully contracted, while the red voxels are fully expanded. As the blue begins to expand, it lifts the body off the ground, while the green expands, and the red contracts, which moves the body forward. The blue voxels contract until they are no longer in contact with the ground (the mass is supported by the non-actuated grey voxels). As the cycle continues, the red and green voxels move the blue voxels forward, and the cycle repeats.

The ability to control the actuation phase of each voxel individually enables more sophisticated gaits. We were able to create a snake-like design that used differential actuation at the upper and lower sides of its

body to raise a section of the body off the ground. The raised section is then moved forward by expanding the sections immediately behind it, while simultaneously contracting those ahead of it. This raised section is passed forward through the body in a wave, resulting in a net forward displacement of the entire body after one cycle.

Each of the designs described rely on volumetric actuation, with linear expansion and contraction in only one dimension. The magnitude of this expansion/contraction was +/- 10% of the resting size. These relatively modest actuation displacements should be achievable with a variety of different techniques, as we describe later.

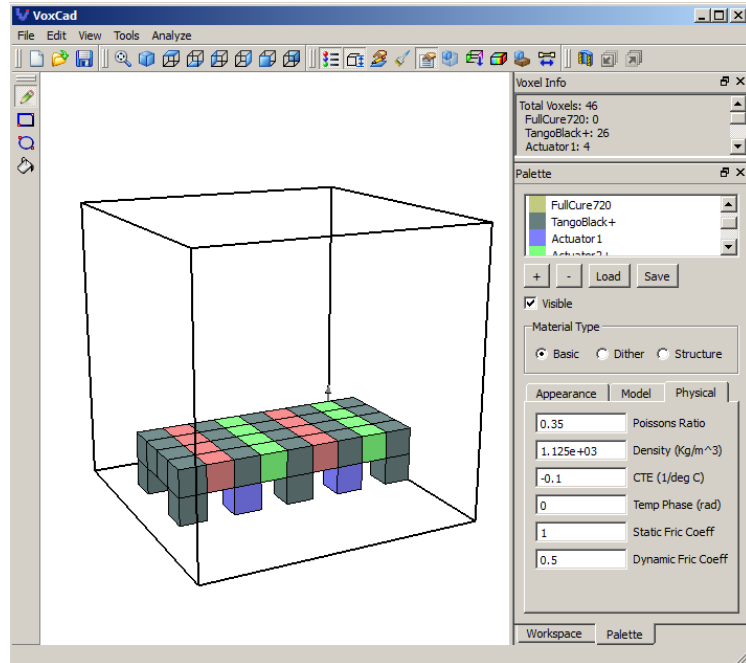


**Figure 1. VoxCad simulation display, showing the simple walking robot model. VoxCad allows easy graphical design and simulation of electromechanical, voxel-based structures.**

### Challenges

The existing simulator uses separate threads for the user interface and simulation portions of the code, but it is not optimized to take advantage of multi-core processors. Additionally, the user interface and graphical display impose a substantial processing load. As a result, the simulator runs relatively slowly. This can be partially addressed by running the simulation process as a batch, without the user interface.

The current simulator works well for relatively soft, and relatively dense materials, but we have found inaccuracies in the calculations of the moments between adjacent voxels. These errors become significant as the materials become stiffer and less dense.

Currently, the entire structure is composed of evenly sized voxels. Although functional subassemblies can be created and combined into a structure, when the structure is simulated, the simulator runs at the voxel level, testing each voxel's connection to its neighbours, irrespective of which subassembly the voxel belongs to. This becomes inefficient when we want to create long, very rigid beams that will be connected by much more flexible materials. It would be more efficient to model all the voxels in the stiff beam as a single, asymmetric voxel.

The earlier version of simulator was capable of simulating robots composed of 1000+ voxels on a single-core CPU, but moving to larger assemblies, and using the simulator within the evaluation loop of a evolutionary algorithm requires a faster method. This motivated us to evolve a simulator suitable for HPC. We demonstrated such a mechanical simulator, capable of simulating 10,000+ voxels at reasonable

execution speeds on a multi-core CPU, in our earlier quarterly report. This simulator runs as a module within the VoxCAD design framework that we have developed, and though it uses a multi-threaded implementation, the simulation engine runs in a single thread which limits the execution speed.

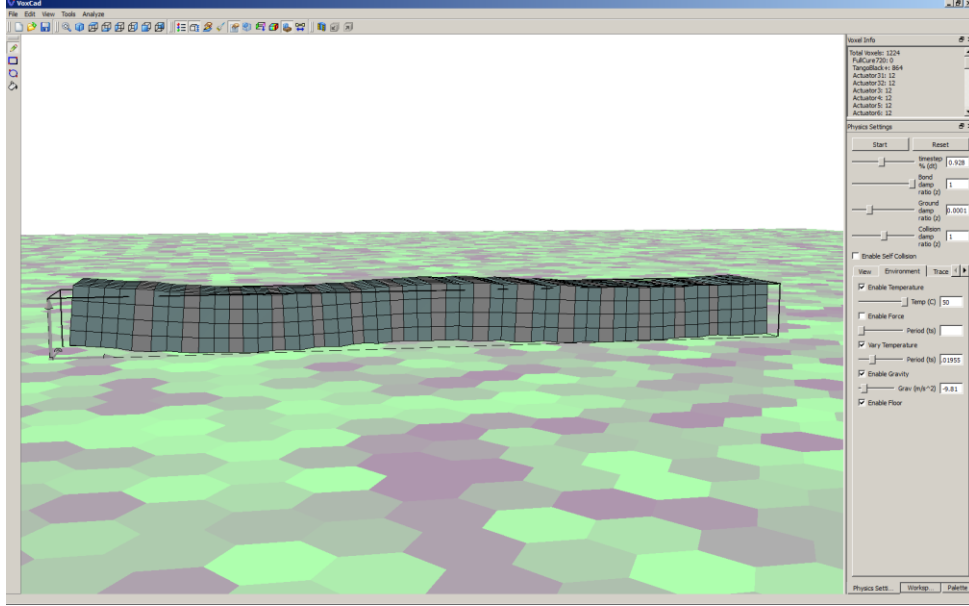


**Figure 2: A snake-like robot model with 1000+ voxels using travelling wave-type locomotion**

Our parallel simulator is based on an implicit finite difference relaxation method; essentially the computations for each node in the simulation are carried out as if all the other nodes are stationary. The computations are iterated until the positions and velocities of every node converge. This approach is relatively straightforward to parallelize, and using an implicit scheme maintains simulation stability. For more details, see the references at the end of this section. The algorithm breaks up the system of  $n$  nodes into different sub-regions by attempting to segregate regions with high connectivity from those with less connectivity between the nodes. This idea is shown in Figure 3, where the original set of nodes (red circles) and connecting spring/damper elements (blue lines), are broken into two different groups. The only shared data required are the positions (and time derivatives) of the yellow circles. Each parallel-compute unit then operates on its section of the problem, and shares the small amount of common data when requested.

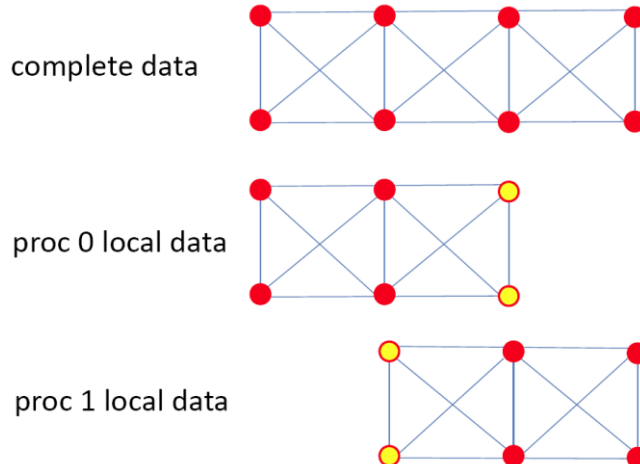


**Figure 3: Partitioning a large problem into smaller problems in order to perform the simulation in parallel. Yellow nodes contain shared data.**

The parallel simulator has been tested across different numbers of CPU processors to calculate the parallel speedup (the decrease in execution time for multiple processors compared to using only one processor). The results, shown in Figure 4, indicate good parallel algorithmic efficiency. Notice that systems with larger numbers of nodes are able to more efficiently make use of larger numbers of processors.

We also worked on simulation engine that leverages multiple parallel compute cores to achieve substantial simulation speedup. This simulator allows voxel designs with greater complexity to be solved much faster - an important feature for a simulator that will be used within an evolutionary computation framework. The use of heterogeneous computing environments, including GPUs, to perform general purpose computation, referred to as GP-GPU, is gaining favor in the high performance computing community, and we have investigated two competing languages: CUDA and OpenCL. Our initial evaluation led us to choose CUDA because it is currently better supported. This is likely to change in the coming years, and the cost of switching languages is not so prohibitive that it would prevent us from doing so. Both major participants in the GP-GPU area (NVIDIA and AMD) will be introducing significant hardware improvements within the next twelve months that we also hope to leverage. We are currently re-writing a library for GPU compatibility, and are working to validate our results.

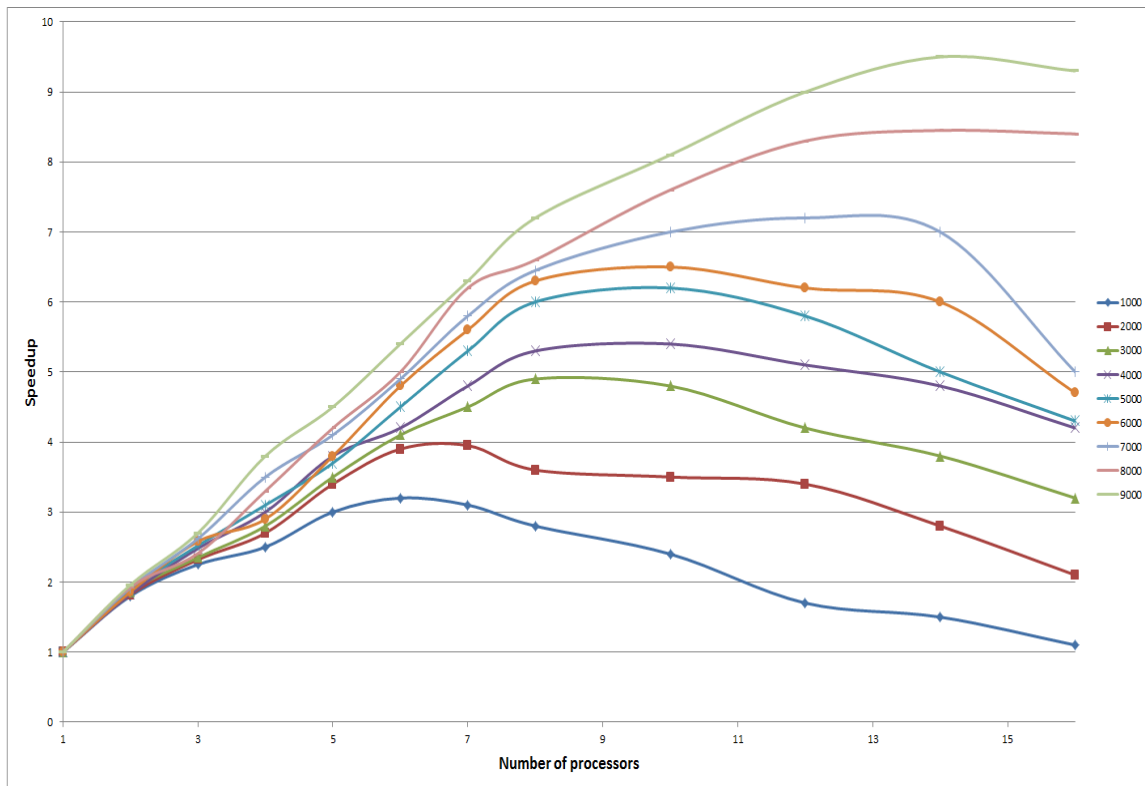


**Figure 4: Speedup vs. Number of Processors vs. Number of simulated nodes**

Since our simulator works with materials of any stiffness, existing rigid-body simulators can be used to compare results for numerical accuracy. We have access to the Comsol simulation suite, and are comparing our simulator against several test designs in order to calibrate the simulation. The simulator uses a particle-based framework, with a relaxation approach that uses implicit stepping. This approach yields better stability than the explicit method when simulating stiff systems. The simulator consists of two primary components: the simulation engine and the visualization engine. Each are specifically designed to handle very large numbers of particles Figure 5.

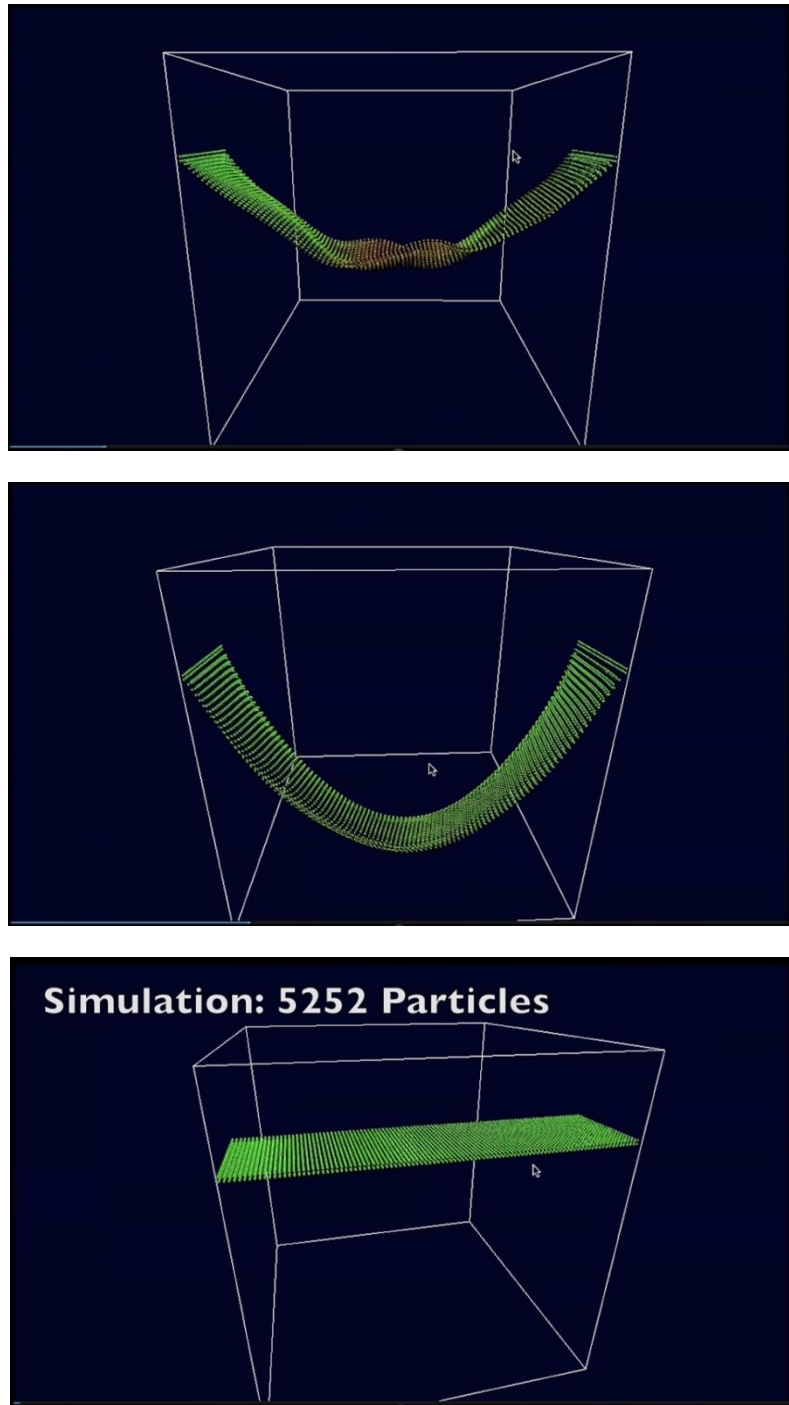


**Figure 5: OpenGL visualization of a 5252 particle simulation of a soft, rubber-like material that is fixed at each end, falling in a gravitational field.**

#### References

- [1] A. Nealen, M. Muller, R. Keiser, E. Boxerman and M. Carlson. Physically Based Deformable Models in Computer Graphics. Computer Graphics Forum, pages 809–836, 2006.
- [2] B. Eberhardt, O. Etzmuss and M. Hauth. Implicit-Explicit Schemes for Fast Animation with Particles Systems. Proceedings of the Eurographics workshop on Computer Animation and Simulation, pp 137-151, 2000.
- [3] H. Courtecuisse and J. Allard. Parallel Dense Gauss-Seidel Algorithm on Many-Core Processors. High Performance Computation Conference (HPCC), IEEE CS Press , 2009.

[4] P. Volino and N. Magnenat-Thalmann. Comparing Efficiency of Integration Methods for Cloth Simulation. Computer Graphics International'01, 2001.

[5] U. M. Ascher, S. J. Ruuth and B. T. Wetton. Implicit-explicit methods for time-dependent partial differential equations. SIAM Journal of Numerical Analysis, 32(3):797-823, 1995.

## Task 2: cm-scale voxels for prototypes

### Task overview and milestones

We fabricated operational voxels of a variety of functional types at the centimeter scale. These units then were assembled manually or robotically in order to formulate and test communication protocols, electrical interfacing, and mechanical interlocking issues. This task included an initial proof of concept task that required the fabrication of a working electromechanical voxel-based assembly. During Q2 we demonstrated several actuation options. In Q3 we integrated some of those options into the existing voxel framework. We designed a robot in simulation that used the new actuators, and built a physical instance of the robot, composed of 40 voxels, that locomotes as simulation predicted. Since then we have primarily focused on reducing the voxel dimensions. We also fabricated operational voxels of a variety of functional types at the centimeter scale. These units will then be assembled manually or robotically in order to formulate and test communication protocols, electrical interfacing, and mechanical interlocking issues.

### Technical Progress

Previous work in our group has investigated several different tiling approaches, and explored the various symmetries that are necessary for tiling in 2.5 and 3 dimensional structures. This effort included one trial that used a single electrical connection at each mechanical interface. Though electrical circuits can be realized with this approach, adding more connections at each mechanical interface reduces the number of voxels required to implement any particular circuit. We decided to use two electrical connections at each mechanical interface (this choice, its consequences, and alternatives will be explored in more detail in a publication). The electrical connectors used must be rotationally symmetric in order to preserve the proper net connections when two adjacent voxels are connected. This necessitates three connections at each mechanical interface. We also chose a four-sided voxel because it allows straightforward tiling. These choices imply twelve contacts per voxel; small contacts are necessary in order fit into a 1cm<sup>2</sup> area, and allow adequate room for electronics on the same printed circuit board.



**Figure 6: Three examples of different candidate electrical contacts. From left to right, they are: a single contact scavenged from a PLCC socket; a thru-hole pin and socket connector; a surface mount pin and socket connector**

We evaluated many miniature electrical contacts and found 3 types that fit the design space. They are shown in Figure 6. The first type is scavenged from a commercially available PLCC socket connector, since custom contact fabrication is an expensive, time consuming step. These contacts must be contained within a plastic back-shell, and mate face-to-face when two voxels are mated (see Figure 7). The second contact type is a commercially available thru-hole connector that allows stack-through voxel assembly. This contact is readily available, and therefore was used for the proof of concept demonstration; however, the stack-

through nature of this connector causes all vertical layers of a multi-layer assembly to share the same electrical net. This naturally causes electrical assemblies to become more planar, since free nets can only be gained by spreading the design horizontally. The last contact in Figure 8 addresses this problem by mounting only on the surface of the circuit board. Special isolation voxels can be used that do not route signals from the top to the bottom. Unfortunately, this contact is only manufactured by a single supplier, and is not readily available. Voxels using this part will be built when it becomes available.

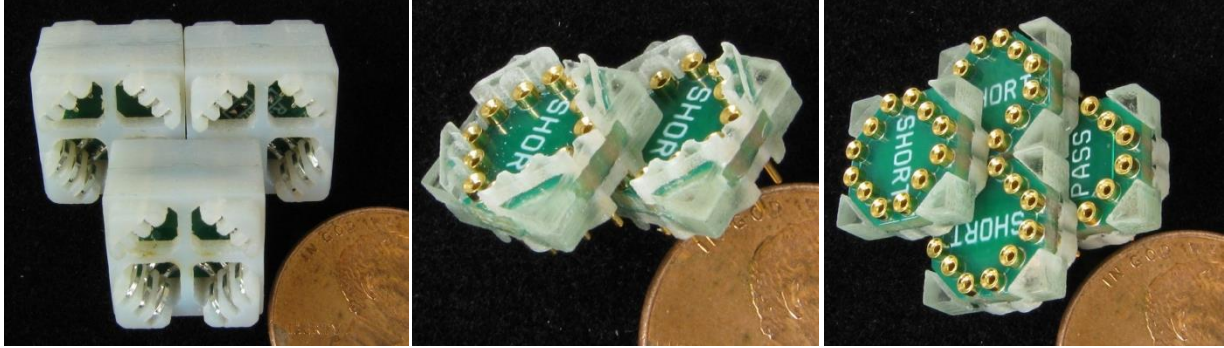


**Figure 7: Three examples of different voxel mechanical configurations**

The three different contact styles enable three different voxel board designs; however, the lack of the surface-mount connector prevented experiments using it. Instead we focused on integrating the PLCC and thru-hole contacts in to a cm-scale voxel design. Three different versions are shown in Figure 9. The left-most image shows the PLCC contacts integrated into mating backshells that were printed on an Object 3D rapid prototyping machine. The plastic backshell provides a snap-lock mating force and holds the opposing faces of the contacts together. It should be noted that the feature-sizes used in this demonstration are at the limit of the Objet machine's capability, and required a significant manual post-processing effort. Other plastic fabrication methods, including injection molding, would yield better results. The second and third images in Figure 10 show other attempts to integrate a plastic shell with the circuit board and thru-hole contacts. Our tests showed that the mating force of the thru-hole contacts alone is sufficient to hold the assembly together. Additionally, producing a backshell small enough to accurately fit the voxels proved infeasible with the Objet. For these reasons we chose to abandon the plastic backshell when using the thru-hole contacts.

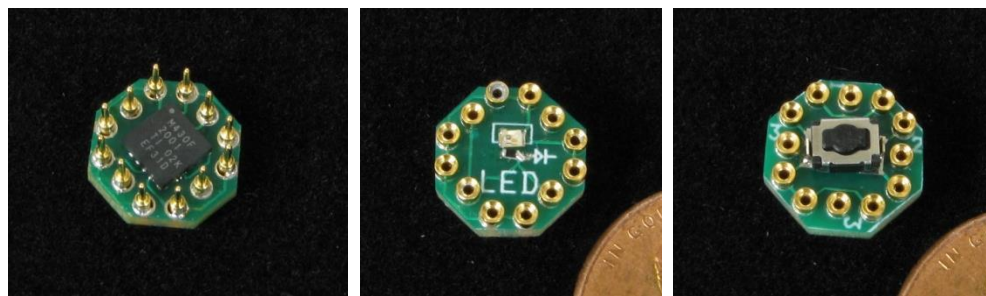


**Figure 8: Three examples of different voxel electrical circuit types. From left to right, they are: a 16 bit microcontroller, an LED, and a tactile switch. Many other types have been implemented**

We fabricated 10 different types of voxels using the thru-hole contacts; voxel types include: switches, batteries, microcontrollers, LEDs, resistors, capacitors, inductors, and various types of signal routing among the pins on each voxel. The signal routing voxels are useful because we broke rotational symmetry and in doing so gained functionality, since the electrical function of each voxel now depends on its position and rotation in each assembly. Several of these prototype voxels are shown in Figure 8. The electrical schematics for several voxels are shown in Figure 9, as are the relative orientations of the connectors. This simple circuit uses a microcontroller and battery to blink an LED. Notice that the rotations of some voxels, in this case the battery and microcontroller, dictate the netlist that is realized Figure 10.

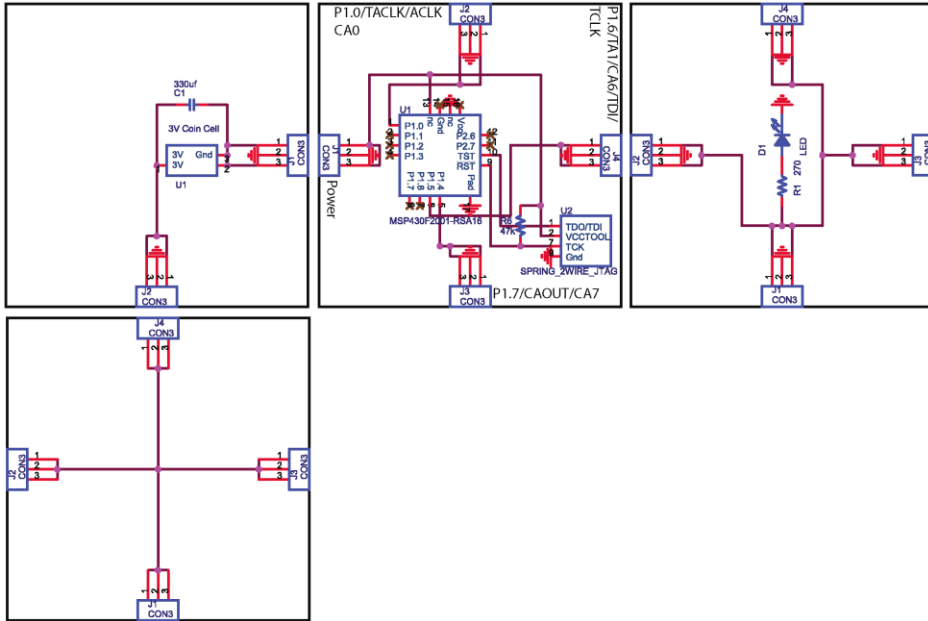


**Figure 9: A simple blinking LED circuit composed of four different voxel types: (clockwise from lower left) short, battery, microcontroller, and LED**

More complicated assemblies can be implemented with larger numbers of voxels. We demonstrated a working infra-red remote control that is built from more than 130 voxels. This particular design used functionally discrete sub-modules (one for each button's function), and combined them with shared a shared power supply. In principle, very complicated circuits could be implemented with this approach.

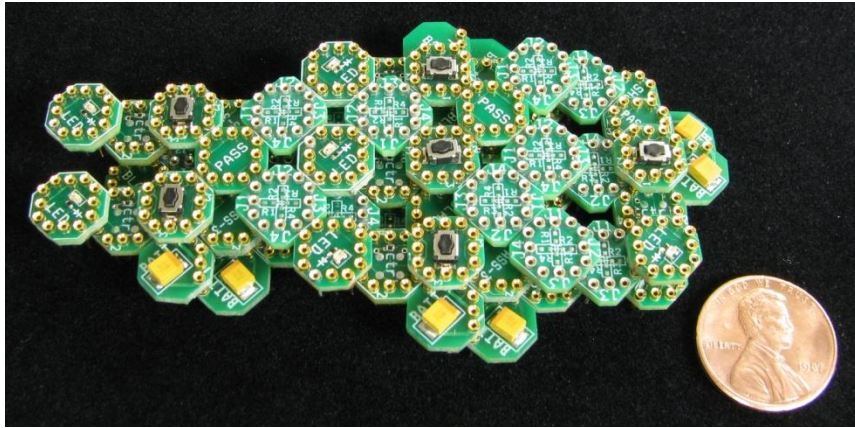


**Figure 10: A five channel (Play/Pause, Stop, Skip Forward, Skip Back, Volume+, Volume-) infrared remote control. This design uses approximately 130 voxels, and relies on seven different voxel types**

A working robot will require actuation in addition to computation. However, selecting an actuator that is small enough for our current voxels, and that can be scaled down to micro-scale proved challenging. We pursued three different actuation modalities: shape-memory alloys (SMA), DC motors and thermo-expansion wax. We think each actuation type could plausibly be scaled down, though the specific implementation will need to change. Each effort is described below.

- SMA

Shape memory alloys, based on a blend of Nickel and Titanium and referred to as Nitinol, can be configured to produce useful work when heated above a certain transition temperature. When cooled below the transition temperature the material can be strained up to 8% without suffering permanent deformation (though design strains in the 3-5% range produce actuators with better cycle lifetime). Nitinol is widely available as drawn wire, and is often used in this configuration with a displacement multiplier linkage to

achieve the desired actuator displacement, since the wire is limited to an 8% direct displacement. Helical coils of wire can be heat-treated to produce actuators with much larger displacements [1], though the actuation force is relatively low. These actuators are wound into a long narrow helix and work best in tension. In contrast, the actuation scheme envisioned in the voxel design requires an actuator that has an active extension stroke.



**Figure 11: Nitinol sheet and ribbon stock, as well as the mandrel that holds the material during heat-treating.**

We designed an alternative Nitinol actuator that overcomes these two limitations (actuation force and active stroke). The actuator is based on Nitinol sheet or ribbon stock, and can produce bending, extension or contraction forces, depending on where the heat-treatment set point is. We fabricated a steel mandrel (see Figure 11) with a series of welded cylinders that force the Nitinol ribbons into a serpentine shape and hold the shape during heat treating. The Nitinol is placed into an oven, held at 900 degrees Fahrenheit for 25 minutes, and then quenched in water. The resulting material has a resting serpentine shape set (Figure 12), and allows repeatable 20% displacement at high force (relative to the mass of Nitinol used).

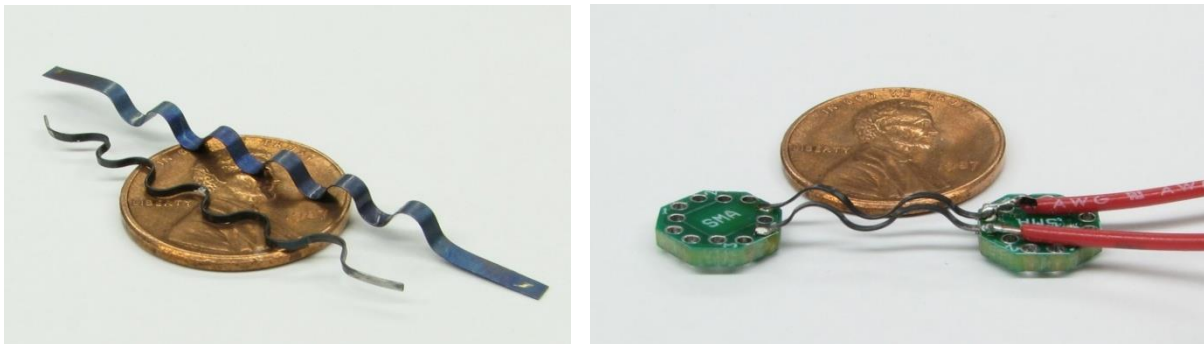


**Figure 12: Heat-set Nitinol and the Nitinol used as a linear actuator.**

Figure 12 shows the two different sizes of material that we tried. We measured the current and temperature of each material as a function of applied voltage. Figure 13 plots this result, and a linear fit allows the actuator's resistance to be measured. This actuator has a measured resistance of 0.3 Ohms. The dimensions of the actuator allow the material's resistivity to be calculated. The actuator shown in Figure 12 has a resistivity of  $1.2 \text{ e}^{-6}$  (Ohm-meters).

- DC MOTORS

We chose to implement three different types of DC motor-based actuation: vibration with an eccentric mass, thrust via a propeller, and force via a lead screw. These variants were chosen more for their availability than their direct applicability in a micro-machine, though it should be noted that MEMS DC motors do exist [2].

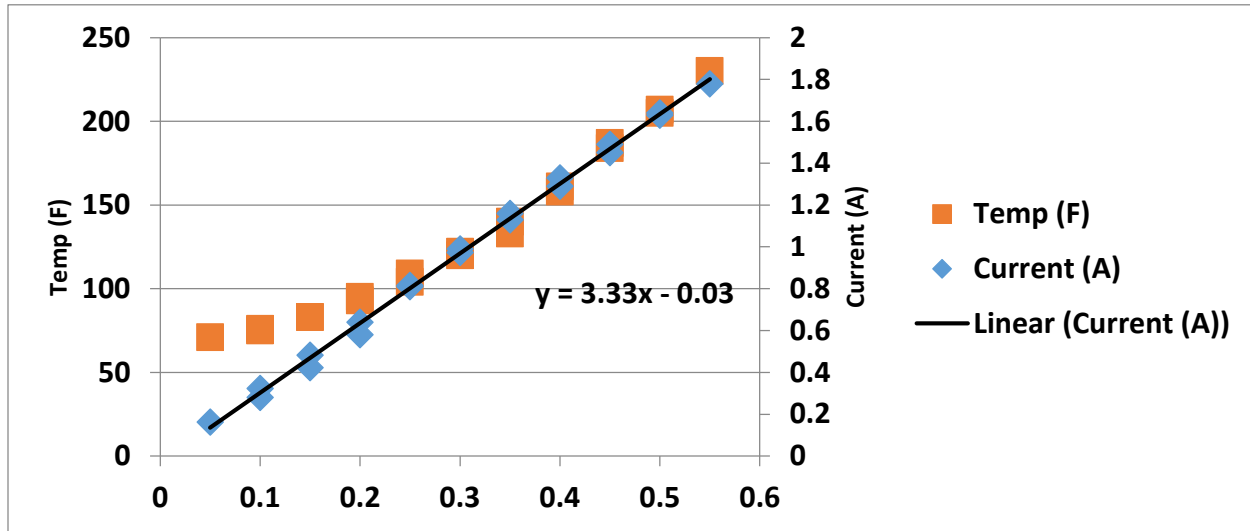


Figure 13: Temperature and current vs voltage for the smaller SMA actuator in the second image of Figure 12.

- Random vibration

Very small (mm to cm scale) motors are readily available, and the addition of an eccentric mass to the output shaft causes the assembly to vibrate. The out of balance vibration force, which is in a plane normal to the motor shaft, can be used to cause translation in a particular direction by adding a material with directional friction. We printed directional friction blocks with an Objet Connex 500 multi-material printer. This printer allows two different materials with different properties to be used in a single part design. The directional friction block has a rigid top material and a set of flexible bristles that are angled away from the top. The rigid top plate has holes that receive the pins from the motor tile above it (see Figure 14). This approach (inspired by the Bristlebot toy) works well, and may be suitable for miniaturization, since it requires no external linkages or direct contact between the motor and the environment.

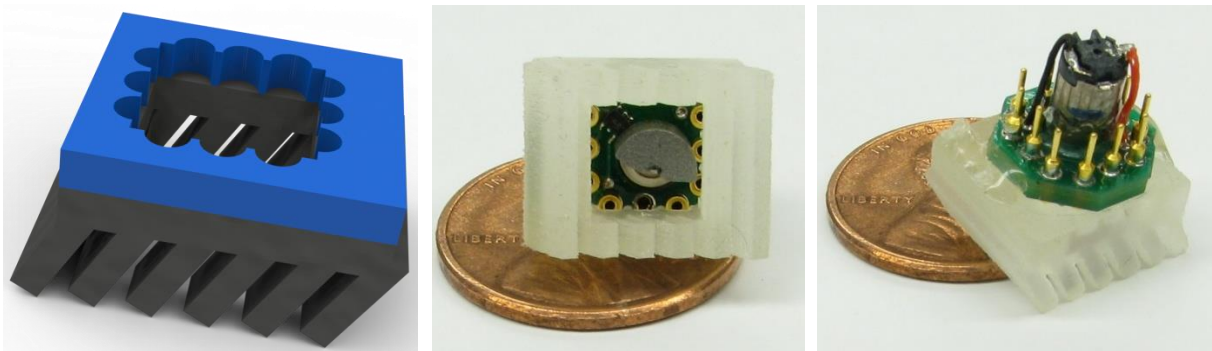
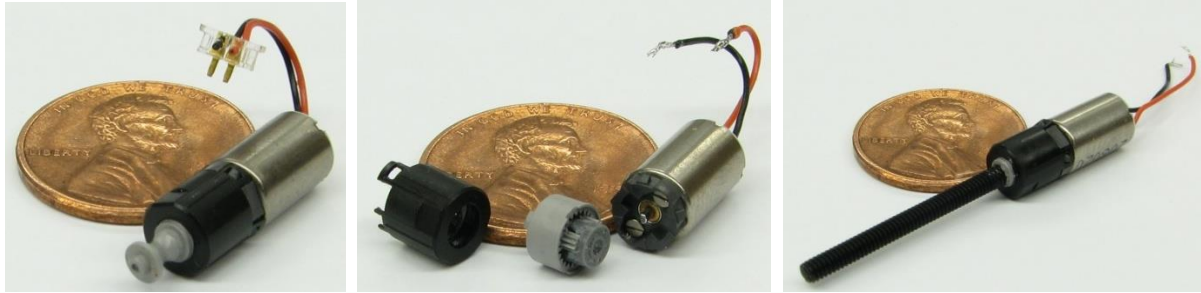


Figure 14: Directional friction block, printed with hard and soft material; shown with motor attached (note that hard and soft material are the same color in the actual part)

- Leadscrew

The two simulated robots shown in the previous report require volumetric actuators, though each one will also work with a simpler linear actuator. The mechanical design of the robot can be simplified if the actuator is capable of exerting force in both directions of travel. A geared DC motor with a leadscrew meets this requirement. We found very small (6mm dia, 16mm long) DC motors with a 25:1 gearbox at a surplus vendor. The motors, shown in Figure 15, had a molded plastic pulley that must be removed. We removed the pulley, then drilled and tapped a hole using a precision lathe. Finally, the plastic leadscrew was threaded into place and secured with cyanoacrylate glue.



**Figure 15: Geared DC motor; with gearbox disassembled; with output shaft tapped and leadscrew glued in place.**

The plastic leadscrew assembly is attached to the voxels with a glue that is compliant, and the plastic leadscrew also can flex to accommodate motion. However, a compliant voxel is necessary to permit the roughly +/- 10% elongation that our simulations assume. We used the Object printer to fabricate a dual-material tile with rigid outer segments that are connected by a flexible midsection. This voxel, shown in



**Figure 16: Flexible voxel rendering; resting configuration; deformation when stressed.**

Figure 16, allows the rigid printed circuit board voxels to move relative to each other when the leadscrew is actuated. Note that the actual part uses rigid and soft materials that are similar in color. The leadscrew voxels and flexible voxels can be connected to form actuated joints; Figure 17 shows a 3DOF actuator, capable of translation, and two rotations.

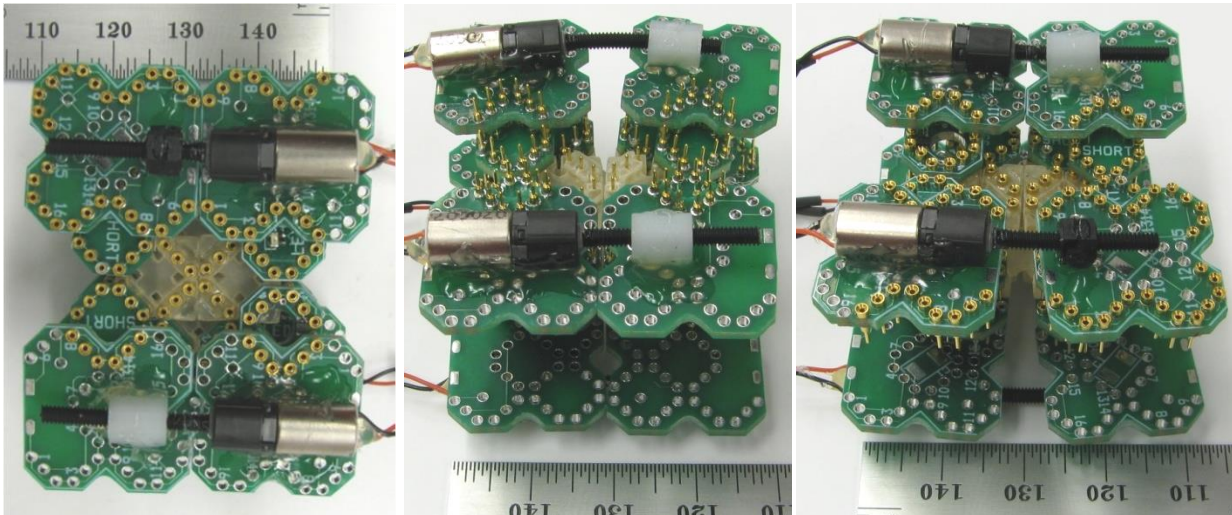


**Figure 17: 3DOF actuated joint composed of 4 leadscrew voxels, 6 flexible voxels, and 20 passive voxels.**

- Thrust via propeller

High power DC motors make modular vertical takeoff structures possible. We decided to build a simple proof-of-concept quadrotor to demonstrate the potential. The structure shown in Figure 18 has no control

circuitry, and is therefore unstable. However, as the video shows, it has sufficient thrust to takeoff aggressively. If gyro sensors were integrated into a voxel, a similar structure could use the existing motor control and microcontroller voxels to stabilize the assembly. If built, it would be the world's smallest quadrotor helicopter.

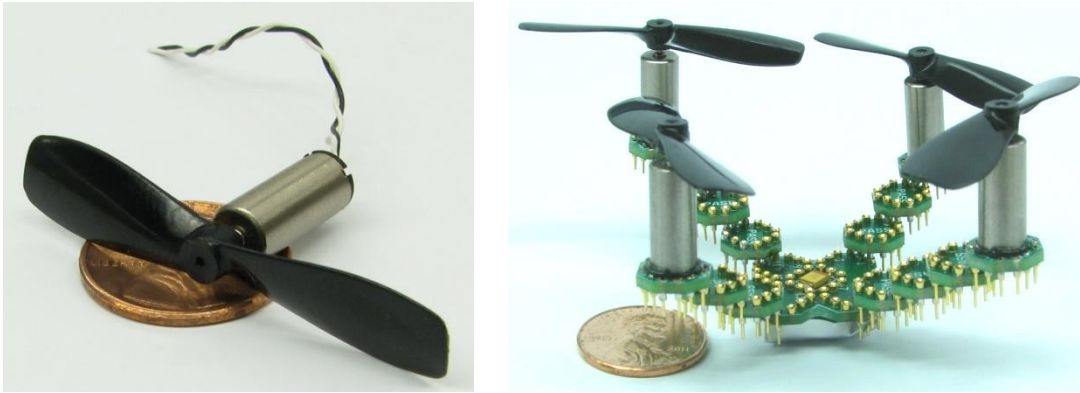


**Figure 18: DC motor with propeller; voxel-based quad-rotor.**

- Thermo-expansion Wax

Materials with a high coefficient of thermal expansion have been used as volumetric actuators; thermal waxes are widely used as actuators in automobile thermostats and hot water tank pressure relief valves. The wax undergoes a significant volumetric change when it changes from solid to liquid state. Typical volumetric changes range from 5 to 18 percent. We are experimenting with wax from two suppliers and are currently investigating various enclosure designs.

- Battery

The electrical circuits shown in the previous report relied on coin-cell batteries with high energy density, but low power density. Each of the actuators presented requires relatively high power, necessitating a battery with higher power delivery. Fortunately, suitable lithium-polymer batteries are readily available. We made a voxel (Figure 19) that supports a rechargeable LiPo cell, and used these voxels in several of the demonstration videos. At least one company [3] is pursuing thin-film rechargeable batteries that are fabricated directly on silicon die. This approach may be appropriate for the micro-scale voxel implementation.

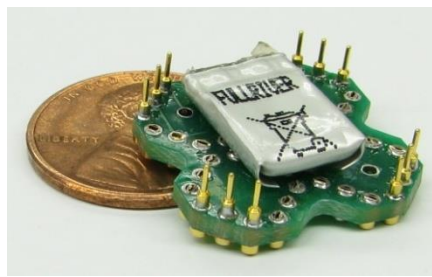


**Figure 19: LiPo battery voxel.**

### Challenges

The thru-hole contacts that are used in the proof of concept assembly require that the signal present at the top of a voxel also be present at the bottom. This creates vertical columns of nets within an assembly that cannot be broken unless a voxel is intentionally left absent from a structure. This is a disadvantage from a design perspective, since it requires that the assembly grow horizontally as more nets are added – the assembly isn't really 3-dimensional. There are two ways to overcome this. The first is to simply use the surface mount contacts shown earlier. This requires a relatively substantial upfront cost, so we have been waiting to order the parts in order to be certain that they are required, and that the design is stable enough to justify the cost. The second method to break the vertical nets is to fabricate some “spacer” voxels that

will not pass any signals. These could be constructed by gluing two circuit boards together, so that they are mechanically, but not electrically coupled. The thru-hole contacts could be cut in half, with the pin side soldered to the bottom circuit board, and the socket side soldered to the top. This approach will impose a substantial manufacturing penalty, since every contact must be manually cut, but it could be feasible for a small demonstration.

The second major challenge is in actuation. The present design is quite rigid, and therefore does not lend itself to the soft types of voxels that we have simulated. We have addressed this constraint by adding the flexible voxels shown in Figure 16, but it may be possible to fabricate unified flexible, actuated voxels. We desire actuators that are small enough to fit inside our cm-scale demonstration voxels, and that could plausibly be applied to the microscale. We are currently evaluating additional actuation packages. One obvious approach to increasing the flexibility of the voxels is to fabricate the printed circuit boards from a hybrid rigid-flex material. Essentially, the boards would have two rigid halves, joined by a ribbon of flex material. This approach might have the opposite problem of being excessively flexible, but this could be overcome by printing an appropriate-durometer shape with the Objet that would connect the halves.

Of the actuation methods mentioned above, the SMA and wax approaches seem most amenable to transitioning to the micro-circuit scale. Nitinol has been widely applied to MEMS devices [4], and wax can be applied in very small volumes; it is nearly scale-independent. Piezoelectric actuators also seem promising, since they have been widely applied in MEMS devices [5].

During Q2 we demonstrated several different actuator concepts. One of them was a linear actuator based on a geared DC motor. Though this approach clearly offers challenges at smaller size scales, it offers the best combination of actuation force, size, power draw and availability at the 1-cm scale.



**Figure 20: Fabrication of linear DC motor/leadscrew actuator**

We fabricated the actuator by attaching a leadscrew to the smallest commercially available geared DC motor. The motor's gearbox was disassembled, and the output shaft was turned-down to a flat in a precision lathe. The flat was drilled and tapped to accept a 2-56 plastic screw, which was then glued in place. The motor's electrical leads were soldered to a printed circuit board that supports stacking electrical connections. These connectors allow adjacent voxels to interconnect electrically. The entire assembly was then placed inside a plastic shell that we designed with a CAD package, and fabricated with our rapid

prototyping system (Object Connex 500). The plastic shell provides structural support, and allows adjacent voxels to connect. The fabrication process is shown in

It is worth noting here that although we're using the term "voxel", we are not requiring that all the shapes that interconnect be identical cubes. In fact, one of the strengths of this fabrication approach is that the system allows shapes that are heterogeneous, in both the physical and electrical sense, to interconnect. The interconnection strategy does not guarantee that a particular morphology will actually do anything useful; however it does provide a uniform mechanical interface, which reduces the design space, and in doing so eases design synthesis and assembly.

We designed a simple robot in VoxCad, and simulated its movement. The structure has 6 actuators and performs an inchworm-like gait, extending one segment of its body while keeping the others motionless. Once that segment has been extended, it contracts one set of actuators, while equally extending another, so that only the next body segment moves. It repeats this process until all body segments have moved. This gait does not rely on directional friction, and therefore can move the robot in either direction. It can turn by preferentially actuating one side more than the other. Figure 21 shows the design of the robot, and Figure 22 shows the physical implementation. Each set of actuators is shown in a different color in the CAD design.

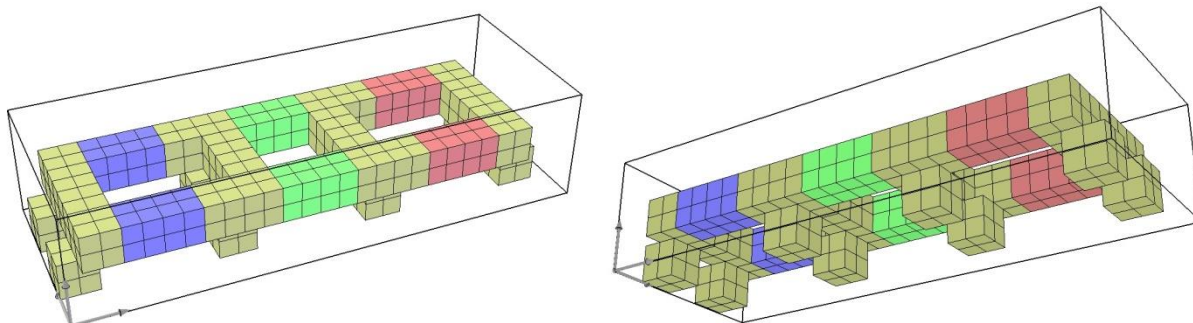


**Figure 21: Design of an inchworm-like robot in VoxCad**

In the simulated robot, each actuator moves with the same amplitude, but a different phase. This very simple control scheme will be improved on in subsequent simulator versions, as concurrent electrical simulation is added. The physical robot was powered externally (each motor was connected to a wire leading to a power supply), and the sequence of the motors was manually controlled. The videos that have been provided with this report show the simulated and real gaits. The behavior predicted by the simulator is very similar to the physical robot's observed behavior.

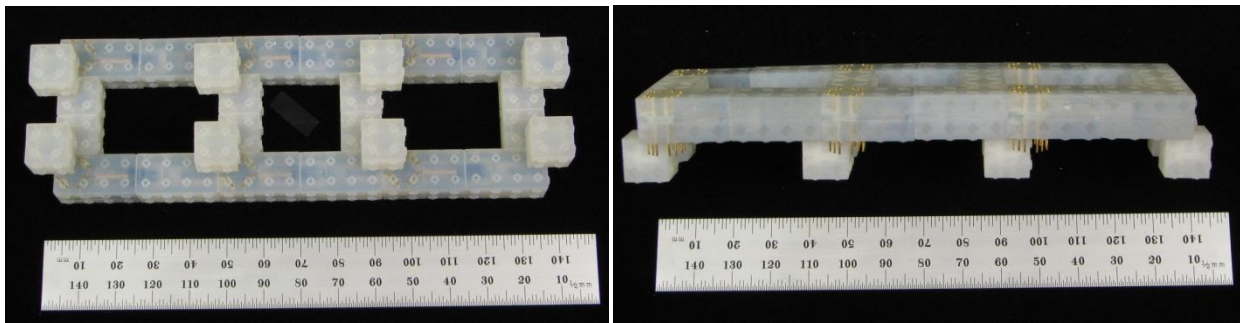


**Figure 22: Physical implementation of inchworm robot using 6 linear actuators**

The robot shown in Figure 22 was constructed by hand, by gluing together individual voxels that had been printed by the Objet Connex 500. This approach is fine for building prototypes, but is not how we envision actually producing larger actuated structures. A complete model can be created in a simulator like VoxCad, either by a human or automated designer, and then whole sections of the design will be printed simultaneously as single pieces, rather than as discrete voxels. The pieces that cannot be printed, like electronics and actuators, will be added in layers, as the model is fabricated. Future printers may allow this

type of interactive construction, or they may automate this with pick-n-place functionality. We can emulate this behavior by slicing the model appropriately, so that whole sections can be printed as a single piece, electronics and actuators are placed appropriately, and then the sections are glued together. This approach offers an appealing hybrid approach to current 3D printing; by using a standardized mechanical interface we can easily add relatively coarse-grained, but functional "digital" voxel blocks to the "analog" model. A 3D printer like the Connex 500, that also had a supply of 10 (for example) different types of pre-fabricated electromechanical voxels, could automatically fabricate complete working robots. This approach sidesteps the large advances in material science that will be necessary to directly print working DC motors.

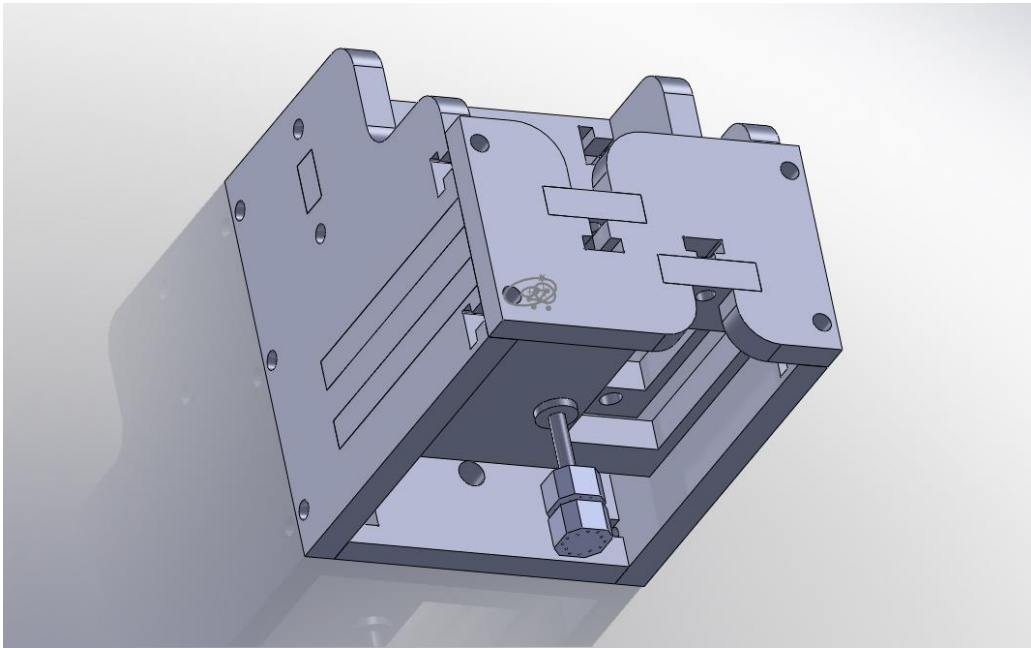


**Figure 23:** Build tool head for the Fab@Home-based desktop voxel assembler.

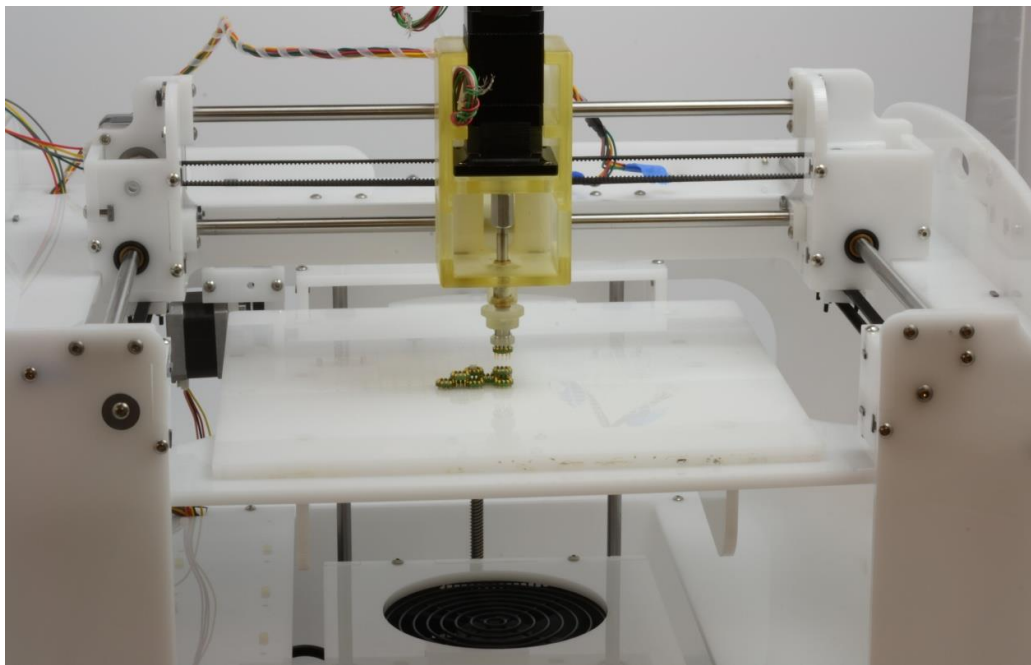


**Figure 24:** Build tool head for the Fab@Home-based desktop voxel assembler.

We envision a technology for desktop assembly of working devices using these electromechanical voxels. We are building an assembler that will enable desktop printing of complete working circuits. The first circuits will be solely electronic (no active mechanical parts), but subsequent parts will have actuators built-into the available tiles. This printer relies heavily on the Fab@Home printer that has been in development within our group for many years. The Fab@Home hardware and software enable generic N-axis coordinated motion machines to be constructed. The voxel printer will combine a 3-axis gantry system with a 2 axis pick-n-place head and a voxel loading system. It will be capable of sequential assembly of small structures; since it is a serial device it is not suitable for large assemblies. We estimate that assembly speeds of 5 sec/voxel will be immediately attainable, and that assembly speeds are not likely to be reduced below 1 sec/voxel with this approach. Nevertheless, this means that assemblies containing several thousand voxels could be automatically assembled in an afternoon. We have already shown a working IR remote (hand-assembled) that required 130 voxels.

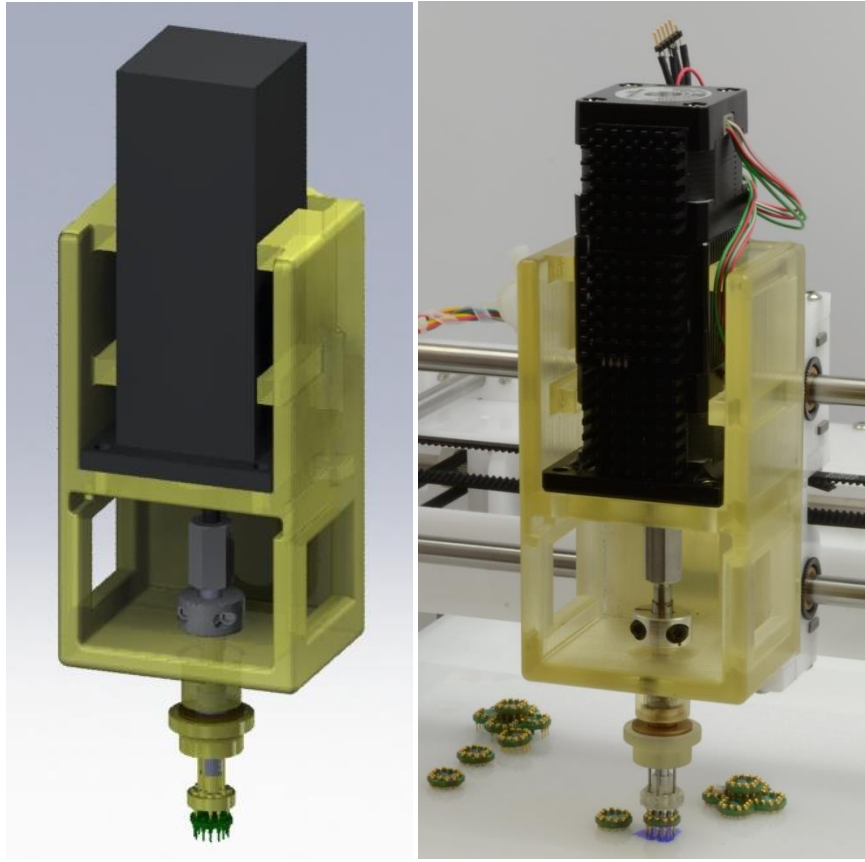


**Figure 25: CAD design and physical realization of the Bitblox assembler toolhead.**

Until now we demonstrated several different types of electrically active voxels, including voxels with microcontrollers, resistors, capacitors, batteries, and actuators based on small DC motors. We call these parts Bitblox, and intend to use them as the "ink" in a system that automatically designs and prints electromechanical devices. Our work in this quarter focused on developing a pick-n-place printer for Bitblox. We adapted the open source Fab@Home 3D printer to serve as the assemble chassis for this printer. We modified the existing Fab@Home chassis by adding two additional motor drives to the z-axis, in order to provide a stiffer build platform, and to also provide sufficient mating force. The assembler, including the tool head is shown in Figure 24. The toolhead, shown in Figure 25 uses a two axis motor that allows the end effector to have both linear travel as well as rotation. The linear travel of the end effector is used to drive ejector pins into each Bitblox piece, which releases the part from the toolhead and deposits it onto the part that is being built. The rotational degree of freedom allows the Bitblox to be rotated as they are being assembled, a requirement since each piece's rotation is part of the design file. The overall part that will be constructed from a Bitblox assembly is currently designed manually and specified using a MATLAB-

based GUI, shown in Figure 26. This GUI automatically generates the G-code toolscript required to move the 5-axis machine through the correct sequence of actions to assemble the desired part.

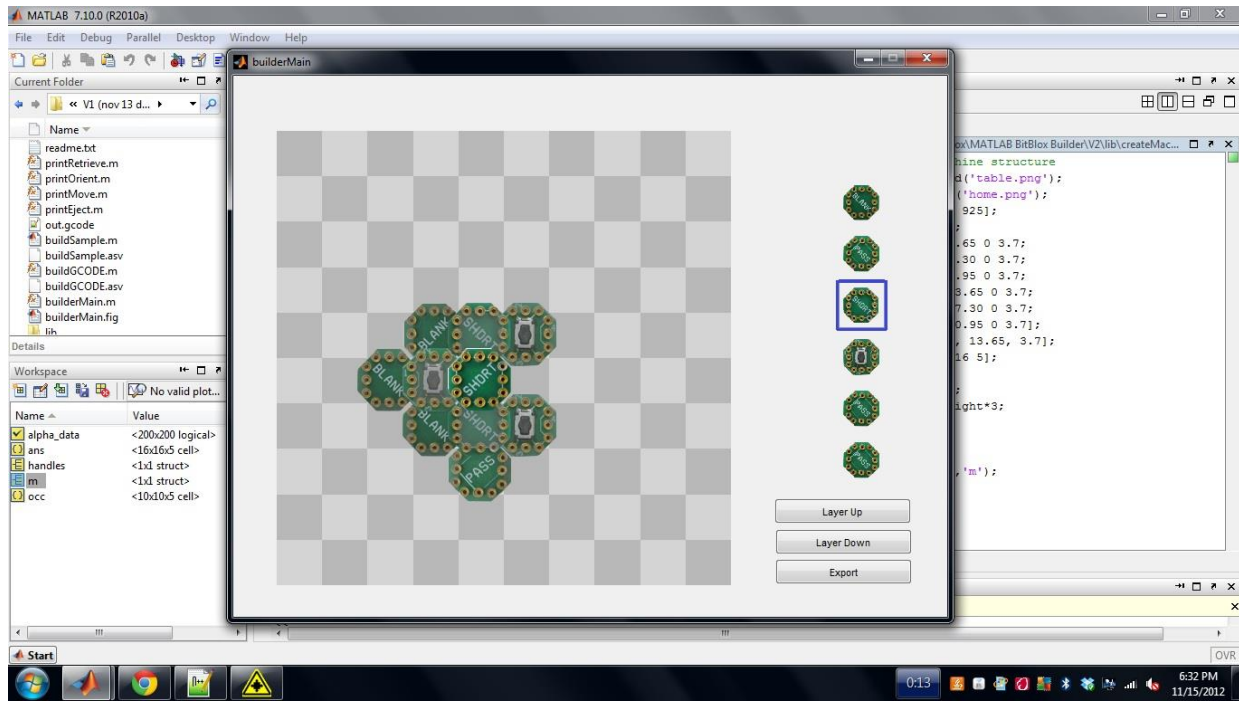


**Figure 26: Design software that allows a particular Bitblox design to be manually defined.**

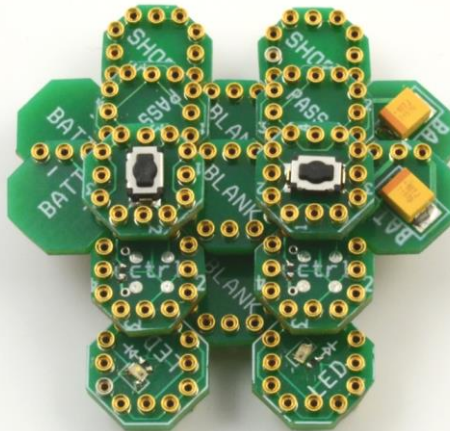


**Figure 27 - Printed IR remote control, using 17 tiles, with 6 different types.**

Though we demonstrated the pick-n-place assembly capability of this approach, we moved parts from pre-existing positions on the build tray, rather than from a feeder system, that would allow larger numbers of parts to be assembled. We have designed a feeder system that accepts reels of plastic tape with Bitblox modules already placed in them, in much the same way that individual electronic components are mounted in tape-reel systems for automatic circuit board fabrication. The design is illustrated in Figure 28 and Figure 29, which show a rendering of the CAD model, as well as the physical prototype. The sprocket shown in the figures is turned by a servomotor, and engages the holes in the carrier tape. An optical sensor provides fine alignment, via a feedback signal to the drive circuitry.

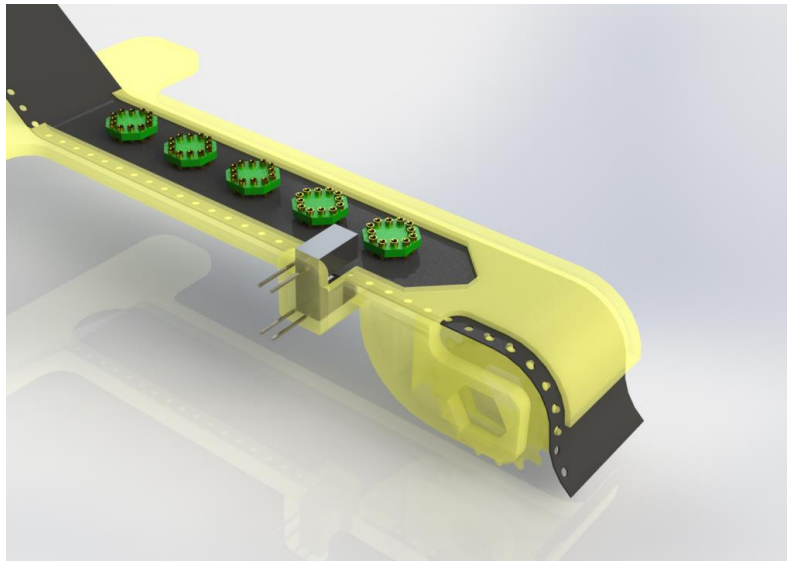


**Figure 28 - Rendering of the CAD model of the Bitblox feeder mechanism. The Bitblox tiles are carried in a tape that contains drive/alignment holes along the edge. A servomotor (not shown) rotates a cog that interlocks with the holes in the tape. An optical sensor provides fine alignment.**

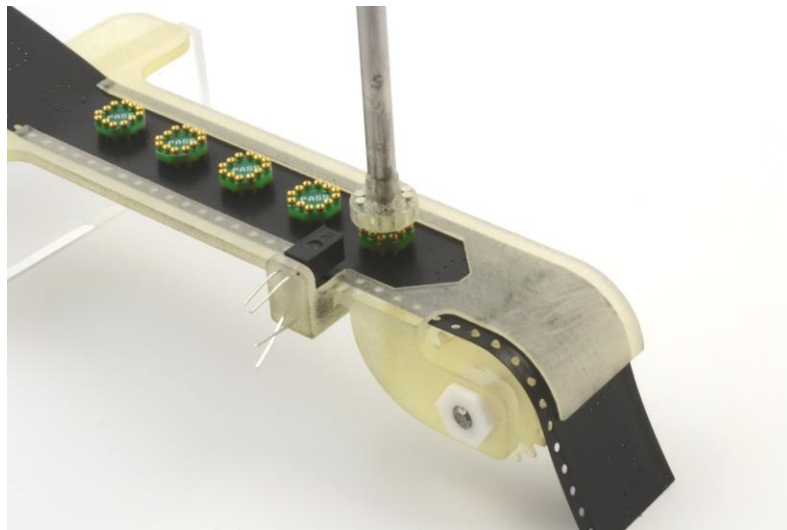


**Figure 29 - Physical implementation of the Bitblox feeder. Fabricated using an Objet 3D printer.**

### References

- [1]. Sangbae Kim, Elliot Hawkes, Kyujin Choy, Matthew Joldaz, Joe Foley and Robert Wood, "Micro artificial muscle fiber using NiTi spring for soft robotics", IEEE/RSJ International Conference on Intelligent Robots and Systems, October 11-15, 2009 St. Louis, USA
- [2]. Multi-Wafer Rotating MEMS Machines, Jeffrey Lang and Sauparna Das, Springer 2010, ISBN: 978-0-387-77747-4
- [3]. <http://www.cymbet.com>
- [4]. Yongqing Fu, Hejun Du, Weimin Huang, Sam Zhang, Min Hu, "TiNi-based thin films in MEMS applications: a review", Sensors and Actuators A: Physical, Volume 112, Issues 2-3, 1 May 2004, Pages 395-408.
- [5]. Muralt, P., "Recent Progress in Materials Issues for Piezoelectric MEMS". Journal of the American Ceramic Society, (2008) 91: 1385-1396

## *Task 3: Assembler development and construction*

### Task overview and milestones

This task requires the use of parallel stacks of feeders of components and roller type deposition with an escapement mechanism to control the deposition. Alternatively, the use of layer-wise parallel assembly will be used. Mock voxels were to be designed and built in order to decouple this task from the voxel-development tasks. We developed three different kind of assemblers: hypodermic needles, Electroosmosis Device (EODS), Electroadhesion based assembler. We also worked on an electrowetting based assembler, but due to various physical limitations on electrowetting phenomena, such a device was found to be infeasible.

### Technical Progress

#### *I. Hypodermic Needles*

In order to test the ability of water droplets to pick up the tiles, as well as to test the ideal droplet diameter, various gauges of hypodermic needles and syringes were used to pick up the tiles. (See Figure 30)

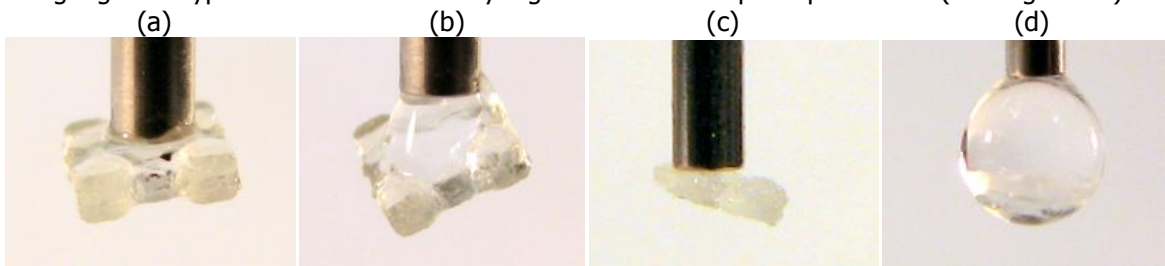


**Figure 30: Figures (a) and (b) display water droplets being dispensed from a 15 gauge needle picking up 1000 $\mu\text{m}$  tiles. While Figure (a) seems to be picking up the tile well, it can be seen that too much pressure and too large of a water droplet can cause instability in the surface tension. Figures (c) and (d) show a 21 gauge needle picking up 500 $\mu\text{m}$  tiles. Alignment issues can be seen in (c), and in (d) too large of a droplet has actually engulfed the tile entirely**

In using these needles as well as microfluidic relationships between contact angles, it is possible to determine the best size diameter for the droplets to pick up the 500 $\mu\text{m}$  tiles.

$$\gamma_{LV} \cos \theta = \gamma_{sv} - \gamma_{sl}$$

where gamma represents the surface tension or energy between the different interfaces. For instance  $\gamma_{LV}$  would represent the surface energy between the liquid and vapor, which could be looked up in common surface tension tables. Based on the fact that the contact angle,  $\theta$ , cannot be measured due to the uneven surface of the tiles, this relationship can only give an approximation. Based on these trials, the ideal water droplet diameter would match the largest dimensions of the tile, that being 500 $\mu\text{m}$ .

#### *3D Printed Assembler Heads*

In order to rapidly create a multi-needed assembler head, an Objet 3D printer was used to print three different types of heads. The first design tested consisted of four needed heads of inner diameter 400 $\mu\text{m}$ , outer diameter of 500  $\mu\text{m}$ . This would allow for the device to pick up every other tile for placement. Using a syringe to control the water supply, this head was tested for its ability to accurately and consistently pick up and place tiles. (See Figure 31).

From these tests, a number of major issues were encountered. While the 3D printing allowed for rapid creation of the assembler heads, support material that must be removed from the outside of the body and from the inside of the needles proved to be a very difficult task. When removing support material from inside the needles, there was great risk of damaging the symmetry and the circularity of the needle end, which is necessary to create a round droplet. Furthermore, some of the tubes were clearer of excess support materials than others, meaning that the water distribution between the tubes was often uneven.

Finally, since the needles were printed using FullCure720 plastic material and were of such small size, they were easily damaged in transit and in regular usage.

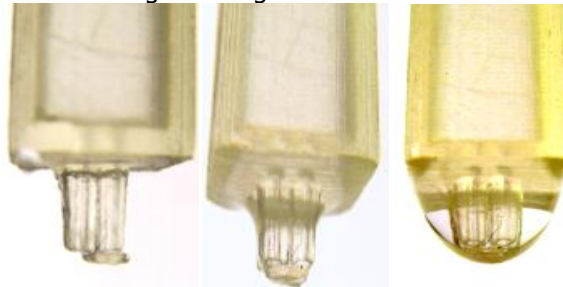


**Figure 31:** The three figures from left to right show the progression of water addition into the tubing. If given just the right amount of surface tension, the tile could be picked up securely. However, from the second and third images it can be seen the even the slightest addition of excess water can cause the tile to be lost in one large water droplet encompassing the tubes

The second step was tests a comb submersion technique, which used an outer tube diameter of 500  $\mu\text{m}$  with no hole in the center of the tubes. In this experiment, the tips were dipped lightly into a plate of water, then lowered onto the platelet of tiles. As it can be seen in Figure 32, the tiles were successfully picked up. However, the alignment of the raised tiles were not necessarily in line with the geometry of the object they could be added to, which could later be solved by creating a pinned base that would allow for all the tiles to be initially inline before the pick and place action were to occur.



**Figure 32:** Several trial of the comb submersion technique can be seen, along with some of the difficulties of keeping a square alignment

After further analysis, the microfluidic effects of the water interacting with the outsides of the tubes was determined to be a large factor in the failure of consistent pick and place action. Due to the close proximity of the tubes to one another, and the slightly hydrophilic properties of the Objet printed material, water was being drawn upward between the tubes creating one large water droplet. The main reason for this is due to the hydrophilic material properties, but also due to the fact that the distance between the tubes is less than the capillary length of water.

There exists a particularly length, capillary length ( $\kappa^{-1}$ ), beyond which gravity must be considered in surface tension calculations. Therefore, under this length, gravity is not in effect, per say, and this causes the water to move up between the tubes [1]. The capillary length can be calculated by:

$$\kappa^{-1} = \sqrt{\gamma/\rho g}$$

Therefore the capillary length of water is about 2mm, which is much greater than both the radius of the tube holes and the distance between the tubes. In order to remove some of these effects, an oil based coating was added to the outer tubing. The added hydrophobic coating helped marginally in removing some of the droplet coalescence, but wore off quickly.

#### *Hypodermic Needles with 3D Printed Base*

In order to increase the accuracy of the tile placement, hypodermic needles were inserted into a 3D printed base. This removed the issues regarding uneven tip circumference and uneven inner tube diameter along the length of the device. The inner and outer diameter mimicked that of the 3D printed tubes. The results

of this trial proved slightly better than the 3D printed tubes. There were still issues with even distribution of water through the tubes, and the oil based coating on the metal tubes wore off over time and restored the hydrophilic surfaces.

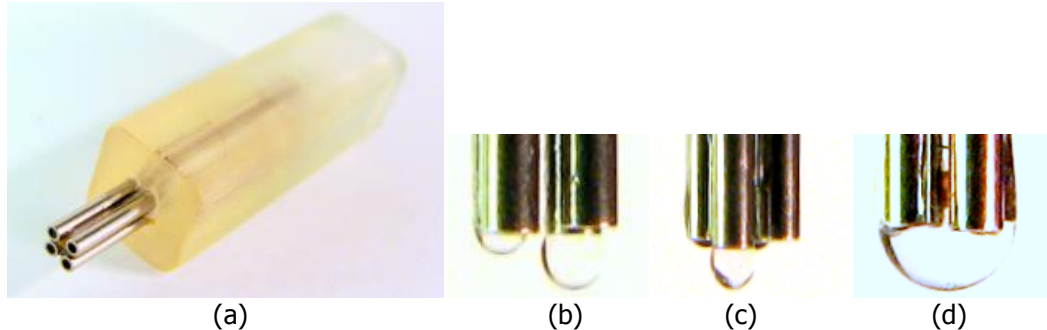


**Figure 33:** (a) Shows the hybrid hypodermic needle/3D printed device. (b) and (c) Show complications with uneven water distribution between tubes. (d) Shows the individual droplets merging due to close proximity and violation of capillary length

#### Mock Tiles

From past work in the Cornell Creative Machines Laboratory, the initial voxel designs have been initialized, and all assembler testing has utilized these geometric constraints as a control. While future versions will include electronic and programmable components, the general shape is to be 2.5D, with an interlocking, flip invariant geometry (See Fig. 12 [2])

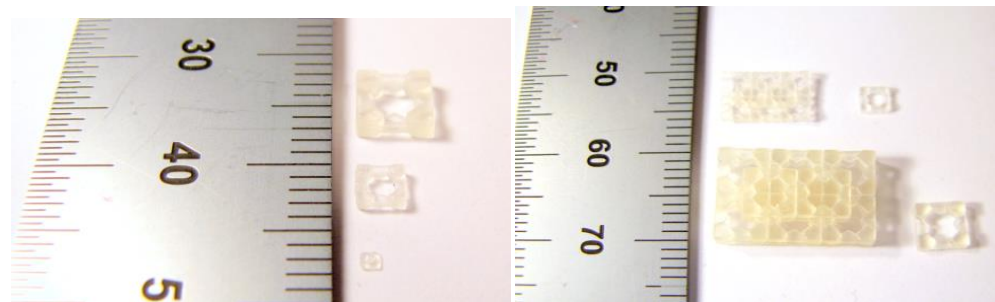


**Figure 34:** Image of 3D printed tiles of sizes varying from 1, 3, and 5mm square, and 3D tiles manually assembled

Based on this current geometry, it is already obvious that using water droplets will have minor complications in the attempt to pick up and hold the tiles. Due to the sharp corners, the large center hole, and the various heights of the tile, a single water droplet will not be able to have a constant contact angle, and will not be able to maximize surface contact area. Therefore when testing the surface tension and contact angles of the water droplet on a flat, square tile of the same material (either the SU-8 from the photolithography tiles or the FullCure720 plastic from the Objet 3-D printed tiles), there is an extreme over estimate in calculated surface tension values.

#### Base plate design

In order to ensure that the tiles will be correctly aligned and spaced when being deposited, multiple 2.5D platforms were designed and 3D printed in order to test for the best geometry for adhesion, easy release, and correct alignment. The three platforms that were tested (for the 3mm tiles) can be seen below.

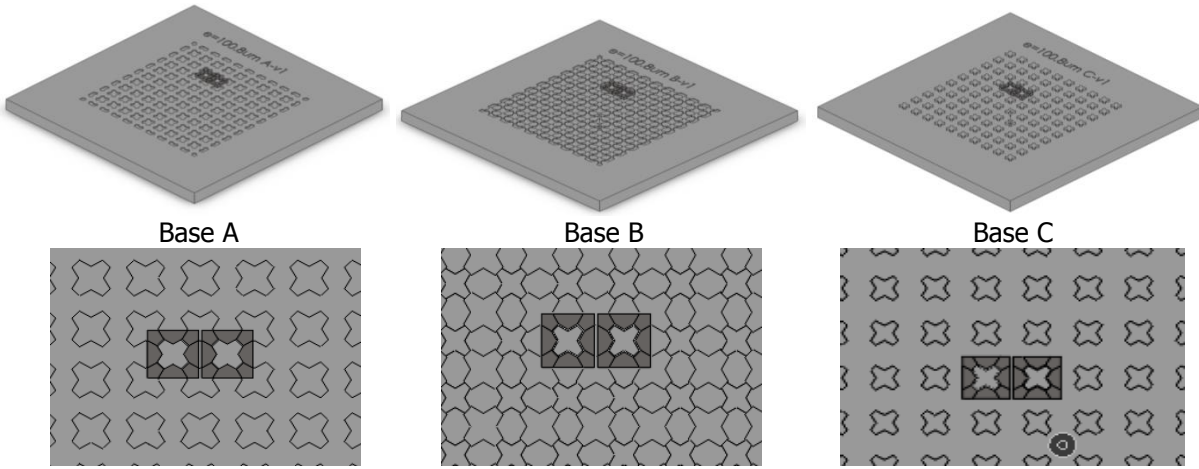


**Figure 35.** The upper and lower figures show the 3D model of the three different base plates. Base A has only the feet inset, Base B has the feet inset and half of the center hole inset, and Base C has only the center inset.

These three different bases were tested for two main requirements: mechanically holding the voxels in place, and hold them in place with a force less than that of the forces that hold the tiles together when assembled. The importance of these two requirements means that the tiles can easily be placed and aligned for assembly, and also allow for ease of part removal from the base when the assembled component is complete. Another view of these three bases can be seen from the tile point of view.

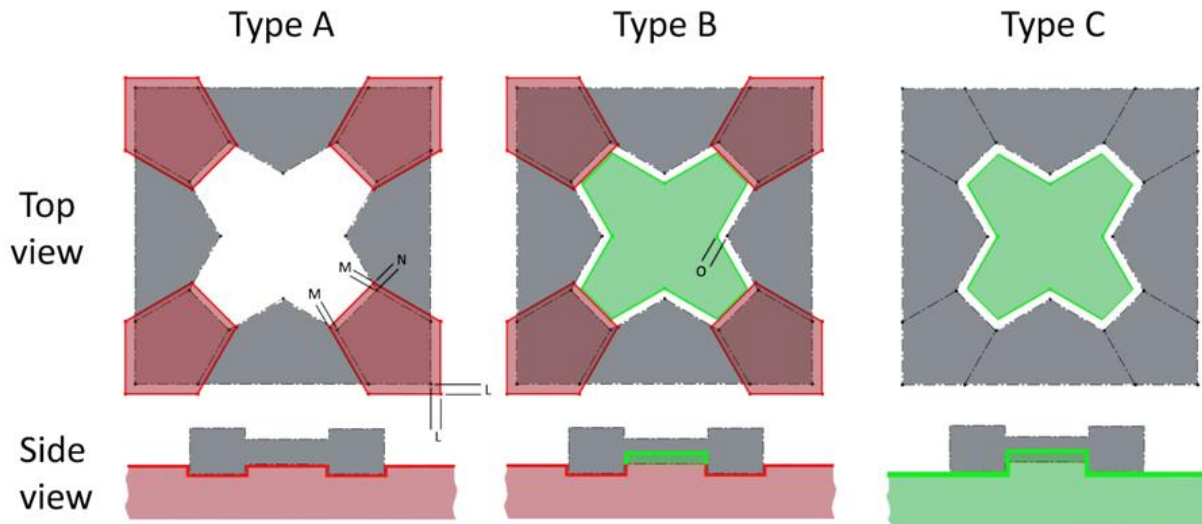


**Figure 36.** In alphabetical order from left to right, the tiles show which parts of the tile interact with the platform. M, N, E, and O refer to different error values that needed to be considered in designing the platform.

In designing these platforms error needed to include based on the error of the 3D printer, error in cleaning the tiles, and error in manipulation. Based on the Objet Connex 500 printer error given by the manufacturer of 600DPI. A variety of E was looked at, but it was found that due to the inconsistencies in cleaning and handling, the error was not consistent between voxels or between base plate holes. Therefore an error, E, of 0.6mm was used and an error, O, of 0.51mm was used.

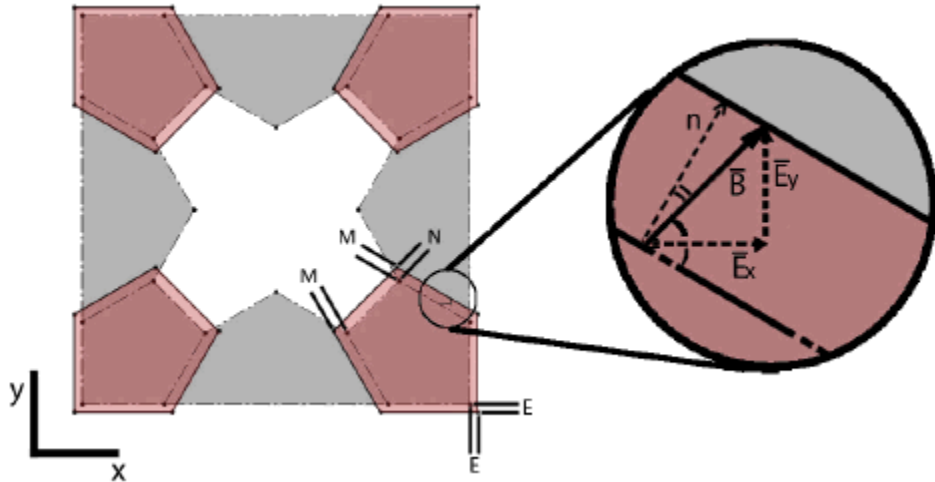


**Figure 37.** The theoretical feet covered by the feet with incorporated error (in red) can be seen, and how E was determined.

Actual from there the tiles were manually assembled using tweezers or syringes to determine which platform allowed for easiest assembly, and ease of release. Below is Base Plate B with tiles.

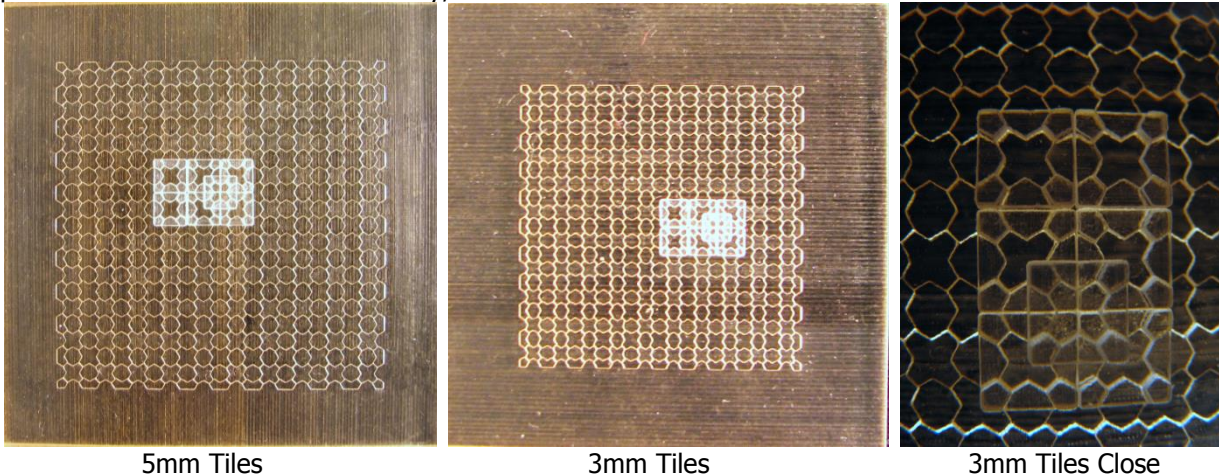


**Figure 38.** Actual photographs of the 3D printed tiles and Base Plate B in the assembled configuration.

#### *Base plate testing using syringes*

The base plates were tested using needles and syringes of a range of sizes. The goal was to pick up the tile in its center from a flat base and move it to its position on each of the three different base plates. The next test was to try to use the same technique to remove these tiles from the platform and to move them either to a flat base or to another platform hole. The results of these tests showed that often the needles did not pick up the tile in the center or keep the tile parallel to the platform, showing some rotation in all x, y, and z axes. If the tiles happened to be picked up correctly and moved to the platform, it was difficult to release the tiles due to the surface tension of the water working to keep the tile connected to the end of the needle. Not all trials were unsuccessful; some trials the tiles were picked up, moved and deposited without residual water forces. However, since it was just a needle tip, it was unsure as to whether or not the tiles were fully pushed into their base or if they were floating slightly on the surface. This happened with all three base plates. Each trial was videotaped.

In addition, the reverse process was tested. Tiles were placed on the platform and tested for syringe removal. This was found to be the most difficult task, since the error incorporated in the tiles allowed for the water droplets to spread into the foot holes or platform base, destroying the surface tension

concentration necessary to remove the tiles. This scavenging of water could be due to the hydrophilic/hydrophobic properties of the materials, or due to the fact that the surface tension was not enough to overcome the frictional forces between the tiles and the base plate walls. On a more general note, the surface tension and other water properties do not scale linearly. Therefore, while the surface tension may not have been strong enough to pick up the tiles from the center on the 3mm scale, it may be enough on the micron scale that will be the final product of this study.

#### *Base plate testing using prongs*

Another approach to moving these tiles involved using a dipping technique and a four pronged 3D printed device designed to pick up the tiles from the feet instead of from the center. The prong was dipped into the water, allowing small droplets to form on the bottom of the four prong ends. Once in contact with the tiles, a bridge was formed between the tile and the prong, and capillary forces and surface tension were able to remove the tiles from their positions in the platforms. While this seemed to be more successful than the syringe attempts, this technique will be much harder to scale down. Furthermore, the bases of these prongs would be smaller than the holes of the syringe, which on a smaller scale could cause evaporation during motion of moving from the water source to the tiles.

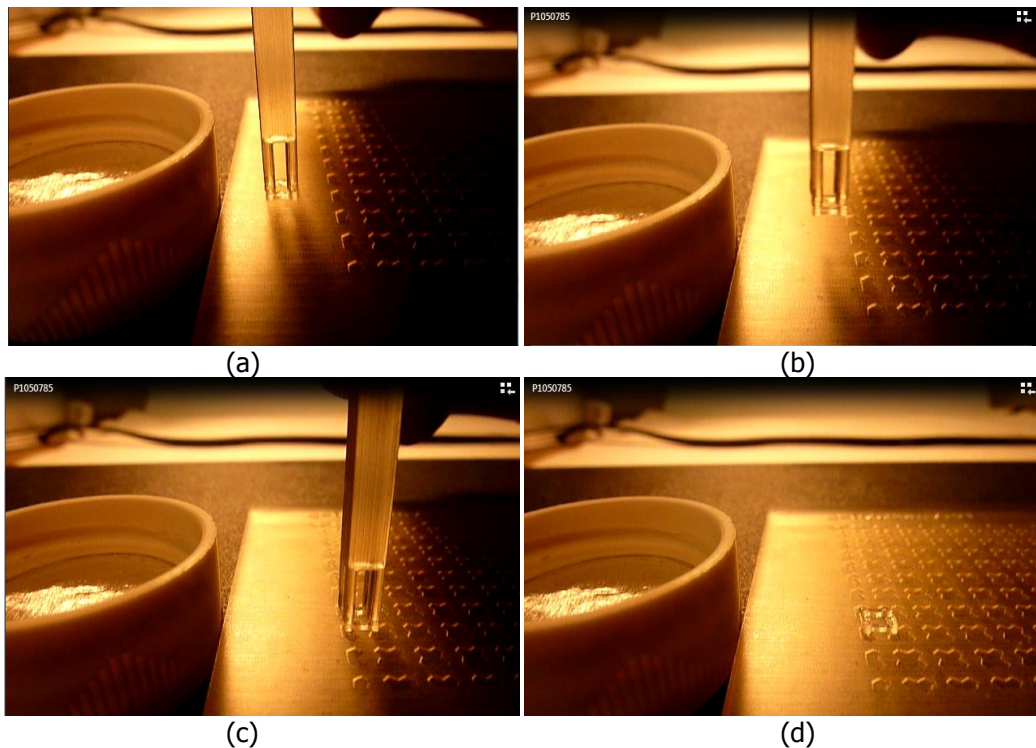


**Figure 39. Actual photographs of the 3D printed tiles and Base Plate B in the assembled configuration.**

#### *Electroosmosis Device: EODS*

Within the School of Chemical and Biomolecular Engineering, Dr. Paul Steen and his research group have developed electro-osmosis droplet switches (EODS) that can move water from one tunnel to another, as seen in Figure 39. Electroosmosis relies on a layer of excess ions, the electric double layer or Debyelayer, naturally present in the liquid adjacent to a solid. An electric field imposed in the surface parallel direction moves the ions, which drag the liquid along a tube or channel by means of viscosity. The net velocity in a tube can be expressed as the superposition of Poiseuille and moluchowski electro osmotic velocities when the electric double layer is much smaller than the tube size [3]. This concept could be used to control individual droplets within the assembler tool head. In order to test the chemistry and physics behind this phenomenon, an EODS was created and tested to ensure that the water could be controlled using only changes in voltages, as seen in Figure 40.

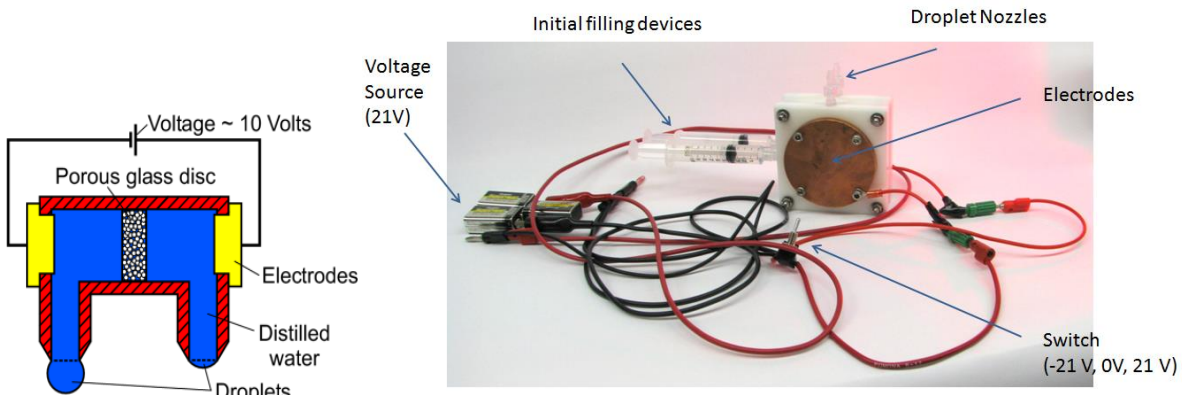


**Figure 40. Theoretical depiction of EODS and actual EODS experimental test bed.**

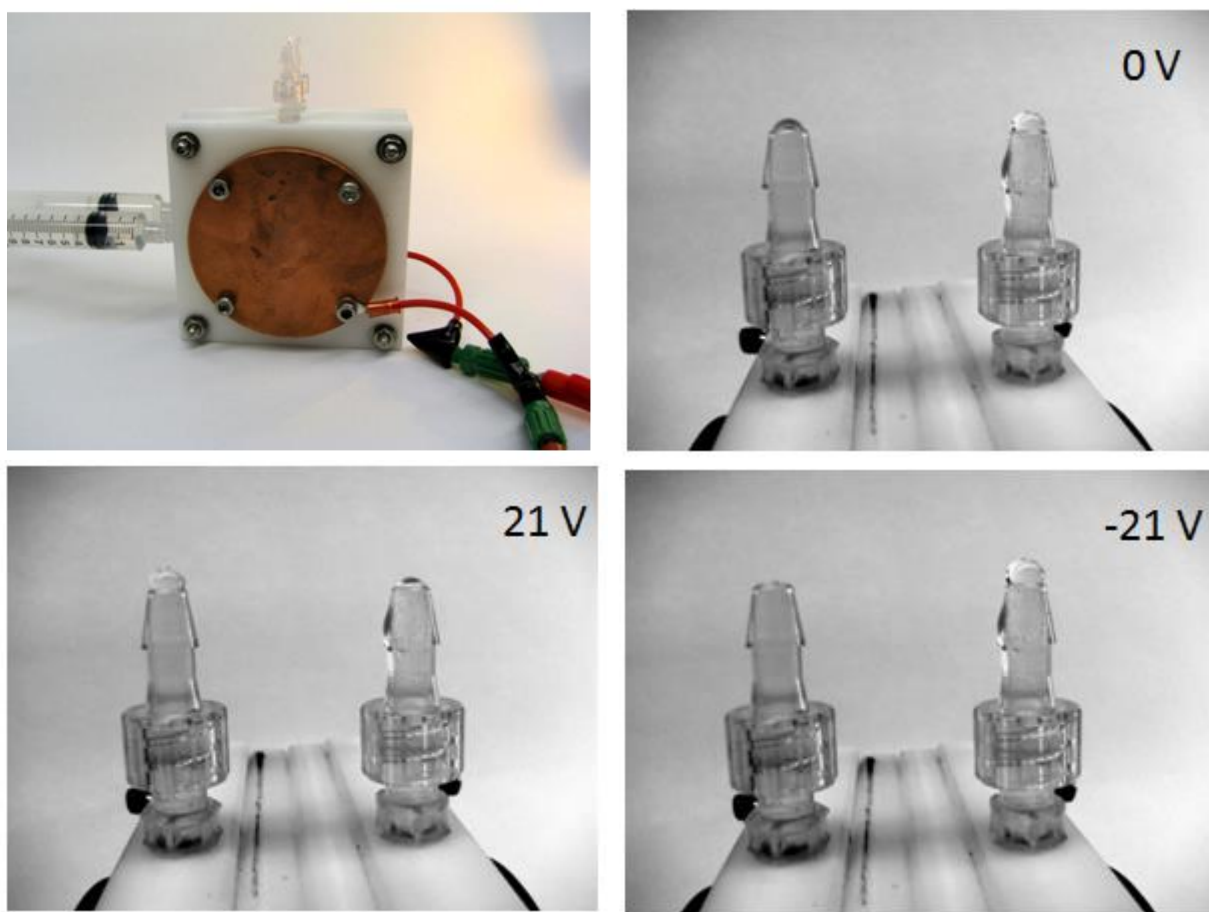


**Figure 41. In the four photographs, the EODS device can be seen, and three close ups of the nozzles and droplets throughout the electro-osmosis process. As the voltage changes the water moves from one side of the frit to the other, pushing up the droplet on one side, and pulling down on the droplet on the other.**

The porous glass disc that was used was a 50 mm Ultra Fine Filter Frit Disc. The body was machined out of delrin. The syringes attached were only used to fill the device, and were not used at all during the experiment. The experiment was performed by first pushing droplets into the two heads using the syringes. Due to scavenging the two droplets will inevitably be unequal. The syringes were then disconnected, and a positive voltage was applied, causing an induced velocity of the water and the droplet sizes switched. The voltage was then brought back to zero, and looked the same as in the beginning of the experiment.

Finally the voltage was switched to a negative value and again the velocity was induced but in the opposite direction causing the other droplet to grow. These stills can be seen below.

## *II Electro-Osmosis Device: SECAD design*

The Switchable Electro-Osmosis Capillary Adhesion Device (SECAD), which has been designed by the Steen Group at Cornell University, offers a means of using this electro-osmosis phenomenon to create individual droplets that can be controlled using a voltage source with no movable parts besides the mechanical switch itself [4].

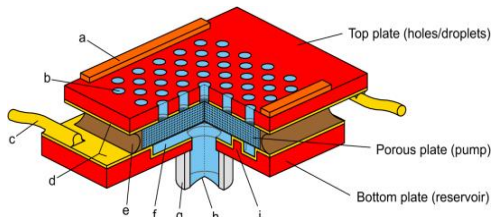


**Figure 42.** The left figure shows the theoretical set-up, while the right figure shows the actual experimental set-up.

The original device was made using a number of rubber gaskets to channel water through a delrin reservoir. This design was altered using a 3D printed device to increase accuracy and repeatability. From there water is channeled through a number of gaskets, electrodes and a single frit and front plate. This design can be seen in Figure 43. The top line shows the original set up, and the bottom line used 3D printed design to eliminate all but one gasket. The O-Ring is necessary in either set-up.

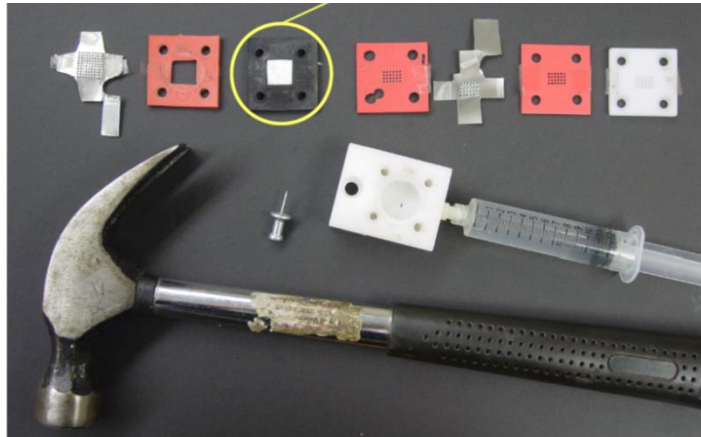
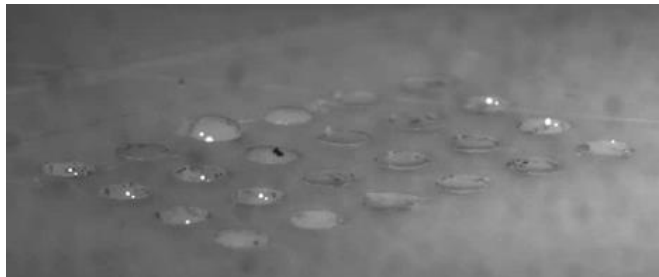
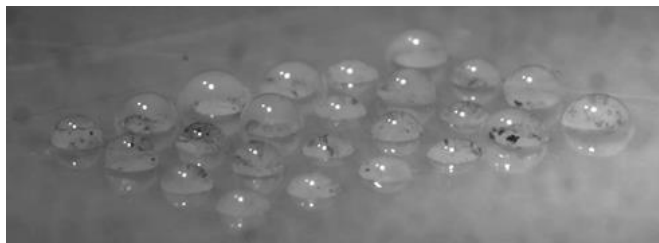


**Figure 43.** The left figure shows the two sets of inner reservoir fluidic channels. The right figure shows the top layers used to channel the water droplets through the frit, gaskets, and finally the delrin top evenly.

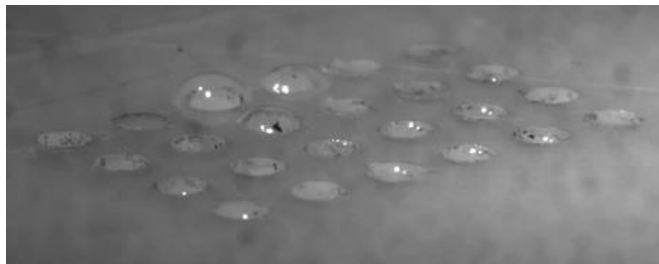
Above the reservoir is a series of electrodes, gaskets, a frit, and a delrin plate in order to channel the water droplet velocity. See Figure 43 above. This was replicated based on work from the Steen group paper "Capillarity-based switchable adhesion" [4], but the results were extremely difficult to repeat due to the fact that the original pieces were individually hand-made. Therefore, 3D printing was used to replace some of the gaskets using Tango+, a more flexible material (the circled gasket in Figure 43 shows the place where the new material was used). Therefore the frit was able to fit much more snug into its position and remove chances of scavenging between layers. The electrodes were made using 3/1000" thick steel, and the holes created using a tack and hammer. This device was shown to work as seen in the video stills below.



(a)



(b)



(c)

**Figure 44.** Figures a-c show the process of alternating currents. Figure a shows the initial condition with no voltage applied. Figure b shows water droplet formation when a positive voltage is applied. Figure c shows the droplets retracting when a negative voltage is applied.

It can be seen that the device does not offer evenly sized droplets or even rates of droplet growth. These issues could be due to the fact that precision is lost when creating holes using the tack/hammer method, as well as errors in the machined gasket and delrin holes. See below for close up of machined gasket holes.

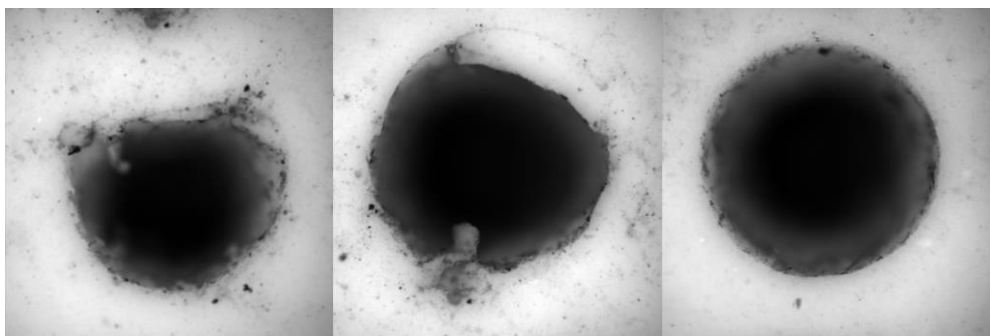


**Figure 45.** Microscope images of the 900 micron gasket holes punched in the Cornell machine shop. It can be seen that some come out very spherical, while others do not. This difference could lead to scavenging and other issues in water flow in the SECAD. Photos by Ashley Macner, Cornell University Steen Lab.

Furthermore, the effect of the tightness of the screws has not yet been determined. It has been found that when under-tightened there are leaks in between the layers, but when over-tightened the frits could crack and the delrin top layer has been found to bow. Therefore these effects will have to be further

analyzed. Another issue is water droplets "walking". This can be seen in the second and third images where the water droplet dome diameters are actually larger than the holes themselves. This can be prevented in machining using a "volcano" technique where the drill is positioned in such a way that about a 70 micron ridge is formed around the holes helping to prevent the water droplets from walking. However, these rims are unpredictable and often uneven as seen below:

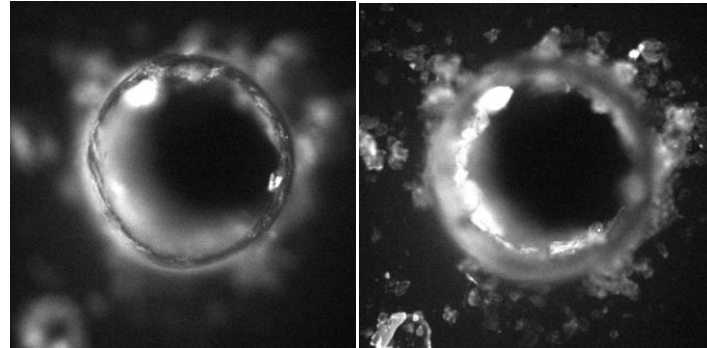


**Figure 46.** The volcanoes can be seen under a microscope. The left image shows an ideal volcano with a circular rim and even thickness, while the right image shows volcanoes that "bleed" or overflow in such a manner that does not discourage scavenging. Some holes displayed no volcanoes at all. Photos by Ashley Macner, Cornell University Steen Lab.

#### *Electro-Osmosis Device: PICEM (Pick and Place Individual Controlled Electroosmosis Machine) design*

We propose a Switchable Electro-Osmosis Capillary Adhesion Device as a possible means of picking and placing individual tiles. Inspired by the previous work by the Steen Group at Cornell University and their SECAD device [1,2], a robust and repeatable design had been established using columns that were individually connected in order to test the idea of individual control. This device offers a means of using electro-osmosis phenomena to create arrays of droplets that can be controlled using a voltage source with no movable parts besides the mechanical switch itself, which will later be removed and incorporated into the platform control system. The original device can be seen below in Figure 42. The printed circuit board (Figure 49) was connected to the voltage source through a number of wires soldered to the board itself. The results of these tests, and the issues with electric field line interference were explained in the previous report. A new design was created with a printed circuit board that had holes of diameter 20 mils and a Sn/Pb coating of diameter 0.66mm. This new design was a 5 X 5 array of holes spaced at 2mm from center to center channel. This allowed for further analysis of the effects of the electric field lines while still allowing for the advancement of individual control. Again the materials were created using mainly 3D printed materials.

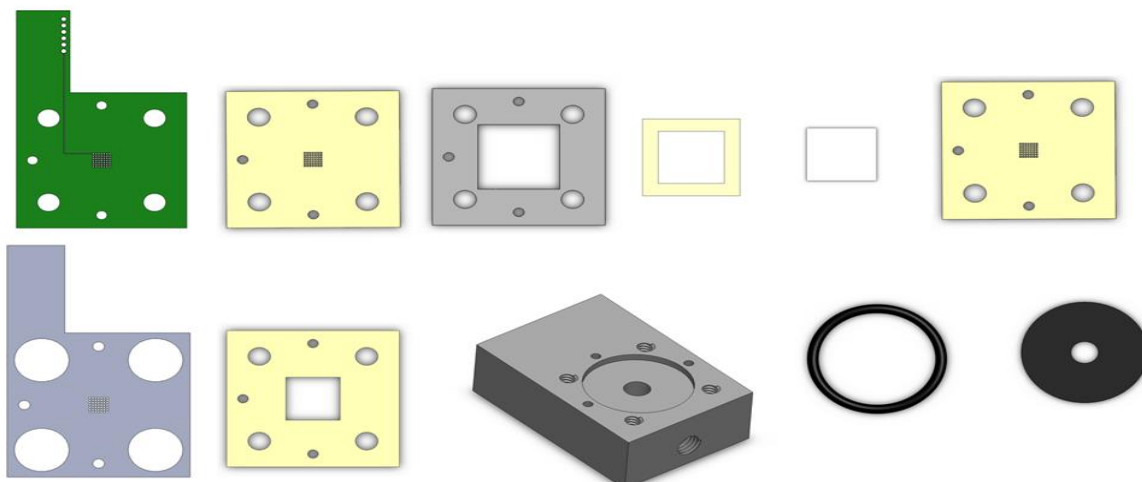


**Figure 47:** Circuit board leads made of copper with a tin-lead alloy (most likely 63/37 Sn/Pb). Green represents circuit board, yellow: Tango+, grey: Fullcure 720, light grey: stainless steel, black: rubber.

The resolution of the 3D printer is in the tens of microns scale. The SolidWorks model was created, as seen in Figure 47 and it was used to print the different components of the device using Tango+ for the gasket material, and FullCure720 for the delrin substitution. Beyond just substituting more accurate printed materials for the hand crafted pieces, a printed circuit board and laser cut electrodes were outsourced in order to again increase accuracy of spacing, hole size, and alignment between layers. Many of the issues of droplet walking and varying droplet size could have been due to these factors, so by creating more precise components, these variables could be eliminated creating more consistent and repeatable devices. The laser cut electrode was made by LPKF Laser & Electronics, while the printed circuit board was created using OrCad and sent to PCBexpress to be created.



**Figure 48: PICEM components.** From left to right: printed circuit board, Tango + gasket, Fullcure 720 outer support, Tango+ inner frit support, Tango+ gasket, stainless steel electrode, Fullcure 720 plate, Fullcure 720 reservoir. Below: secure pins, borosilicate

The printed circuit board also allowed for rows of droplets to be addressed and stimulated independently of the other rows of the board. The board, as seen in Figure 48, consists of a 6 by 6 matrix of holes. The rows were divided into sets of two, allowing for testing of different size holes, and therefore different size droplets. The diameter sizes from left to right are 14, 20, and 25 mils. The coating of the holes was a base of copper with a Sn/Pb (ratio of 63/37) coating. The coating diameter varied for each row to test the ability of the holes to have a consistent ring of Sn/Pb coating around the edges since the accuracy in punching the holes into the top coated circles was reaching the limits of precision for the company. However, it can be seen that the rings were able to encircle the holes for all arrays, meaning that smaller electrode rings can be used to allow for closer placement of the droplet holes. Besides altering the printed circuit board, the configuration of the frit layer was altered as well. Instead of using a Tango+ layer to hold the frit, which was subject to expansion and tearing, a new double shell was created. The outer shell was made of the stiff Fullcure 720, and the inner layer was made of the soft Tango+. The frit itself sits inside of this inner layer. This reduces any ripping from stress at the screw holes and decreases the liquid expansion of the Tango+ layer that may be causing alignment issues. The actual disassembled device can be seen in Figure 48, the assembled PICEM can be seen in Figure 49, and the cross section can be seen in Figure 50.

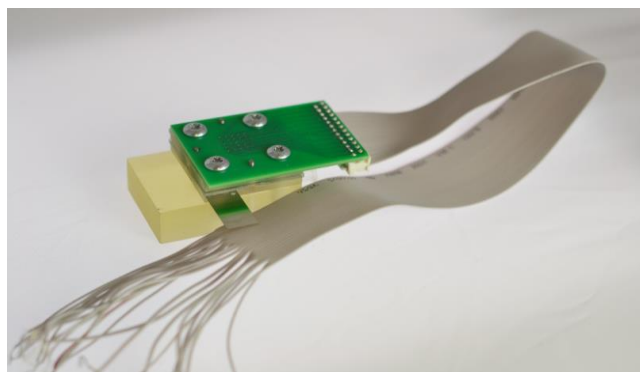


**Figure 49: Assembled PICEM Device**

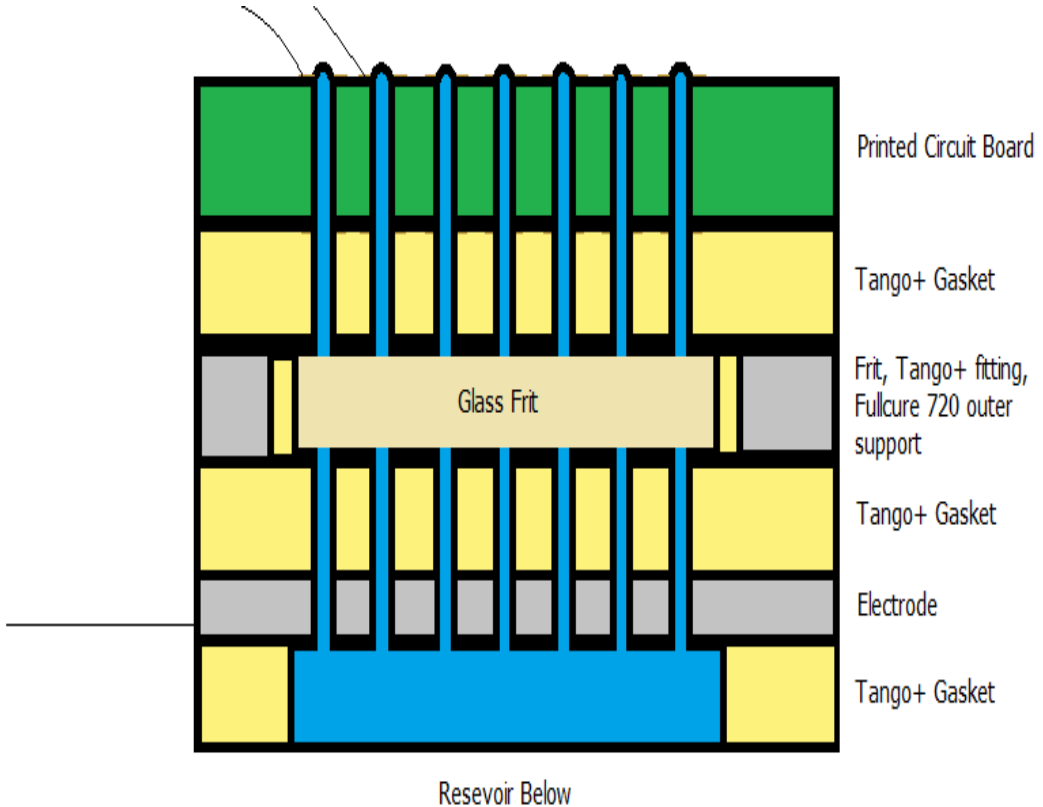


**Figure 50: Cross section of PICEM device.**

#### *Individual Control:*

Once exploring how the intricacies of the printed circuit board worked, it was decided to utilize the 20 mils diameter holes with the 0.66 mm diameter plating. This was chosen due to the comparative droplet size created (ideally 20 mils without walking) which would be ideal in contacting as much surface area of a tile or sphere as possible. It was chosen to space the channels three millimeters apart (which would mean it could pick up every 6th 500 micron tile. Or each 1.5mm sphere). This spacing was chosen to better analyze the effects of spacing with regards to the vector components of the generated electric field in the inactivated channels. See Figure 51 for successful test trials for "C" shape.

#### *The XYZ Platform:*

An XYZ platform was build in order to allow mobility of the PICEM device in all three axes. This would allow the device to pick up tiles or spheres from any location on the platform and place them to any other location on the platform. This would be most helpful when tiles of varied materials are being assembled, since the XYZ platform would be able to pick from a number of reservoirs and place the tiles or voxels accurately into the base construction platform. The device electronically consists of three servo motors and a snap hub, while structurally it is composed mainly of laser cut acrylic, 3D printed joints and connectors, and metal poles to connect the structure.

It is controlled using a Visual Basic program modified from previous work done by Jonathan Hiller [12], whose work was the inspiration for this current platform. The program allows for homing, selection of speeds, accelerations, and positions of the assembler head.

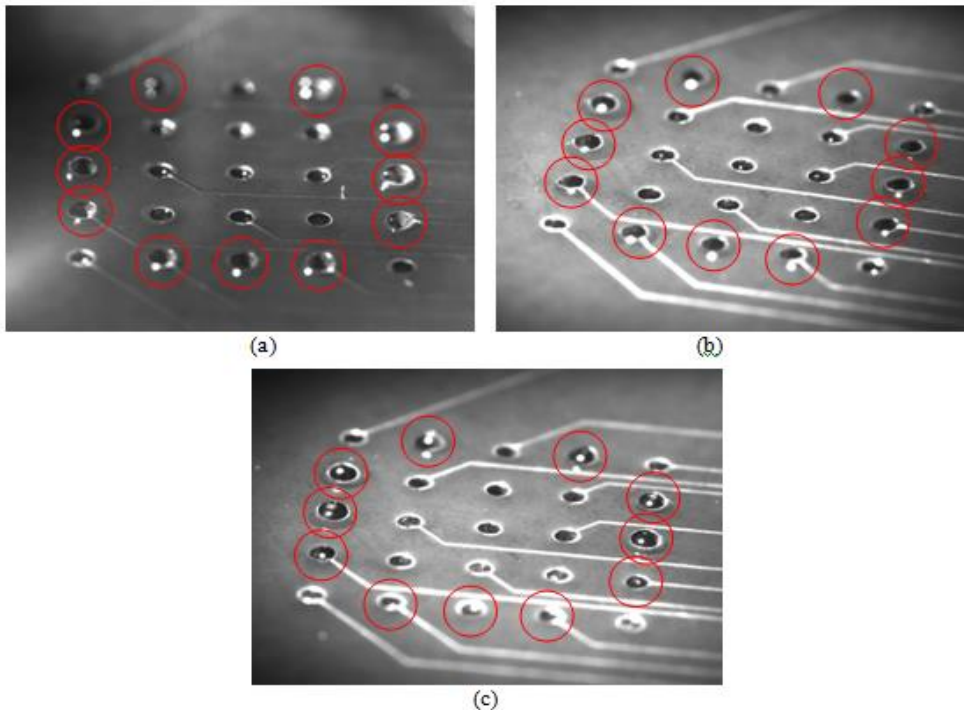
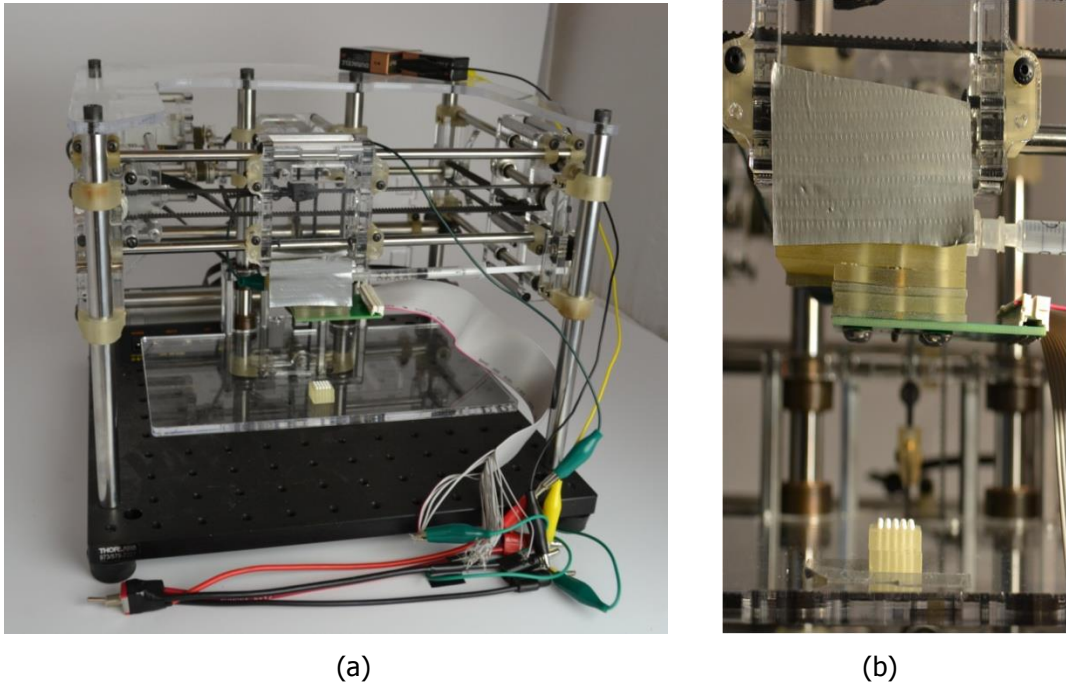


**Figure 51: Three successful trials of creating a "C" shaped configuration using individual control. Circled droplets are activated channels with droplet growth.**

#### *Under the Microscope:*

In order to better evaluate the droplet growth, a microscope was used to view the microscopic changes inside of the channels and water droplets on an individual and collective scale (referring to how each channel effects the others). The device was hooked up to 9V and the second to bottom row was activated (b), deactivated (c), re-activated with a negative voltage. It can be seen that throughout this process, based on the rings of light on the water droplets, growth and recession can be seen from an overhead view in Figure 15. By looking at the other channels around the row, it is possible to determine if any other channels were activated as shown in the connected column tests as previously mentioned. It can be seen at this lower voltage and higher channel spacing, minimal unwanted growth is experienced. In (c) some of the channels in the lower right hand corner seem to show some activation with both positive and negative voltage. However, it seems that these tend to be much less extensive than those chosen to be actuated. This issue could be resolved using a control system with negative voltage being supplied to the nearby channels to prevent actuation. On a more practical note, these droplet growths are of no concern as long as they are not large enough to become visible above the level of the circuit board or large enough to have a surface tension high enough to pick up a sphere or tile. Furthermore, very little bubbling has been seen due to hydrolysis, which is coupled to the lowered voltage.



(a)

(b)

**Figure 52:** (a) XYZ platform with PICEM device attached. (b) Close up of sphere platform positioned under PICEM device.

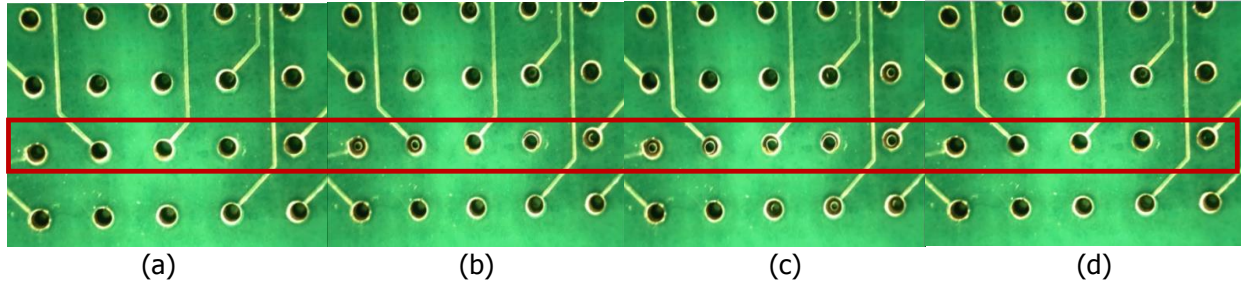


**Figure 53:** (a) Time: 28 seconds, 0V (b) Time: 46 seconds, 9V (c) Time 68 seconds, 9V (d) Time: 79 seconds, -9V. Note growth in (b) as voltage was added, further growth over time in (c), and the reversal and retreat of the droplets once a negative voltage was added

#### *Electroosmosis Device: PICEM (Pick and Place Individual Controlled Electroosmosis Machine) Testing:*

To test the device, the PICEM device was attached with adhesive tape to the translating head. The device was then aligned using pins to the base plate which was a 3D printed Fullcure720 cube with cylindrical holes of diameter 0.7 mm. The plastic spheres of diameter 1.5 mm were placed on this platform spaced in such a way that the PICEM would pick up all spheres with no space in between, were all channels to be activated. This same configuration would work for smaller tiles; however, it would only pick up every sixth 500 micron tile or every third 1 mm tile, meaning it would thus require multiple passes to complete a row on a tile platform. Tile platforms have been created using both photolithography and 3D printing, but have not been thoroughly tested since the tile geometric configurations are much more complex than the spherical objects currently studied. In future tests, these tiles could be used in order to test interlocking abilities, as well as stacking capabilities.

Once all PICEM channels were tested for current flow capacity, individual channels were activated by selecting the proper wire from the ribbon cable and connecting it to the voltage source. A switch was created in which the device would allow for positive voltage, negative voltage, or no voltage to pass through the channels. This allows for the droplets to grow and shrink on command. The first of many tests looked at a single channel. The single wire corresponding to the leftmost forward sphere was activated (15 V), and using the Visual Basic Program, the platform was lifted such that the spheres made contact with the formed water droplet. No other droplets were formed since the other channels were not activated. After

contact was made, the platform was then lowered, showing the single chosen sphere to have been removed from the platform and adhered to the circuit board. The voltage was switched off and the sphere continued to stay in place. This shows the novelty that this device uses low voltages only periodically to control droplet motion, while still allowing peak performance. This test was repeated for a number of individual channels, all showing similar results (See Figure 54, Figure 55).

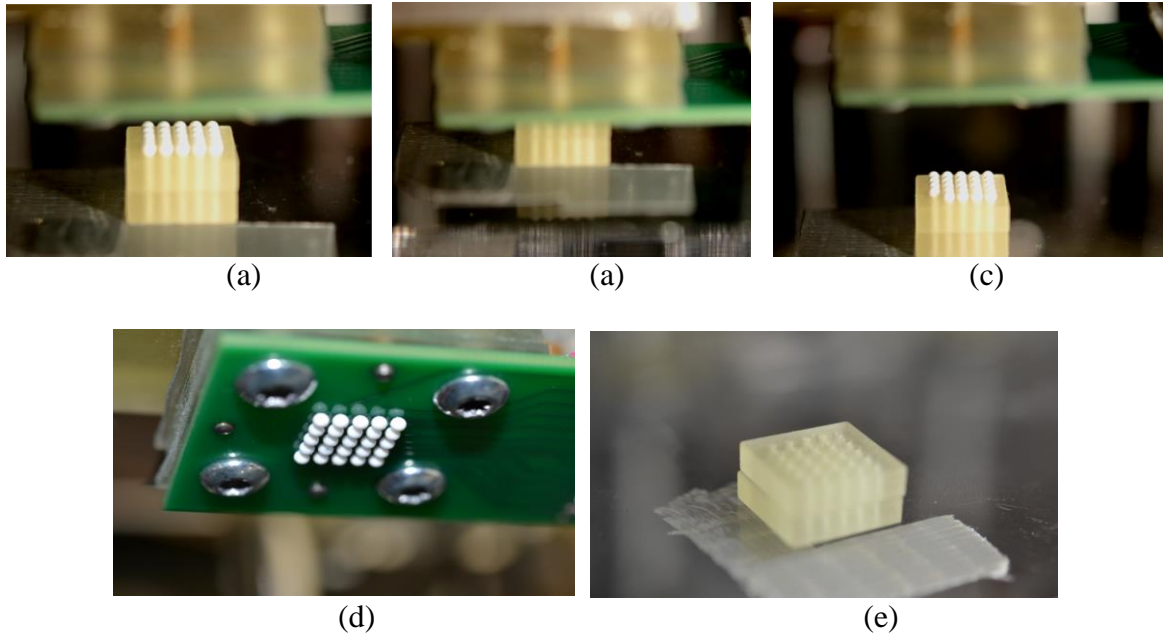


**Figure 54:** (a) Initial platform with all spheres, (b) sphere making contact with water droplet, (c) single droplet removing forward, left-most sphere, (d) view of circuit board, (e) view of empty sphere platform.

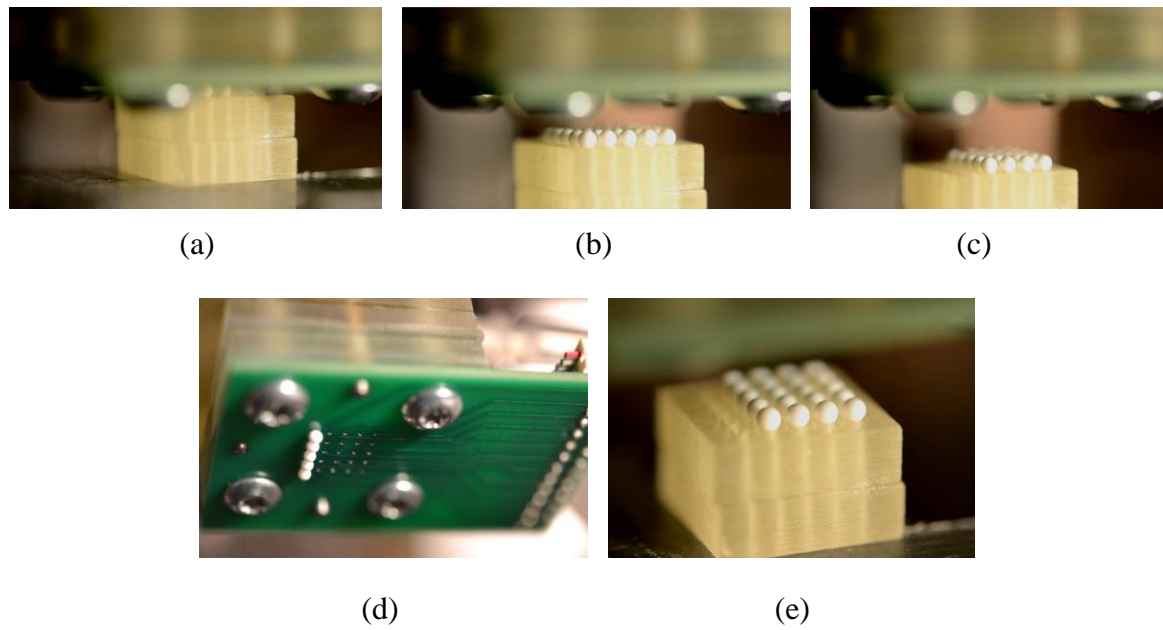


**Figure 55:** (a) Initial platform with all spheres, (b) spheres making contact with water droplets, (c) droplets removing entire row, (d) view of circuit board and droplets, (e) final view of platform with missing row.

This test was repeated for a number of individual channels, all showing similar results. The next step was to activate multiple channels at once. Therefore, a row was chosen to be activated. In the following images (Figure 55) the process can be seen again, but with multiple channels activated.

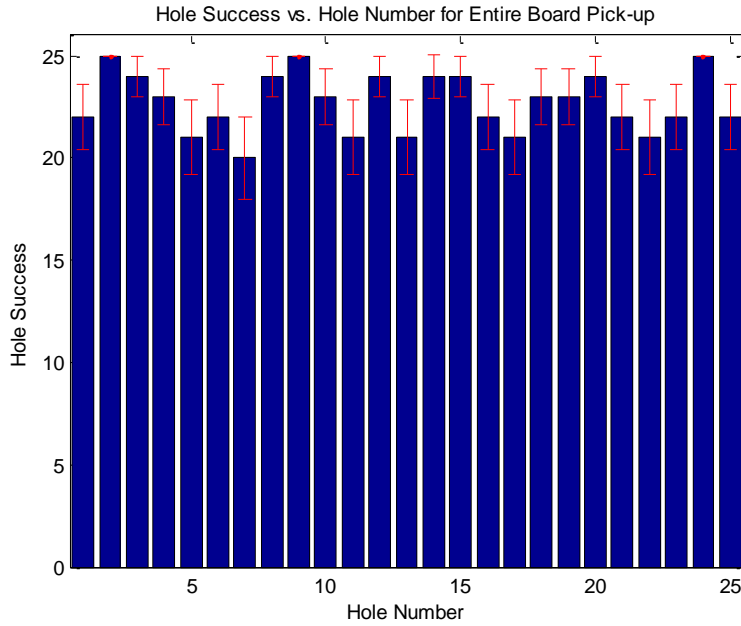


**Figure 56: Hole success vs. hole number for entire board pick-up.**

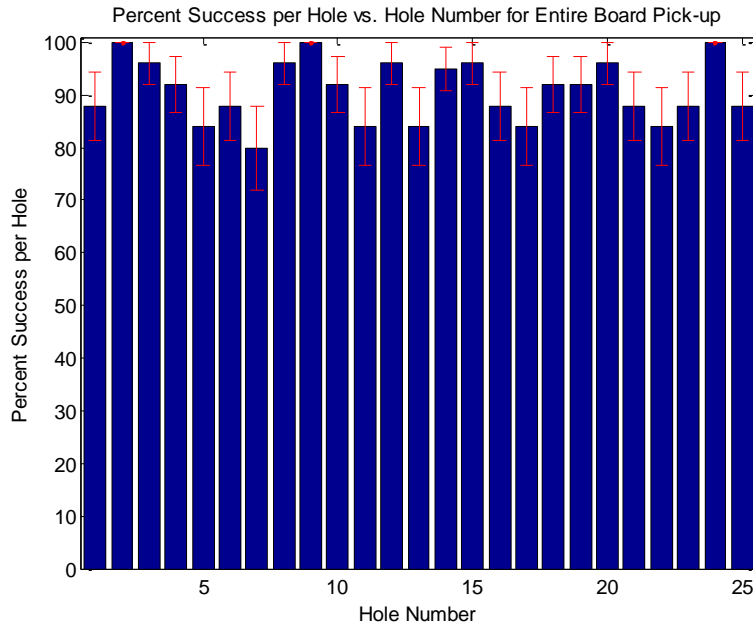


**Figure 57: Percent success vs. hole number for entire board pick-up.**

#### *Picking of All Spheres Testing:*

The next step was to attempt to pick up all spheres at once using the PICEM device. This test was performed 25 times, with a voltage of 15 V. The success rates and number of successful pick-ups per hole can be seen below in Figure 18 and 19. From these tests it was found that the lowest success rate was

80%, while the highest was at 100% for the 25 trials (Table 1). The mean and standard deviation amongst all the trials were calculated, with a mean of 22.72, standard deviation of 1.45, and an average success rate of 90.88%. These statistics were based on the Binomial Distribution. What is more important to note, however, is the success rate of water droplet formation. Although pickup was not 100% for each channel, the water droplet growth for the activated channels was seen in every trial, giving a success rate of 100% for every channel. This means that the electroosmosis process and the individual addressability features are fully functional, accurate, reliable, and repeatable.

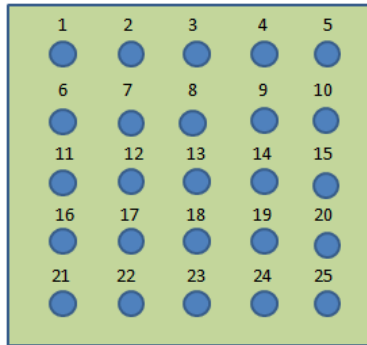


**Figure 58: Basic numbering system for plots.**

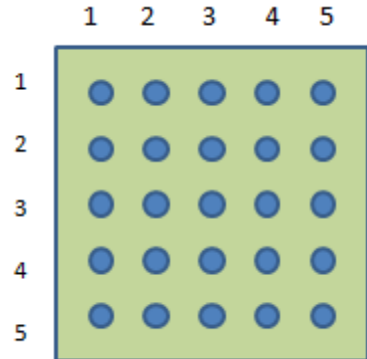


**Figure 59: Basic Numbering system for data collected in tables.**

**Table 1: Collected data for 25 trials with standard deviation.**

Number of Successful Pick-ups Per Location					Percent Success Rate per Location for 25 trials						
Location	1	2	3	4	5	Location	1	2	3	4	5
1	22	25	24	23	21	1	0.88	1.00	0.96	0.92	0.84
2	22	20	24	25	23	2	0.88	0.80	0.96	1.00	0.92
3	21	24	21	24	24	3	0.84	0.96	0.84	0.95	0.96
4	22	21	23	23	24	4	0.88	0.84	0.92	0.92	0.96
5	22	21	22	25	22	5	0.88	0.84	0.88	1.00	0.88
Standard Deviation Statistics :					Standard Deviation Statistics (s/n):						
Location	1	2	3	4	5	Location	1	2	3	4	5
1	1.625	0.000	0.980	1.356	1.833	1	0.065	0.000	0.039	0.054	0.073
2	1.625	2.000	0.980	0.000	1.356	2	0.065	0.080	0.039	0.000	0.054
3	1.833	0.980	1.833	1.041	0.980	3	0.073	0.039	0.073	0.042	0.039
4	1.625	1.833	1.356	1.356	0.980	4	0.065	0.073	0.054	0.054	0.039
5	1.625	1.833	1.625	0.000	1.625	5	0.065	0.073	0.065	0.000	0.065

#### *Picking of Checkerboard Pattern:*

In order to test the accuracy of the individual control, a checkerboard pattern was tested. This configuration allowed for the testing of the ability to isolate channels in close contact, while still providing a deliberate

pattern. Furthermore, it examined the effect of unwanted droplet growth on picking up individual spheres (Figure 60).

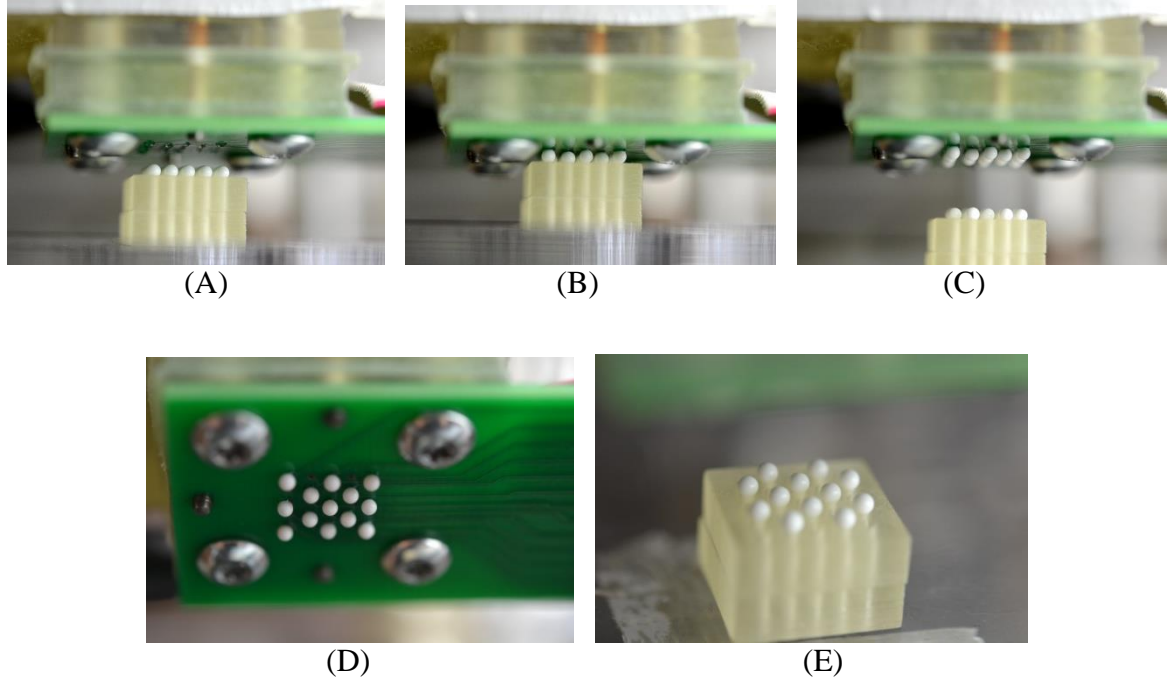


**Figure 60:** (A) Set at 15V, water droplets begin to form on the circuit board of the PICEM device, (B) the platform is raised so that the droplets make contact with the spheres, (C) the activated channels (those creating a checkerboard pattern) pick up the spheres from the platform, leaving behind all spheres on the grid corresponding to inactivated channels, (D) view of checkerboard pattern from under the circuit board, (E) view of left over spheres from inactivated channels.

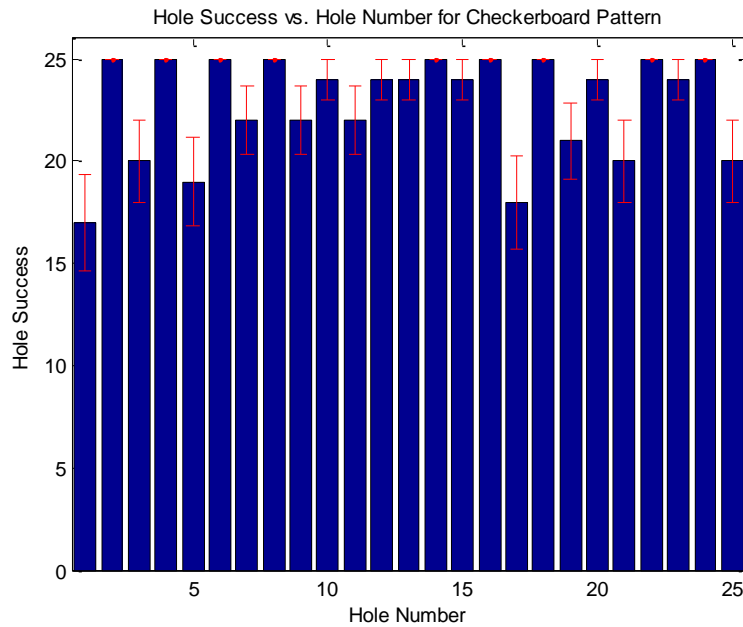


**Figure 61: Hole success vs. hole Number for checkerboard pattern.**

In order to test the reliability of this process, the test was repeated 25 times. The standard deviation and mean was calculated for both the number of successes per channel as well as for the probability of pick up (Table 2). Success is defined as an activated channel picking up a sphere or an inactivated channel not

picking up a sphere. Starting with position 1, every other bar (1, 3, 5, etc.) correspond to activated channels. All even numbered bars correspond to inactivated channels.

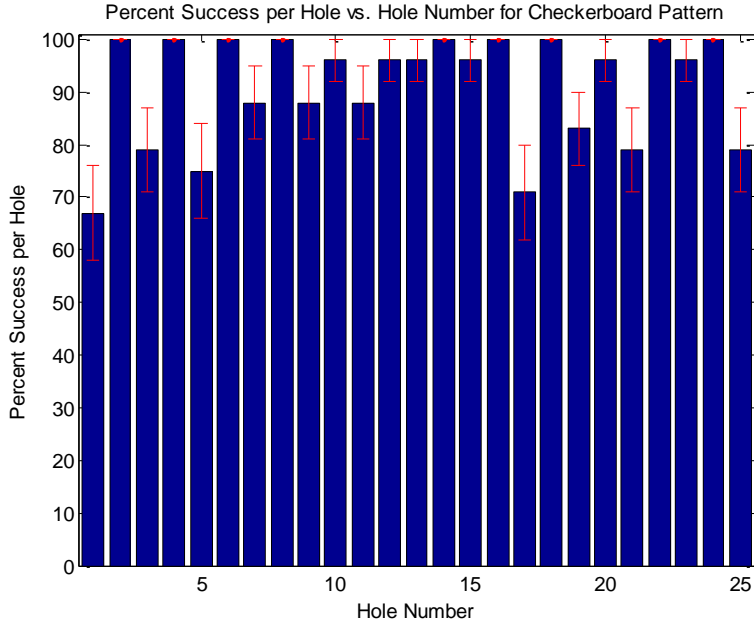


**Figure 62: Percent success per hole vs. hole number for checkerboard pattern.**

**Table 2: Collected data for 25 trials with standard deviations.**

Number of Successful Pick-ups Per Location					Percent Success Rate per Location for 25 trials						
Location	1	2	3	4	5	Location	1	2	3	4	5
1	17	25	20	25	19	1	0.67	1.00	0.79	1.00	0.75
2	25	22	25	22	24	2	1.00	0.88	1.00	0.88	0.96
3	22	24	24	25	24	3	0.88	0.96	0.96	1.00	0.96
4	25	18	25	21	24	4	1.00	0.71	1.00	0.83	0.96
5	20	25	24	25	20	5	0.79	1.00	0.96	1.00	0.79
Standard Deviation Statistics :					Standard Deviation Statistics (s/n):						
Location	1	2	3	4	5	Location	1	2	3	4	5
1	2.357	0.000	2.031	0.000	2.165	1	0.094	0.000	0.081	0.000	0.087
2	0.000	1.654	0.000	1.654	0.999	2	0.000	0.066	0.000	0.066	0.040
3	1.654	0.999	0.999	0.000	0.999	3	0.066	0.040	0.040	0.000	0.040
4	0.000	2.273	0.000	1.863	0.999	4	0.000	0.091	0.000	0.075	0.040
5	2.031	0.000	0.999	0.000	2.031	5	0.081	0.000	0.040	0.000	0.081

Again, these statistics were based on the Binomial Distribution. It can be seen that the lowest success rate was 67%, while the highest was 100% for the 25 trials. The mean and standard deviation amongst all the trials was calculated, with a mean of 22.80, standard deviation of 2.52, and an average success rate of 90.83%. Again, what is more important to note, however, is the success rate of water droplet formation. Although pickup was not 100% for each channel and avoided pickup was not 100% for every channel, the water droplet growth for the checkerboard pattern was seen for every trial, giving a droplet generation success rate of 100% for every channel.

#### *Superhydrophobic Coating Picking up All Spheres:*

In many cases, when the water droplets were growing from the channels, the water droplets did not stay pinned to the holes, and instead “walked”. This means that the water droplets no longer kept a spherical shape and bled out onto the circuit board. This could cause the picking up of unwanted spheres or for the inability to pick up desired spheres since the droplets were no longer in their designated location. Therefore, a superhydrophobic coating was applied to the circuit board using vapor deposition by

Integrated Surface Technologies. The goal was to ensure pinning the droplets at the holes to increase reliability in the picking process. This coating, called "Repellix" guaranteed 25-85 times more resistance to water than uncoated surfaces. The coating was 10-100nm thick and was applied using vapor deposition [3].

Using this new coating, the trials were repeated and it was found that the average pick-up rate for the 25 trials was 23.72 spheres per trial with a standard deviation of 1.6 spheres. The average success rate was 94.9%. The average pick up without the coating was 22.72, with a standard deviation of 1.5 spheres, and an average success rate of 90.9%. While all but the standard deviation made a substantial improvement, it is important to note that for the superhydrophobic trials, most of the error was on the left row, particularly the top left channel. This channel had 7 failed pick-ups, which is much larger than the average. Water was being filtered through the channel, and droplets were being formed. However, the sphere was not being picked up. Just like the uncoated trials, the water droplet formation had a 100% success rate. Therefore, this leads to suggest that there was error due to alignment, and was not due to the electroosmosis device. See Table 3 for data.

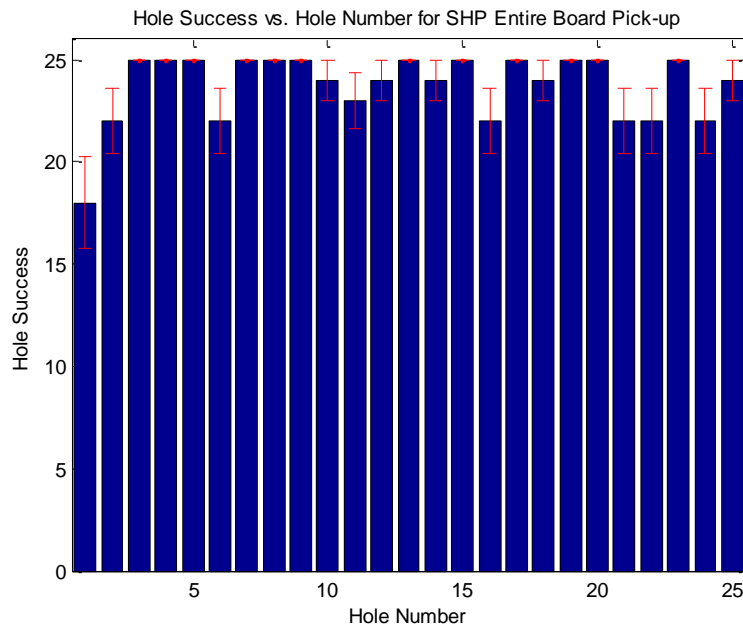


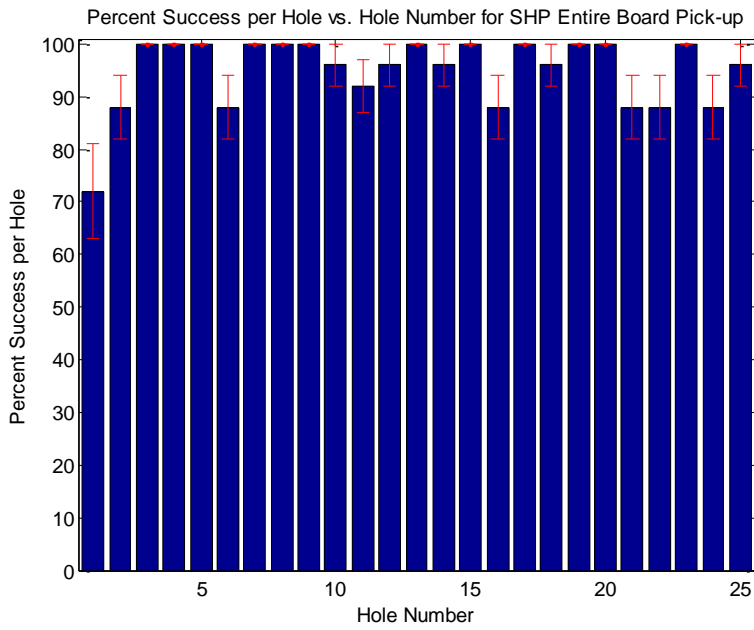
**Figure 63: Hole success vs. hole number for SHP coating entire board pick up.**

**Table 3: Collected data for trials with standard deviations.**

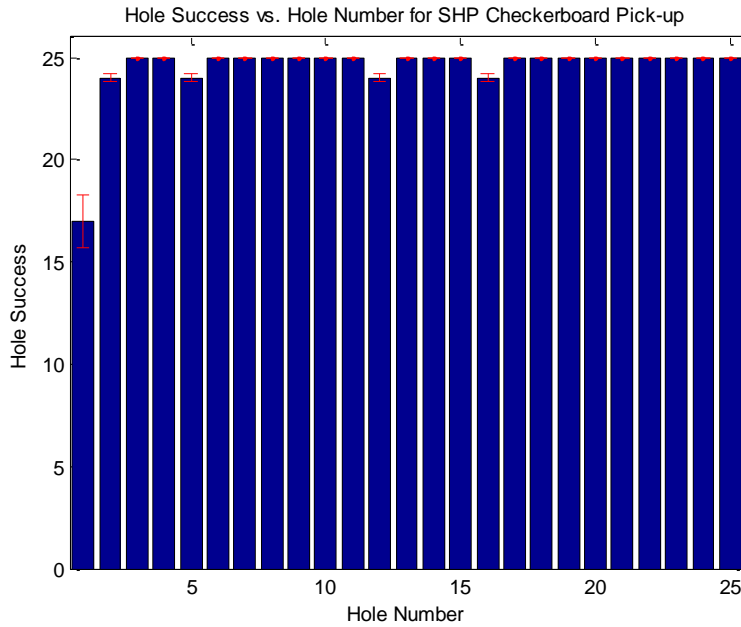
Number of Successful Pick-ups Per Location					Percent Success Rate per Location for 25 trials						
Location	1	2	3	4	5	Location	1	2	3	4	5
1	18	22	25	25	25	1	0.72	0.88	1.00	1.00	1.00
2	22	25	25	25	24	2	0.88	1.00	1.00	1.00	0.96
3	23	24	25	24	25	3	0.92	0.96	1.00	0.96	1.00
4	22	25	24	25	25	4	0.88	1.00	0.96	1.00	1.00
5	22	22	25	22	24	5	0.88	0.88	1.00	0.88	0.96

Standard Deviation Statistics :					Standard Deviation Statistics (s/n):						
Location	1	2	3	4	5	Location	1	2	3	4	5
1	2.24	1.62	0.00	0.00	0.00	1	0.09	0.06	0.00	0.00	0.00
2	1.62	0.00	0.00	0.00	0.98	2	0.06	0.00	0.00	0.00	0.04
3	1.36	0.98	0.00	0.98	0.00	3	0.05	0.04	0.00	0.04	0.00
4	1.62	0.00	0.98	0.00	0.00	4	0.06	0.00	0.04	0.00	0.00
5	1.62	1.62	0.00	1.62	0.98	5	0.06	0.06	0.00	0.06	0.04



**Figure 64: Percent success vs. hole number for SHP for entire board pick up.**



**Figure 65: Hole success vs. hole number for checkerboard SHP.**

#### *Superhydrophobic Coating Picking up Checkerboard Pattern:*

Using this new coating, the new average pick-up rate for the 25 trials was 24.52 spheres per trial with a standard deviation of 1.6 spheres. The average success rate was 98.1%. The average pick up without the coating was 22.8, with a standard deviation of 2.5 spheres, and an average success rate of 90.8%. In this case, the superhydrophobic coating improved all general success metrics. However, again the left, top-most channel skewed the data, having 8 failed pick-ups, which is much larger than the average. Water was being filtered through the channel, and droplets were being formed. Just like the uncoated trials, the water droplet formation had a 100% success rate. Therefore, this leads to suggest that there was error

due to alignment, and not due to the electroosmosis device. This argument is even stronger, given that this hole also was an issue in the previous trials for picking up all spheres. See

Table 4 that has a much higher failure rate than the other channels. Assuming this is an anomaly, the average, percent average, and standard deviation were calculated leaving this point out for the SHP checkerboard pattern. The values for these three statistics are 24.83, 99.3%, and 0.381 respectively. These values are much more desirable than those including the inconsistent channel.

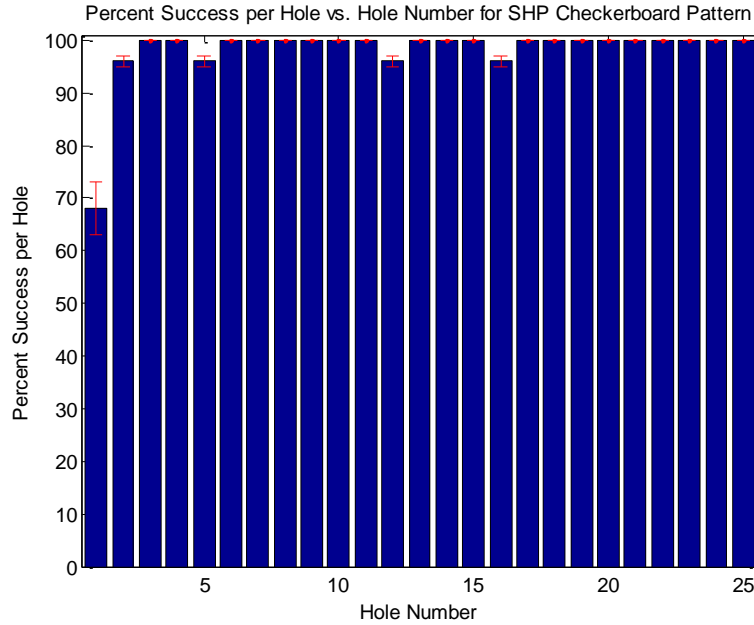


**Figure 66: Percent success vs. hole number for SHP checkerboard pattern.**

**Table 4: Collected data for 25 trials with standard deviation.**

Number of Successful Pick-ups Per Location					Percent Success Rate per Location for 25 trials						
Location	1	2	3	4	5	Location	1	2	3	4	5
1	17	24	25	25	24	1	0.68	0.96	1.00	1.00	0.96
2	25	25	25	25	25	2	1.00	1.00	1.00	1.00	1.00
3	25	24	25	25	25	3	1.00	0.96	1.00	1.00	1.00
4	24	25	25	25	25	4	0.96	1.00	1.00	1.00	1.00
5	25	25	25	25	25	5	1.00	1.00	1.00	1.00	1.00
Standard Deviation Statistics :					Standard Deviation Statistics (s/n):						
Location	1	2	3	4	5	Location	1	2	3	4	5
1	1.32	0.20	0.00	0.00	0.20	1	0.05	0.01	0.00	0.00	0.01
2	0.00	0.00	0.00	0.00	0.00	2	0.00	0.00	0.00	0.00	0.00
3	0.00	0.20	0.00	0.00	0.00	3	0.00	0.01	0.00	0.00	0.00
4	0.20	0.00	0.00	0.00	0.00	4	0.01	0.00	0.00	0.00	0.00
5	0.00	0.00	0.00	0.00	0.00	5	0.00	0.00	0.00	0.00	0.00

#### *Other Configurations:*

In order to test the reliability of the PICEM, other configurations besides the all-sphere and checkerboard pattern were tested.

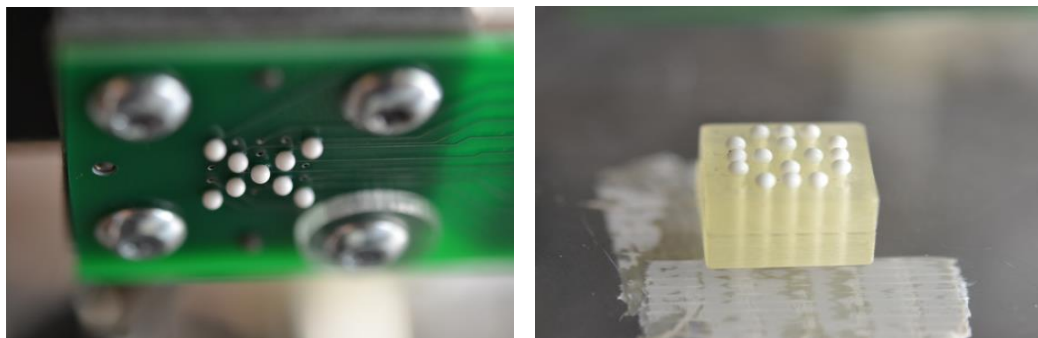


Figure 67: "X" configuration.

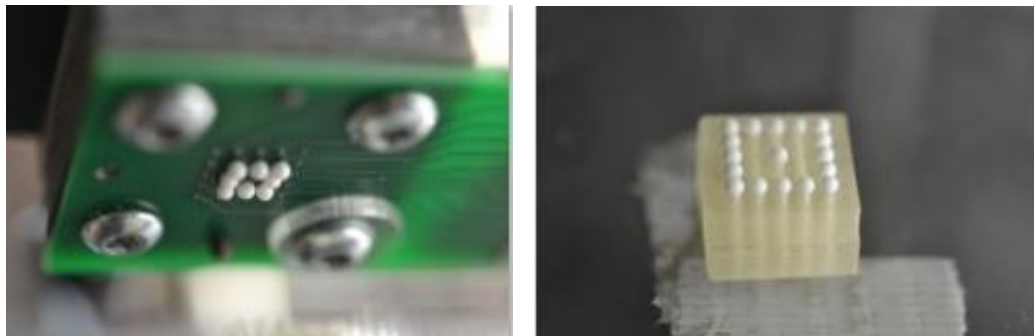


Figure 68: Square shape.



Figure 69: "#" shape.



Figure 70: Top hat shape.

#### Velocity Testing:

In order to determine the velocity of the water droplets coming out of the channel experimentally, individual channels were activated with a set voltage (15 V) and recorded with a camera. The size of the water droplet was measured over time, and the volume of the droplet at that time stamp was calculated using the spherical cap formula. The velocity was calculated by dividing the flow rate (volume/time) by the area through which this flow travels,  $\pi*(0.508 \text{ mm})^2$ , (Table 5).

**Table 5: Velocity data from video trials.**

Location	Time (s)	Volume (mm <sup>3</sup> )	Velocity (mm/s)	Time (s)	Volume (mm <sup>3</sup> )	Velocity (mm/s)	Time (s)	Volume (mm <sup>3</sup> )	Velocity (mm/s)
right	0.375	0.014	0.179	0.875	0.024	0.133	2.000	0.034	0.084
second to right	2.215	0.017	0.037	2.750	0.022	0.039	3.750	0.037	0.048
second to right	2.875	0.022	0.037	3.750	0.035	0.046	5.125	0.033	0.032
center	1.063	0.022	0.101	2.215	0.031	0.070	3.500	0.047	0.066
center	1.625	0.022	0.066	2.250	0.029	0.064	3.500	0.044	0.062
second to left	0.560	0.017	0.147	1.125	0.027	0.118	2.125	0.057	0.133
left	2.500	0.068	0.134	4.375	0.117	0.132	8.250	0.188	0.112
left	0.750	0.022	0.142	1.750	0.036	0.101	3.250	0.056	0.085

From this data, the velocity can change over time, and may show different velocities at different locations. This could have much to do with the pore distribution of the frit, or channel alignment issues inside of the device. However, these velocities are all relatively close in scale, and an average is used to compare to theoretical data. The average velocity for all locations and for all time steps is 0.09 mm/s.

#### Analytical Solution:

Beyond just looking at the repeatability of this device, it is necessary to look at the theoretical and experimental flow rates and velocity to determine if there is any interference that could affect the reliability and consistency of the device. In order to determine the velocity or fluid flow through the pores at the base of the circuit board, it was necessary to determine whether or not a bulk flow model could be used. In order to do this the Debye length was calculated and compared to the diameter of the pore. The Debye length was calculated to be 971 nm using the equation:

$$\lambda_D = \sqrt{\frac{\epsilon_w RT}{F^2 \sum_{i=0}^N c_i z_i^2}}$$

where  $\epsilon$  is the permittivity of water, R is the universal gas constant, T is the temperature, F is Faraday's constant,  $c_i$  is the molar concentration of species i, and  $z_i$  is the valence number of species i normalized by the elementary charge. The diameter of the pore was found to be 1.15 nm [4]. Given that the ratio ( $d^*$ ) of pore diameter to Debye layer (1.18) was greater than 1, a bulk flow model cannot be used. This is an upper bound on the double layer thickness. In practice, the double layer is likely to be thinner because there are likely to be impurities in the water from contact with the frit and exposure to the air allowing for dissolution of gases (i.e., CO<sub>2</sub>).

The net axial velocity of fluid through a channel as a result of an externally applied electric field is a superposition of the Helmholtz-Smoluchowski electroosmotic velocity and Darcy's law modified with the appropriate coefficients to account for finite thickness of the double layer [4]:

$$\bar{v}_{net} = \bar{v}_{eo} - \bar{v}_{Darcy} = c_{11} \frac{\epsilon_{w/f} \psi_s \bar{E}_{ext}}{\mu} - c_{12} \frac{\kappa \bar{\nabla} P}{\mu} \quad (1)$$

where  $\epsilon_{w/f}$  is the reduced permittivity of water due to  $\phi$ ,  $\mu$  is the dynamic viscosity,  $E_{ext}$  is the applied electric field, grad P is the pressure gradient, and  $\psi_s$  is the surface potential. While this equation is a vector, the velocity of most interest is that exiting the channel, which will also be in the downward y direction. Assuming that the double layer thickness does not affect the viscosity, the functional dependence of the second term on the right hand side remains the same as that for thin double layers (i.e.  $c_{12}=1$ ). The double layer is finite, so  $c_{11} \neq 1$ . The surface potential,  $\psi_s$ , for a borosilicate glass frit in contact with distilled water is typically around 100 mV [5], which does not justify the use of the Debye-Hückel approximation (must be less than 25mV) in deriving the electroosmotic component of the velocity. To account for this non-linearity of bulk flow and high surface potential,  $c_{11} \approx 1/\{1 + \exp[-\alpha(\log d^* - \log d_0^*)]\}$  is incorporated ( $\alpha \approx -0.15|\psi_0| + 3.5$ ,  $d_0^* \cong -0.01\psi_0^{*2} - 0.1|\psi_0^*| + 2$ ) [6]. The permeability (which is assumed to be isotropic) can be estimated analytically for a bed of packed spheres by relating it to the permeability of a series of parallel straight cylinders [7]. Since permeability of spherical packed bed of spheres can be derived analytically, using this derivation, it is possible to estimate the permeability of a porous media using manufacturer's specifications. The resulting equation is:

$$\kappa = \frac{\phi R^2}{24} = 6.613e^{-15} m^2 \quad (2)$$

In this case,  $\phi$  is the porosity based on manufacturer's specifications, 0.48, and the  $R$  is the manufacturer's radius. This theory operates by taking the pore size of the frit and assuming it is approximately equivalent to the cylindrical diameter model from which this equation was derived. It is important to note, however, that this  $R$  is assumed to be the radius of a cylindrical channel, which can be equated to the radius of a sphere in a packed bed. As mentioned before, due to the compression process in the frit manufacturing, the glass beads are no longer perfectly spherical, which could alter the validity of applying this theoretical model.

Since the electric field is equivalent amongst all channels if all channels are activated, the velocity will also be the same, theoretically, as well. The most simplistic measure of the electric field could be thought of as  $E=V/L$ , where  $L$  is a constant value of the frit thickness (4.76 mm), and  $V$  is the voltage applied in the experiments (15 V). This gives an electric field of approximately 3138 N/C. However, the experimental set-up uses a large plate electrode and single rings of Sn/Pb on a printed circuit board. Therefore, if a single droplet is activated, it is still influenced by the electric field produced by the other locations on the electrode besides the one directly below the top activated channel, which will be treated as a point since its area in relation to the entire electrode is much smaller. Therefore, it is necessary to look at the contribution of the electric field by the rest of the electrode. This could be done by using the method of images, and modeling the PCB electrode ring as a point charge, and the stainless steel electrode as an infinite plate:

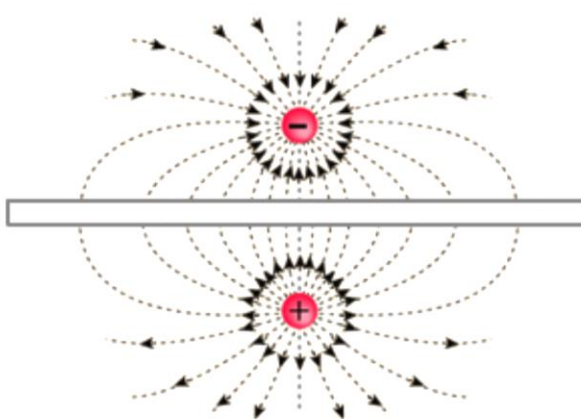


**Figure 71: Method of images with two point charges is used to find the voltage and electric field at various field at various points between a point charge and infinite plate [8].**

Based on this method, the voltage at any point in the region is described as [9]:

$$V = \frac{Q}{4\pi\epsilon_{w/f}} \left( \frac{1}{\sqrt{\rho^2 + (h-y)^2}} - \frac{1}{\sqrt{\rho^2 + (h+y)^2}} \right) \quad (3)$$

Since the voltage used for all the tests is known to be 15 V, it is simply a matter of determining the coordinates of the point at which we want to look at the electric field and finding a representative point charge ( $Q$ ). Here,  $h$  is the height from the bottom electrode to the top printed circuit board (9 mm), and is a constant. The  $y$  term will also be constant (7.08 mm), since the electric field and velocity desired is that exiting the frit, which will be constant from there through the channel to the top of the printed circuit board where the droplets grow. To determine the electric field, the partial derivative of  $V$  with respect to  $y$  is taken because it is the scalar potential of the electric field. It is only with respect to  $y$  since the electric field and velocity we are interested in are only in the  $y$  direction (the direction that aligns with the channels). The horizontal distance from the point charge,  $\rho$ , is first set to zero to determine the equivalent point charge,  $Q$ , which would produce a voltage of 15 V. From there it is possible to find the electric field  $y$  component at any  $\rho$  by evaluating the electric field equation at the calculated point charge and the same  $h$  and  $y$ :

$$E_y = \frac{Q}{4\pi\epsilon} \left( \frac{h-y}{\sqrt{\rho^2 + (h-y)^2}} + \frac{h+y}{\sqrt{\rho^2 + (h+y)^2}} \right) \quad (4)$$

Now knowing the E-field, the velocity can be determined by equation (1). It is important to note, however, that the electric field crosses through a number of different materials, as well as directly through the water in the channels. The Tango+, VeroBlack or FullCure720, and frit material block some of the effects of the electric field. By looking at the dielectric constants of these materials, it is possible to tell how resistive they are to allowing electric fields to pass through the medium. The dielectric constants for FullCure 720, VeroBlack, Tango+, and Borosilicate Glass (frit material) are 1.98, 1.7, 3.8, and 4.6 respectively (given by manufacturer), while the dielectric constant of water is 80 [4].

The main area of interest, however, only includes the area above and below the frit, which is where water flows. Therefore, the materials of interest include only the frit, Tango+, and water. When looking through the channels, there is no Tango+ present, and the electrical permittivity can be based on only the frit and water. Since the porosity of the frit is 0.48, the reduced permittivity of the water/frit combination can be thought of as 48% of the electrical permittivity of water. This assumption can be made because the permittivity of glass is so low, it acts almost as an insulator, cutting out 52% of the area that the electric field may pass through. This reduced water electrical permittivity is then  $3.398e -10 \text{ F/m}$  (dielectric constant is equal to the electrical permittivity divided by the dielectric constant).

Now that all the variables are known, it is possible to solve for the velocity at a number of locations given one active channel. The velocity exiting the activated channel ( $\rho=0$ ) is calculated to be 0.131 mm/s. This same equation could be used to find the velocity at other channels due to the active channel by changing the value of  $\rho$ .

### *Simulations:*

In order to better understand the fluid flow through the channels and frit, COMSOL Multi-physics Simulator was used to determine the fluid velocity of the fluid due to electroosmosis. In the simulation, the frit was drawn, as well as a single channel. In order to simulate this, two physics systems were used: Transport of Dilute Species and General Form PDE. In the first part of the model (Transport of Dilute Species), the continuity equations for the flow velocity and the current density at steady state are solved ( $\nabla \cdot \bar{u} = 0$ , and  $\nabla \cdot \bar{i} = 0$ , where  $u$  is velocity and  $i = -\kappa \nabla V$ , is the current-density vector). The governing equation for the entire model is:

$$\bar{u} = -\frac{\epsilon_p a^2}{8\mu\tau} \bar{\nabla} P + \frac{\epsilon_p \epsilon_w \zeta}{\mu\tau} \bar{\nabla} V$$

The governing equations for the dilute species include:

$$\nabla \cdot (-\bar{D}_i c_i - z_i u_{mi} F c_i \bar{\nabla} V) + \bar{u} \cdot \nabla c_j = R_j$$

$$\bar{N}_i = -D_i \nabla c_i - z_i u_{mi} F c_i \nabla V + \bar{u} c_i$$

where  $N$  is the flux vector given by the Nernst-Planck equation (equation ), where the partial derivative of the concentration of ions with respect to time plus the gradient of  $N$  is zero. These equations are describing the conservation of mass of a dilute dielectric species under the convective influence of an electric field. The governing equations for the general PDE include:

$$\begin{aligned} e_a \frac{\partial^2 \bar{u}}{\partial t^2} + d_a \frac{\partial \bar{u}}{\partial t} + \nabla \cdot \Gamma &= \bar{f} \\ \bar{u} &= [p, V]^T \\ \nabla &= \left[ \frac{\partial}{\partial x}, \frac{\partial}{\partial y} \right] \end{aligned}$$

where  $e_a$  is a zero matrix (since this is a general form equation and there are no second partial derivatives governing the physics of electroosmosis),  $d_a$  is a  $2 \times 2$  Identity matrix,  $f=0$  since there is no forcing function, and  $\Gamma$  is a matrix, "u\_flow v\_flow, -kappa\*Vx, -kappa\*Vy". These equations use the general PDE form to apply the principles of conservation of momentum (Laplacian of pressure is zero) and the conservation of

momentum in Darcy flow (Laplacian of voltage is zero). Throughout the simulation, these equations are used coupled with the above listed boundary conditions in order to solve for the electroosmotic flow throughout the frit and the frit channels.

In the first simulation the frit was modeled with a single channel (2D). See Figure 72. Flow was allowed through the inlet and outlet only (since the other areas are blocked off by Tango+, the electrode, and printed circuit board). The first plot shows the combined velocity terms due to all of the preset physics and is dependent upon both the dilute species and general form PDE models. The velocity at the inlet and outlet are much higher than the other areas. This is due to the fact that the driving force is the electrode on top and the point charge at the outlet. All arrows that come from the inlet, eventually lead to the outlet, and the velocity through the rest of the porous medium tapers off quickly within a millimeter. This model shows that while much of the liquid is going through the channel, some of it is also going through other parts of the frit before coming back to the outlet. A surface plot was created in order to determine magnitudes of the velocity in and around the channel (Figure 73). All red areas indicate zero velocity. The area of most interest is the outlet at the bottom, which shows a range of velocities between 0.25-0.35 mm/s. At the corners of the outlet, there are sharp changes in velocity due to the fact that the water that has spread throughout the frit is now gathering back to the outlet. The velocity through the channel in the frit changes due to this dispersion; however, once the water leaves the frit the velocity is constant at the designated outlet velocity. Furthermore, there is a discontinuity at the corners due to the interface of two different boundary conditions meeting. One allows flux (the outlet); the other (the frit surface blocked by Tango+) does not. Therefore, there are sharp changes in velocity at these points.

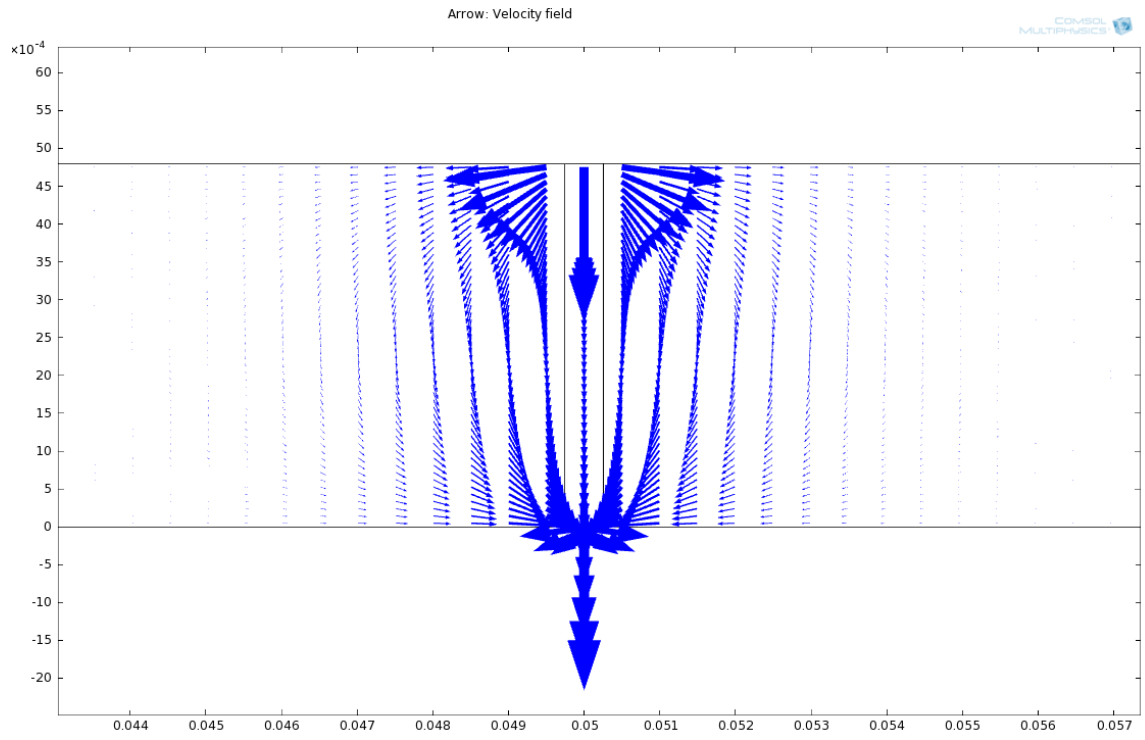


**Figure 72: Velocity arrow plot due to electroosmosis.**

### *III. Electro-Wetting and its Adaption for our Device: PICEM (Pick and Place Individual Controlled Electrowetting Machine)design*

We envision another massively parallel assembly device based on the principle of electrowetting. Electrowetting refers to the modification in wetting properties of a surface induced by an applied electric field Figure 74. A surface which is in general a hydrophobic one turns into hydrophilic and thus switches its adhesion property [5]. This phenomenon has been widely exploited in the various microfluidic devices to

transport and modify liquid droplets. While adhesion switching can be brought in various ways: electrostatic, electrochemical, photochemical, pH; we choose to pursue electrostatic method over others for their short switching time, reliability and easy parallelizability.

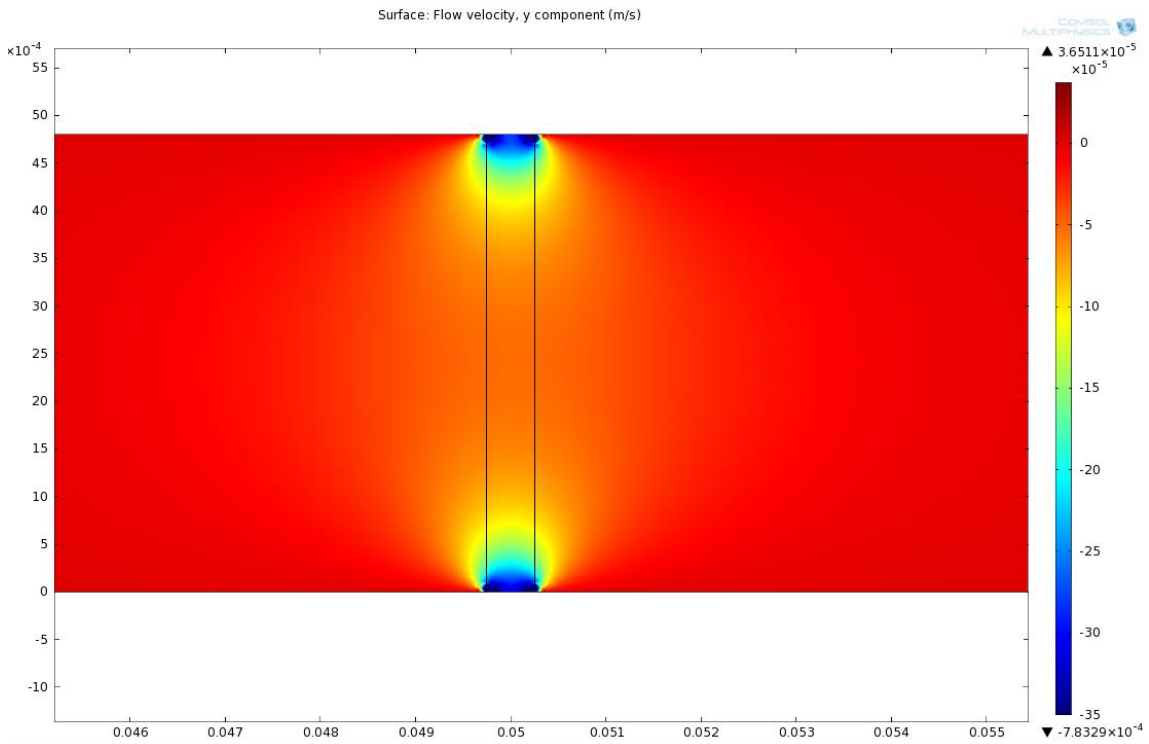


**Figure 73: Surface plot for y component of velocity.**

As shown in the Figure 75 a typical electrowetting setup consists of an electrode coated with an insulator and a hydrophobic dielectric. The conducting droplet is pierced by a wire electrically connected to the bottom electrode. To suit it to our purpose we propose a grounding-from-bottom design which helps to achieve adhesion switching on a single planar surface. The proposed design of a single picking unit is given in Figure 76.

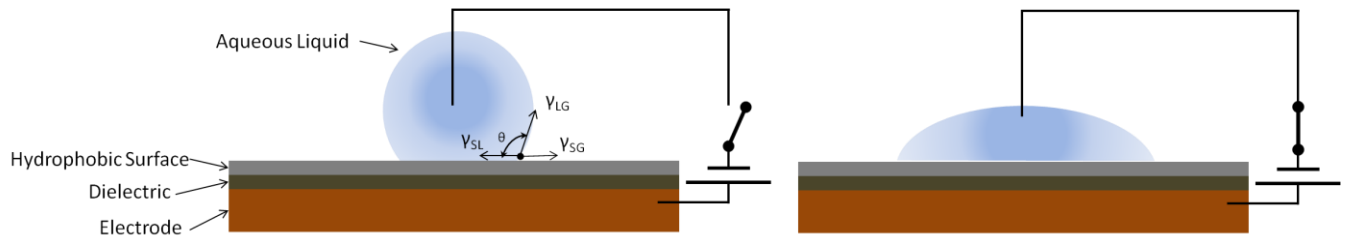


**Figure 74: Principle of Electrowetting: A voltage across the dielectric and metal plate enhances  $\gamma_{SL}$ .**

We developed an electroosmosis based assembly device during 2011-2012. A critical issue with the earlier assembly device is that while it can pick voxels pattern selectively in a massively parallel way, release of the voxels has been inefficient. In this device, the residual water combined with the Vander-Wall effect makes the release the voxels challenging. We have been looking for an alternative technology which could help in picking of voxels pattern and at the same time could be efficient at releasing too. The process must be massively parallel and to realize the significance of parallel handling of voxels one needs to compare the size of each tiles ( $10 \mu \text{m} \times 10 \mu \text{m} \times 10 \mu \text{m}$ ) and a general device size (say an object of  $10 \text{ cm} \times 10 \text{ cm} \times 10 \text{ cm}$ )

size). To achieve such a device we need 1000 billion such tiles. A serial way of pick and place at a rate of 1  $\mu$ /sec would take 278 hours to finish the job!

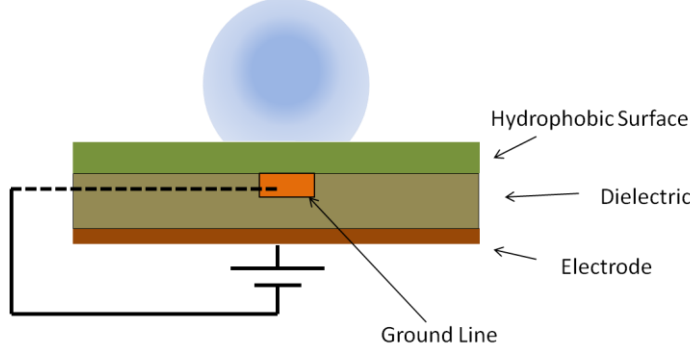


**Figure 75: Grounding from below Design.**

Our requirement is to develop a device with the following abilities: (a) micro scale precision, (b) an ability to reverse the forces, (c) a quick response time, and (d) must be massively parallel i.e. millions of them could be controlled independently[1]. An Electrowetting based device meets these requirements. It is a low power efficient technology with a micro scale precision phenomena and currently many sophisticated microfluidic devices exploit this principle.

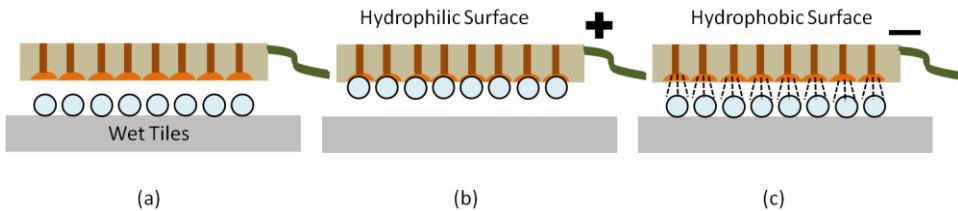


**Figure 76: A schematic of envisioned device and its working.**

The device will be comprised of a flat plate with an array of electrically controlled nodes which would be hydrophilic while picking the wet tiles and would reverse its surface nature to a hydrophobic one while releasing them as shown in Figure 75, Figure 76 and Figure 77. Furthermore, it will be a low maintenance device by possessing a self cleaning property by the virtue of adhesion switching. The surface, which will be hydrophobic in ground state, would drive away aqueous remains and help to keep the surface clean. While this device design is primarily to assist a 3-D printer in assembly process, it can be also used for making a heavy application *hooks*, *Spiderman globes* etc.. By increasing the number of switching nodes per unit area, higher forces can be generated.

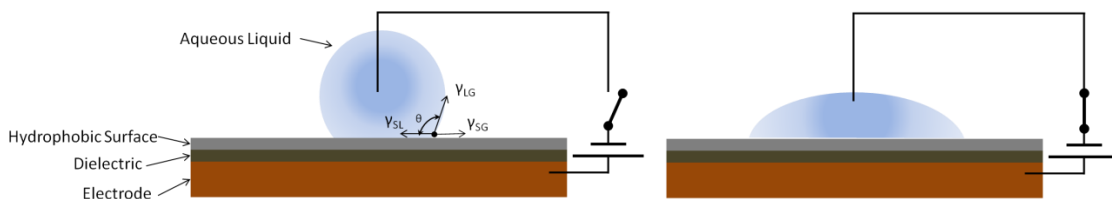


**Figure 77: Electrostatically actuated wetting between a conducting droplet and dielectric substrate.**

The phenomena of electrowetting was first realized as a capillary rise in mercury as a result of an applied voltage across the column [2]. It was explained by Gabriel Lippman in 1875 and by 1935 scientific community had started using this phenomena for altering adhesion behavior of various surfaces. Till 1990s it was mostly regarded as a phenomena limited to conducting droplets when it was discovered that by placing a dielectric layer between the electrode and droplet, not just the actuation power multiplies, it empowers to manipulate a droplet of *any* conductivity. When a conducting droplet, an electric double layer (EDL) is formed at the electrode-droplet interface. This development of EDL enhances the surface tension

$\gamma_{SL}$  resulting in the spreading of the droplet. A dielectric between electrode and droplet mimics like an EDL except that the voltage droplet registered across the dielectric can be much higher than across an EDL, and this holds the key to efficient adhesion switching on a dielectric surface. A capacitor model of electrowetting proposed by Lipmann suggests [2,3]:

$$\gamma_{SL} = \gamma_{SL}^o - \frac{1}{2} \frac{\varepsilon_d}{t} V^2$$

where  $\varepsilon_d$  is the permittivity of dielectric (EDL),  $t$  is thickness of dielectric layer (EDL) and  $\gamma_{SL}^o$  is the solid-liquid surface energy in the absence of electric field. When combined with the Young's equation of triple junction stability, it gives the modified contact angle:

$$\cos(\theta_{SL}) = \cos(\theta_{SL}^o) + \frac{1}{2} \frac{\varepsilon_d}{t \gamma_{SL}^o} V^2$$

A simple free diagram for the picking process is given in Figure 78. Intuitively the meniscus between tile and the device should have a curvature on the sides which would create a lower pressure inside the droplet. This effect dominates rest of the capillary forces if the weight of tiles is too high. We ignore this effect. Other assumptions like curvature of picking slot on device is same as that of voxel (tile) simplifies the analysis further. The force analysis boils down to following equation:

$$2 \pi R (\gamma_{GL} \cos \theta - \gamma_{DL}) \sin^2 \alpha = W_{Tiles}$$

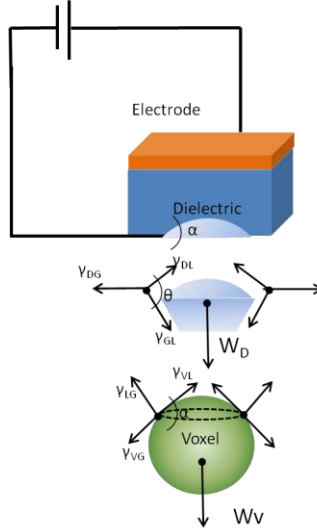


**Figure 78: Free Body Diagram for a tile in equilibrium with the capillary forces.**

Subscript *Tiles* stands for voxel or tile, *L* for the droplet liquid, *D* for dielectric and *G* for surrounding gas phase. To incorporate the geometry and material property of the tiles, we modify above expression to the following form:

$$2 \pi R (\gamma_{GL} \cos \theta - \gamma_{DL}) \sin^2 \alpha = \frac{4}{3} \pi R^3 \rho_{Tiles} g$$

The wetting angle  $\theta$  is a function of the potential  $V$  maintained across the electrodes. We evoke electrowetting equation to get an expression dependent on  $V$ .

$$2 \pi R \left( \gamma_{GL}^o \cos \theta_{SL}^o + \frac{1}{2} \frac{\varepsilon_d \gamma_{GL}^o}{t \gamma_{SL}^o} V^2 - \gamma_{DL} \right) \sin^2 \alpha = \frac{4}{3} \pi R^3 \rho_{Tiles} g$$

$$\frac{1}{2} \frac{\varepsilon_d \gamma_{GL}}{t \gamma_{SL}} V^2 \sin^2 \alpha = (\gamma_{GL} \cos \theta_{SL}^o - \gamma_{DL}) \sin^2 \alpha + \frac{2}{3} R^3 \rho_{Tiles} g$$

In the above expression  $\alpha$  is function of surface tension properties associated with the tile material.

$$\sin\alpha = \frac{\sqrt{\gamma_{Tiles,L}^2 - (\gamma_{Tiles,L} - \gamma_{Tiles,L})^2}}{\gamma_{GL}}$$

Effectively we get the following equation in term of all the known physical parameters:

$$V = \left[ \frac{2t\gamma_{LG}^2 (\gamma_{GL}\cos\theta_{SL}^o + -\gamma_{DL})\sin^2\alpha + \frac{2}{3}R^3\rho_{Tiles}g}{\epsilon_D \sqrt{\gamma_{Tiles,L}^2 - (\gamma_{Tiles,L} - \gamma_{Tiles,L})^2}} \right]^{\frac{1}{2}}$$

#### Experiment:

The key idea of this experiment is not to get detailed quantitative insight into the physics of electrowetting, but rather as a catalyst for an expedition to device development. The set up was prepared with in-home materials and was a crude one. The results were poorer than expected, and the only valuable knowledge obtained was that the hydrophilic nature of the surface was retained even after circuit was switched off. This turned out to be the key to scalability of device. In the later part of this report we propose a multiplexing scheme for parallel handling of device based on this principle.

#### Setup:

The initial experimental set up consisted of a flat copper plate, an electrode on top and DC/AC power supply. The plate was coated with parylene, which is an excellent dielectric and a hydrophobic coating on top of that. We chose 300 nm thick fluorinated amorphous carbon film for hydrophobic one. This coating helps to achieve a contact angle of 120°. The power supply was controlled with the help of an amplifier *kepco BOP 1000M*. An aqueous solution of NaCl (table salt) was used for droplets. We also studied the effect of high voltage and low current AC and DC on the electrowetting.

#### Observation:

The experiments with copper plate were conducted to study the physics of electrowetting and decide the design parameters for the device. We observed that with parylene coating of 12  $\mu m$  thickness, we could actuate the droplets at <50 V, as shown in Figure 79. Beyond that voltage, coatings undergo dielectric breakdown and an electrolysis initiates, that ends in destroying the hydrophobic coating.



**Figure 79: (a) Without Current: Water beads up (b) Under an applied voltage: Droplet sticks to the surface**

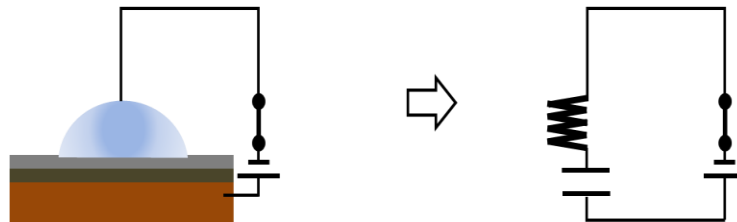
It was observed that once a surface switches to hydrophilic nature under the effect of an applied field, it stays the same even after this field is switched off, until the circuit is shorted. This may seem counterintuitive but can be explained by considering the capacitive nature of this setup [2,3]. As mentioned earlier, the droplet-dielectric layer acts as a capacitor, and a capacitor is nothing but a means of storing charge and energy. When a voltage is applied across the dielectric, it charges up and stays the same even after we have switched off the power supply.

When AC voltage is applied it is found that droplets undergo an instability. The amplitude of instability is a sharp function of the frequency applied. It seems to be a resonance phenomena which is prominent only at specific frequencies 3Hz, 9Hz, 25 Hz and so on. A video of droplet dynamics under AC supply is attached

with this report. This suggests that we should use a weak AC pulse to release the droplets, which solves the issue we faced with our earlier device.

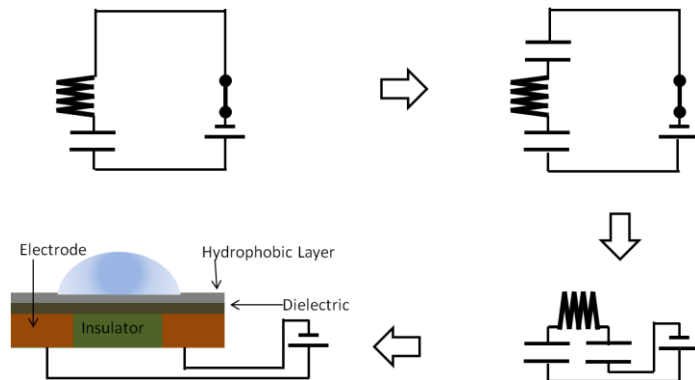
#### Printed Circuit Board: design

The experiment reported here was done with a droplet sandwiched between two electrodes. A picking device must have the droplets facing tiles or wall, it has stick to and hence, one needs to come up with a design where both electrodes lie on the same side of the dielectric.



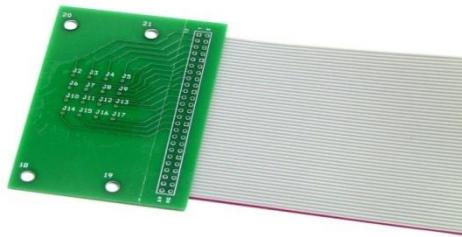
**Figure 80: Analogy between classical electrowetting set up and a CR circuit: Dielectric-electrode combination.**

Figure 80 draws an analogy between a real capacitor-resistance circuit [3] and the classical electrowetting experimental set up. The dielectric layer can be thought of as a capacitor and the conducting droplet as a “resistance”. Similarly one can imagine another circuit with two capacitors and a resistance in between. The design we aim for is inspired from such a circuit, and its evolution is shown in Figure 82. Not only are the two electrodes are on same side, it also has faster switching time than the previous one. The classical design comprises of a capacitor  $C$  and a resistance  $R$  giving a switching time  $\tau \sim CR$ . The current design has two capacitors  $C$  and a resistor  $R$  with net capacitance  $\frac{C}{2}$  and hence switching time  $\tau \sim \frac{CR}{2}$ . This rough analysis assumed that droplet size is same and ignored the fact that capacitor also depends on the area of two capacitor plates.



**Figure 81: Inspiration of device design: The proposed device depicted as a combination of two capacitors.**

We imagine that a design shown in Figure 81 could be the one, useful for current application. Figure 82 shows the circuit board based on this design and we plan to test them next. The circuit has an annulus, connected to the positive terminal and another electrode coming from the bottom of the circuit, that connects to the negative terminal.



**Figure 82: Circuit board for electrowetting based assembly device.**

### Challenges

As previously mentioned, the major challenges with this device involves fine tuning the thickness and surface property of dielectric and the hydrophobic layer. The voltage requirement of this device has to be low enough so that transistors can be used for switching the device.

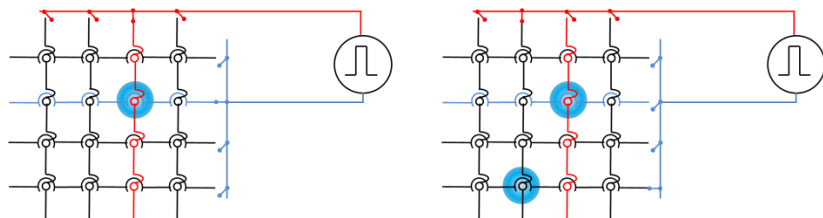


**Figure 83: Multiplexing:** A droplet once actuated to hydrophilic nature remains hydrophilic even if circuit is switched off. This means that a  $1000 \times 1000$  tiles can be “independently” controlled by 2000 switches. This would allow a massive parallelization with a dense circuitry on the device.

As mentioned in the experiment section, a unique behavior- retention of wetting property till the short circuit, was observed. This observation is largely ignored in literature but is critical to massive parallelization of picking process. The “retention till shorted” can be exploited to multiplex the actuation. For manipulating an array of  $n \times n$  nodes independently of each other, the most dumb way will be to have  $2n^2$  wires coming of the device whose switching will be controlled by  $n^2$  switches. Now this kind of wiring is required only if continuous supply of power is required to retain the tiles at its position. Because a pulse is sufficient to trigger the picking, it means that a scheme as shown in Figure 83 can be employed. This would require just  $2n$  switches and this can be further reduced to  $4\log n$  switches by deploying the multiplexing method proposed by Thorson[4].

### Next Steps

Our next step is to test the PCB design shown above and see if the design could be extended to pick and place a  $30 \times 30$  voxels pattern. We also need to decide an appropriate way to exploit the AC-effect on Electrowetting to achieve release of voxels.

## Assembler development and construction- Electroadhesion Based Pick and Place Device

### Task overview and milestones

This report describes an electroadhesion based massively parallel pick and place device, and demonstrates its capability in handling a large number of mm scale tiles. In our previous report we had conceptualized an electrowetting based device and presented relevant experiments conducted in an attempt to develop such a device. During this investigation we recognized the possibility of a much simpler dry electroadhesion assembly technology. Subsequently, the research in the direction of electrowetting was abandoned to pursue electroadhesion. We successfully developed a low power portable assembler and demonstrated its

capability by handling 100 tiles simultaneously. Our next goal is to achieve repeatability and an automation of the whole process.

### Technical Progress

Electroadhesion is a dry adhesion achieved by the virtue of electrostatic force of attraction between electrodes and an adjacent object where the electrostatic force is a result of interaction between the electrodes and the charge it induces on the facing object. This force is very similar to one observed between the two parallel plates of a charged capacitor. A typical electroadhesion based device can achieve a force as high as 2 N/m<sup>2</sup> and does not need a special microstructure or wet agent to achieve the adhesion. The most attractive attribute of electroadhesion is its easy and fast switching, turning off the powersupply can instantly switch off the adhesion! A device with naked electrodes can be used to adhere with a conducting object, sticking it to a metallic surface creates a short circuit and a work around to this problem is to coat the electrode with a dielectric. Thus an electroadhesion is versatile adhesion method independent of the material property of an object.

While electroadhesion has existed since a long time its application has been primarily limited to electrostatic chuck[1,2]. These electrostatic chucks are widely used in Silicon Fabs to hold down silicon wafers to various work tables. A more recent work related to electroadhesion come from SRI technology, who developed a wall climbing robot that exploits electroadhesion to achieve adhesion between the robot and the wall [3]. A commercially available product call Justick a desktop Board to hang office items, works on a similar principle [4].

The electrostatic force between two charges is given by

$$\vec{F} = \frac{Q_1 Q_2}{6\pi\epsilon d^2}$$

Where,

$Q_1$ =first charge

$Q_2$ =second charge

$\epsilon$ = permitivity of medium in between

$d$ = distance between the charges

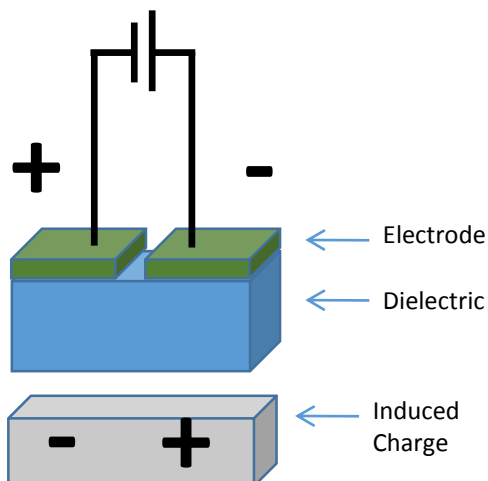


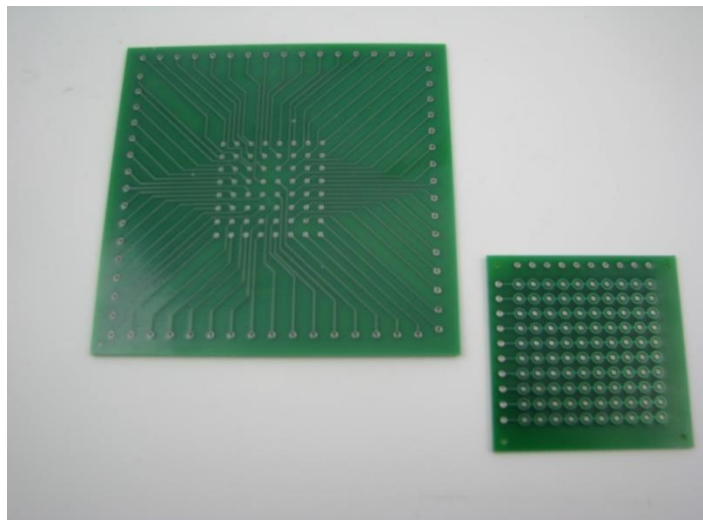
**Figure 84 - Electroadhesion:** Electrodes maintained at high voltage induce charge opposite of their own polarity on the near by object, resulting in to an electrostatic force of attraction between electrodes and the object .

The force  $\vec{F}$  is highly sensitive to the distance  $d$  and it decreases sharply as one goes away from the charge. This makes electroadhesion extremely sensitive to the surface roughness. Also the charges involved in electroadhesion are induced charges and predicting their dynamics has been difficult. It has been found

that modeling electroadhesion is difficult due to dynamic nature of charge and the difficulty in accounting for the surface roughness. Most of the calculations predict various quantities way off from what is in general observed in experiments. Hence we have prevented us from predicting various qualities and have mostly relied on experiments. We observed that owing this effect flat tiles stick much better than one with surface aberration or a curvature.

### **Device Design:**

The working principle of electroadhesion is described in Figure 84 where two electrodes are activated to induce charge on the other object. The pick-and-place device has such a pair of electrodes at every grid. To actuate a particular tile one activates two electrodes of the corresponding grid point. Such a grid can easily be printed on top a board by regular PCB fabrication. Figure 85 shows the two PCB designs where the first electrode comes from top side of the PCB through via and second electrode is in form of a concentric annulus around the via padding, Figure 85. The circumferential distance between two electrodes is a critical parameter and depends on the voltage the device is going to be subjected to which in turn is dependent on the weight of tiles. The current device is aimed to pick a tile weighing  $\sim .1\text{gm}$  and applies a voltage in the range of 100s of volt to pick them. The PCB is coated with a dielectric which serves two fold; it enhances the adhesion force by increasing the net capacitance between the electrodes, and prevents any possible short circuit that may result due to picking a conducting tile. The current device is vapour deposited with a  $3\mu\text{m}$  thick parylene C coating. Parylene C has a high dielectric strength (6800 Volts/mil), making it suitable for high voltage application.



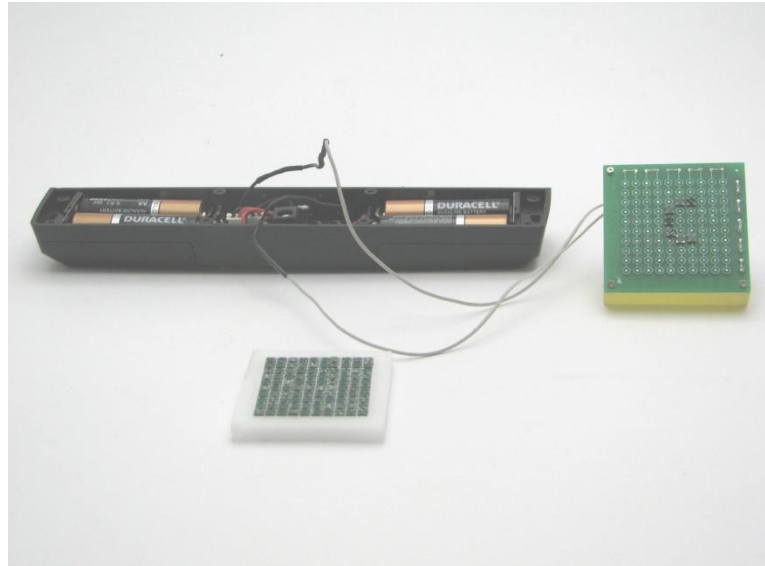
**Figure 85 - Two PCB design used. The first one has individually addressed 8x8 grid and the second has 100x100 grid meant for multiplexing**

Figure 86 shows the complete assembly of pick and place device. The device consists of a low power DC-DC low to high voltage converter operated by 4A cell batteries and an assembler, which is a grid of electrodes powered by the DC-DC converter, as shown in Figure 86. While the device shown in Figure 85 actuates all the grid points simultaneously, by applying a multiplexing one can achieve individually addressing of grids. The electroadhesive device was attached to an inhouse developed digital 3D printer called VoxJet (Figure 87), which relies on three snap motors to move around the stage and printing head.

### **Modeling Electroadhesion:**

Electroadhesion has been widely used in industry for various applications, but there has been little or no effort towards modeling it. Most of the modeling efforts were in direction of applying a simple model which predicted force to be in a range, which were order of magnitude higher than observed in reality. We believe that micron scale surface features reduce the net contact area between electrodes and the object to be picked, hence by accounting for surface roughness we should be able to capture the reality. In this section we present an electrostatic based model and solve it as a boundary value problem. In this preliminary model we have not introduced the surface roughness and have focused on a simple 2D model. The reason for

starting with a 2D model without surface roughness is primarily to set up a simple problem that can be verified with literature and intuition. The second stage of modeling would involve inclusion of a 3D model and a realistic surface roughness model to take it closer to the reality.



**Figure 86 - Electroadhesion-based portable assembler operated by 4A batteries picks a "C" pattern.**

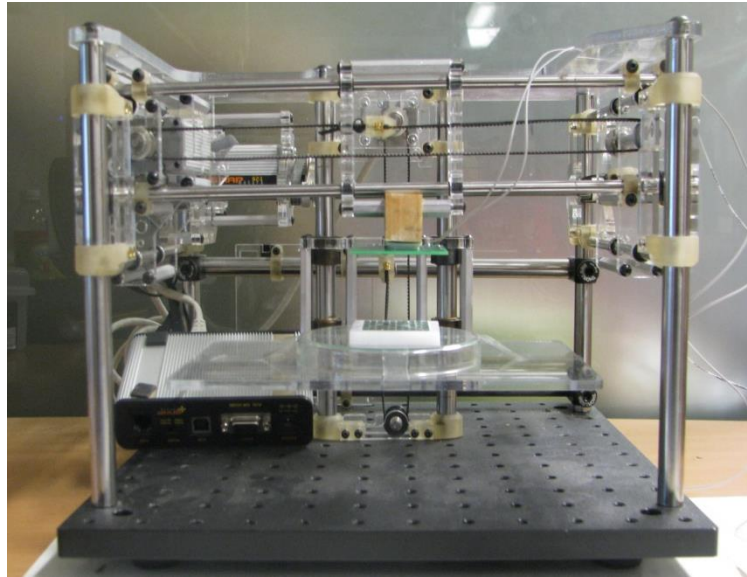


**Figure 87 - The printer used for picking the tiles**

A very simple model of capacitor can be used to discuss the case electroadhesion. In a capacitor the dielectric between two plates induces a charge on its two sides, which subsequently gives rise to a force of attraction between the capacitor and the dielectric.

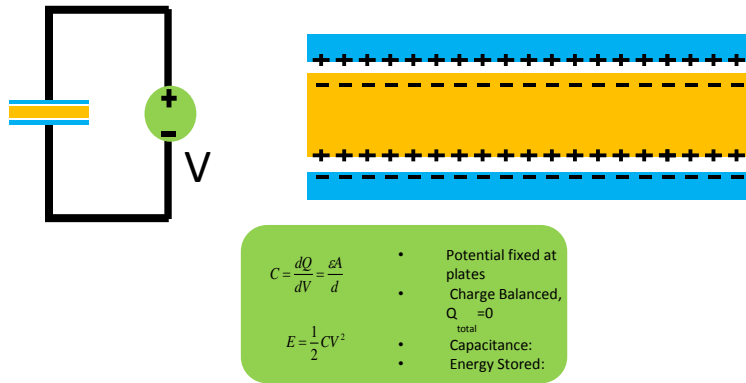


**Figure 88: A capacitor and the distribution of charge on the surface of two plates and the sandwiched dielectric**

The electrostatic force between the dielectric and the capacitor plates is as shown in Figure 88. The expression for the net force is derived by energy principle and has been summarized in the figure itself. While the case of capacitor is simple, in electroadhesion a closed form for electrostatic force can not be obtained and hence the problem is solved by a boundary value problem. The geometry of the problem is shown in Figure 89. There are two electrodes, cathode is ground where as the anode is maintained at voltage  $V_0$ .

There is periodic boundary condition maintained in  $x$  direction to account for the array of electrodes built on either side. In vertical direction geometry has been kept a bit long to accommodate the boundary condition of  $V=0$  at a large distance. The problem is solved in a multiphysics based simulator, COMSOL for  $V_0=1000$  and dielectric's  $\kappa=10$ . We study potential distribution, electric displacement and resulting force. Figure 91 and Figure 92 shows the numerical results obtained for the test case. As we can see the presence of dielectric reduces the potential field in and around dielectric. This suppression of potential is because of the induced charge on the surface of dielectric. Similarly an enhancement in displacement field can be seen in and around dielectric tile.

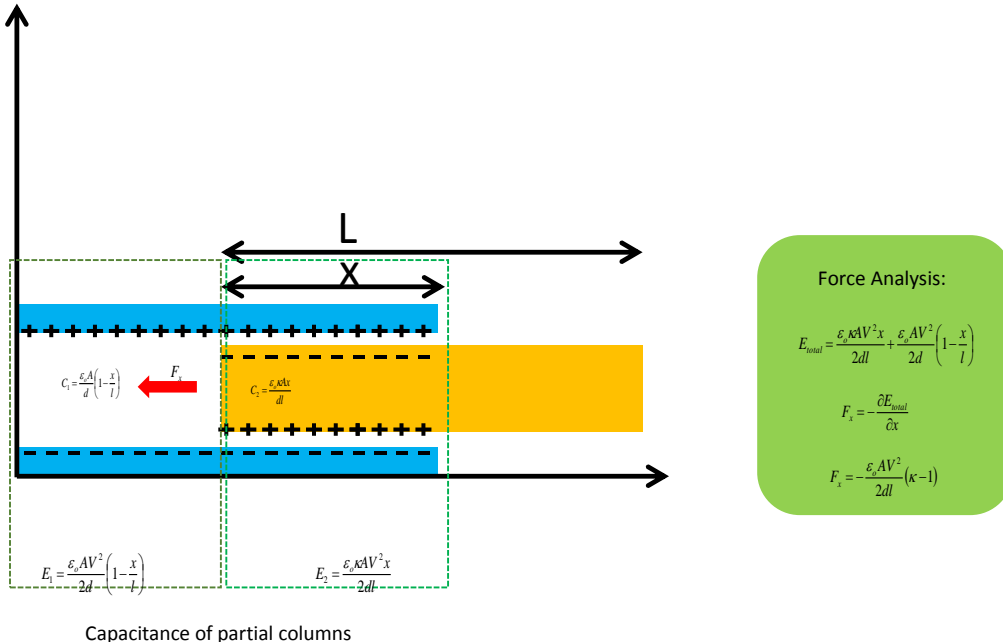


**Figure 89: The evaluation of force acting on dielectric as a result of electrostatic force between the capacitor plates and the dielectric layer**

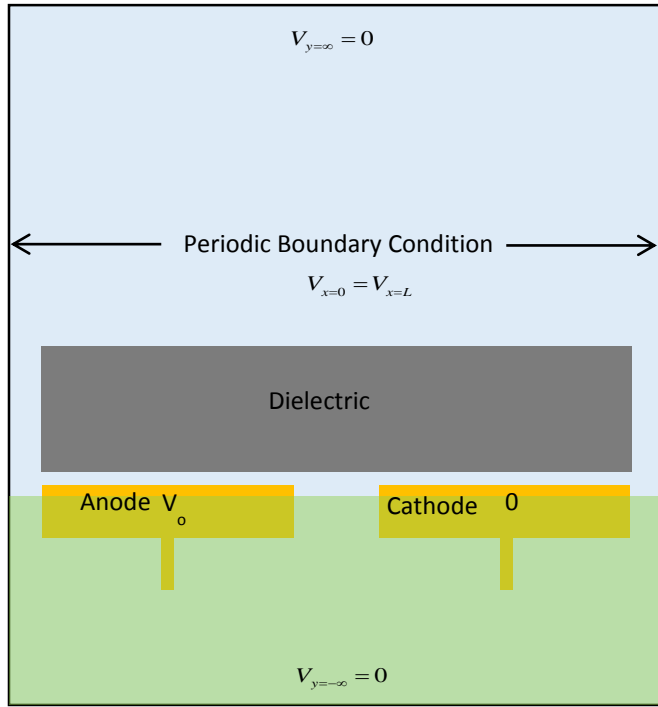


**Figure 90:** The schematic of boundary volume problem set in Comsol. There are two electrodes one at voltage  $V_0$  and the second at 0. There is periodic boundary condition set in x direction.

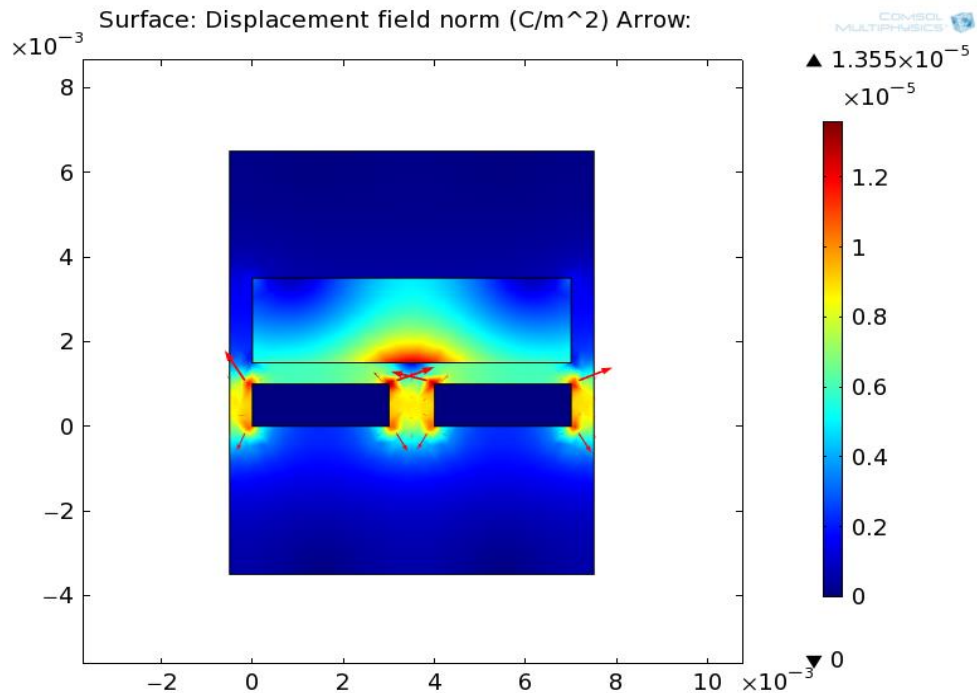


**Figure 91:** The electric displacement field established around dielectric tile as result of potential difference between two electrodes

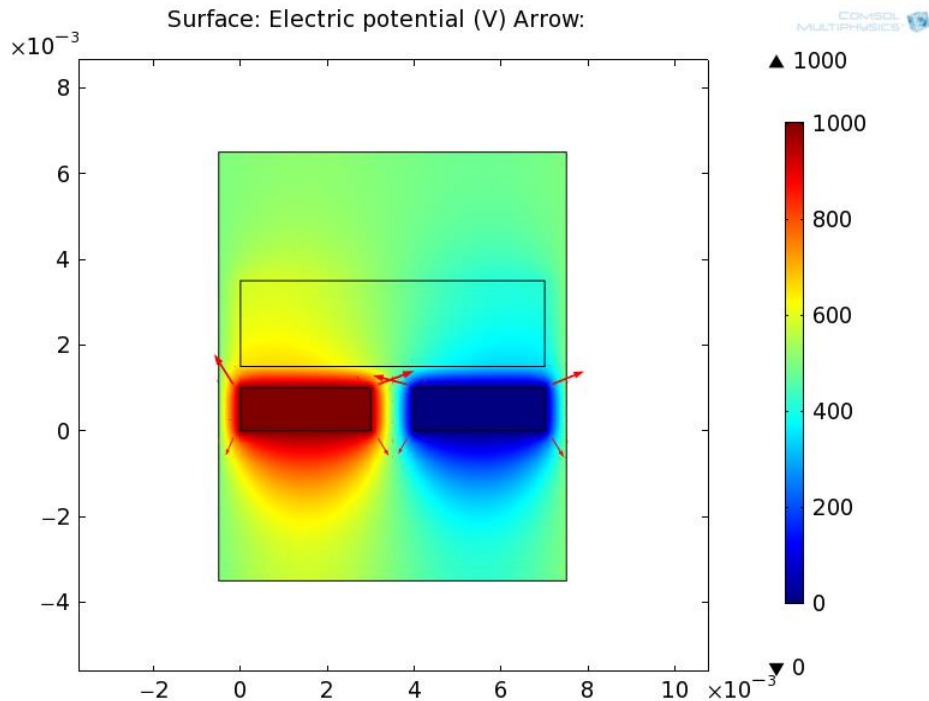


**Figure 92: The Electric potential field established because of maintaining a constant potential difference between two electrodes**

#### Device Testing:

We are attaching two video with this report to demonstrate the working of pick and place device. In our experiment where tiles are placed manually on each grid point shows 100% success at adhering the tiles Figure 86, where as in our second set of experiment where we tried to pick and place 100 tiles using this device and VoxJet Printer, only 50% of tiles could be picked the way we intended. We believe that 100% success could be achieved in first case because perfect alignment tiles with the grid where the failure at picking 50% (Figure 93) of the tiles by device owes to the wobbling of VoxJet printer and the incorrect alignment of tiles tray with the device. Implementation of alignment mechanism and a sturdier platform is expected to significantly improve the reliability and repeatability.

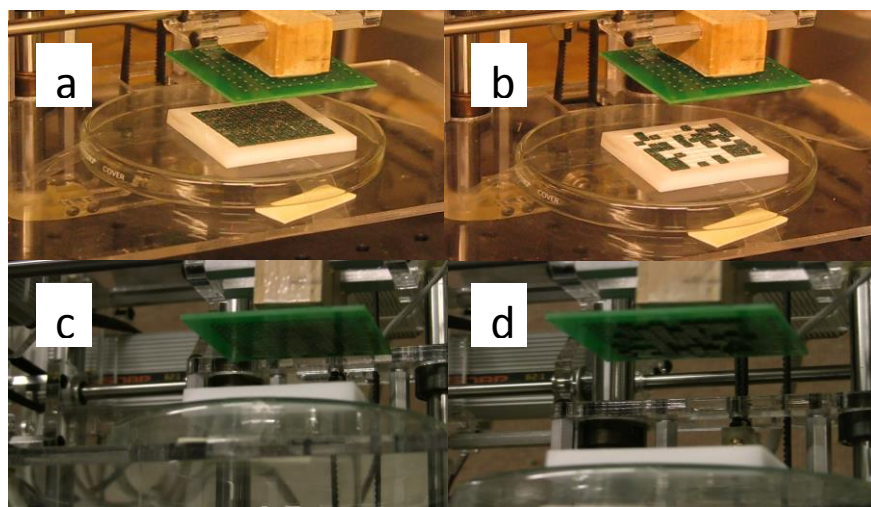


**Figure 93 - Pick-and-place device in action:(a) tiles aligned in a tray before the device is started (b) half of tiles from the tray picked (c) The device PCB in the beginning (d) PCB shows a the tiles sticking to the PCB which were successfully picked up.**

## References

- [1] Vogel, Michael J., Ehrhard, P., Steen, Paul H. "The electroosmotic droplet switch: Countering capillary with electrokinetics" *PNAS*, August 23, 2005 vol. 102 no. 34.
- [2] Vogel, Michael J., et al. "Capillarity-based switchable adhesion." *PNAS*, February 23, 2010; vol 107, no. 8.
- [3] Information about Repellix coating: <http://www.insurtech.com/> Date visited: April 1, 2012.
- [4] Kirby, Brian. "Chapter 6: Electroosmosis." *Micro- and Nanoscale Fluid Mechanics: Transport in Microfluidic Devices*. New York: Cambridge UP, 2010. 131-52. Print.
- [5] Gennes, Pierre-Gilles De., Francoise Brochard-Wyart, and David Quere. "Chapter 10: Transport Phenomena." *Capillarity and Wetting Phenomena: Drops, Bubbles, Pearls, Waves*. New York: Springer Science Business Media, 2010. 261-87. Print.
- [6] Pierre-Giles de Gennes, Francoise Brochard-Wyart and David Quere; Capillarity and Wetting Phenomena: Drops, Bubbles, Pearls, waves. *Springer*, 2002.
- [7] Hyejin Moon, Sung Kwon Cho, Robin L. Garrell, Chang Jin and C J Kim; Low voltage electrowetting on dielectric. *Journal of Applied Physics*, 2002(Vol-92).
- [8] Christopher G. Cooney, Chao-Yi Chen, Michael R. Emerling, Ali Nadim and James D. Sterling; Electrowetting droplet microfluidics on a single planar surface. *Microfluid Nanofluid*, 2006(Vol-2).
- [9] Todd Thorsen, Sebastian J. Maerkli and Stephen R. Quake2; Microfluidic large-scale integration. *Science*, 2002(Vol-298)
- [10] Cheryl A. Perich; Parallel Manipulation of mm Scale Components using Electroosmosis. *Masters Thesis to be defended @ Cornell*, 2012.
- [11] Kirby, Brian. "Chapter 15: Fluid Transport." *Micro- and Nanoscale Fluid Mechanics: Transport in Microfluidic Devices*. New York: Cambridge UP, 2010. 336-350. Print.
- [12] Hill, Reghan J., Donald L. Koch, and Anthony J.C. Ladd. "The first Effects of Fluid Inertia on Flows in Ordered and Random Arrays of Spheres." *The Journal of Fluid Mechanics*. 448 (2001): 213-41. Print.
- [13] Image of testing apparatus: <http://pmiapp.com/testing/index.html> Date visited: April 12, 2012.
- [14] Method of Images: <http://www.astro.uvic.ca/~tatum/elmag/em01.pdf> Date visited: April 20, 2012.
- [15] Moon, Hyejin, et al. "Low voltage electrowetting-on-dielectric." *Journal of Applied Physics*. October 1, 2002. Vol 92, No. 7.
- [16] Cooney, Christopher G., et al. "Electrowetting droplet microfluidics on a single planar surface." *Microfluid Nanofluid*. March 24, 2006. Vol. 2, No. 5.
- [17] Hiller, J., Miller, J., Lipson, H. (2011) "Microbricks for 3D Reconfigurable Modular Microsystems," *IEEE Journal of Microelectromechanical Systems*, Accepted.

## *Task 4: Voxel development and fabrication*

### Task overview and milestones

This task involves development and fabrication of 500-micron scale voxels for use with the assembler. Initially, the voxels will be passive for static structures. As the process matures, we will explore alternative materials and coatings (e.g. for flexible or conductive voxels) as well as layering circuitry for active voxels (sensing and actuation, processing and power).

### Technical Progress

#### *I. Recreating Voxels*

Since previous voxels were found to have major issues with "extra feet", misaligned layers and cracking (see below), it was necessary to rebuild the voxels using nanofabrication and photolithography [1].

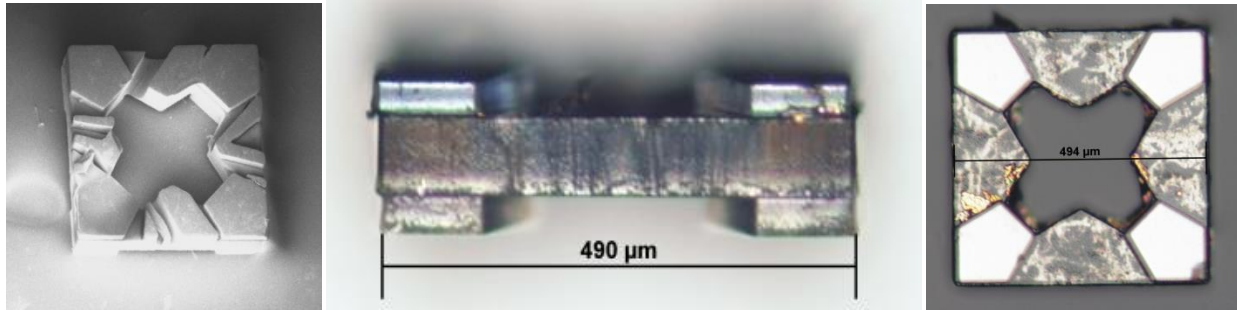


**Figure 94.** From left to right, the extra “feet”, misaligned layers, and surface cracking can be seen. Photos by Dr. Jonathon Hiller, former Ph.D student.

Therefore, instead of only using chrome, two test batches were used: one with a chrome layer to protect the feet, and another with copper to protect the feet. When repeating the chrome tests, similar results were found to the original experiments. However, the copper trials were found to have consistently better results due to the decrease in thermal stress and increased coefficient of thermal expansion. In addition thermal ramping was included in the process instead of immediate heat immersion. Below a typical copper layered voxel and the consistent results can be seen.

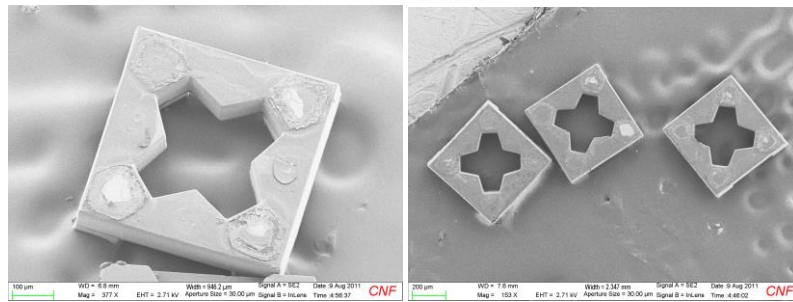


**Figure 95.** The tiles that use a copper layer show no extra feet or major cracks. Photos by Andrey Dotsenko CCML REU intern.

While these tiles were overall better than the previously designed tiles, there were still misalignment issues that could not be accounted for.

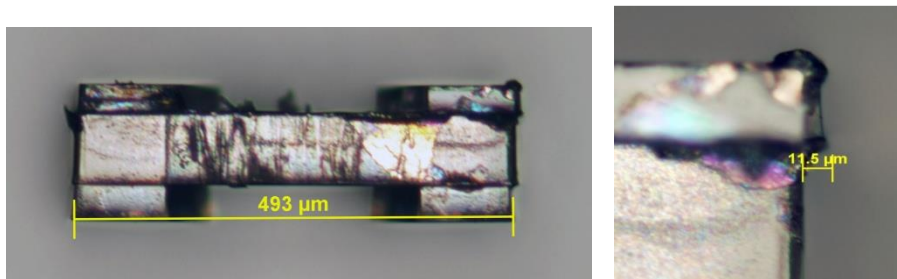


**Figure 96.** Errors ranging in tens of microns can be seen between layers of SU-8. Photos by Andrey Dotsenko CCML REU intern.

While these size errors seem to be quite small, it causes issues in the alignment of the tiles with each other.

## *II. Creating Base plates*

Base plates were created in the Cornell Nanofabrication Facility (CNF) using silicon etching. Since the Base A was found to be the most reliable and best performing plate, it was chosen for nanofabrication. The tiles were then placed onto the platforms using tweezers and the results can be seen below.

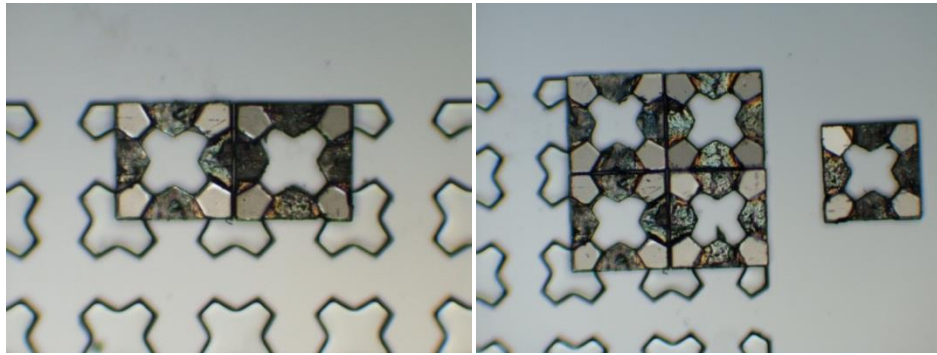


**Figure 97. 500 micron tiles placed onto silicon etched base plate design A. Photos by Andrey Dotsenko CCML REU intern.**

While the tiles were able to be placed into the base plate, there were issues in stacking above one layer. Do to the misalignment in the layers, the tiles pushed against each other, making it difficult to fit tiles on upper layers. This also is a problem since this creates high forces between the base and tiles, making it difficult to release a final product were tiles to be stacked. In order to rectify this, the tiles could be individually inspected for ideal specimen as a short-term solution. Otherwise, the base plate seemed to be consistent along the length and width, with no noticeable errors. Different values of E were chosen for the base plate (from 5-23 microns), and all allowed for ease of tile placement. Therefore smaller values of E could be used in the future.

### Challenges

Most of the difficulty came from working in the Nanofabrication Facility. Not only does training take an extensive amount of time, but there are many “tricks” to understanding the best way to spin SU-8, etch, and make masks, among other things. Furthermore time is always an issue. The process to make these tiles is very long, making it difficult to make small changes or iterations among designs. The main issue to overcome at this point is to determine why there is shifting amongst tile layers, and how to prevent this in the future.

#### *I. Recreating Voxels*

In past trials both chrome and copper were used as a protective layer to prevent the bottom feet of the voxels from dissolving when going through the exposure process. It was previously determined that the copper produced consistently better results due to the decrease in thermal stress and increased coefficient of thermal expansion. However, when trying to release the tiles from the silicon base, it was found that the bottom feet and copper coating were sealed together to the wafer, making it impossible to remove the tiles without breaking off the bottom feet. The copper was able to withstand the chemical strength of the SU-8 developer. After speaking with many of the Cornell Nanofabrication Facility (CNF) members, it was still unclear as to why the copper would cause the fusion between the three layers. The pictures shown below exhibit the lack of feet, but show increased accuracy in the dimensions of the voxel. Therefore, further investigation must be conducted to determine how to rectify these differences. 3D printed, nylon laser cut, and past nanofabricated tiles will all be used to test the efficiency and consistency of the electro-osmosis pump. However, issues have developed using the 3D printed tiles in that the support material is extremely difficult to remove on such small scales. NaOH solutions have been used to soak and help dissolve away the support material, but could not remove all of the FullCure702 material. See Figure 37.

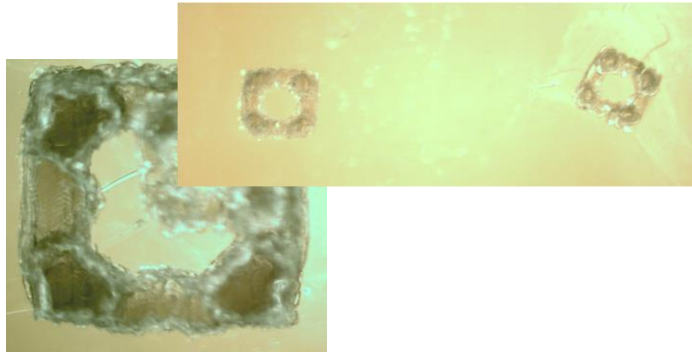


**Figure 98:** On the left is an image of a 1mm square tile on top of a 2mm square tile. On the right are two 1mm square tiles. It is possible to see the uneven edges and excess support material that hides the features of the tile.

Three members of the technical team participated in an initial round of technical training at the Cornell Nanofabrication Facility (CNF). The CNF is part of an NSF-sponsored nationwide network of academic nanofabrication facilities. We plan to continue using CNF tools to build the smaller versions of voxels. In the interim, we continue to decrease the size of the voxels (also referred to here as tiles). The newest version of the tiles (see Figure 99) is 3mm on each edge, and uses 4 electrical connections per tile (8 contact pads are present, but the top/bottom connections are shared). This basic design with 4 unique terminals supports a variety of different electronic payloads, including resistors, capacitors, inductors, diodes, transistors, and microcontrollers. Different electric circuits can be implemented with combinations of these primitive circuit elements. The simple circuit shown in Figure 100 illustrates this capability.

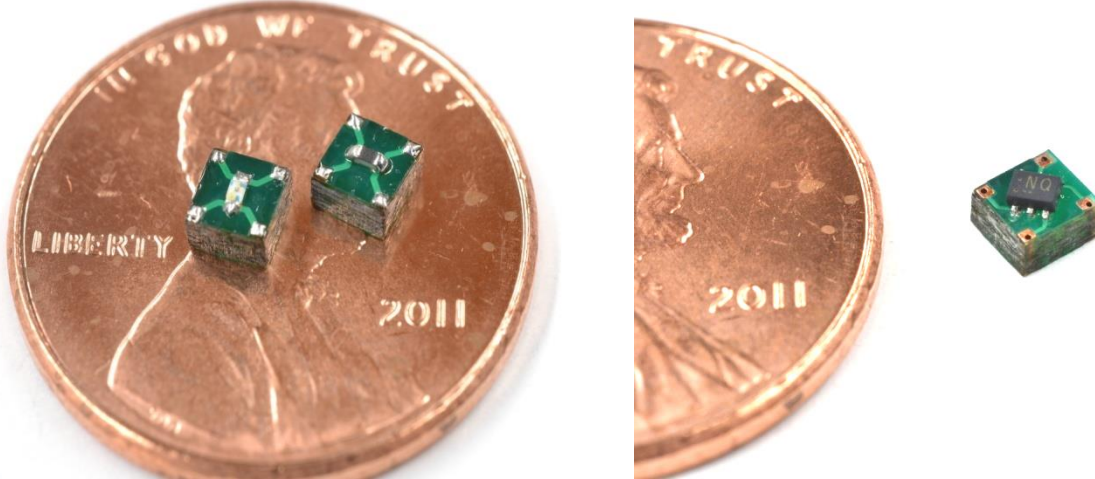


**Figure 99:** 3mm tiles constructed with commercial PCB process. Shown from left to right: LED, resistor, microcontroller.

Though tiles smaller than 3mm will be built, the current form factor already enables interesting structures. The images shown in Figure 101, and illustrate the concept. The tiles interconnect on a regular lattice, while the spaces between can be used for cooling, energy storage (electrolytes for batteries), or as additional structural material. These figures also illustrate our concept for hybrid digital/analog manufacturing. The "digital" voxels create physical structures with well defined spatial relationships; our previous publications have described the advantages of this approach. The clear material in the figures represents the "analog" material. This material is deposited in an extrusion or droplet; this deposition

process implies an inherent uncertainty in the amount of material applied as well as the position. This limitation is more pronounced as the desired feature size is reduced. A hybrid analog/digital manufacturing approach leverages the existing low-cost of analog printing methods, while allowing more sophisticated blocks to be embedded within the structure.

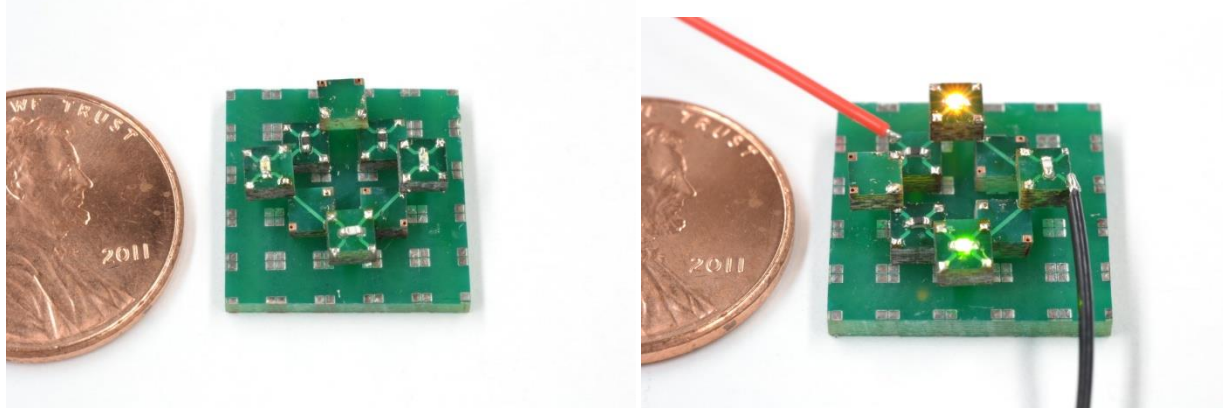


**Figure 100:** Electrical circuit constructed from 3mm tiles. Two parallel circuit paths with current-limiting resistors to light LEDs.



**Figure 101:** A "leg" composed of several hundred (simulated) 3mm tiles and a clear, flexible polymer.

## *II. 3mm-Scale Voxel Development:*

We pursued two areas during the last quarter: hybrid assemblies and actuated voxels at the 3mm scale. The idea behind hybrid assemblies is to combine prefabricated voxels with continuously deposited materials in one "print" job. This approach enables the fine geometries that are possible with continuous printing technologies while allowing complex circuits and actuated structures to be created. The objects in were created by adding prefabricated voxels to an analog inkjet-printed model. In this case the model was sliced appropriately so that the voxels could be added into each layer; however we are currently trying to do the voxel-embedding on the fly, at print time. If successful, this approach could be readily adapted to existing 3D printers with the addition of a pick and place head.



**Figure 102:** A hexapod composed of several thousand (simulated) 3mm tiles with a flexible polymer skin.

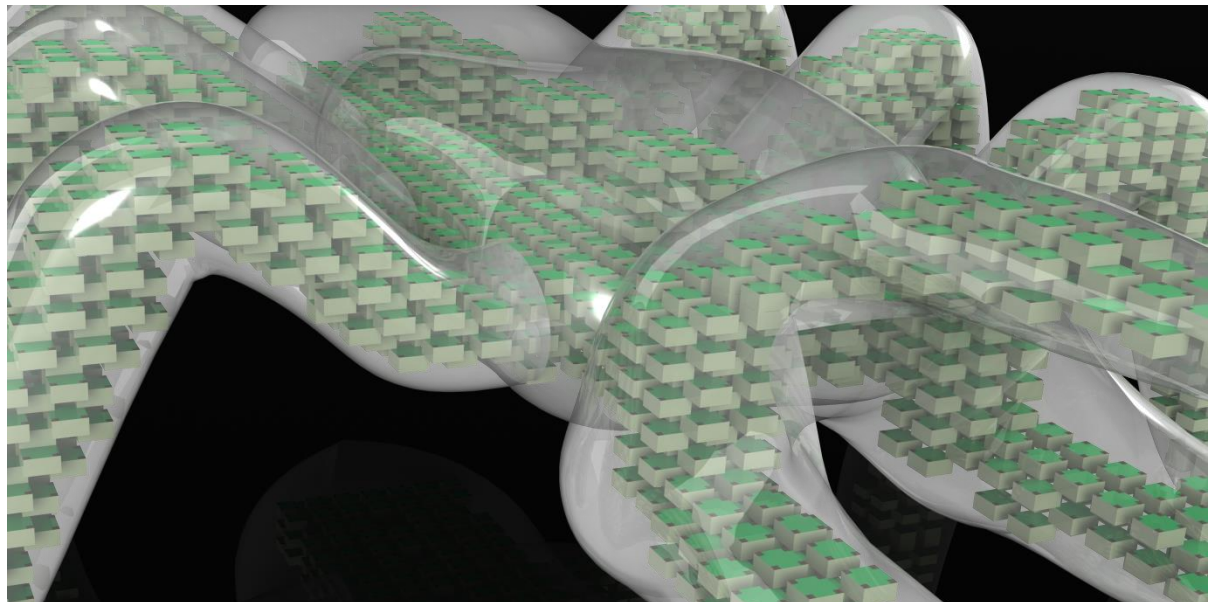


**Figure 103:** Rendering of the hexapod showing the tile layout.

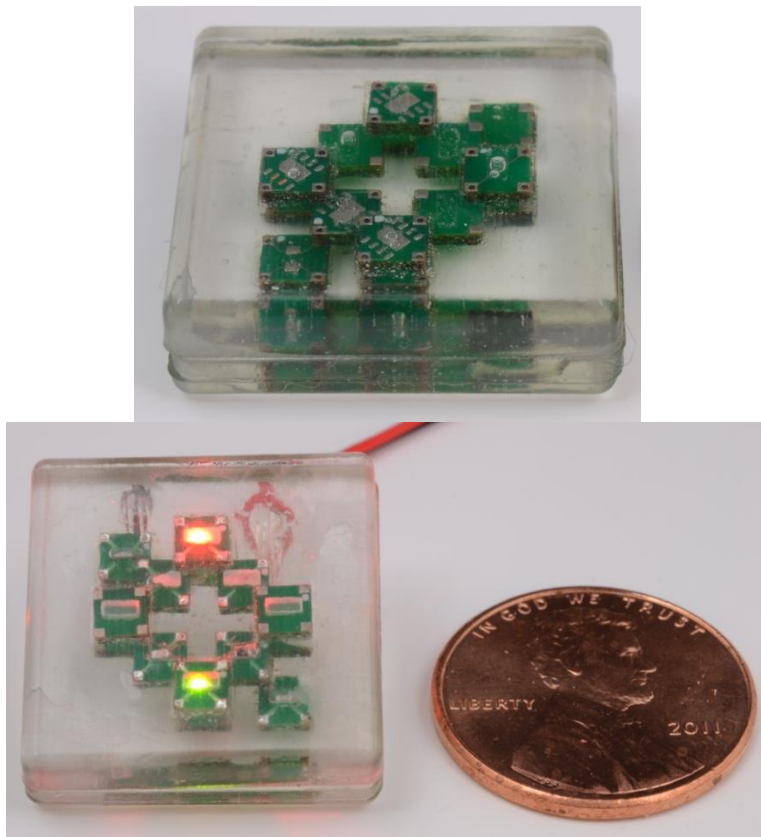


**Figure 104: Hybrid continuous/digital objects created with a combined inkjet and voxel assembly process. The lit LEDs illustrate a working electrical circuit within this hybrid object.**

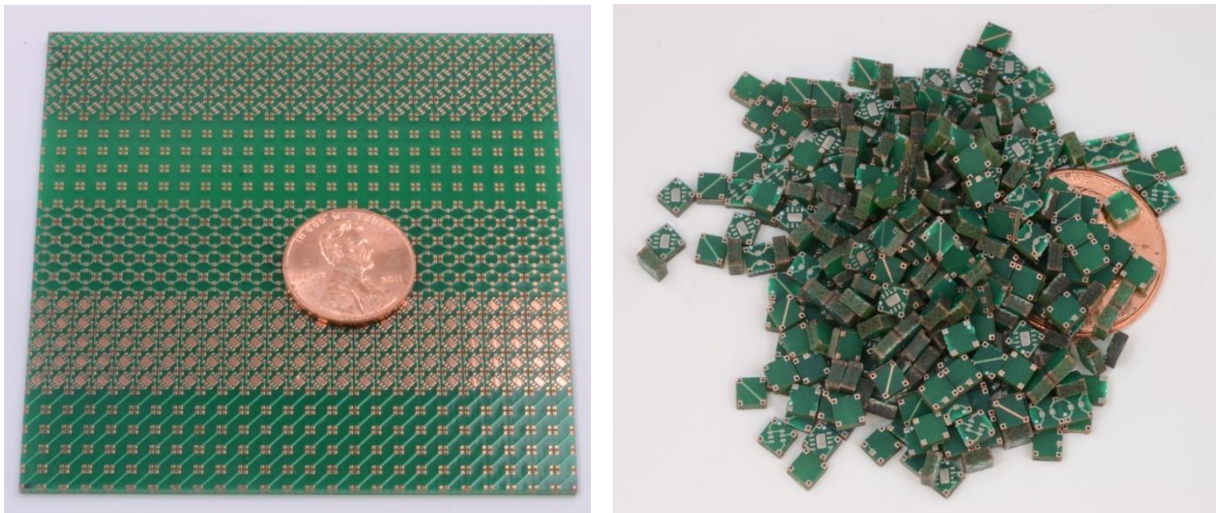


**Figure 105: Voxels are fabricated using conventional circuit board manufacturing techniques from arrays containing 625 voxels. The individual voxels are then freed from the array using a UV laser cutting system. Each individual voxel is 3mm X 3mm X 1.57mm.**

The voxels shown in Figure 105 were fabricated using conventional printed circuit board manufacturing techniques. Each of five different voxel types (Isolation, Crossover, FET, Microcontroller, and RLDC) was tiled in a large array. This step reduces manufacturing costs and makes the circuit board panels large enough to handle. The panels of voxels are cut apart using an LPKF UV laser (Protolaser U). The laser makes repeated passes through the epoxy/resin material and cuts a 25 micron wide channel through the substrate. Gentle cleaning with 90% isopropyl alcohol using a slow magnetic stirrer for 1-hour removes remaining cutting residues.

### *III. Design for Smaller-Scale Voxels:*

Our goal is to eventually develop voxels at sub-millimeter scales, and we've begun developing designs that can be fabricated using conventional parallel microfabrication methods (i.e. photolithography). The basic design, shown in Figure 105, is composed of a cross-shaped silicon core with square pads of SU-8 added to both ends. This geometry is invariant under both flip and rotation, ideal geometric properties for voxels that will eventually have to be sorted for manipulation by an assembler [1]. The SU-8 pad not only makes the design space-filling, but also may protect any delicate electronic components on the central part of the silicon core and make it possible to bake completed assemblies to add adhesive strength. Voxels with onboard electronic components can be fabricated by conventional photolithographic methods as outlined in Figure 106.

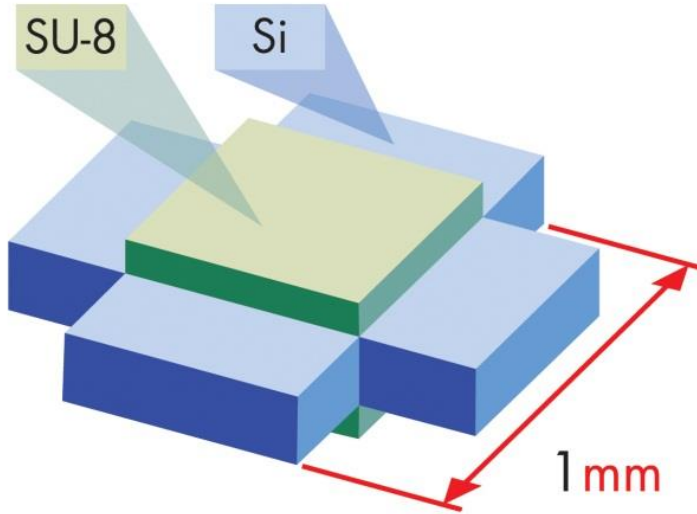


**Figure 106" Simplified voxel geometry for 1mm-scale or 500 $\mu$ m-scale voxels.**

An ideal geometry would also be interlocking to provide in-plane tensile strength to assemblies; however, this design sacrifices an interlocking geometry for the sake of geometric simplicity. Interlocking can be restored to assemblies by the incorporation of 3x3 structural voxels, as shown in Figure 107. The use of multi-sized voxels may also have applications in the design of electronic and actuating voxels by adding additional uniquely identifiable flip and rotation invariant inputs. A proof-of-concept assembly of 7mm prototypes of these voxel designs is shown in Figure 108 and Figure 109.

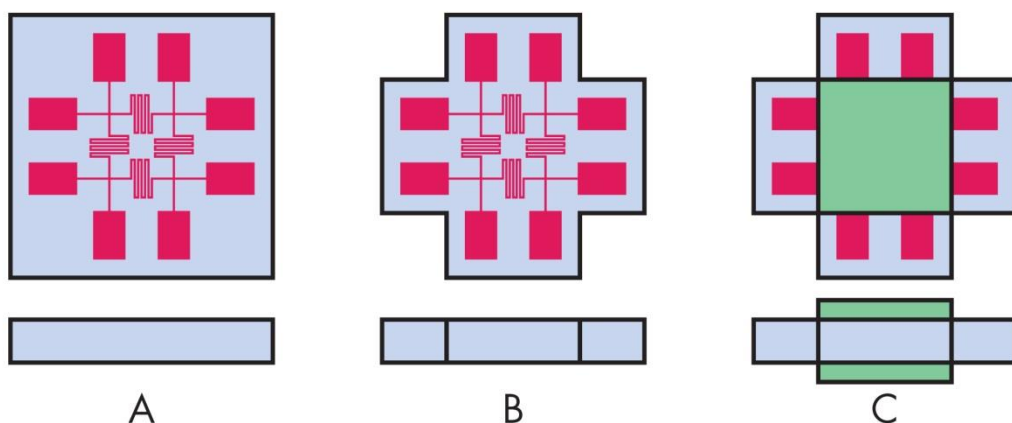


**Figure 107: Fabrication method for small-scale electronic voxels: (A) Electronic components are fabricated on a silicon wafer using conventional photolithographic techniques, (B) shape of middle layer is etched out of silicon wafer using photolithographic methods.**

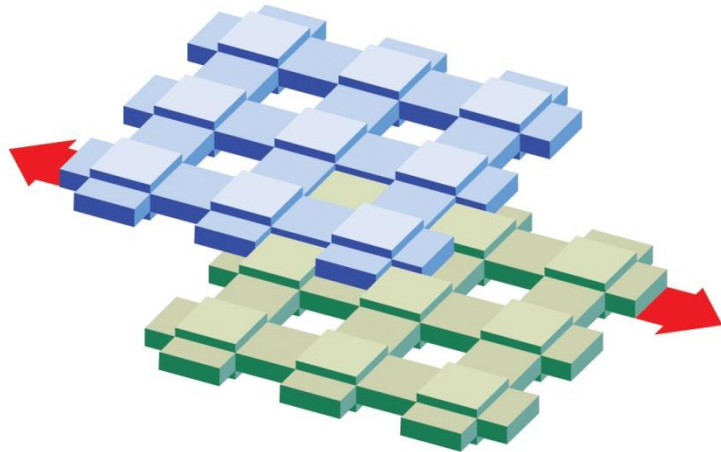


**Figure 108: 3x3 interlocking voxels allow for assemblies to support in-plane tensile loads.**

### Next Steps

#### *II. 3mm-Scale Voxel Development:*

Large-scale circuit fabrication using 3mm tiles: We think that sacrificial scaffolds could make more complicated electrical circuits much easier to produce. One fabrication technique requires an oven to heat all the tiles simultaneously so that solder bonds between the tiles can be formed; in this case a supporting scaffold will be required. We are investigating potential materials for this approach. The top candidate approach uses thin acrylic sheets that are perforated with many small holes. Acetone vapors rapidly dissolve acrylic, and we think that the acrylic scaffolds could be easily removed using this approach, which would avoid aggressive heating that might damage the voxels.

Actuation using 3mm tiles: The most obvious actuation candidate for the tiles is a shape memory alloy (Ni-Ti alloy) that restores to its original shape when heated. This material is available in sheet form. We plan to laminate Nitinol sheet stock between FR4 circuit board material to create 3mm circuit board tiles with an inner Nitinol layer. We will then use a UV laser to pattern the FR4 material and the Nitinol in order to create the desired mechanical shape/cutouts.

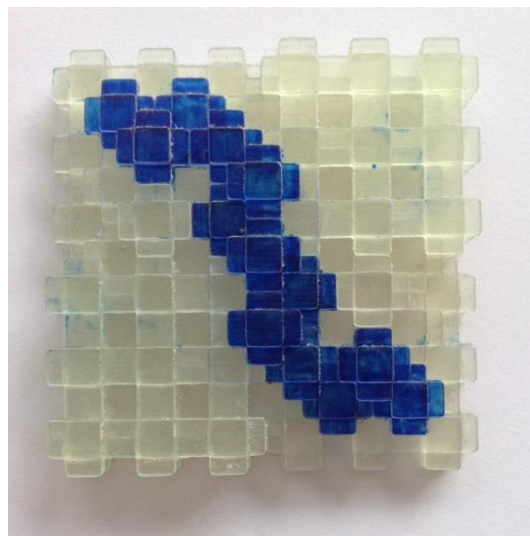


**Figure 109: Proof-of-concept assembly of 7mm voxels and 21mm 3x3 voxels demonstrating in-plane tensile strength; voxels in blue demonstrate a theoretical circuit trace of conducting voxels.**

### *III. Design for Smaller-Scale Voxels:*

We plan to fabricate small-scale structural voxel prototypes using any one of several possible candidate fabrication methods, with conventional photolithography and high-resolution stereolithography (SLA) being the front-runners. It may be possible to fabricate conductive voxels through high-resolution SLA by applying a conductive coating; this option will be explored. The fabrication of 2x1 actuating voxels with the silicon cores replaced with Nitinol films has also been proposed and will be explored.

We focused this quarter on the design and fabrication of actuator tiles for the modular system that we are building. We chose to nickel-titanium shape memory alloy material (nitinol or NiTi), because it is readily available as a commercial product, and can be cut/patterned with various techniques. NiTi contracts when heated, and can be strained to 5-7% before permanent deformation occurs, though lower localized strain results in better actuator cycle reliability. For this reason, designs that minimize localized strain are desirable. We have produced several different candidate designs and simulated their performance, as shown in Figure 110 and Figure 111. We also demonstrated a bidirectional actuator that employed two of these actuators in an antagonistic configuration, shown in Figure 112. This actuator yielded +/- 10% strain, and consumed 100mW. The blocked force has not yet been measured, but efforts are underway, as described below.

We fabricated the NiTi tiles with a UV laser system, the Protolaser U from LPKF. This tool uses a software suite to import DXF cutlines and define the actual pattern that the laser will traverse. In the typical use case, individual drawn cut lines must be turned into several parallel laser cut lines in order to allow the beam to penetrate the material being cut. In regions with very narrow cuts, this is not possible, and single-width cuts must be performed. Multiple material calibration cuts are necessary to determine the correct combination of laser power, scan rate, pass count and focal point adjustment for a particular material type and thickness. We also discovered several undocumented bugs in the laser driver software, which the LPKF staff have since corrected.

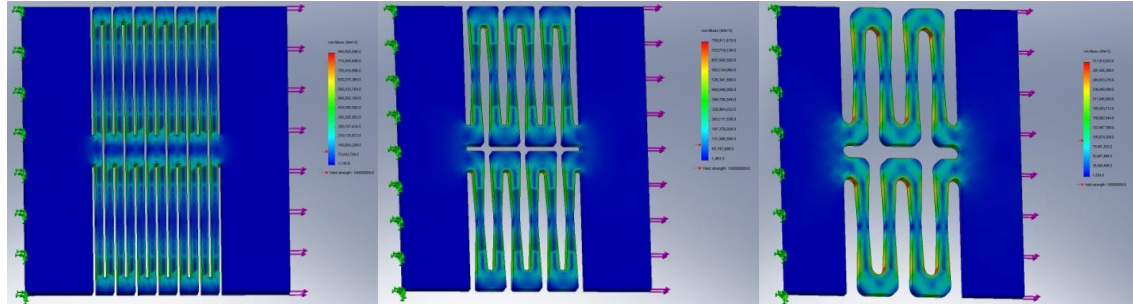


**Figure 110: Small-deformation strain modeling of three alternative NiTi actuator designs.**

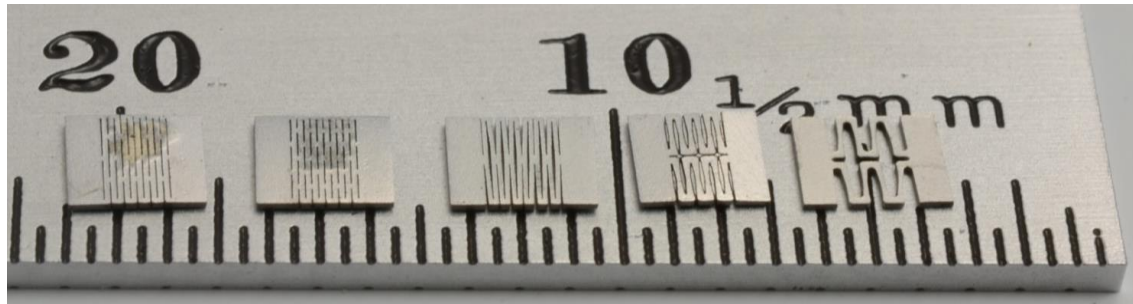


**Figure 111: Five candidate designs implemented in 250um NiTi sheet material.**

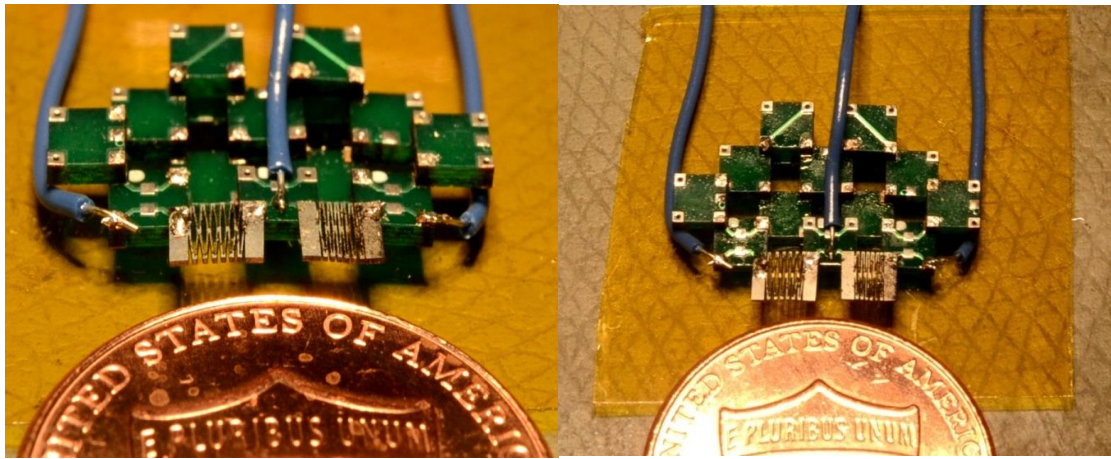
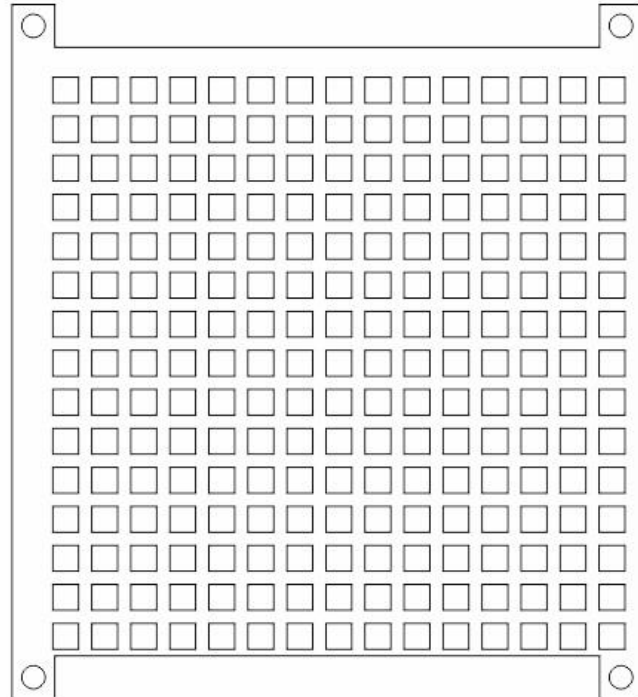


Figure 112: Prototype antagonistic actuator implemented with two NiTi tiles.



Figure 113: TA Instruments DMA Q800 dynamic thermal analyzer and the custom test fixture that we developed for the NiTi tiles.

Cornell's Center for Materials Research (CCMR) has a suite of testing instruments, including the TA Instruments DMA Q800, a dynamic thermo-mechanical analyzer capable of precisely controlling the force and temperature applied to a sample and measuring the resulting displacement (or other combinations of these inputs and outputs). This tool will allow us to precisely characterize the performance of the NiTi actuators, allowing us to verify and cross-validate our material models. The DMA Q800 uses interchangeable material clamps, allowing samples of different sizes to be tested. Our tiny actuators were too small for the existing clamps, so a new clamp set was designed in CAD and the physical part was fabricated by a quick-turn CNC job shop (FirstCut in Maple Plain, MN). The DMA Q800 and the fabricated clamp are shown in Figure 113.



**Figure 114: Automatically generated SVG-format image for laser cutting support scaffold material.**

The electromechanical tiles that we are building are assembled in batch form, typically via a heating process that fuses solder joints between the tile's corners. A sacrificial support scaffold material is required to hold the tiles in place during the assembly step. Since each design is potentially unique, each layer of the scaffold must be tailored to the corresponding layer in the design. We used a Python script to automatically generate a vector graphics image suitable for use as input to a laser cutter. The laser cutting tool is used to pattern sacrificial sheet material. A fully populated layer design is shown in Figure 114. We initially tried several different plastic sheet materials, including 0.015" thick High Impact Styrene, 0.007" thick Lexan, 0.030" thick Polypropylene, 0.5mm thick Plexiglas, and 0.031" thick HDPE. All but the HDPE cut well with the laser cutter (the HDPE suffered excessive thermal deformation), however none of these plastics were sufficiently susceptible to the solvent we were using (Acetone). The Plexiglas was most affected by the solvent, and almost completely dissolved, however it left behind a tough plastic film that had a very strong solvent odor. We rejected this approach and are still looking for a suitable sacrificial scaffold material.

We did not develop any new actuators in this quarter, however we did perform mechanical testing, using the TA Instruments Q800 dynamic testing machine described in previous quarters. This testing allows us to validate our existing designs, and refine our material models. Figure 117 shows the complete time-history of the testing regime for two cycles, while Figure 118 illustrates the hysteresis loop for the same data.

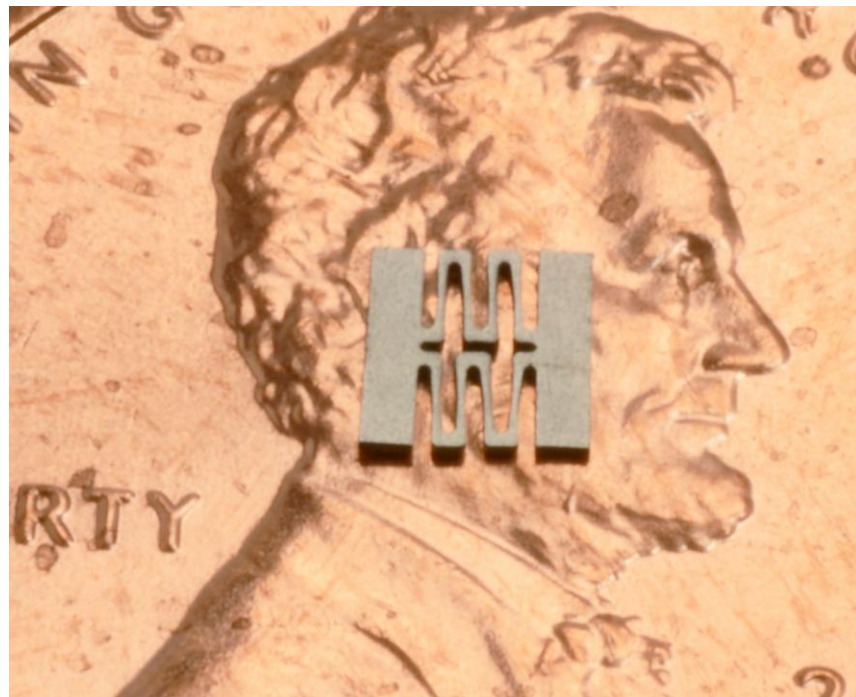


**Figure 115 - Image of the design that was mechanically tested in Figure 117 and Figure 118 below.**

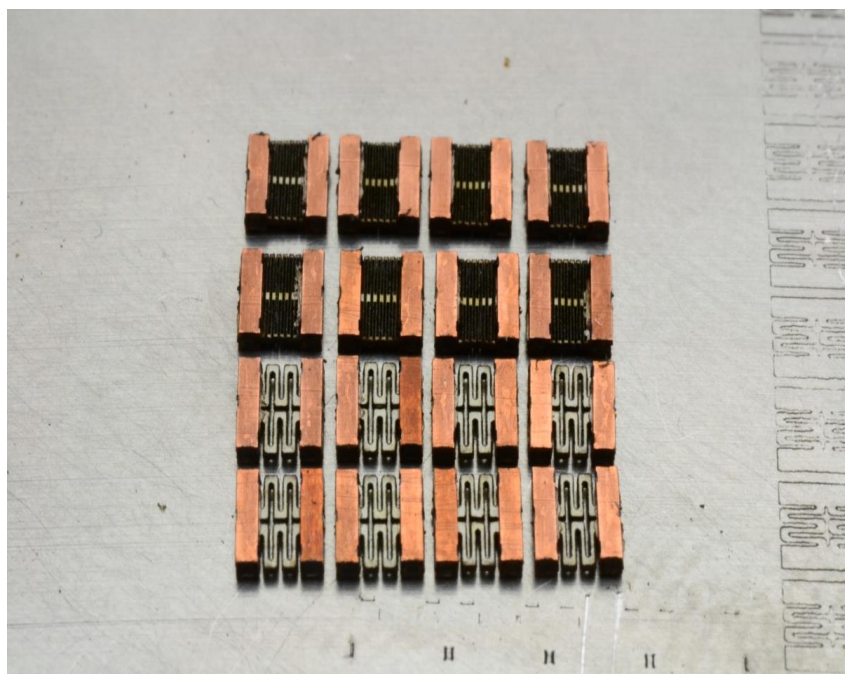


**Figure 116: Two different kind of actuators**

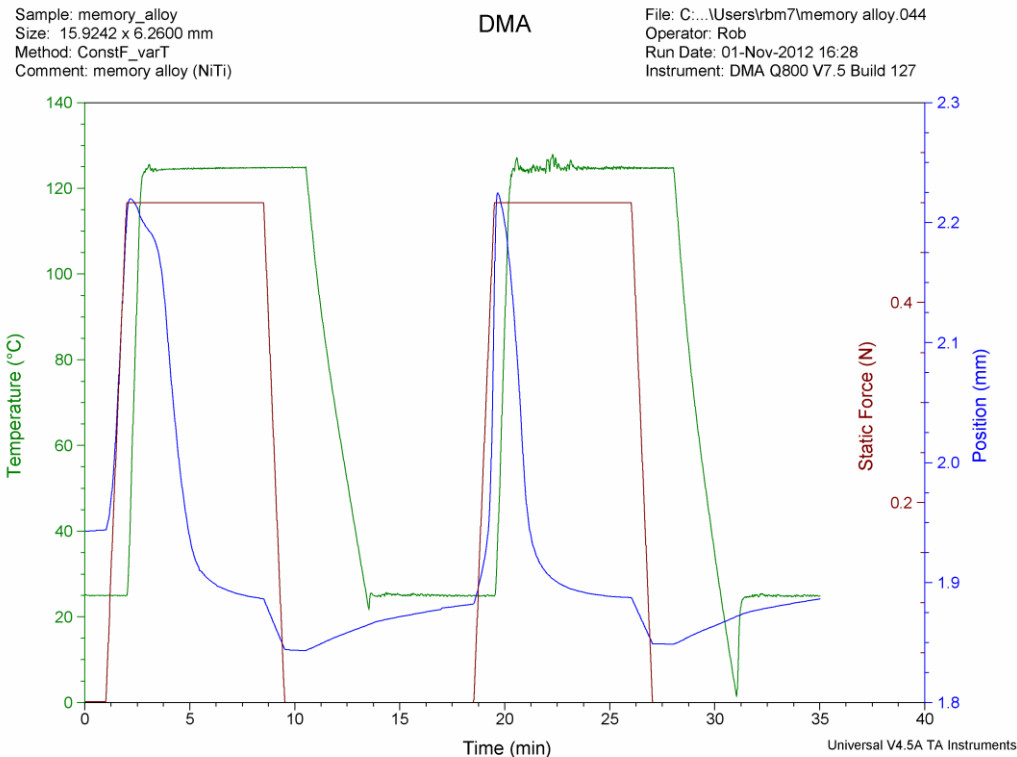


**Figure 117 - Typical force vs displacement vs time vs temperature curves for our nitinol actuators. Data from the DMA Q800.**

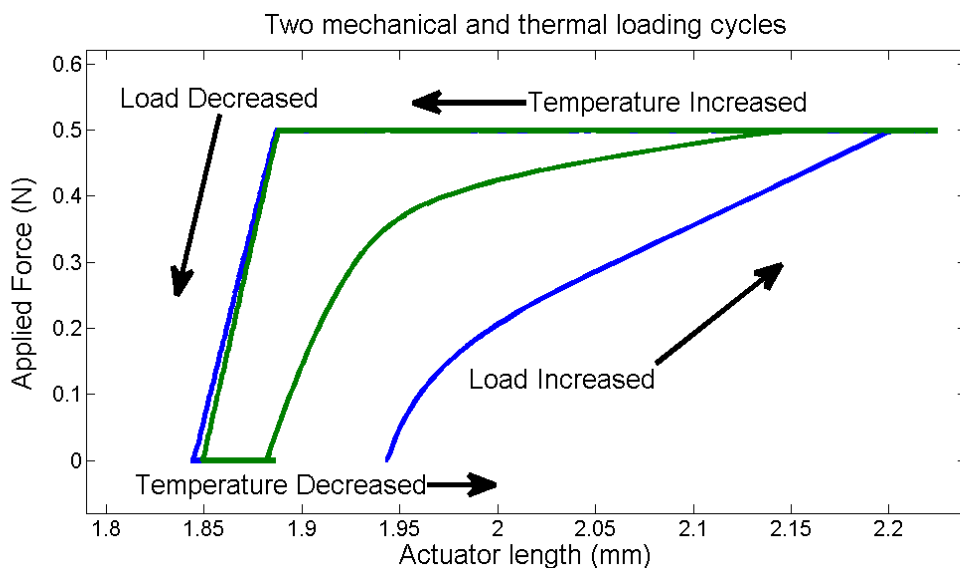


**Figure 118 - Hysteresis loop for our actuators when driven by thermal cycling, and exposed to varying load.**

The demonstrate the proof of concept a robotic limb with 2 degree of freedom was built with these actuators and tested. Fig 33 shows such a robotic limb. This device consisted for three different kind of

tiles: dormant, connector and actuator. By varying the current in three actuators one controls the movement of trunk.

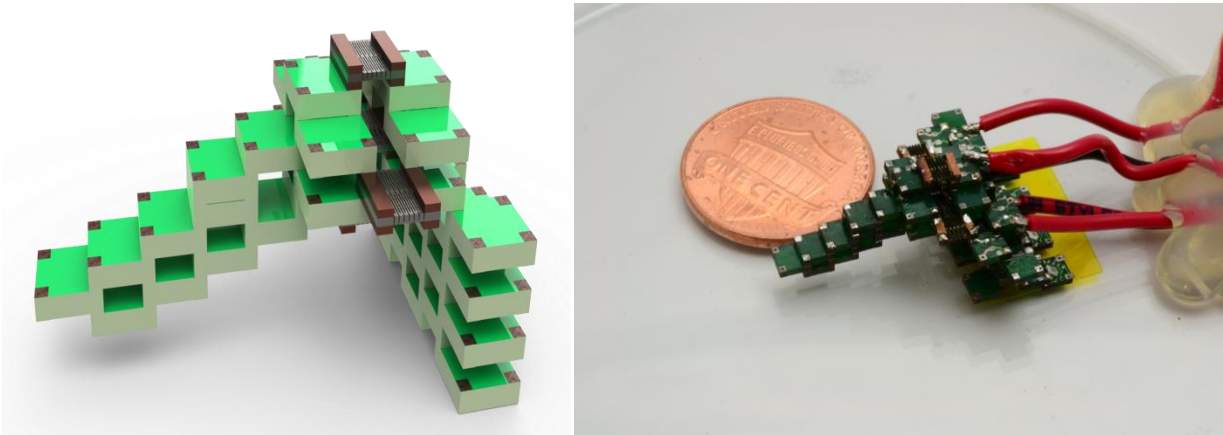


**Figure 119: 2 degree of freedom robotic limb with three actuators (a) The design (b) Physical realization**

## *Task 5: Design Automation*

### Task overview and milestones

This task involves development and testing of design automation software that can assist designers in specifying target structure. This task will proceed from direct design tools to automated tools that compile a high level functionality and constraints into a target design.

### Technical Progress

The simulator progress reported in Task 1 is related to this task (in fact it is a precursor), since a fast simulator that can handle large numbers of voxels is critical for the evolutionary computation approaches that we are developing. We also spent a portion of the last quarter investigating suitable electrical circuit simulation engines. We selected NgSpice because it is open source, appears to have a wide user base, and includes the ability to simulate programmatic code in addition to the traditional passive and active electrical circuit primitives (resistors, transistors, etc). This feature is significant, since the electromechanical structures that we envision will incorporate computation voxels with state machines in order to realize more sophisticated behavior. We have begun incorporating the NgSpice code into VoxCAD. Since the existing VoxCAD mechanical simulator computes the future node positions at a known time step, that same time step can be used to compute the expected electrical state of the network. The mechanical and electrical behavior will be independently computed at each time step, and relevant sensor/actuator data can be exchanged at these intervals.

We began this task in earnest this quarter, and used evolutionary computation techniques to create a variety of robots, using soft materials, that could potentially be implemented with the voxels/tiles that are being created in this project. We used the HyperNEAT algorithm, which employs a generative encoding, known as a Compositional Pattern Producing Network (CPPN). The CPPN is a generative encoding similar to a neural network, but its nodes contain multiple math functions (in this work: sine, sigmoid, Gaussian, and linear). CPPNs evolve according to the NEAT algorithm. The CPPN produces geometric output patterns that are built up from the functions of these nodes. Because the nodes have regular mathematical functions, the output patterns tend to be regular (e.g. a Gaussian function can create symmetry and a sine function can create repetition). These patterns specify phenotypic attributes as a function of their geometric location. In this paper, each voxel has an x, y, and z coordinate that is input into the network, along with the voxel's distance from center ( $d$ ). One output of the network specifies whether any material is present, while the maximum value of the 4 remaining output nodes (each representing an individual material) specifies the type of material present at that location (see Figure 120). This method of separating the presence of a

phenotypic component and its parameters into separate CPPN outputs has been shown to improve performance Figure 120, Figure 121, Figure 122. By producing a single CPPN representing the functional structure of an individual robot, and iteratively querying it for each voxel, we can produce the entire structure of the robot at any resolution. If there are multiple disconnected patches, only the voxels connected to the most central material patch are considered when producing the robot morphology.

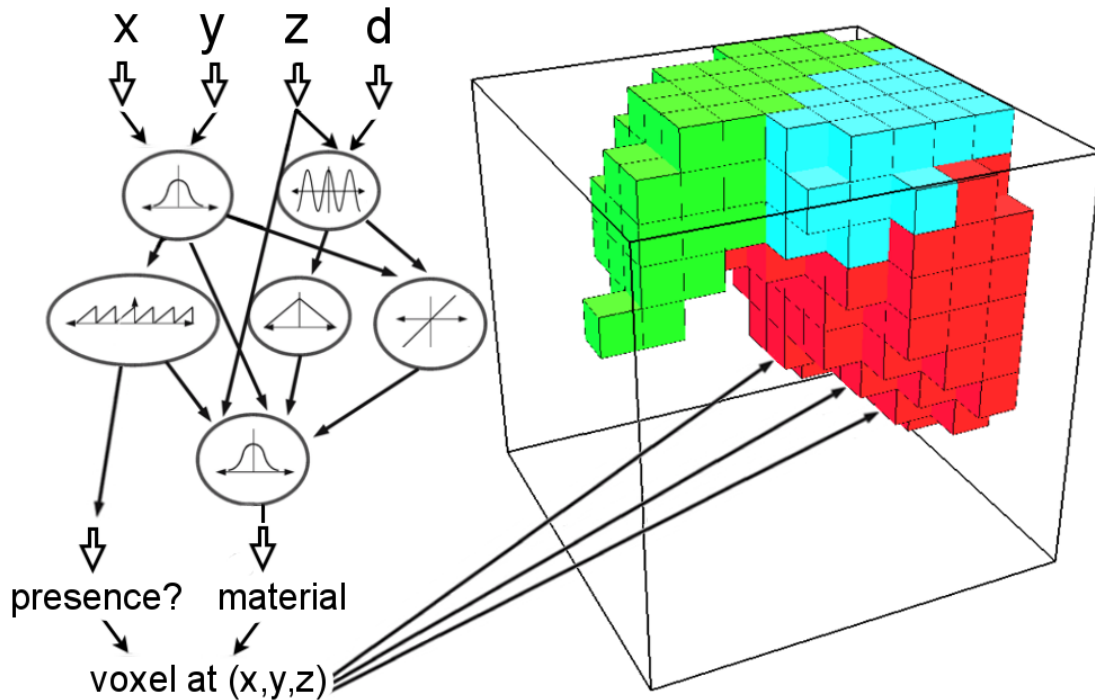


**Figure 120 - A CPPN is queried to create a robot morphology in Voxel space. The CPPN is evolved, based on the fitness score achieved by the robot.**

We used this approach to generate populations with 30 individuals, and then evaluated each individual using a command-line version of the simulation engine behind VoxCAD, Voxelyze. Figure 121 shows six of the individuals that emerged after 1000 generations of evolution. Each was among the fastest individuals from its evolutionary run (individuals were ranked according to speed).

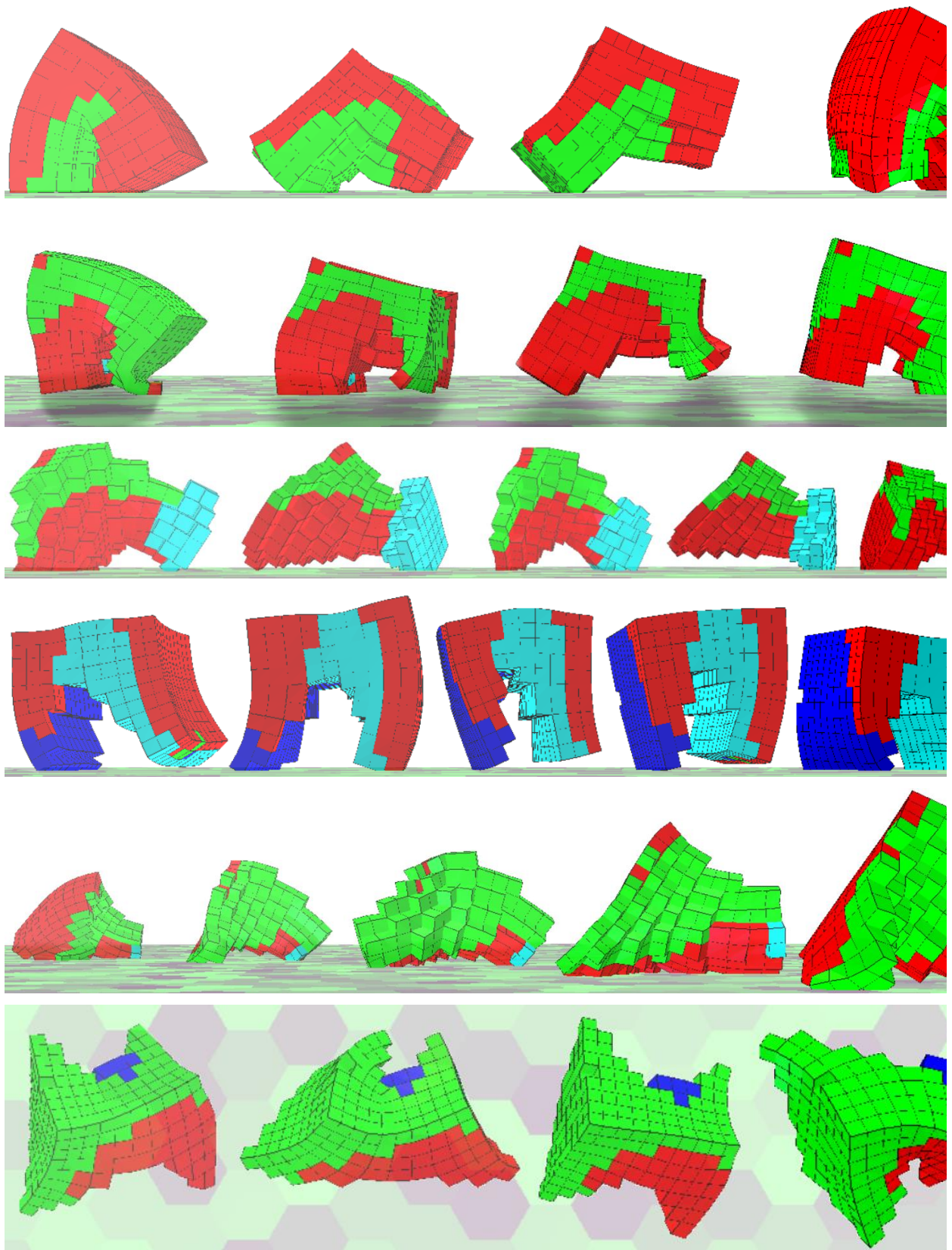


**Figure 121 - Six example time-series images of different individuals locomoting from left to right.**

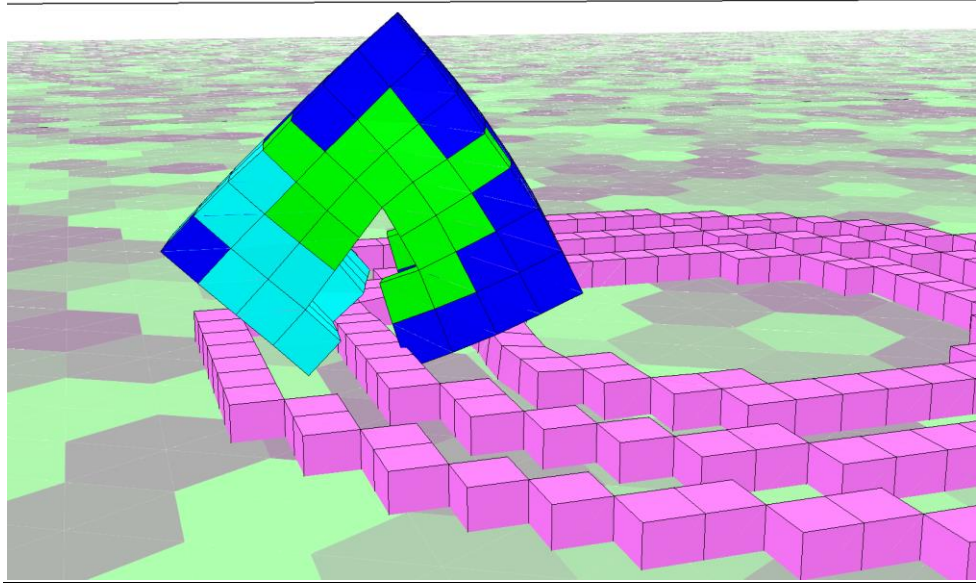


**Figure 122: A demonstration of softrobot's capability: Preliminary study suggests that it be more effecient on a difficult terrain**

Publications based on research supported by Project Number W911NF-11-1-0093:

- [1] Jonathan Hiller, Joseph Miller, Hod Lipson (2011) "Microbricks for 3D Reconfigurable Modular Microsystems," *IEEE Journal of Microelectromechanical Systems*. vol. 20, no. 5, october 2011.
- [2] Cheryl A. Perich, Ashley Macner, Robert MacCurdy, Paul Steen, Hod Lipson, "Toward massively parallel manipulation of mm-scale components using elec-troosmotically controled drops", In Review
- [3] Robert MacCurdy, Anthony McNicoll, and Hod Lipson, "Bitblox: A Printable Digital Material for Electromechanical Machines", In Review

Patents based on research supported by Project Number W911NF-11-1-0093:

- [1] Fnu Apoorva, Robert MacCurdy, and Hod Lipson, "System and Methods for Electrowetting Based Pick and Place Assembly", Publication No-WO2014014892 A2, Application No- PCT/US2013/050650
- [2] Fnu Apoorva and Hod Lipson, "Electroadhesion Based Rapid Assembler", Patent Application No-US61/790, 139.

# Microbricks for Three-Dimensional Reconfigurable Modular Microsystems

Jonathan D. Hiller, Joseph Miller, and Hod Lipson, *Member, IEEE*

**Abstract**—This paper explores the design of “microbricks”—interlocking microscale building blocks that can be used to assemble and reconfigure 3-D structures on a regular lattice. We present the design and fabrication of a space-filling rotation and flip-invariant 500- $\mu\text{m}$  microbrick architecture suitable for 3-D assembly. We describe the design considerations used to optimize mechanical, fabrication, and assembly properties of the components and the finished structures. The final brick geometry was fabricated using two different fabrication techniques: Silicon bricks were micromachined out of silicon, and SU-8 polymer tiles were built up in a three-layer process. The resulting bricks were characterized, and proof-of-concept structures comprising ten bricks were assembled to demonstrate the physical interlocking and compatibility between the two materials. We suggest that the presented interlocking geometry could serve in the future to fabricate passive and active modular macroscale structures from microscale components.

[2011-0024]

**Index Terms**—Integrated systems, microbrick, modular architecture, rapid assembler.

## I. INTRODUCTION

MODULAR architectures comprising functional components with standard interfaces have been recognized as a key to the growth in complexity in microelectronic systems [1]–[3]. Mechanical systems and components, however, have largely resisted standardization, thus hindering the ability to quickly assemble complex systems out of standardized components. One challenge to realizing 3-D modular microsystem architectures is the identification of a basic mechanical building block. Once such a module is designed, it can be fabricated of various materials in independent processes. Both passive and functionalized bricks can be simulated, fabricated, and assembled, spanning a large design space of potential integrated systems.

Once a standardized interface between microbricks is defined, the fabrication methods and functional complexity of each individual brick are decoupled from the final assembly

Manuscript received January 25, 2011; revised March 31, 2011; accepted July 7, 2011. Date of publication August 30, 2011; date of current version September 30, 2011. This work was supported by the U.S. Defense Advanced Research Projects Agency Defense Science Office under Grants W911NF-11-1-0093 and W911NF-08-1-0140. The work of J. D. Hiller was supported in part by the U.S. National Science Foundation. The work of J. Miller was supported by the Cornell Center for Materials Research summer Research Experience for Undergraduates program. Subject Editor C.-J. Kim.

J. D. Hiller and H. Lipson are with the Sibley School of Mechanical and Aerospace Engineering, Cornell University, Ithaca, NY 14853 USA (e-mail: jdh74@cornell.edu; hod.lipson@cornell.edu).

J. Miller is with the Department of Physics, North Dakota State University, Fargo, ND 58102 USA (e-mail: joseph.b.miller@ndsu.edu).

Color versions of one or more of the figures in this paper are available online at <http://ieeexplore.ieee.org>.

process. This allows for a compatible industry-wide infrastructure to develop around a given microbrick architecture, enabling exponential growth of complexity. Unlike the analogous Moore’s law, which defines the growth of the semiconductor industry by the exponentially decreasing transistor size, the analogous scaling law for the microbrick industry would describe the exponentially increasing design space reachable in multiple physical domains.

A number of systems have explored the use of modular interlocking components [4], [5]. While these systems are inherently serial in their assembly, they demonstrate the feasibility of manipulating and assembling interlocking shapes at this scale [6]. However, the components used in these systems are not geared toward the assembly of general 3-D integrated structures. For example, they are porous, a property that is well suited for their use in tissue scaffolds, but could negatively affect the mechanical properties.

In this paper, we explore the considerations for the geometric design of a modular building block, based on mechanical properties, as well as fabrication constraints and assembly requirements. We do not consider electrical interconnectivity, although we have begun exploring this elsewhere [7].

## II. BRICK DESIGN

### A. Design Requirements

It quickly becomes evident that many competing objectives factor into the optimal design of the individual microbricks. Perhaps the most important tradeoff is between the geometric complexity of each brick and the complexity of mechanically connecting adjacent bricks. On the one hand, the geometry must be as simple as possible to facilitate ease of mass fabrication, yet the shapes must rigidly interlock in three dimensions to create structures [8]. The design requirements that we consider here for the microbricks are as follows:

- 1) physically interlocked in three dimensions;
- 2) simple geometry;
- 3) ease of alignment for assembly;
- 4) ease of fabrication in bulk;
- 5) mechanically robust.

Physically interlocking bricks are desirable over gluing or otherwise adhering adjacent bricks for several reasons. First, this decouples the material properties of the brick from the assembly process. This allows bricks to be composed of any solid material, even materials that are mutually incompatible in any given fabrication process. Second, each brick self-aligns with

its neighbors upon assembly, ensuring that a regular lattice with well-defined interfaces is preserved throughout the structure. This enables discrete (digital) feedback of the assembly process that would not be possible if continuous errors in position between adjacent bricks were possible. However, the result is that the need for physical interlocking in all three dimensions prohibits the possibility of using simple 2-D shapes that would be easier to manufacture.

Another tradeoff exists between the number of redundant orientations of a brick and the geometric complexity. If each brick must be actively aligned to a single correct orientation before assembly, there will be a large penalty in assembly complexity and efficiency. This problem can be mitigated in one of two ways. First, alignment can be maintained throughout the brick manufacturing, distributing, and assembly process. Although some brick manufacturing processes may allow the rotation and orientation to be maintained throughout the fabrication and assembly process [9], there are many brick fabrication processes where this would be prohibitive. For instance, when the substrate on which the bricks are manufactured on is costly and reusable, each microbrick would need to be transferred to an intermediate substrate while maintaining orientations.

Alternatively, to better meet the goals of a mass fabrication process, we propose that the microbrick geometry should be rotation and flip invariant. This allows the bricks to be manufactured, stored, and transported without regard to absolute orientation and then passively aligned in parallel for assembly. Because any possible incorrect brick orientations are eliminated by design, the assembly process becomes significantly more simple and robust.

Other important considerations that are critical to a successful microbrick architecture regard the scaling of structures from the tens of bricks presented here to objects composed of millions, billions, or even more microbricks. It quickly becomes apparent that not only will massively parallel assembly methods be required but also massively parallel microbrick manufacturing methods [10]. Ideally, the geometry would be naturally suitable for fabrication processes such as micromachining [11], hot embossing [12], [13], [14], microcasting [15], or additive layered manufacturing [16], [17]. All of these processes leverage reusable complexity, in which a single complex template with many individual brick templates is fabricated which can then be used to easily and repeatedly fabricate many bricks in parallel. Given this class of manufacturing methods, it is desirable for the objects to be 2.5-D or composed solely of extruded 2-D profiles in a single plane. In order to facilitate all of these manufacturing processes, there should be no internal or undercut surfaces that would prevent having a single parting plane for a mold.

Finally, the shape design of the individual bricks will have a large effect on the aggregate material properties of an object composed of many such bricks. Although a block of bricks made of a given material will never be as strong as a homogeneous block of this material in the same dimensions [18], the differences between the two can be minimized by a directed choice of brick geometry. In order to maximize the mechanical properties of the material, it is desirable that the bricks tile in 3-D space such that they are space filling. With such a system,

voids may still be introduced by leaving empty locations in the lattice in applications where weight savings or porosity is desirable.

### B. Brick Geometry

To begin the discussion of selecting a brick geometry, we first broadly consider the space-filling requirement presented earlier. There are a finite number of tessellation modes that fill 3-D space. Of these, there are 3-D tessellating shapes based on platonic solids and 2.5-D extrusions of 2-D shapes that also fill 3-D space. Although cubes are the only 3-D platonic solid that tiles directly in Euclidean space [19], truncating tetrahedra and octahedra can also fill Euclidean space [8]. 2.5-D tessellating shapes such as equilateral triangles, rectangles, and hexagons tessellate in two dimensions to form a complete layer, and then, subsequent layers may be stacked to achieve a 3-D lattice.

For both the 3-D and 2.5-D tiling shapes, geometry must be added at some or all of the interfaces to enable interlocking. If care is taken, this can be done with no loss of possible brick orientations, thereby maximizing the rotation and flip invariance. If the layers are suitably offset laterally from each other in the layer-based 2.5-D schemes, a rigid structure can be created by interlocking only between bricks of adjacent layers and not between adjacent bricks in the same layer. This allows a much simpler design while also allowing bricks within a given layer to be assembled in any order, even simultaneously in a parallel assembly process.

For these reasons, 2.5-D square interlocking tiles were selected for fabrication due to the ease of assembly and maximum degrees of rotation and flip invariance. Offset between layers was logically selected to be half a tile dimension in both lateral axes to allow for maximal redundancy and interconnection area. The simplest interlocking scheme between bricks in adjacent layers could be achieved using a simple peg-and-hole design, but when mechanical characteristics are considered, it quickly becomes apparent that more mechanically robust designs are possible.

An improved design (see Fig. 1) was developed that minimizes both the geometrical complexity of the tile and the internal stress concentrations as the tile is physically loaded. The chosen microbrick design has eight redundantly identical orientations and no “partially correct” orientations that could cause problems in a passive alignment process. The geometry consists of a ring structure into which 4 ft of the four adjoining bricks in the next layer press. Each foot sticks up approximately 1/4 of the total height  $H$  [see Fig. 1(a)]. Thus, when feet are inserted into a given brick from both above and below, they touch in the middle, yielding a space-filling design.

Given the constraint of filling 3-D space, there were four parameters to vary: the tile edge dimension ( $D$ ), the tile height ( $H$ ), the tab width ( $L$ ), and the tab interface angle ( $A$ ). All other dimensions are derived from these to satisfy the space-filling criterion. The tile edge dimension was selected to be 500  $\mu\text{m}$  based on the desired scale of the bricks. 500- $\mu\text{m}$  tiles are small enough that a structure composed of many such tiles would appear smooth to the human eye, yet large enough to be manipulated by hand when necessary. The tile height

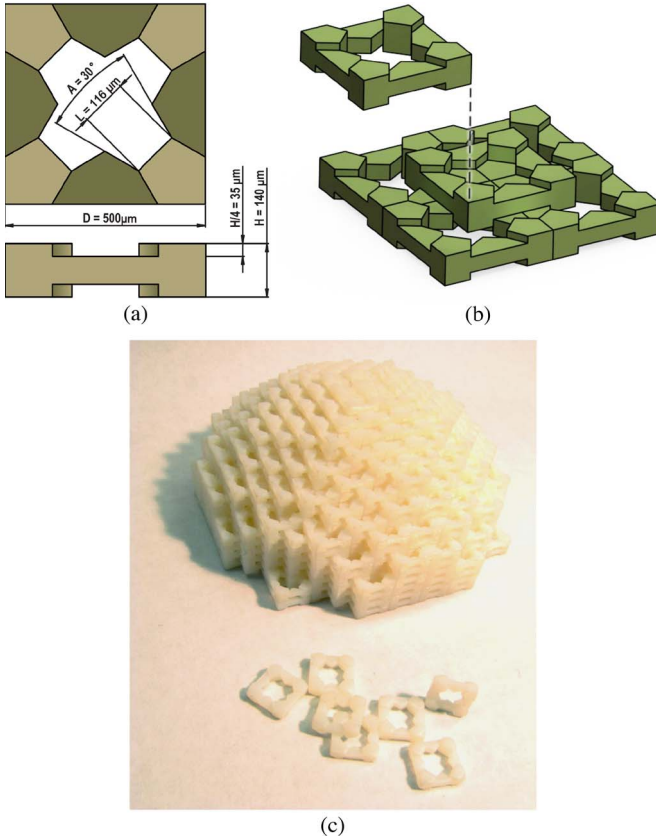


Fig. 1. Selected square tile design is (a)  $500\text{ }\mu\text{m}$  square and  $140\text{ }\mu\text{m}$  thick. The tab angle  $A$  was selected to be  $30^\circ$  with a tab width of  $116\text{ }\mu\text{m}$ . The space-filling tiles interlock by offsetting each layer by  $1/2$  a tile dimension in  $X$  and  $Y$ . Millimeter-scale mock-ups assembled into a hemisphere demonstrate (c) a large-scale assembly.

of  $130\text{ }\mu\text{m}$  was selected as a compromise between the two manufacturing processes that were pursued to fabricate the bricks. The polymer bricks were built up from layers of SU-8 photoresist in an additive process. Given the relative difficulty of spinning very accurate and thick layers of SU-8 and the processing difficulty of aligning a large number of separate SU-8 layers, the geometry was kept as thin as possible. On the other hand, the silicon bricks were created with a subtractive process. Since the initial thickness of the wafer dictated the height ( $H$ ) of the bricks, there were constraints on the thinnest possible wafer that could be reasonably handled. The  $130\text{-}\mu\text{m}$  thickness was an appropriate compromise between manipulating silicon wafers that were thick enough to handle while not necessitating unreasonably thick SU-8 layers.

The other two free parameters dictate the size and shape of the tab feet and, by extension, the size and shape of the ring geometry. The tab width  $L$  was selected to be  $116\text{ }\mu\text{m}$  as a starting point. Then, the brick geometry was analyzed to determine the optimal tab interface angle  $A$ . There are many arbitrary metrics that could be used to decide the best geometry. Here, we chose to use a combination of two metrics to capture information about the geometric complexity of the shape along with an estimate of how strong a structure composed of such microbricks would be.

The first metric was a measure of the compactness of a 3-D shape. Here, we define compactness as the total surface area of

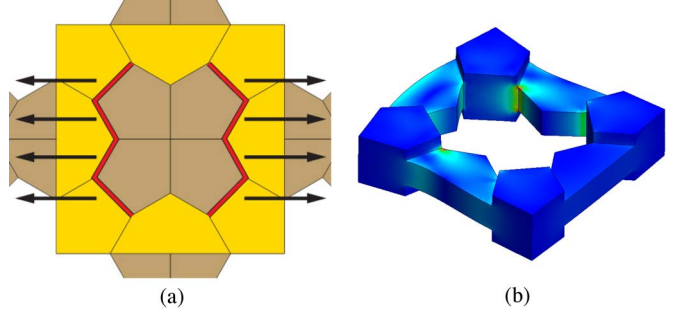


Fig. 2. (a) Tiles were loaded in simulation in a manner consistent with the forces that an individual tile would undergo when a larger structure is subjected to an axial tension load. An example output of the finite-element simulation shows the exaggerated deformation and stress concentrations resulting from the loading.

the brick divided by the total volume of the brick. In this case, the total volume of the brick was constant due to the space-filling constraints. Essentially, varying the tab dimensions adds and subtracts equal quantities of material at different locations of the brick shape. Bricks with higher surface area are less compact and thus less desirable.

The second metric for each candidate brick geometry was obtained by performing finite-element analysis to approximate the tile's behavior in a lattice of tiles under tensile load. The axial tension scenario was selected as a worst case scenario because the space-filling nature of the bricks will give them favorable compressive properties as compared to tensile properties. The tiles were loaded as shown in Fig. 2(a), which is a good approximation of the forces that a tile will undergo within a structure under axial tension. One interface surface was fixed while the other had unit force applied in the outward direction. A linear elastic simulation was used with a mesh of approximately 230 000 elements. A sample output of the simulation is shown in Fig. 2(b). The maximum stress was output and normalized by the stiffness of the material used by the simulation to obtain a dimensionless qualitative indicator of the strength of each geometry. Due to the variation of meshes between geometries and the sensitivity of finite-element simulations to the mesh structure at sharp corners of a stress concentration, a line of best fit was calculated to the data using the least squares method with respect to the tab interface angle.

To obtain a single metric from the complexity and strength metrics, each unitless metric was normalized, and then, the two values were added to obtain the final geometry metric. The results of this analysis are shown in Fig. 3 for tab angles varying from  $0^\circ$  to  $90^\circ$ . The optimal design at the minimum of the curve was found to be very close to  $30^\circ$  with favorable overall properties. The final step before generating masks for the microfabrication processes was to include a  $5\text{-}\mu\text{m}$  offset between all mating surfaces to mitigate concerns that the brittle tiles would fracture upon assembly.

### III. BRICK MANUFACTURING

#### A. SU-8 Polymer Bricks

Standard photolithography techniques were used to create MicroChem SU-8 polymer microbricks. SU-8 is an ideal

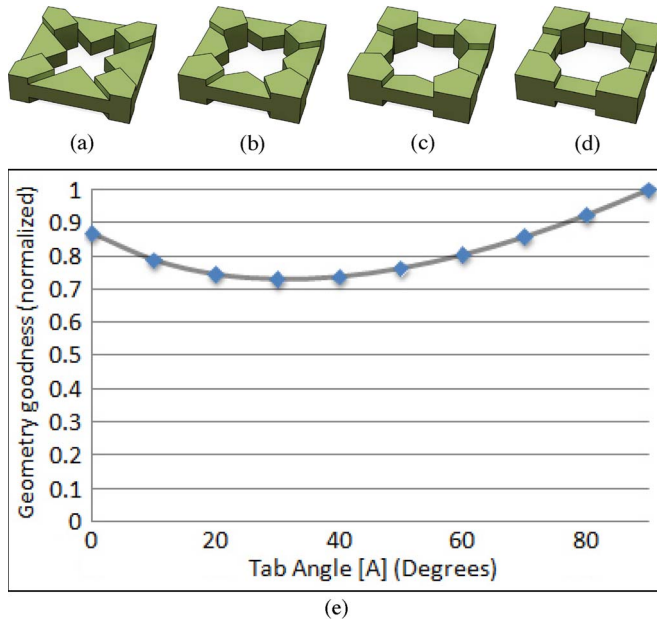


Fig. 3. Interface angle of the tabs was optimized based on a combination of minimizing the total surface area of the tile and minimizing the internal stress when stacked microtiles are put under lateral load. Tab angles of (a) 0°, (b) 30°, (c) 60°, and (d) 90° illustrate the range of geometries under consideration. The optimal angle was determined to be 30°, which corresponds to a relative compact shape that performs well under mechanical loading.

negative epoxy-based photoresist for this purpose for two reasons. First, high aspect ratio structures are routinely fabricated with excellent accuracy [20], [21]. Second, it has a relatively large thickness allowance [22] and is available in a wide range of viscosities. The 2.5-D design of the microtiles enabled the SU-8 tiles to be created with three layers of separately spun and exposed SU-8. Overexposure of underlying SU-8 was minimized by masking the first layer with a vacuum-deposited metal layer. Process details are detailed hereinafter.

Before any layers of SU-8 were deposited, alignment marks were etched on the bottom side of the wafer to provide a reference to keep subsequent layers in proper alignment. SC 1827 photoresist was spun for 30 s at 2000 r/min on the underside of the wafer, prebaked for 1 min at 115 °C, and passively cooled to room temperature. A generic alignment mark photomask was used to expose the wafer for 15 s, and then, the wafer was developed normally. Twelve loops in a Uniaxis plasma etcher resulted in alignment marks etched approximately 4.8 μm deep, which was sufficient to be visible in subsequent alignment steps. The wafer was then stripped clean of the remaining photoresist.

In order to facilitate the removal of the SU-8 tiles from the wafer substrate, a sacrificial layer of MicroChem Omnicoat was first deposited. To ensure the reliable release of the finished bricks, it was found that this layer should be no less than 17 nm thick. After the layer was spun, the wafer was placed on a hot plate for 1 min at 200 °C to harden and then passively cooled to room temperature.

SU-8 2020 was selected for the thinner bottom and top layers in order to achieve the desired 35-μm layer thickness. SU-8 2050 was used for the thicker 70-μm center layer. For the 30-μm layers, the wafer was subjected to a spin process

TABLE I  
SUMMARY OF MEASURED TILE DIMENSIONS. DIMENSIONS AND STANDARD ERRORS ARE BASED ON MEASUREMENTS OF TEN TILES

	Silicon		SU-8	
	Dimension	StdErr	Dimension	StdErr
Tile Width	497.08 μm	0.14 μm	500.75 μm	0.13 μm
Total Thickness	113.39 μm	0.21 μm	153.65 μm	0.53 μm
Center Layers Thickness	56.35 μm	0.18 μm	75.53 μm	0.34 μm

involving a closed bowl spin of 500 r/min for 10 s followed by 3000 r/min for 30 s, with accelerations of 1000 r/s. The sequence was completed with an uncovered continuous spin of 1000 r/min to facilitate the edge bead removal. During this final stage, a SU-8 remover solvent was applied for 15 s at a distance of 10 mm from the edge of the wafer followed by a sweeping application starting outside the edge of the wafer and then moving inward until 8 mm from the edge of the wafer. The wafer was then allowed to continue spinning uncovered for 60 s to enable uniform solvent evaporation.

The wafer was then soft baked and exposed with a bottom side soft contact alignment. A filter was used to eliminate light below a 350-nm wavelength to prevent flawed exposure and rough edges of the SU-8. The wafer was then placed on the hot plate for a postbake. A longer hotter postbake (30 min at 95 °C) is required to help cross-link the exposed SU-8 and remove as much remaining solvent in the SU-8 as possible. This is crucial to provide a stable substrate for the remaining process steps since the unexposed SU-8 must remain in place to provide a flat substrate for the next layers.

Because the tiles have overhanging regions by necessity of design, care must be taken when exposing subsequent layers so that no UV light can reach this first layer and cross-link any unexposed regions of SU-8. To this end, a UV-opaque metallic layer was deposited between the first and second SU-8 layers. Chrome was selected for this task. A thermal evaporation of 100 nm of chrome was applied at 4 Å/s and 10 kV. This slower chrome deposition rate yielded more favorable chrome layers than faster depositions.

The second and third layers of SU-8 were done in a similar manner to the first layer of SU-8, with appropriate adjustments to the spin schedule to attain a 70-μm center layer with the SU-8 2050. Once all layers were in place and exposed, the SU-8 was developed to remove the superficial supporting material. After rinsing the wafer with isopropyl alcohol (IPA), it was placed in a chrome etch bath for 90 s to remove the now-revealed chrome layer. Next, the wafer was dried and placed in another SU-8 developer bath to develop the bottom layer. The wafer was then rinsed with IPA and air dried to remove the unexposed SU-8 of the initial layer. To finally release the bricks from the substrate, the wafer is placed in an MF 321 developer (tetramethylammonium hydroxide) bath for approximately 30 min until the bricks are released from the Omnicoat layer. The bricks were then strained out of solution and set aside to dry for assembly. Complete SU-8 tiles are shown in Fig. 5. A pictorial process table is included in Appendix A.

Although silicon is a more traditional material for micro-fabrication, fabricating free bricks out of silicon had its own

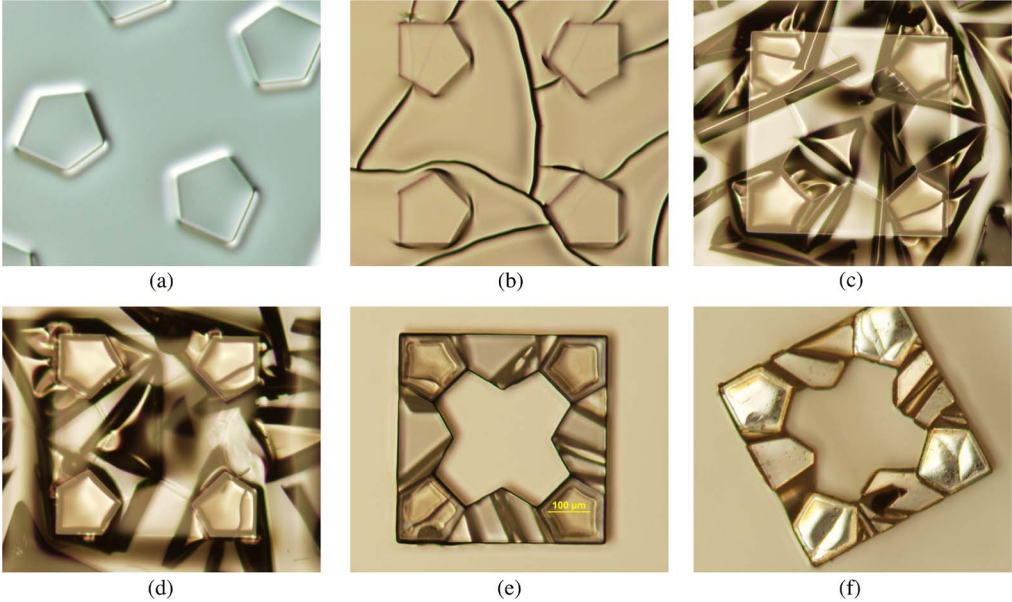


Fig. 4. Process of creating SU-8 microbricks. (a) First layer of SU-8 was deposited over a sacrificial layer, exposed, and baked. (b) Chrome layer masked the first SU-8 layer from being further cross-linked in later steps. Then, (c) the second and (d) the third layer of SU-8 were spun, exposed, and baked. (e) Top layers of SU-8 were then developed away, and the tiles were placed in a chrome etch to remove excess regions of the chrome layer. Then, the final layer of SU-8 was developed away, and the sacrificial layer was etched away, leaving free tiles.

challenges. Given that the target brick thickness was approximately  $130 \mu\text{m}$  thick, the silicon bricks were fabricated by two-sided etching of a thin silicon wafer. Normal silicon wafers were first commercially ground to the correct thickness. Each side of the brick underwent two etching steps to reach the center plane of the wafer and impart the correct geometry.

To do a two-step silicon etch, a layer of  $\text{SiO}_2$  was first deposited on one side of the wafer. This  $\text{SiO}_2$  was then patterned to mask the area corresponding to the feet of the bricks. This was accomplished by masking with a positive photoresist and then reactive ion etching the surface to selectively remove the  $\text{SiO}_2$ . Then, another layer of photoresist was deposited over the patterned  $\text{SiO}_2$ . This layer was patterned and developed to leave the negative shape of the middle layer of the brick exposed. At this point, the exposed regions of the wafer were etched down by  $35 \mu\text{m}$  with an inductively coupled plasma etcher utilizing the Bosch process for deep silicon etching. Then, the remaining layer of photoresist was stripped off, leaving only the previously patterned  $\text{SiO}_2$  layer. Another  $35\text{-}\mu\text{m}$  etch was done so that areas exposed for the first etch were now approximately  $65 \mu\text{m}$  deep, corresponding to the approximate midplane of the wafer.

Before the same process could be completed from the opposite side to complete the brick geometry, a sacrificial membrane was deposited on the recently etched side to hold the bricks in place during the final silicon etching step from the other side. A combined layer of  $\text{SiO}_2$  and nitride was deposited using plasma-enhanced chemical vapor deposition. The wafer was then flipped, and the two-layer etching process was repeated. The final etching step was allowed to continue until the silicon wafer was etched completely through in the exposed regions. The membrane holding the bricks together was then dissolved to leave the free bricks. A pictorial process table is included in Appendix B.

## IV. RESULTS AND CONCLUSIONS

### A. SU-8 Bricks

Overall, the SU-8 tiles displayed excellent feature accuracy in the horizontal plane. However, the SU-8 tiles ended up slightly thicker than the target dimension, although not detrimentally so. In the horizontal plane, the tiles were  $0.75 \mu\text{m}$  large (see Table I). This is likely due to the mild bleeding of the UV at the edge of the mask, which cross-linked slightly more than the nominal amount of SU-8. The most difficult to control parameter in the SU-8 process was spinning an accurate thickness of the SU-8 layers. Based on the steps outlined earlier, the tiles ended up being  $153 \mu\text{m}$  thick on average, which was slightly thicker than the target height of  $140 \mu\text{m}$ . However, the relative thicknesses of the layers were very close to the desirable ratios, with the center layer being 49.2% of the total thickness (nominally 50%).

The main processing challenge of the SU-8 brick fabrication process was obtaining a suitable UV masking layer after the first SU-8 layer. This masking layer needed to be thick enough to successfully block light from penetrating and curing the SU-8 below, while not being so thick as to be brittle and crack. This, in turn, would also allow curing of the underlying SU-8 beneath the cracks. Even with the successful 100-nm chrome layer, this masking layer was observed to have a few minor ruptures [see Fig. 4(b)] after cooling from deposition. Subsequent steps in the fabrication process introduced dramatic wrinkling of the chrome layer, likely from the thermal stresses of baking and cooling the SU-8. However, UV bleeding was still kept to a minimum, as evidenced by the lack of unwanted cured SU-8 in Fig. 5(b).

Another option to mask the lower layer of SU-8 was to replace the chrome in the process with an aluminum layer. This yielded very smooth and effective masking layers that were not prone to cracking or wrinkling. However, aluminum is more

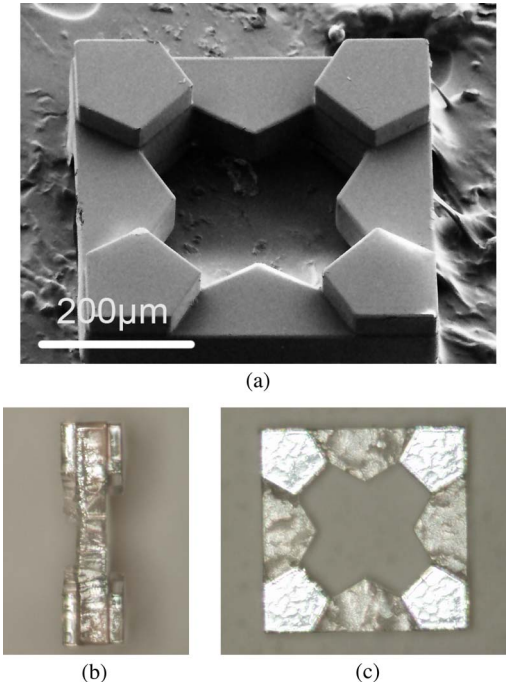


Fig. 5. Completed SU-8 microbricks. The SEM image shows (a) excellent feature accuracy. (b) Side and (c) top views show the individual layers of SU-8 clearly, as well as the finished aspect ratio of the tiles.

reactive than chrome to the SU-8 developing solution. This led to unwanted dissolving of the aluminum that holds the bottom of the feet to the rest of the tile. With these significant incuts between the first and second layers of SU-8, the tiles did not hold together well enough to assemble (see Figs. 6 and 7).

### B. Silicon Bricks

In contrast to the SU-8 tiles, the silicon tiles ended up smaller than the target dimensions. In the horizontal plane, the tiles were  $2.92 \mu\text{m}$  small (see Table I). This can likely be attributed to the plasma etching mildly undercutting the masked region. However, the wafers that were used in these experiments were on average only  $113 \mu\text{m}$  thick, which gave the silicon bricks a significantly different aspect ratio than the SU-8 tiles. However, the relative thicknesses of the feet with respect to the thickness of the center layer were 49.7%, which was very close to the desired nominal 50%.

The challenges of fabricating the silicon bricks revolved around the use of very thin and fragile silicon wafers. Aside from needing extra care in all stages of processing, the correct proportions of  $\text{SiO}_2$  and nitride for the retaining layer were critical. The retaining layer had to be tensile so that, as the final micrometers of silicon were etched away, the tiles would hold in the correct position. However, a tensile layer on one side of a very thin silicon wafer introduces unwanted stresses that would repeatedly shatter the wafer in the final stages of etching. To address this, the membrane was tuned to be only very slightly tensile by correctly proportioning  $\text{SiO}_2$  and nitride.

### C. Tile Assembly

In order to demonstrate the tiles interlocking in three dimensions, a proof-of-concept structure was assembled by hand from

SU-8 bricks. The structure contains nine tiles in three layers and demonstrated the effectiveness of purely friction-based adhesion at the  $500\text{-}\mu\text{m}$  scale rendering adhesives unnecessary. A SEM image is shown in Fig. 8(a), with a tenth tile unattached for reference. At  $500 \mu\text{m}$ , the tiles can be manipulated by tweezers, although to assemble any significant number of tiles will necessitate further development of an automated system. Even though the SU-8 tiles were slightly on the large side, the surfaces were compliant enough to allow for assembly without undue breakage of the microbricks.

The silicon bricks, however, proved relatively fragile when pressed together, even though slightly undersized. This can be attributed to the relatively uncontrolled forces of assembling them by hand with tweezers. However, the more robust SU-8 tiles had enough compliance to assemble a structure that combined SU-8 and silicon tiles (see Fig. 9). Even though the aspect ratios were significantly different, they were still compatible with respect to the interlocking mechanism of feet fitting within the central ring.

### V. CONCLUSION AND FUTURE WORK

Here, we have demonstrated the fabrication and assembling of a hybrid 3-D structure with both semiconductor and polymer components. The key to scaling up the complexity of microsystems lies in modularizing material and function, which requires standardizing the interface between components. In this way, each module type can be efficiently fabricated in independent optimized processes and then combined into a functional hybrid system. This enables materials and functions that would otherwise be mutually incompatible to be combined in a single integrated system. The first step in this process is to define a suitable mechanical module that is both robust and suitable for a massively parallel 3-D assembly process.

The mechanical architecture presented here fulfills these requirements. Components have simple 2.5-D geometric shapes that could be fabricated in bulk by a wide variety of common parallel microscale fabrication techniques. The bricks physically interlock yet can be assembled in a layer-by-layer process without complex 3-D alignment or manipulation. The bricks also maximize mechanical properties by utilizing a space-filling design and minimizing internal stress under tension.

There are many potential applications for 3-D multimaterial microbrick systems. Even with just two bricks of differing material stiffnesses, there are many possibilities for creating structures with novel properties [18]. Once modularity is enabled by well-defined interfaces between components, there are many ways to accelerate the design and assembly process. In the future, one can envision hierarchical assembly processes where individual components are assembled functional macrostructures which are then assembled into larger systems. Alternatively, more complex subsystems (e.g., a microcontroller component) could be prefabricated in a larger package such as a  $3 \times 3 \times 3$  cube that is compatible with the smaller components or even with existing electrical interfaces.

In the distant future, we envision a library of compatible bricks spanning not only the range of properties of materials currently available to engineers but also incorporating specific

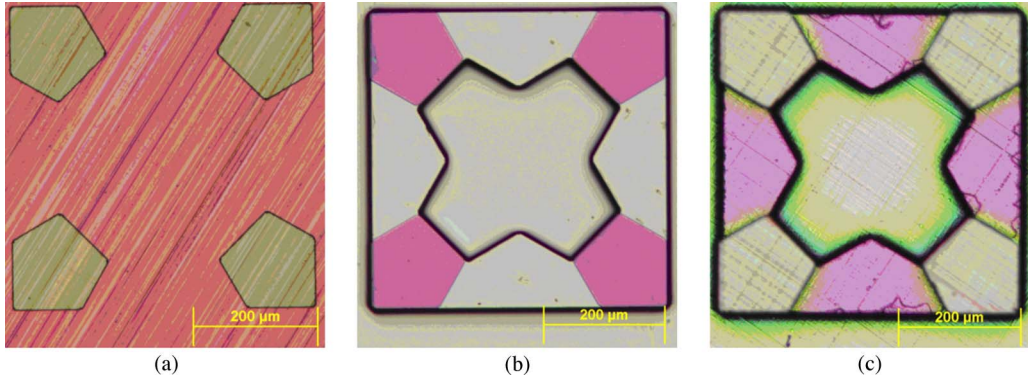


Fig. 6. Process of creating silicon microbricks. (a) Silicon wafer preground to the correct total brick thickness had  $\text{SiO}_2$  deposited and etched to mask the second silicon etching process. (b) Then, another layer of photoresist was patterned, and the first silicon etching stage was completed, etching away the center and outside of each tile. (c) Then, the most recent layer of photoresist was stripped, and another silicon etching stage was completed, leaving the feet higher than the rest. A retaining membrane was then deposited on this side to hold the bricks in place while the process is completed from the opposite side.

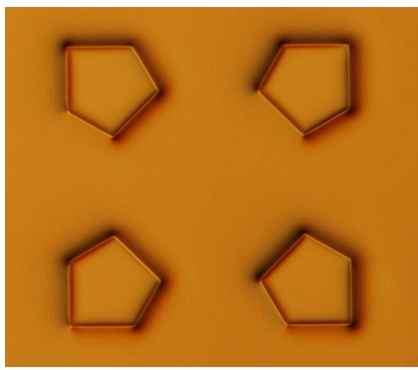
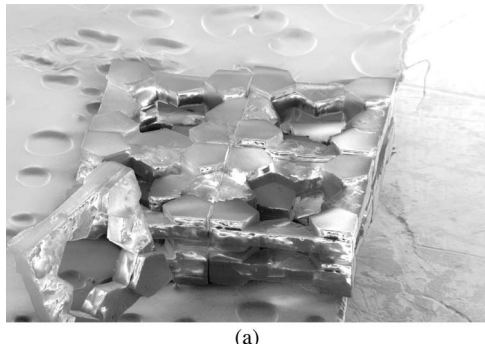
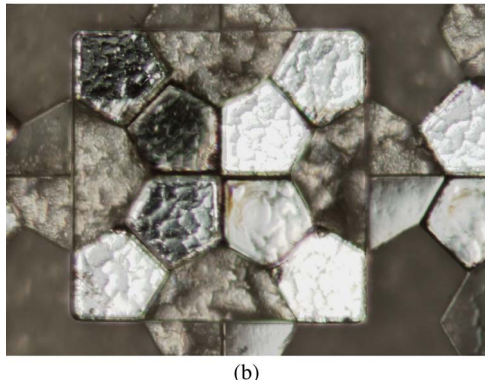


Fig. 7. Using aluminum instead of chrome [compare directly to Fig. 4(b)] in the SU-8 brick fabrication yielded less cracking, but aluminum reacted significantly with SU-8 developer which led to incutting of the tiles at the interface between the aluminum and the SU-8 in subsequent steps.



(a)



(b)

Fig. 8. Assembly of 500- $\mu\text{m}$  tiles demonstrates a 3-D interlocking structure. (a) SEM image shows the whole structure, (b) while optical image shows the feet of the tiles in the lower layer inserted into the ring of the top voxel.

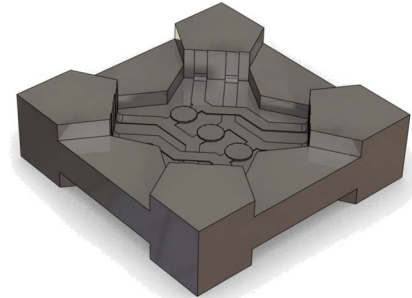


Fig. 10. Future microbricks will contain specific functionality. The internal part is not structural and therefore not considered in this analysis.

functionalities that would enable 3-D electromechanical objects to be fabricated quickly and cheaply from microbricks (see Fig. 10). This would allow for the exponential industry-wide growth of the complexity and functionality of multidomain microscale objects. Because of the reversible nature of the mechanical assembly, these objects could be just as easily decomposed back into individual tiles for reuse in other objects. In this way, the advantages of a modular architecture can be leveraged in the physical world to enable reconfigurable 3-D functional macroscale structures composed of microscale components.

## APPENDIX A SU-8 BRICK FABRICATION PROCESS DIAGRAMS

Step	Description	Diagram
1	Substrate patterned with sacrificial release layer	
2	First layer of SU-8 is spun and patterned	
3	Masking chrome layer is deposited	
4	Second layer of SU8 is deposited and patterned	
5	Third layer of SU8 is deposited and patterned	
6	SU-8, exposed chrome, and release layer are developed away	

## APPENDIX B SILICON BRICK FABRICATION PROCESS DIAGRAMS

Step	Description	Diagram
1	Silicon patterned with SiO <sub>2</sub>	
2	Photoresist deposited and patterned	
3	First silicon etching step is performed	
4	Photoresist is stripped and second silicon etching step is performed	
5	Retaining layer of SiO <sub>2</sub> and nitride is deposited	
6	Process is repeated from the opposite side	

## ACKNOWLEDGMENT

The authors would like to thank J. Heil and B. Lundberg for their preliminary work leading up to these results.

## REFERENCES

- [1] E. Puik and L. van Moergestel, "Agile multi-parallel micro manufacturing using a grid of equiplets," in *Precision Assembly Technologies and Systems*, vol. 315, S. Ratchev, Ed. Boston, MA: Springer-Verlag, 2010, ser. IFIP Advances in Information and Communication Technology, pp. 271–282.
- [2] A. Gutierrez, "Infrastructure driven strategies for microsystems business success in a market driven era," in *Proc. Commercial. Microsyst. Conf.*, San Diego, CA, Sep. 1998.
- [3] A. Gutierrez, "MEMS/MST fabrication technology based on microbricks: A strategy for industry growth," *MST News*, vol. 1, no. 99, pp. 4–8, 1999.
- [4] G. Skidmore, M. Ellis, A. Geisberger, K. Tsui, R. Saini, T. Huang, and J. Randall, "Parallel assembly of microsystems using Si micro electro mechanical systems," *Microelectron. Eng.*, vol. 67/68, no. 1, pp. 445–452, Jun. 2003.
- [5] G. Skidmore, M. Ellis, A. Geisberger, K. Tsui, R. Saini, T. Huang, and J. Randall, "Parallel assembly of microsystems using Si micro electro mechanical systems," in *Proc. 28th Int. Conf. Micro-Nano-Eng.*, Lugano, Switzerland, 2002.
- [6] H. Zhang, D. W. Hutmacher, F. Chollet, A. N. Poo, and E. Burdet, "Microrobotics and MEMS-based fabrication techniques for scaffold-based tissue engineering," *Macromolecular Biosci.*, vol. 5, no. 6, pp. 477–489, Jun. 2005.
- [7] M. T. Tolley, A. Baisch, M. Krishnan, D. Erickson, and H. Lipson, "Interfacing methods for fluidically-assembled microcomponents," in *Proc. IEEE Int. Conf. Micro Electro Mech. Syst.*, Tucson, AZ, 2008, pp. 1073–1076.
- [8] J. Hiller and H. Lipson, "Design and analysis of digital materials for physical 3D voxel printing," *Rapid Prototyping J.*, vol. 15, no. 2, pp. 137–149, 2009.
- [9] H. Zhang, E. Burdet, A. Poo, and D. Hutmacher, "Microassembly fabrication of tissue engineering scaffolds with customized design," *IEEE Trans. Autom. Sci. Eng.*, vol. 5, no. 3, pp. 446–456, Jul. 2008.
- [10] J. Hiller and H. Lipson, "Methods of parallel voxel manipulation for 3D digital printing," in *Proc. 18th Solid Freeform Fabrication Symp.*, 2007, pp. 200–211.
- [11] M. Elwenspoek and H. V. Jansen, *Silicon Micromachining*. Cambridge, U.K.: Cambridge Univ. Press, 2004.
- [12] H. Becker and U. Heim, "Hot embossing as a method for the fabrication of polymer high aspect ratio structures," *Sens. Actuators A, Phys.*, vol. 83, no. 1–3, pp. 130–135, May 2000.
- [13] R. W. Jaszewski, H. Schift, J. Gobrecht, and P. Smith, "Hot embossing in polymers as a direct way to pattern resist," *Microelectron. Eng.*, vol. 41–42, pp. 575–578, Mar. 1998.
- [14] R. W. Jaszewski, H. Schift, J. Gobrecht, and P. Smith, "Hot embossing in polymers as a direct way to pattern resist," in *Proc. Int. Conf. Micro-Nanofabrication*, Athens, Greece, 1997.
- [15] L.-A. Liew, W. Zhang, V. M. Bright, L. An, M. L. Dunn, and R. Raj, "Fabrication of SiCN ceramic MEMS using injectable polymer precursor technique," *Sens. Actuators A, Phys.*, vol. 89, no. 1/2, pp. 64–70, Mar. 2001.
- [16] I. G. Foulds and M. Parameswaran, "A planar self-sacrificial multilayer SU-8-based MEMS process utilizing a UV-blocking layer for the creation of freely moving parts," *J. Micromech. Microeng.*, vol. 16, no. 10, p. 2109, Oct. 2006.
- [17] A. Mata, A. J. Fleischman, and S. Roy, "Fabrication of multi-layer SU-8 microstructures," *J. Micromech. Microeng.*, vol. 16, no. 2, p. 276, Feb. 2006.
- [18] J. Hiller and H. Lipson, "Tunable digital material properties for 3D voxel printers," *Rapid Prototyping J.*, vol. 16, no. 4, pp. 241–247, 2010.
- [19] O. Delgado Friedrichs and D. H. Huson, "Tiling space by platonic solids, I," *Discrete Comput. Geometry*, vol. 21, no. 2, pp. 299–315, 1999.
- [20] H. Lorenz, M. Despont, N. Fahrni, J. Brugger, P. Vettiger, and P. Renaud, "High-aspect-ratio, ultrathick, negative-tone near-UV photoresist and its applications for MEMS," *Sens. Actuators A, Phys.*, vol. 64, no. 1, pp. 33–39, Jan. 1998.
- [21] H. Lorenz, M. Despont, N. Fahrni, J. Brugger, P. Vettiger, and P. Renaud, "High-aspect-ratio, ultrathick, negative-tone near-UV photoresist and its applications for MEMS," in *Proc. 10th IEEE Int. Workshop Micro Electro Mech. Syst.*, 1997, pp. 518–522.
- [22] A. Bertsch, H. Lorenz, and P. Renaud, "3D microfabrication by combining microstereolithography and thick resist UV lithography," *Sens. Actuators A, Phys.*, vol. 73, no. 1/2, pp. 14–23, Mar. 1999.



**Jonathan D. Hiller** received the B.S. degree in mechanical engineering from the University of Washington, Seattle, in 2006, and the M.S. degree in mechanical engineering from Cornell University, Ithaca, NY, in 2009, where he is currently working toward the Ph.D. degree in the Cornell Computational Synthesis Laboratory.

He is a recipient of a National Science Foundation graduate research fellowship. His research interests are focused on the boundary between the physical and the digital world, specifically the automated design and fabrication of microbrick-based materials and systems.



**Joseph Miller** received the B.S. degree in physics from North Dakota State University, Fargo, ND, in 2010, where he is currently working toward the Ph.D. degree in the Materials and Nanotechnology Program.

He is currently working on a project involving the implementation of silicon quantum dots as a biological sensing device.



**Hod Lipson** (M'98) received the B.Sc. degree in mechanical engineering and the Ph.D. degree in mechanical engineering in computer-aided design and artificial intelligence in design from the Technion—Israel Institute of Technology, Haifa, Israel, in 1989 and 1998, respectively.

He is currently an Associate Professor with the Mechanical and Aerospace Engineering and Computing and Information Science Schools, Cornell University, Ithaca, NY. He was a Postdoctoral Researcher in the Department of Computer Science, Brandeis University, Waltham, MA. He was a Lecturer in the Department of Mechanical Engineering, Massachusetts Institute of Technology, Cambridge, where he was engaged in conducting research on design automation. His current research interests include computational methods to synthesize complex systems out of elementary building blocks and the application of such methods to design automation and their implication toward understanding the evolution of complexity in nature and in engineering.

# Toward massively parallel manipulation of mm-scale components using electroosmotically controlled drops

Cheryl A. Perich\*, Ashley Macner<sup>◊</sup>, Robert MacCurdy\*, Paul Steen<sup>◊</sup>, Hod Lipson\*†

\*Sibley School of Mechanical and Aerospace Engineering,

Cornell University, Ithaca, NY 14853

◊School of Chemical and Biomolecular Engineering,

Cornell University, Ithaca, NY 14853

†To whom correspondence should be addressed. E-mail: hod.lipson@cornell.edu.

Key Words: Capillarity, Electroosmotic Pump, Controlled Wet Adhesion, Individual Droplet Control

## Manuscript information:

Number of Text Pages: 8

Number of Figures: 7

(All figures are one-column)

Number of Tables: 1

Number of words in abstract: 250

Total number of characters in manuscript: 30200

(Includes space for figures, table, equations, etc)

# Toward massively parallel manipulation of mm-scale components using electroosmotically controlled drops

Cheryl Perich \*, Ashley Macner \*, Robert MacCurdy \*, Paul Steen \*, and Hod Lipson \*

\*Cornell University

Submitted to Proceedings of the National Academy of Sciences of the United States of America

The quest to move small objects quickly, efficiently, and safely has been a goal of robotics and manufacturing since the beginning of mass production. The challenge has grown with the decreasing size of components of technological interest (i.e. electronic components and other similar materials). While there is a lot of diversity in the mechanism of transport such as the number of degrees of freedom in a robotic arm as well as the type and number of end effectors handling the object, there is still a lack of consistency, accuracy, and delicacy in moving millimeter, micro- and nano-scale objects. This paper demonstrates the use of electroosmosis to transport mm-sized spheres which are used to assemble large scale objects. In contrast to previous works, which focused on using arrays of droplets to grab a single substrate, we control each element in the array individually to pick up objects from positions of our choosing. The advantage of this droplet method is that it allows for delicacy in transport due to the lack of mechanical grabbing mechanisms. A model was developed to predict the drop velocity and a comparison was made with results from image analysis and COMSOL simulations under conditions of thick and thin electrical double layers (EDL). Based on these studies, it is shown that electroosmosis can be used as a means to control massively parallel motion of small objects.

Capillarity | Electroosmotic Pump | Controlled Wet Adhesion | Individual Droplet Control

In this work, electroosmosis is to create droplets that are used to pick and place 1.5 mm spheres not only in parallel but also in individual predetermined configurations by use of the PICEM (Parallel and Individually Controlled Electroosmosis Mechanism). The comprehensive, long-term goal of this work is to create a device to pick and place millions of tiles, spheres, or other objects (ranging in size from millimeters to nanometers) in parallel and in a predetermined configuration. What makes this process and the device invented unique is the ability to pick up objects in parallel, to control the picking of individual objects using no mechanical devices (only voltage), and the ability to decrease the necessary picking precision due to the induced self-assembly as a result of using capillary bridges.

There are three main issues to consider when deciding on a transport method for a small (less than 1 mm) object. First, the end effector has to be uniquely and specifically designed for a predetermined shape and has to be able to pick up the object without destroying or damaging the part. Second, the devices currently designed to pick up these small objects tend to be extremely fragile, often as fragile as the objects they are trying to pick up. This leads to major issues in speed of motion, since all objects must be carefully controlled. Finally, repeatability of the picking motion is essential for large scale operations; picking each object individually, one at a time, is an extremely slow and tedious process. The repeatability and reliability of the end effector can be increased by using parallel pick and place operations.

Common end effectors include pipette vacuums [3], nano- or micro-fabricated tweezers [4, 5, 6] attached to parallelogram robots [7], and electrostatic singular or dual cylinders [8]. Others use SEM and Atomic Force Microscopy to move small objects [9, 10]. These techniques lack parallel manipulation to move many objects at once and lack a universal end effector which allows for picking up objects with different shapes. Another technique involves the use of chemically activated micro grippers. While this technique requires low energy input, it requires the submersion of materials into chemicals,

which could degrade and deform components [11]. Self-assembly via capillary bridges has been used previously to align tiles, removing some of the precision boundaries in assembly [12, 13, 14]. However, these techniques still require external grippers or mechanisms to manipulate the tiles.

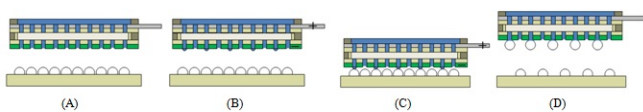


**Fig. 1.** Picking process: (A) PICEM is brought into alignment with base and spheres. (B) A voltage is applied causing droplets to form at selected positions. (C) PICEM is brought into contact with spheres. (D) Base and PICEM are separated to remove selected spheres.

## PICEM

**Device Overview.** The PICEM was inspired by the Switchable Electronically-controlled Capillary Adhesion Device (SECAD) [1, 2]. The SECAD uses electroosmosis to move an array of droplets which form capillary bridges upon contact with a single substrate (i.e. a piece of aluminum foil) or an array of objects. The main difference between the PICEM and the SECAD is that the PICEM incorporates individual channel addressability to selectively pick and place small objects. While the physics of electroosmosis have been well studied, its use for pick and place has not been fully explored. By using the PICEM device as described in this paper, it is possible to avoid the complications involved in creating micro-fabricated tweezers or end-effectors. Another benefit is the self-alignment of objects as a result of the capillary bridges seeking the lowest energy state. The main steps of the picking process are shown in Fig.1.

When a solid and a liquid come into contact (i.e. distilled water in a borosilicate glass frit), the surface groups of the solid are removed leaving behind a layer of charge. Counter-ions from the bulk migrate to the liquid-solid interface to neutralize the excess charge creating an electric double layer. When a tangential electric field is applied, the ions in the diffuse layer respond to Coulombic forces and move towards the electrode of opposite polarity. As a result of viscosity, the surrounding bulk fluid is convected creating a bulk flow [18]. This phenomenon allows for fluid motion without any mechanical devices necessary to control a constant, pulse-free fluid flow. If a porous frit is used as the solid, a considerable pressure drop occurs across the frit. This must be taken into consideration when looking at bulk fluid flow through the medium. The smaller

## Reserved for Publication Footnotes

the channels or pores, the larger the capillary pressure is across any menisci in the frit [20]. Desirable properties of the pump include large flow rates and high maximum pressures. This can be induced by small pores and a large surface charge density to ensure maximum flow rate [20].

The PICEM was created using mainly 3D printed components (see Fig.2B). Besides the electrodes, printed circuit board, O-ring and connectors, all layers were created using Objet 3D printed soft and hard materials (photocurable plastic and rubber-like materials). The soft Tango+ material (tensile strength 0.8-1.5 psi) allows for a rubber like flexibility, which, under the compression of the screws and top plate, serves as a means of keeping the water in their directed channels (see Fig.2A) [16].

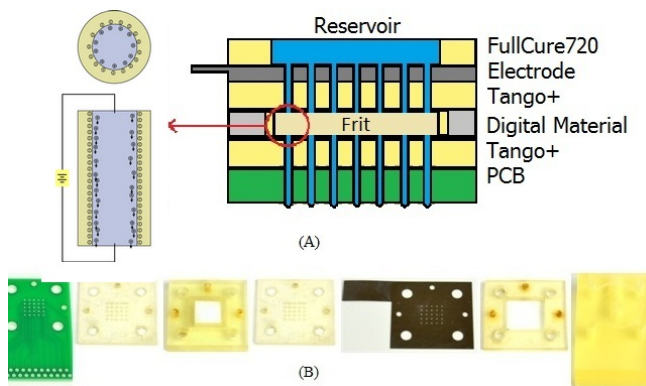


**Fig. 2.** Device schematic: (A) PICEM cutaway and ion motion in an idealized cylindrical channel [26]. (B) PICEM components. From left to right: printed circuit board (PCB), Tango+ gasket, Fullcure720 outer support and Tango+ inner frit support, Tango+ gasket, stainless steel electrode, Fullcure720 plate, Fullcure720 reservoir. Not shown: reservoir O-ring, circular rubber gasket, secure pins, screws, syringe fixture.

## Results

**Individual Control.** The printed circuit board has a 5x5 array of 508  $\mu\text{m}$  diameter holes with a 0.66 mm diameter Sn/Pb plating. The center-to-center distance between adjacent channels was 2 mm (allowing it to pick up every 4th 500  $\mu\text{m}$  tile or each 1.5 mm sphere). This spacing was chosen to better analyze the effects of the generated electric field in adjacent inactivated channels. An XYZ platform was built for 3D mobility of the PICEM allowing it to pick and place tiles or spheres from any location on the platform. The device electronically consists of three servo motors and a motor port. Structurally, it consists of mainly laser cut acrylic, 3D printed joints and connectors, and metal poles to connect the structure. It is controlled using a Visual Basic program modified from previous work [15]. The program allows for homing and also selection of speeds, accelerations, and positions of the assembler head (Fig.S1).

**Testing the Picking Ability.** The PICEM was attached with adhesive tape to the XYZ platform. The device was then aligned using pins to the base plate, which was a 3D printed Fullcure720 cube with cylindrical holes of diameter 0.7 mm. Once all PICEM channels were tested for flow capacity, individual channels were activated by applying a voltage to the electrode via ribbon cables. A three-way electrical switch was created to control the polarity of the applied voltage across the device. This allows for manipulation of droplet volume on command.

The first test looked at a single channel. The wire corresponding to the channel above a single sphere was activated (15 V) and using the Visual Basic Program, the platform was lifted such that the sphere made contact with the formed droplet. No other droplets were formed since the other channels were not activated. After contact was made, the platform was then lowered, showing the single chosen sphere to have been removed from the platform and adhered to the circuit board. The voltage was switched off and the

sphere continued to stay in place. This illustrates how the device uses low voltages only periodically to control droplet motion, while providing static holding force with no externally applied energy.

**Picking up All Spheres.** The next step was to attempt to pick up all spheres at once using the PICEM. This test was performed 25 times, with 15 V applied to all channels. Success rates for each hole were calculated based on a Binomial Distribution. In the results to follow, the success of the pickup was determined by either a sphere being picked up by an activated channel, or a sphere being left behind by an inactive channel. The lowest success rate was 80%; the highest was 100% for the 25 trials. A mean of 22.72, standard deviation of 1.45, and an average success rate of 90.88% was achieved. To improve the device, a superhydrophobic (SHP) coating was applied via vapor deposition to decrease droplet migration by pinning the drops to the channel circumference. The tests were repeated (Fig.S1) and the results showed a much higher average success rate of 95% with an average pick up of 23.72 and a standard deviation of 1.7.

**Picking of Checkerboard Pattern.** A checkerboard configuration tested the ability to isolate channels in close contact, while still exhibiting a deliberate pattern (Movie S1). Furthermore, it allowed for examination of unwanted droplet growth while picking individual spheres (Fig.3).

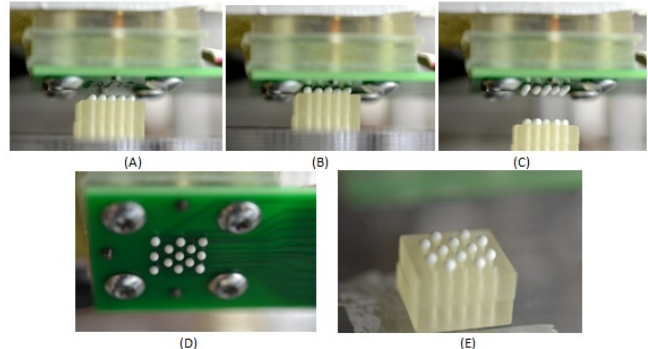


**Fig. 3.** (A) Set at 15 V, droplets begin to form on the circuit board of the PICEM, (B) the platform is raised so that the droplets make contact with the spheres, (C) the activated channels (those creating a checkerboard pattern) pick up the spheres from the platform, leaving behind all spheres on the grid corresponding to inactivated channels. (D) View of checkerboard pattern from under the circuit board. (E) View of leftover spheres from inactivated channels.

Again, this test was repeated 25 times. In the results to follow, the success of the pickup was determined by either a sphere being picked up by an activated channel, or a sphere being left behind by an inactive channel. Any unwanted pickup was due to droplet walking or misalignment. The average success for SHP coated boards was 98% with an average pick up of 24.52 and a standard deviation of 1.6. Other configurations were also tested in order to assess the accuracy and reliability of the device. These configurations included an "X" shape, "#" shape, small square and top hat shape.

When looking at these statistics, it is also important to look at the droplet formation success rate, meaning, how often did the PICEM form droplets in the selected channels, and how well it avoided droplet formation in inactivated channels. This is different from the previous statistics, in that a droplet may have formed, but may not have picked up a sphere, or an unwanted sphere may have been picked by water that walked from another channel. By looking at the droplet formation success rates, it is possible to determine if the electroosmosis process and the individual addressability features are fully functional, accurate, reliable, and repeatable. In all trials, the droplet formation success was 100% for all channels (it formed the desired pattern). This leads to the conclusion that most error in picking or not picking was due to platform misalignment or walking of the contact line. See Fig.4.

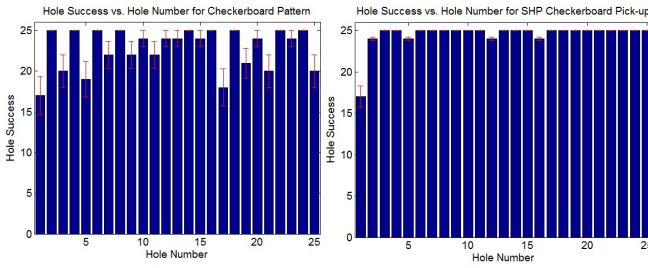


**Fig. 4.** Plots of success rates for picking up checkerboard pattern with error bars for standard deviation. Odd columns correspond to activated channels.

**Velocity Measurements.** Given the current configuration of materials and frit, the most important factor in understanding performance in picking and placing is the velocity of the water droplets. The speed at which these droplets grow is the limiting factor in how quickly items can be picked and placed in a repeatable fashion. Therefore, the velocity is characterized both analytically and through simulation to better understand the liquid motion both through the frit and as a growing droplet.

In order to determine the velocity of the water droplets coming out of the channel experimentally, individual channels were activated with a set voltage (15 V) and image acquisition was performed with MotionPro video analysis software. The size of the water droplet was measured over time by an in house MATLAB routine that combines image analysis with a volume calculation that uses a Riemann sum of frustum image elements. The droplets were calibrated using 1.5mm spheres placed on the channels. The volume vs. time was plotted (S#), and the velocity was calculated by dividing the flow rate (volume/time) by the area through which this flow travels,  $*(0.508 \text{ mm})^2$ . The spatial variation might be a function of the pore size distribution and/or channel alignment issues inside the device. A global exit velocity was found by taking the average of the 14 trials. This is used to compare with both theory and simulation. The average velocity was found to be  $0.136 \pm 0.024 \text{ mm/s}$ .

**Analytical Solution.** Use of a modified form of the electrokinetic coupling matrix to calculate the velocity at the base of the channels in the circuit board requires that the flow is unidirectional and that the electrochemical equilibrium of the ions in the double layer is decoupled from the bulk flow. For the latter to be satisfied,  $\text{Pe} \frac{d}{L}$  must be small [21]. For an average pore diameter,  $d$ , of  $1.15 \mu\text{m}$  and a frit thickness,  $L$ , of  $4.76 \text{ mm}$ ,  $d/L = \frac{d}{L} \approx 2 \times 10^{-4}$ . The Peclét number,  $LU/D$ , where  $U$  is the characteristic velocity ( $0.1 \text{ mm/s}$ ) and  $D$  is the diffusivity of ion species ( $1 \times 10^{-9} \text{ m}^2/\text{s}$ ), is 476, meaning that  $\text{Pe} \frac{d}{L} = 0.1$ , which is small enough to justify this approach [21].

The modified form of the electrokinetic coupling matrix is dictated by the ratio of the pore diameter to the Debye length,  $d^* = \frac{d}{\lambda_D}$ . The Debye length is given by the equation [21]

$$\lambda_D = \sqrt{\frac{\epsilon_w R_g T}{F^2 \sum_{i=0}^N c_i z_i^2}} \quad [1]$$

where  $\epsilon_w$  is the permittivity of water,  $R_g$  the universal gas constant,  $T$  the temperature,  $F$  Faraday's constant,  $c_i$  the molar concentration of species  $i$ , and  $z_i$  the valence number of species  $i$  normalized by the elementary charge. For distilled water at  $T=25^\circ\text{C}$ ,  $\lambda_D=971 \text{ nm}$  [21, 23]. This yields a value of 1.18 for  $d^*$  indicating the double layer thickness is comparable to the pore diameter. This is the upper bound on the double layer thickness. In practice, the double layer is likely to be thinner due to impurities in the water from contact with the frit and exposure to the air allowing for dissolution of gases (i.e.  $\text{CO}_2$ ) [21, 23]. In addition, the frit was not chemically cleaned (i.e. piranha solution) prior to use so there is likely to be

contamination as a result of handling the frit directly. This would also decrease the double layer thickness.

The net axial velocity of fluid through a pore as a result of an externally applied electric field is a superposition of the Helmholtz-Smoluchowski electroosmotic velocity and Darcy's law modified with the appropriate coefficients to account for the finite thickness of the double layer [21].

$$v_{net,z} = v_{eo} - v_{Darcy} = c_{11} \frac{\phi \epsilon_w \psi_s E_{ext,z}}{\mu} - c_{12} \frac{\kappa \Delta P}{\mu L} \quad [2]$$

where  $\phi$  is the porosity (0.48),  $\psi_s$  is the surface potential,  $E_{ext,z}$  is the applied electric field,  $\mu$  is the dynamic viscosity,  $\kappa$  is the permeability (which is assumed to be isotropic), and  $\Delta P$  is the pressure drop. The surface potential,  $\psi_s$ , for a borosilicate glass frit in contact with distilled water is typically around -100 mV [19, 25]. Assuming that the double layer thickness does not affect the viscosity, the functional dependence of the second term on the right hand side remains the same as that for thin double layers (i.e.  $c_{12}=1$ ). As for the first term,  $c_{11} \neq 1$ , since the double layer is finite and of comparable size with respect to the pore diameter. To account for the non-linearity of the bulk flow while also accomodating for a large surface potential a correction factor is incorporated. [21]

$$c_{11} \approx \frac{1}{1 + \exp[-\alpha (\log_{10} d^* - \log_{10} d_0^*)]} \\ \alpha \approx -0.15 |\psi_s^*| + 3.5 \\ d_0^* \approx -0.01 \psi_s^{*2} - 0.1 |\psi_s^*| + 2$$

This approximation is accurate to within 10% if the condition on the dimensionless surface potential,  $\psi_s^* = \psi_s/25 \text{ mV} < 6$ , is satisfied. Here, 25 mV corresponds to the thermal voltage at  $T=25^\circ\text{C}$ .

The permeability can be estimated analytically for a bed of packed spheres by relating it to the permeability of a series of parallel straight cylinders [17],

$$\kappa = \frac{\phi \bar{R}^2}{24} = 6.613 E - 15 m^2 \quad [4]$$

where  $\bar{R}$  is the average pore radius. Due to the compression of the frit during the manufacturing process, the glass beads are no longer perfectly spherical, which could alter the validity of applying this theoretical model. The Darcy term in equation 2 can be neglected because there is no external pressure being supplied to drive the flow.

The simplest expression for the electric field is  $E = \frac{V_{app}}{\lambda_D}$ , where  $V_{app}$  is the applied voltage. For a frit thickness of  $4.76 \text{ mm}$  and an applied voltage of 15 V, this yields an electric field of  $3138 \text{ V/m}$ . However, since the electrode configuration consists of a plate electrode below a series of vertically oriented cylindrical electrodes instead of two parallel flat plates, it is necessary to incorporate the effects of geometry on the electric field. This is accomplished by using the method of images. When approaching a channel from below, a straight cylindrical electrode will appear as a ring. But from the perspective of the plate electrode, this ring will appear as a point. The plate is assumed to be infinite in area with zero potential. This serves as the line of symmetry in the problem. The standard solution (in cylindrical coordinates) for the potential at any point in space as a result of a point charge  $Q$  residing above an infinite plate is given by [22, 24]

$$V(r, z) = \frac{Q}{4\pi \epsilon_{w/f}} \left( \frac{1}{\sqrt{r^2 + (z-h)^2}} - \frac{1}{\sqrt{r^2 + (z+h)^2}} \right) \quad [5]$$

where  $\epsilon_{w/f}$  is the weighted average permittivity of the frit and distilled water ( $3.61 \times 10^{-10} \frac{C}{V \cdot m}$ ),  $r$  is the radial coordinate,  $z$  is the axial coordinate, and  $h$  is the distance between the point charge and the flat plate (9 mm). Assuming the applied potential gradient is constant along the fluid path between the flat plate and the point charge, we can find a representative point charge,  $Q$ , that will

satisfy equation 5. The point of interest is the centerline ( $r=0$ ) at the channel exit, which occurs at  $z=7.08$  mm.

The electric field in the axial direction is the gradient of the potential field with respect to  $z$ . Or,

$$E_{ext,z} = \frac{Q}{4\pi\epsilon_{w/f}} \left( \frac{z-h}{[r^2 + (z-h)^2]^{\frac{3}{2}}} - \frac{z+h}{[r^2 + (z+h)^2]^{\frac{3}{2}}} \right) [6]$$

Using the value for  $Q$  calculated with equation 5, the electric field at the coordinates specified above is 8998 V/m. From here, the velocity at the pore exit can be determined by equation 2. Assuming that the velocity is constant along the rest of the flow path above the frit, the centerline velocity exiting a single activated channel is 0.13 mm/s. This equation can also be used to find the effects of an activated channel's electric field on other neighboring channels by varying  $r$ .

This analytical solution treats the electric field as that between a point charge and an infinite plate. In reality, it is not a point charge, but a thin ring of Sn/Pb coating around the channel, and the plate is not infinite. For our experimental setup, this treatment is appropriate because a quick scaling analysis reveals that the ratio of the channel diameter to the distance between the channel inlet and the plate electrode is small ( $\frac{d}{h} \approx .06$ ). If one were to replace the source/image charges with source/image rings of charge, the electric field decreases by about a factor of 1.04.

**Simulations.** COMSOL Multi-physics Simulator was used to simulate the flow field resulting from electroosmosis in the presence of a thick and thin double layer. The computational domain consisted of the frit and the projection of a single channel down onto the frit. Two different models were used to simulate this problem: transport of dilute species and general form PDE. These models are solved simultaneously, using boundary conditions from both the PDE and dilute species physics models to solve for the steady state solutions.

The hydrodynamic equations consist of the continuity equation for an incompressible fluid,  $\nabla \cdot \mathbf{u}=0$ , where the velocity vector,  $\mathbf{u}$ , is given by

$$\mathbf{u} = -\frac{\epsilon_p a^2}{8\mu\tau} \nabla P + \frac{\epsilon_p \epsilon_w \zeta}{\mu\tau} \nabla V [7]$$

In equation 7,  $\epsilon_p$  is the porosity,  $a$  is the average radius of the pore,  $\zeta$  is the potential, and  $\tau$  is the pore tortuosity. The equation for electroneutrality under steady state conditions and uniform composition is  $\nabla \cdot \mathbf{i}=0$  [23], where the electric current density  $\mathbf{i}$ , is given by

$$\mathbf{i} = -\kappa_e \nabla V [8]$$

In equation 8,  $\kappa_e$  is the electrical conductance and is calculated by the program directly based on user specified inputs for the species type.

To completely specify the problem mathematically, we need boundary conditions on the electrodes and the solid walls of the frit. A voltage of 15 V was applied to the top surface, and 0 V at the bottom outlet (simulating plate and point charge in 2D). The pressure at the inlet and outlet of the channel is fixed at zero. At the walls of the frit where water cannot enter or leave,  $\mathbf{u} \cdot \hat{\mathbf{n}} = 0$ . Furthermore,  $\mathbf{i} \cdot \hat{\mathbf{n}} = 0$  for all boundaries except for the electrodes. In the transient simulation, the governing equation for the conservation of mass of a dilute dielectric species under the convective influence of an electric field in the absence of chemical reactions is the Nernst-Planck equation

$$\frac{\partial c}{\partial t} + \nabla \cdot [-D_i \nabla c_i - z_i u_{m,i} F c_i \nabla V + \mathbf{u}_i c_i] = 0 [9]$$

where  $D_i$  is the diffusivity of species  $i$  and  $u_{m,i}$  is the electrophoretic mobility of species  $i$  given by the Nernst-Einstein equation. The boundary conditions are that the diffusive and convective contributions to the flux are zero at the inlet and outlet and that the total flux along the other boundaries is zero.

The governing equation for the general PDE is the matrix equation

$$e_a \frac{\partial^2 \mathbf{u}}{\partial t^2} + d_a \frac{\partial \mathbf{u}}{\partial t} + \nabla \cdot \Gamma = f [10]$$

$$\mathbf{u} = [p, V]^T [11]$$

where  $e_a$  is a  $2 \times 1$  zero column vector (since this is a general form equation and there are no second partial derivatives governing the physics of electroosmosis),  $d_a$  is a  $2 \times 2$  Identity matrix,  $f$  is a  $2 \times 1$  zero column vector since there is no forcing function, and  $\Gamma$  is a tensor, " $\mathbf{u}_{flow} - \kappa^* \nabla x, \mathbf{v}_{flow} - \kappa^* \nabla y$ ". These equations use the general PDE form to apply conservation of momentum for Darcy flow (Laplacian of pressure is zero) and for electric charge (Laplacian of voltage is zero). A correction factor was added to account for the thick double layer, which is equivalent to  $c_{11}$  from the analytical solution. Throughout the simulation, these equations are coupled with the above listed boundary conditions in order to solve for the electroosmotic flow throughout the frit and the superimposed channel. Geometrically, the model consists of a rectangle representing the frit and a channel of proper dimensions projected onto the frit for better visualization of the flow through the area.

The first simulation involves modeling the frit with a single channel in 2D (Fig.5). Flow was allowed through the inlet and outlet only (since the other areas are blocked off above and below the frit by Tango+, the electrode, and printed circuit board). The velocity at the inlet and outlet are much higher than the other areas. This is because the driving forces are assumed to be directly above (plate electrode) and below the frit (point charge) creating stronger local electric fields. All arrows that come from the inlet, eventually lead to the outlet, and the radial velocity through the rest of the frit decreases quickly over a distance of a millimeter. This is a result of enforcing the conservation of mass. Note all plots have vertical and horizontal axes in meters, representing the distance and location along the frit. Orientation of the frit is the same as that of Fig.2.

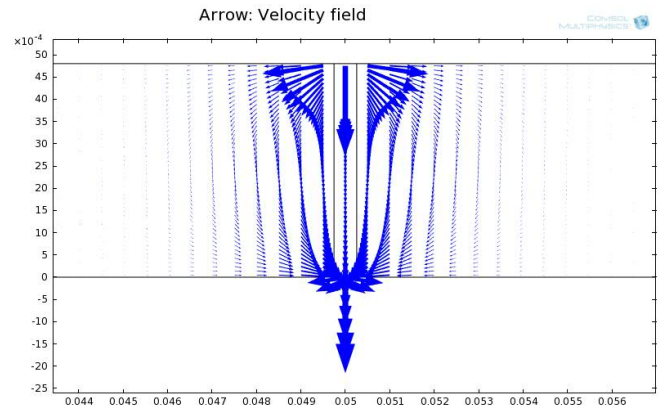


**Fig. 5.** Steady state velocity vector field for a single channel.

A surface plot was also generated in order to better visualize the velocity magnitudes in and around the channel area (Fig.6). All red areas indicate zero velocity. The area of greatest interest is the outlet at the bottom, which shows a range of velocities between 0.12–0.13 mm/s. At the corners of the outlet, there are sharp changes in velocity as a result of the discontinuity of the boundary conditions between the channel exit and the walls of the frit. Simulations performed for multiple activated channels produced similar exit velocities.

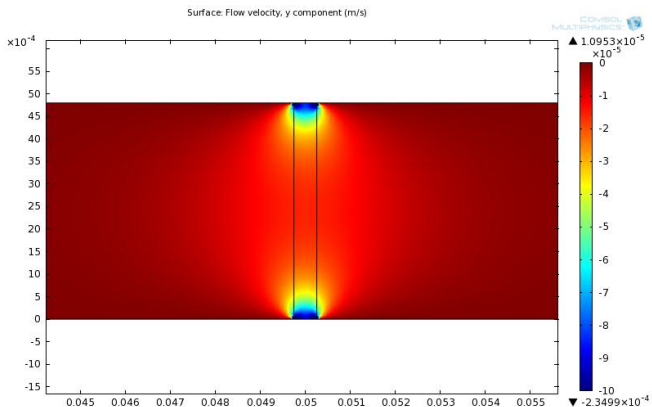


**Fig. 6.** Axial velocity surface plot

The last simulation involves replicating the printed circuit board configuration in the case of picking a checkerboard pattern by placing an inactive channel 2 mm away from an active channel. These results show that the flow of the inactive channel merged with the flow of the active channel (both getting their water from a reservoir in the PICEM) (Fig. 7). However, in some experimental trials, slight droplet growth occurred in inactivated channels as a result of a small portion of the electric field being transmitted through the support materials and influencing the flow in regions other than directly below the activated channel (velocity=0.13 mm/s).

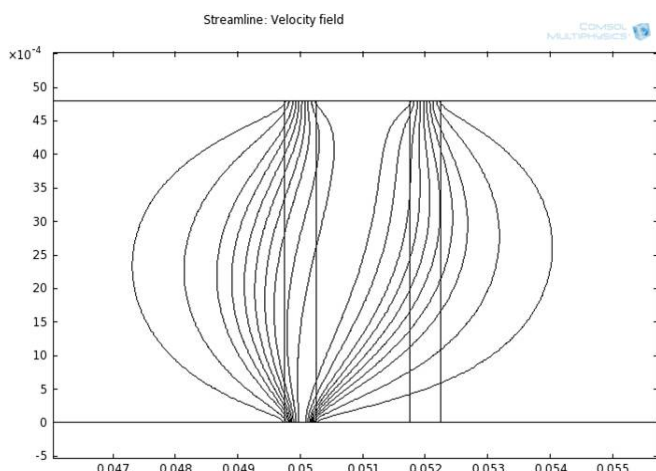


**Fig. 7.** Streamline plot with one active (left) and one passive (right) channel.

## Discussion

In order to fully assess the time scale of the pick and place process, it is necessary to be able to accurately predict the velocity for a variety of fluids operating under different experimental conditions (i.e. applied voltage, channel diameter, frit properties, etc.). In the case of electrokinetic processes, knowledge of the double layer thickness, zeta potential, electric field and surface potential is crucial to getting accurate results. These quantities are typically difficult to measure reproducibly, and so we will now shift our discussion to-

wards a more qualitative description of how the velocity were to change if some of these parameters were to increase/decrease.

	Method	Thick EDL	Thin EDL
Experiment	0.091	0.091	
Analytics	0.131	0.305	
Simulation	0.125	0.300	

In our case, the parameters with the largest uncertainty are the Debye length and the electric field strength. As was mentioned before, the Debye length is most likely smaller than the theoretical upper limit on distilled water of 970 nm. The distilled water resides in a plastic jug and comes into contact with the air each time the container is opened. Not only is there dissolution of CO<sub>2</sub> from the air into the water but contact with the plastic allows for chemicals to leach into the water. There is also the possibility of contamination as a result of handling the frits with our bare hands and not chemically treating them prior to use to rid them of any organic contaminants or loose particulates from processing them into different shapes. There is also the chance that some of the surface groups of the borosilicate glass frit could dissolve. Dissolution of CO<sub>2</sub> alone produces a debye length of 215 nm [21]. Inclusion of the other effects could further decrease the debye length to something on the order of ten nanometers or possibly even smaller. To see the effects of a thin double layer on the axial velocity, coefficient c<sub>11</sub> in front of the electroosmotic term in equation 2 was set to one and both the simulation and the analytical solution were recalculated. The results of these calculations, along with the experimental value determined from image analysis, are summarized in Table 1.

From Table 1, we can see that there is agreement between the analytics and the simulation. This is expected, since the set of equations used in the simulation reduces down to the same equation as the analytical solution under conditions of steady state. Notice that the predicted velocity in the case of a thick double layer is about twice the experimental value whereas in the case of a thin double layer, the predicted velocity is four times greater. The discrepancy might be explained by the uncertainty in the electric field. The electric potential was derived under the assumption that both the point charge and the infinite plate were suspended in a medium with a permittivity equal to  $\epsilon_{w/f}$ . This is not actually true. From Figure 2, we see that both above and below the frit there is only water. And since the permittivity of water is much higher than that of the frit, a lot of the electric field strength is lost to the polarization of the water molecules [24]. Hence, the effective potential difference across the frit is much smaller than the 15 V.

Further complicating matters, is the diversity of the materials along the entire electric field lines from the reservoir to the outlet of the circuit board channel. Some of these materials (i.e. the Tango+) actually absorb some of the water thereby increasing the dielectric constant in those regions. If an inactivated channel does experience flow, the velocity ends up being small because the radial transmittance of the field is substantially decreased as a result of water absorption.

Finally, as a result of the capacitance effect of the double layer, the effective potential difference is decreased even further and becomes a time dependent quantity. For a similar setup [25], it has been found that the effective potential difference is around half of the applied value. Their model takes into account the resistance of the electrode, fluid, and the frit in addition to the capacitive effects of the electrode. A lower electric potential corresponds to a smaller electric field and a smaller electric field corresponds to a smaller velocity. This holds true irrespective of the double layer thickness. Charge accumulation within the droplet further impedes velocity and droplet growth over time.

Also worth noting is that neither the analytical nor simulated solution incorporate the time dependent capillary pressure resulting from changes in the drop curvature as the volume changes. The capillary pressure is in addition to the hydrostatic contribution. Because the pressure term acts as a resistance to the flow, the drop

growth rate will decrease for increasing time, leading to a velocity which also decreases in time [25].

To summarize, all velocities predicted with the analytical solution and the simulations will be lower as a result of the effective potential being lower than the applied potential difference. The experimental velocity is likely to be higher at shorter times where electroosmosis is the dominant mechanism and the backflow resulting from capillarity has not yet had time to develop. As a result, the experimental velocity can be expected to fall in between the velocities predicted by the thick (lower bound) and thin (upper bound) double layer models.

## Conclusion

The experiments have shown that electroosmosis can be used in an individually addressable arrayed device to pick up objects with minimal energy and no mechanical input. Placement only requires reversing the polarity of the voltage and decreasing the volume of the capillary bridges. The constant-volume instabilities of a liquid bridge pinned on a plate at one end and a sphere at the other end are well characterized [27]. Once the sphere or tile is in contact with its base the objects can be force fit using the circuit board platform as a force base to interlock tiles or place spheres. This was tested using an adhesive foam pad for a base to mimic the force fit (See Movie S2). Regarding the accuracy and reliability of the device, the checkerboard platform is the most intricate design possible to show the individual addressable capabilities of the PICEM. Success rates were high in all trials, but a much higher success rate could be established with more precise mechanical apparatuses moving the PICEM. For instance, the platform on which the spheres rest is not completely level, nor was the circuit board face with respect to the sphere array. This causes inconsistencies in pick up, especially around the edges, as shown in the data. However, since the PICEM did have a 100% success rate on creating droplets in the desired configurations, it is only a matter of tweaking the mechanical environment in order to increase success rates. However, the flexibility of the liquid interface does help mitigate issues with imperfect alignment.

Since the current design has 508  $\mu\text{m}$  diameter channels for droplet growth, it has a limited ability to pick up small objects with maximum dimensions around this range. In the future, this limited capability will be removed. Because of the modular design, the top circuit board can be easily customized for the application at hand by altering the density and diameter of the channels. Con-

sequently, the PICEM will be able to pick up objects as large as 2 mm (based on the capillary length of the liquid, which in this case is water), and as small as those on the nanometer scale.

Furthermore, since each of the slices in the device is individually 3D printed, it is already set up for rapid mass production. However, as technology progresses, the two different materials used in the layers (Tango+ and FullCure720) will be able to be printed in one process further removing steps in the assembly process. This multi-material printing is already available, but has limitations in terms of quality of printing small features, something necessary in creating the Tango+ gaskets with small holes.

Beyond just the assembly and hole size, the array size on the circuit board will be able to be expanded to hold millions of channels. Expanding this 5x5 array to a larger scale will only require larger circuit boards and a slightly more complex control system. At this point, the device is controlled by manually connecting a voltage source. However, it would be easily possible to connect this system to a computational controller in order to individually control the voltage flowing through each channel. This would allow for both positive and negative voltage to be used simultaneously to ensure that each droplet is uniform and consistent amongst the array.

In terms of tile assembly, which is studied in this lab, the future holds the creation of nanofabricated tiles that are small enough to appear as sand. These tiles would be put on a shake plate for alignment and the PICEM would be able to hold a million channels (massively parallel) to pick from the variety of plates of tiles for the desired final assembly. However, on a grander scale, this device could be used to pick up objects of varied size, have the ability to stack these objects, and to have an integrated control system to ensure desired droplet size and picking ability. Furthermore, other liquids could be used for different desired surface tensions for the particular surface materials of the objects to be picked.

Based on the comparison between experimental testing, COM-SOL simulations, and analytical calculations, it can be seen that the basic physics of the PICEM can be captured with simple models. Statistical analysis of the picking show that the PICEM is a reliable and accurate means of picking millimeter scaled objects in parallel and with individual control.

**ACKNOWLEDGMENTS.** Special thanks would like to be given to the Steen Group in their support for their initial training on the SECAD device. Furthermore, prior work from Jonathon Hiller served an integral role in the automation of this device, and to Mike Vogel for his previous work on the SECAD. This work was supported by DARPA Grant No. W911NF-11-1-0093 and NSF Grant No. DGE-0707428.

1. M. Vogel, P. Ehrhard, and P. Steen, *The Electroosmotic Droplet Switch: Countering Capillarity with Electrokinetics*, P.N.A.S. (2005), pp. 11974–79.
2. M. Vogel and P. Steen, *Capillarity-based Switchable Adhesion*, P.N.A.S. (2010), pp. 1761–66.
3. W. Zesch, M. Brunner, and A. Weber, *Vacuum tool for handling microobjects with a NanoRobot*, Robotics and Automation (1997), pp. 1761–66.
4. K. Molhave, T. Welch, A. Kortschack, and P. B??ggild, *Pick-and-place Nanomanipulation Using Microfabricated Grippers*, Advanced Engineering Materials (2005), pp. 193–96.
5. D. Tsui, A. Geisberger, M. Ellis, and G. Skidmore, *Micromachined End-effector and Techniques for Directed MEMS Assembly*, Journal of Micromechanics and Microengineering (2004), pp. 542–49.
6. K. Kim, E. Nilsen, T. Huang, A. Kim, M. Ellis, et. al, *Metallic Microgripper with SU-8 Adaptor as End-effectors for Heterogeneous Micro/nano Assembly Applications*, Microsystem Technologies (2004) pp. 689–93.
7. T. Huang, L. Zhanxian, L. Meng, D. Chetwynd, and C. Gosselin, *Conceptual Design and Dimensional Synthesis of a Novel 2-DOF Translational Parallel Robot for Pick-and-Place Operations*, Journal of Mechanical Design 126.3(2004), pp. 449.
8. H. (5) Miyazaki, and T. Sato, *Pick and place shape forming of three-dimensional micro structures from fine particles*, Robotics and Automation, (1996), pp. 2535–40.
9. S. Saito, H. Miyazaki, and T. Sato, *Pick and place operation of a micro-object with high reliability and precision based on micro-physics under SEM*, Robotics and Automation (1999), pp. 2736–43.
10. F. Rubio-Sierra, W. Heckl, and R. Stark, *Nanomanipulation by Atomic Force Microscopy*, Advanced Engineering Materials (2006), pp. 193–96.
11. J. Randhawa, T. Leong, N. Bassik, B. Benson, et. al, *Pick-and-Place Using Chemically Actuated Microgrippers*, Journal of the American Chemical Society (2008), pp. 17238–239.
12. B. Chang, M. Jaaskelainen, and Q. Zhou, *Microassembly combining pick-and-place and water mist*, Micro-NanoMechatronics and Human Science (MHS), International Symposium 7-10 Nov. 2010, pp. 333–37.
13. S. Veikko, M. Jaaskelainen, and Q. Zhou, *Hybrid Microassembly Combining Robotics and Water Droplet Self-Alignment*, IEEE Transactions on Robotics (2010), pp. 965–77.
14. L. Jiang and D. Erickson, *Directed Self-Assembly of Microcomponents Enabled by Laser-Activated Bubble Latching*, Langmuir (2001), pp. 11259–264.
15. J. Hiller, and H. Lipson, *Design and Analysis of Digital Materials for Physical 3D Voxel Printing*, Rapid Prototyping Journal (2009), pp. 137–49.
16. <http://www.objet.com/Portals/0/docs2/Objet%20Materials%20Data%20Sheets.pdf>
17. R. Hill, D. Koch, and A. Ladd, *The first effects of fluid inertia on flows in ordered and random arrays of spheres*, The Journal of Fluid Mechanics (2001), pp. 213–41.
18. H. Chang, Chapter 11: *Bubble/drop Transport in Microchannels*, The MEMS Handbook (2002), pp. 11.1–11.2.
19. P. Gennes, F. Brochard-Wyart, and D. Quere, Chapter 10: *Transport Phenomena, Capillarity and Wetting Phenomena: Drops, Bubbles, Pearls, Waves*. New York: Springer Science Business Media (2010), pp. 261–87.
20. Y. Fintschenko, B. Kirby, E. Hasselbrink, A. Singh, et. al, *Monolithic Materials: preparation, properties, and applications: Miniature and Microchip Technologies*, Journal of Chromatography Library (2003), pp. 675–85.
21. B. Kirby, *Micro- and Nanoscale Fluid Mechanics: Transport in Microfluidic Devices* (2010), pp. 675–85.
22. <http://www.astro.uvic.ca/tatum/elmag/em01.pdf>
23. D. Cooper, J. Batchelder, and M. Taubenblatt, *Investigation of Particle Pairing in Liquids*, Journal of Colloid and Interface Science (1991), pp. 201–09.
24. D. Griffiths, *Introduction to electrodynamics*, 3 ed. Upper Saddle River, NJ (1999).

25. D. Barz, M. Vogel, and P. Steen, Determination of the Zeta Potential of Porous Substrates by Droplet Deflection. I. The Influence of Ionic Strength and pH Value of an Aqueous Electrolyte in Contact with a Borosilicate Surface, *Langmuir*, (2009), Vol. 25, pp. 1843–50.
26. [http://micromachine.stanford.edu/dlaser/research\\_pages/silicon\\_eo\\_pumps.html](http://micromachine.stanford.edu/dlaser/research_pages/silicon_eo_pumps.html) Visited: May 7, 2012.
27. Hotta K, Takeda K, Iinoya K (1974) The Capillary Binding Force of a Liquid Bridge. *Powder Technology*, 10 pp. 231–242.

# Bitblox: A Printable Digital Material for Electromechanical Machines

Robert MacCurdy, Anthony McNicoll, and Hod Lipson

**Abstract**—As additive manufacturing of mechanical parts gains broad acceptance, efforts to embed electronic or electromechanical components in these parts are intensifying. We discuss recent work in printable electronics and introduce an alternative, which we call Bitblox. Bitblox are small, modular, interconnecting blocks, that embed simple electromechanical connectivity and functionality. Not all blocks are identical; instead the unique combinations and positions of Bitblox within an assembly determine the mechanical and electrical properties of the assembly. We describe the design details of Bitblox, compare them to similar materials, and demonstrate their use in a working 3D printer through several examples.

**Index Terms**—Modular robots, printable electronics, rapid prototyping, additive manufacturing, 3D printing, programmable matter, digital material.

## I. INTRODUCTION

Additive manufacturing was commercialized in the early 1980's and has found broad applications in research, industry, and recently, by consumer end-users. Numerous commercial vendors sell machines capable of printing various metals and plastics; these printers are used for prototyping purposes, as well as the production of finished parts. Biomedical researchers have used 3D printers to deposit living cells, and succeeded in fabricating complete living structures, including bone, cartilage and organs (Cohen et al. 2010, Mironov et al. 2003). The advent of very low cost printers, like the Fab@Home (Lipton et al. 2012), RepRap (RepRap 2013), MakerBot (Makerbot 2013) and others has empowered personal, on-demand home-printing of materials ranging from ABS plastic to chocolate. Thus far however, no 3D printer has been capable of printing complete electromechanical systems. In previous work the Golem project (Lipson and Pollack 2000) combined evolutionary design techniques with additive manufacturing in a way that allowed electromechanical systems to first evolve in simulation and then be physically realized automatically. However, although the kinematic mechanisms were printed, the electronics and actuation were added by hand in a post-processing step. This work serves as the inspiration behind the Bitblox project: we seek a mass-producible set of primitives (building blocks) that can be used to automatically synthesize and construct a broad array of electromechanical designs. We ultimately aim for very large scale integrations involving thousands to millions of components. Therefore, we focus on homogeneity and a very small, yet universal repertoire of building block types arranged on a regular lattice, suitable for eventual integration into a rapid automatic parallel assembly process. Though the Golem project is an inspiration, robotics is but one of many potential applications of an electromechanical printer. This paper uses the Bitblox implementation as an exemplar of the new design and construction framework enabled by the emerging field of digital materials. We describe the framework, detail our Bitblox implementation effort, discuss the application areas that might be impacted by printing with digital materials, and demonstrate several functional prototypes built with Bitblox.

## II. BACKGROUND

In our recent book, we report (Lipson and Kurman 2013) that disparate users commonly identify several factors that differentiate additive manufacturing from conventional methods. These “principles of additive manufacturing” are: it makes complexity and customization less expensive; it reduces the requirement for post-processing assembly; it reduces lead times; it expands the reachable design-space of a single machine (relative to a CNC mill, or lathe, for example); it reduces the manufacturing skills required of support staff; it allows portable, compact manufacturing; it creates less waste or manufacturing by-product; it enables new material combinations; it offers precise duplication of existing objects or digital design files. This list is clearly aspirational and because no current additive manufacturing technology fully satisfies each item, taken together, these dimensions offer a spectrum against which the practical impact of new developments can be assessed.

Commercially available 3D printers are capable of printing in a wide array of materials, including different types of steel, titanium, bronze, and many plastics. At least one major vendor (Stratasys Corp. Eden Prairie, MN) sells a printer that can simultaneously print in two different plastic materials, enabling models with near-continuous mixtures of the two materials to be fabricated. To-date, none of the materials currently available in commercial multi-material machines are good electrical conductors; however this is an area of active development. Researchers have demonstrated two-step processes, in which a part is first fabricated from an insulating structural material, and afterward a conductive material is deposited (Grimm 2012). The

development of conductive materials that can be applied as a liquid is ongoing, and solutions employing silver (Russo et al. 2011) or carbon nanoparticles (Zhao et al. 2012) have achieved favorable electrical conductivities, however work remains; the silver formulations have resistivity values that are between 2 to 4 orders-of-magnitude greater than bulk silver. An interesting alternative method based on embossing has been demonstrated (Bulthaup et al. 2001) which enables the creation of active devices (transistors) as well as passive interconnects, including multi-layer vias, with resolutions down to 100nm. A recent review of similar methods can be found in (ten Elshof et al. 2010). Printable sensors (Maiwald et al. 2009) and transistors (Jones et al. 2010) are also in active development.

Although conventional additive manufacturing tools use a wide array of build-materials and deposition methods, virtually all of them use what is essentially an analog technique; they employ sophisticated controllers to carefully meter-out precise amounts of raw material and deposit, or fuse, that material in a particular location. The accuracy of the finished part is completely dependent on the accuracy of the machine that is building it, and has little or no dependence on the material that the part is being made from. Additionally, because they deal with what are essentially raw materials, 3D printers must simultaneously process and deposit the build material. This is asking a great deal from a single device, which should also be cheap and portable.

#### *A. Programmable Matter & Digital Materials*

The relatively recent developments of programmable matter (Toffoli and Margolus 1991) and digital materials (Cheung 2012, Gershenfeld 2005, Gershenfeld 2012, Popescu 2007) seek to change this paradigm by imbuing the materials themselves with properties that influence or determine the nature of the part that the materials are used to create. This idea provides a means to sidestep the current technological limitations of fabricating electromechanical devices with 3D printers by leveraging existing technologies to mass-produce the “ink” used by the printer. This approach allows relatively low-cost printers to assemble complex, user-specified designs from a list of pre-produced building blocks.

Digital materials are discrete, and like identical grains of sand, have pre-defined geometries. These geometries determine the resolution of the finished part; because of this, the synthesized assembly can achieve a build resolution that exceeds that of the printer. LEGO toys illustrate this point: the precision of the highly ordered creations formed by the plastic brick’s pre-defined interconnects far exceeds what would be possible with free-hand fabrication. Embedding geometric relationships into a material, rather than relying on the printer that manipulates it, enables a significant feature of designing with digital materials: every copy of a particular design will be identical, regardless of which printer the copy was produced on. As long as they use the same materials, different printers made by different manufacturers can create functionally perfect reproductions of a design file without resorting to exact calibration.

In addition to an inherent geometry, digital materials incorporate sophisticated, but atomic functionality. For example one digital material element could implement a logic function, while an adjacent transducer element converts the logic signal into a mechanical motion. Still other materials could satisfy energy storage needs, transmit electrical or mechanical signals, or sense the surrounding environment. Numerous distinct digital materials and printers have been implemented, including a system that used spheres to assemble 3D structures (Hiller and Lipson 2007), and systems that relied on interlocking tiles (Popescu 2007), and incorporated electrical connectivity (Ward 2010), (Hiller et al. 2011). Hiller et al performed a comprehensive study of different candidate digital materials, analyzing their mechanical, space-filling and error scaling properties (Hiller and Lipson 2009).

The term Programmable Matter has been used (Gilpin and Rus 2010) to describe a modular material which can be used to build physical machines that can be reconfigured on-the-fly to change their physical state. The concept found early use (Toffoli and Margolus 1991) in building efficient, parallel simulation machines that performed the simulation in a computationally distributed way, mapping the spatial distribution of the simulation onto equivalently spatially distributed compute resources. We seek to borrow ideas from Digital Material and Programmable matter, two overlapping areas of research, to develop a framework for efficiently and automatically producing electromechanical machines.

#### *B. Existing candidate materials*

There are numerous examples of previous work that fit into the combined programmable matter and digital materials category described above; we describe relevant projects next, and discuss their suitability as the constitutive elements of a general electromechanical toolset.

A project called Illuminato X Machina (Introducing Illuminato X Machina 2013) has built small, 2 inch-square circuit boards that contain general purpose CPUs with a 32 bit, 72 MHz arm core. These boards can be plugged together in a 2D network to form distributed computers, in a form that borrows directly from early work (Toffoli and Margolus 1991) on distributed computing with programmable matter. There is no provision for actuation or sensing, and the modules only connect in-plane.

Bug Labs (Bug Labs 2013) is selling a product that they call Bug Modules, which are circuit boards that integrate computers, displays, I/O panels and other functional blocks. These parts snap together, and due to clever code inside them, are preconfigured to work together, plug-and-play with the other modules that are offered. The parts are high-level; each block contains a great deal of complexity in the form of hardware as well as software. Certain block combinations are intentionally limited by the hardware, and only 2D connectivity is supported; these modules are intended as a developer-friendly hardware suite for prototyping specific devices, rather than as a flexible electromechanical building block suite.

The LEGO Mindstorm (LEGO Mindstorm 2013) family of toys integrates many electromechanical elements, including a wide range of sensors, actuators and computational elements. However, this flexibility come with a cost: the number of unique elements in the set has proliferated as special-purpose parts have been added. Although many of these pieces retain the iconic LEGO mechanical interconnects, the large number of different pieces in the set would make their use in a 3D printer difficult; the problem is analogous to having numerous unique inks available in an inkjet printer – stocking the materials becomes increasingly challenging as their number increases. The Mindstorm system also integrates a vast array of physically different pieces, and their mechanical heterogeneity makes manipulating them a complex task; parts that are easy to place with fingers and human coordination would prove extremely challenging for even the most sophisticated robotic manipulators.

B-Squares (B-Squares 2013) are a set of interconnecting modular electronic tiles (their creators refer to them as “squares”), approximately 2 inches square and 1/3" thick, that utilize magnetic interconnects which provide both the mechanical and the electrical connectivity. There are several types of tiles, including battery, LED and computation. Users can create different circuits by connecting different tiles in different mechanical configurations, and the connectors allow tile stacking, which allows true 3D configurations. The computational block can be programmed by the user. This system offers many appealing features, although the tile’s size, relatively weak mechanical interconnections, and the current lack of any sensors or actuators precludes its use.

E-Blocks (E-Blocks rapid electronic development kits 2013) are a set of circuit boards with mating connectors that allow in-plane connections between adjacent boards. This system is geared toward educators and embedded system designers who desire simple functional electrical circuits that can plug together during the development phase, rather than spending time developing custom hardware for each subset of a design. The system includes a large variety of functional blocks that can be quickly plugged together to achieve a particular electrical system design. The E-Blocks system uses what is essentially a hub-and-spoke topology, which prevents it from tiling an arbitrary space. The connectors provide minimal mechanical strength, and the variety of connectors on the individual pieces precludes their use in a system with an automatic assembler.

Cubelets (Cubelets from Modular Robotics 2013) are a set of mechanically similar plastic cubes, approximately 4cm on a side, with magnetic connectors that provide mechanical and electrical connectivity. There are different types of cubes in the set, including light sensing, infra-red range sensing, battery, and LED. The Cubelets set also integrates two actuator types; the first type rotates one of the faces relative to the others, while the second has two small wheels on the bottom, enabling a simple rolling behavior. The magnetic connectors allow the cubes to snap together easily, which would be an asset for a machine-printable material, however they offer low strength. Additionally, since each cube integrates a small amount of functionality, a sophisticated design would require a large

TABLE 1 - COMPARISON OF POTENTIAL DIGITAL MATERIALS

	Module Size <sup>a</sup>	Individual Complexity <sup>b</sup>	Assembly Dimension <sup>c</sup>	Electrical Connectivity	Actuation	Flexible <sup>d</sup>	Suitable for Assembly <sup>e</sup>	Hierarchical Modules <sup>f</sup>
Bitblox	S	M	2.5D	Y	Y	Y	Y	Y
Illuminato X Machina	L	H	2D	Y	N	N	N	N
Bug Modules	L	H	2D	Y	N	N	N	N
LEGO Mindstorm	M	L	2.5D	Y	Y	Y	N	Y
B-Squares	L	H	3D	Y	N	N	Y	N
E-Blocks	L	H	2D	Y	N	N	N	N
Cubelets	L	M	3D	Y	Y	N	Y	N
Miche	L	H	3D	N	N	N	Y	N
Robot Pebbles	S	H	3D	Y	N	N	Y	N
[Gracias et al. 2000]	S	L	3D	Y	N	N	Y	N
[Terfort and Whitesides 1999]	S	L	N/A	Y	N	N	N/A	N
[Srinivasan et al. 2001]	S	L	N/A	N	N	N	N/A	N
[White et al. 2004]	L	H	2D	Y	N	N	Y	N
[Griffith et al. 2005]	L	H	2D	Y	N	N	Y	N
[Popescu 2007]	M	L	3D	Y	N	N	Y	N
[Ward 2010]	S	L	3D	Y	N	N	Y	Y
[Hiller and Lipson 2009]	S	L	3D	N	N	N	Y	N
[Tolley et al. 2010]	S	L	3D	N	N	N	Y	N
[Neubert et al. 2010]	S	L	3D	Y	N	N	Y	N
[Cheung 2012]	S-M	L	3D	N/A	Y	Y	N/A	N
[Kernbach et al. 2008]	M	H	2D	Y	Y	Y	N	N
[Jorgensen et al. 2004]	L	H	3D	Y	Y	Y	Y	N
[Zykov et al. 2005]	L	H	3D	Y	Y	Y	Y	N
[Yin et al. 2008]	S	H	3D	N	Y	Y	Y	Y
[Ke et al. 2012]	S	H	3D	N	N	N/A	Y	Y

N/A - this information was not demonstrated or not discussed in relevant publications.

Author names are used where no specific project name was available.

<sup>a</sup>Module Size - Size of the digital material. L= greater than 4cm on any side. M=between 1 and 4 cm on any side. S=1cm or less on a side.

<sup>b</sup>Individual Complexity - Electrical/Mechanical functional complexity of each module. Ranked into High (H), Medium (M), Low (L).

<sup>c</sup>Assembly Dimension - Planar (2D), Stacked 3D with connections between adjacent layers (2.5D), or full 3D with connections in any dimension (3D)

<sup>d</sup>Flexible - Indicates if the assembled structure can move relative to itself via hinges, flexures or as the result of actuation.

<sup>e</sup>Suitable for Assembly - Indicates that modules can be readily manipulated by a robotic gripper and assembled, or that they can self-assemble.

<sup>f</sup>Hierarchical Modules - The digital material contains modules at different size scales that can interconnect in an assembly.

number of cubes, and because the cubelets are relatively large, the complete assembly would occupy significant volume.

All of the materials discussed to this point have been designed to be assembled by hand, however prior work has also been directed toward materials that can be assembled by an external device, or that can self-assemble. Gracias et al (Gracias et al. 2000) fabricated small (~5mm) octahedra whose faces were covered with flexible circuit board material. The circuit boards were designed to allow rotation and flip-invariant connections, and supported 2 unique electrical nets. The electrical contact points on the circuit boards (pads) were coated with low-melting point solder. When several of the octahedra were placed together in a flask of warm liquid and agitated, the surface tension of the liquid solder on the pads was sufficient to bond the parts together. Once cooled, the completed assembly could be removed from the liquid and a working electrical network of octahedra was formed, allowing LEDs to be illuminated. Though an impressive demonstration of self-assembly, the authors did not show that complex, heterogeneous assemblies could be created with this technique. Related work (Terfort and Whitesides 1999), (Srinivasan et al. 2001) addresses this issue by adopting a bio-inspired design that uses unique mechanical bonding sites to differentiate the materials in the system. Like unique puzzle pieces, this approach allows the designer to pre-condition the system, making bond-pairs between certain materials unlikely or impossible. This approach, while extremely promising, has not yet been shown capable of assembling electrical networks from heterogeneous digital materials. Two related, but larger designs (White et al. 2004), (Griffith et al. 2005) utilized a combination of mechanical alignment features, electromagnetic latches and onboard computation to stochastically self-assemble and selectively make or break bonds.

Assembling a complex structure from individual pieces is a challenging task, requiring dexterity, flexibility and careful planning. An alternative approach has been proposed that works in reverse; rather than starting with an empty space and adding individual materials, the workspace starts out completely filled with material, and the materials are selectively removed to yield the final assembly. This approach is a bit like traditional machining, in which pieces of a block of raw material are selectively removed with a tool until the desired result is achieved; however the raw material in this case is a digital material, and rather than using an external removal tool, the bonds between adjacent pieces of material are removed by the materials themselves. One example of this approach, known as Miche (Gilpin et al. 2008) used cubes that were 4.6cm on each side as the material. Each cube could bond to its neighbors via a permanent-magnetic latch that was mechanically actuated. Communication between adjacent cubes was accomplished via infrared light. Another related project, called robot pebbles (Gilpin et al. 2010), used smaller cubes (1cm), an electrical communication and power interface between cubes, and sophisticated latches based on electropermanent magnets that require no DC current to operate in either a latched or unlatched state.

At least two efforts (Popescu 2007), (Ward 2010) have resulted in digital materials that can be 3D printed, and are based on a novel interlocking design, called a GIK. These digital materials employ a press-fit mechanical mating strategy, and are constructed from a variety of raw materials, including plastic, wood, aluminum and copper. The conductive metal parts allow electrical circuits to be embedded in a mechanical structure as it is constructed, while the insulating plastic parts allow isolation between distinct electrical nets. The mechanical interconnects employed by these systems produce a strong network of connections, and consequently do not allow mechanical flexibility, a drawback if relative motion within the structure is desired, as it would be if actuated components were added. Neither of these efforts integrated actuators into the digital material set.

Hiller (Hiller and Lipson 2009) employed a spherical digital material that self-aligned when deposited, resulting in high resolution prints. The small sphere diameter (1.5mm) allowed relatively high resolution prints, and the deposition process used a parallel assembly technique capable of scaling to very high rates of deposition. However, the spherical material was completely inert, lacking mechanical and electrical interconnects, as well as actuation; it was solidified in a post-processing step via adhesives or chemical sintering.

Tolley (Tolley et al. 2010) and Neubert (Neubert et al. 2010) used a stochastic fluidic assembly strategy to construct various geometries from identical cubic materials. The materials used in these experiments employed either mechanical or phase-change latches. Neither material integrated actuation or computation.

Cheung (Cheung and Gershenfeld 2013, Cheung 2012) employed a sparse matrix of light, stiff elements to construct Digital Cellular Solids, materials capable of attaining much higher stiffness to mass ratios than the raw materials that went into the elements. Depending on the arrangement of the constitutive elements, the composite material could be selectively tuned for stiffness, or achieve complex actuated geometries by manipulating a single degree of freedom tensile member.

The REPLICATOR and SYMBRION projects (Kernbach et al. 2008) developed sophisticated modular robots with modules capable of autonomous locomotion and self-assembly. These projects integrated ideas from the modular and swarm robotics fields. When linked together, adjacent modules could communicate electrically and apply forces, allowing complex, actuated assemblies to automatically form. A related design, ATRON (Jorgensen et al. 2004) employed robust mechanical latches that allow individual modules to selectively attach to neighbors on-the-fly, enabling self-assembly. Another set of modules from (Zykov et al. 2005) implemented similar functionality, but employed magnetic latches and a single rotational degree of freedom in each module.

Finally, no discussion of engineering building blocks should fail to mention the enormously exciting progress being made in the field of synthetic biology. Two consortia, the BioBricks Foundation and the International Genetically Engineered Machines competition (iGEM),(Smolke 2009) are very rapidly expanding our ability to manipulate DNA in order to construct genetic systems from reusable building blocks. Much of this work is focused on the capability to manipulate the genotypes or

phenotypes of living machines (single or multi-cellular organisms), however DNA and RNA have been used on their own to create bipedal walkers (Yin et al. 2008) and logic circuits (Seelig et al. 2006). Recent work (Ke et al. 2012) has used similar techniques to self-assemble 3-dimensional alphabetic characters from smaller, interlinked DNA building blocks. While DNA- and RNA-based building blocks show enormous promise, fabrication challenges and capability limitations currently impede their use as part of a table-top electromechanical printer.

### C. Justification for a new material

The materials discussed in the previous section have been included in TABLE 1 and are compared across several dimensions, selected to illustrate the requirements of a general electromechanical material suitable for use in a portable 3D printer. We desire a material that combines the following features: regular geometry that can be easily manipulated by a machine; robust mechanical and electrical interconnects; small size, with the capacity for further size reductions; hierarchical assembly, with smaller elements integrating seamlessly with larger ones; electromechanical functionality; elements that allow differential motion. Our survey did not yield a suitable existing material that simultaneously satisfied these criteria.

## III. A NEW PRINTABLE MATERIAL

Much of the previous work in the field of modular robotics has focused on building sophisticated modules that incorporate energy storage, sensing, actuation, and computation into each module. Robots are then constructed as assemblies of many identical copies of these modules. Instead, we introduce a class of digital materials directed toward producing electromechanical machines that we call Bitblox. These materials utilize regular, volume-filling shapes (herein referred to as "building blocks") that interconnect on a regular lattice and interact with each other as described below. Bitblox materials are intentionally simple and do not self-assemble; they require an external machine with modest spatial resolution to place them into the desired locations within a design. The requirement to self-assemble, commonplace in the modular robotics field, seems to impose an onerous level of complexity and hence, volume, on the design of robotic modules; none of the active self-assembling modules discussed previously are small enough to be plausibly considered a digital material. Though there is no established threshold for the volume that a piece of digital material may occupy; in the absence of this metric we argue for a secondary criterion: how small could the module plausibly be fabricated five years in the future? This choice has a practical underpinning, since end-users of the material will undoubtedly desire functionality and morphologies that are very different from those that the material's designers envisioned. It seems clear that materials that are physically small, so that they can more closely conform to a given end-user's design envelope, and that implement simple, fundamental functionality will prevail over larger, more special-purpose blocks. Therefore, individual Bitblox building blocks have very limited functionality. No single Bitblox material is capable of performing any useful function alone; it is the combination of many simple blocks that gives this approach versatility and utility. For example, even a trivial circuit that blinks an LED requires 4 separate Bitblox pieces: a battery, a microcontroller, a short, and an LED.

While it is true that each unique Bitblox type conforms to the strict definition of a "module", their extreme functional simplicity and suitability for reductions in scale (as we discuss later) make the material analogy appropriate.

The different material types within the Bitblox class complement each other, and their various combinations enable extensions to the reachable design space, as summarized in TABLE 2. Though not all entries in TABLE 2 have been implemented, we describe the design and performance of several key block types. We also show examples of the reachable space.

### A. Mechanical Connectivity

The modules listed in TABLE 1 interconnect in three distinct ways. The 2D connection type only mates in-plane neighbors. Those that employ a 3D connection strategy attach to their immediate neighbors on all sides, while those that are 2.5D connect only with their neighbors above and below; in-plane connectivity comes from alternating connections with layers above and below. The LEGO brick system is the most familiar example of this type of connectivity. Though the cube is the most common

TABLE 2 - LIST OF DIFFERENT MATERIAL TYPES AND THE DESIGNS THAT COULD BE REALIZED WITH THEM

Basic Material Type	Reachable Design Space
Structural and sacrificial	Arbitrary static and kinematic geometric structures
+ soft	meta-materials with graded and nonlinear properties
+ conductive	embedded wires and 3D interconnect
+ resistors, transistor, capacitors	Embedded 3D analog circuits in arbitrary geometry
+ batteries, photovoltaic	3D energy harvesting and storage
+ CPU , FPGA	3D distributed computational/programmable networks
+ Sensor and actuator	Robots

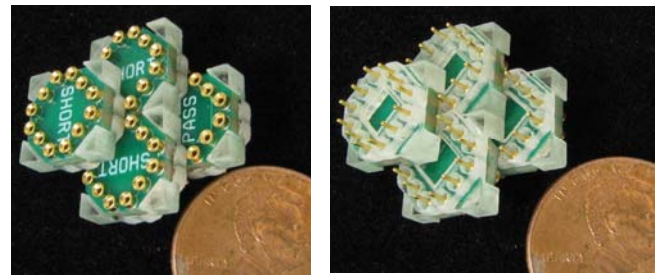


Fig. 1 4-block assembly of Bitblox. Top view (left) and bottom view (right)

space-filling shape, many other shape-primitives may be used to tile their respective spaces. In 2.5D tiling, extrusions of the following 2D shapes can be used: diamond, equilateral triangle, square, hexagon. In 3D, shapes including the rectangular prism, truncated tetrahedron and truncated octahedron may be used (Hiller and Lipson 2009).

Various mechanical attachment approaches were exploited for the materials listed in TABLE 1, including passive and active magnetic latches, mechanical latches, press-fit connectors, phase-change metals (solder), surface tension, and adhesives. In most cases, the mechanical contacts also provided electrical connectivity.

Of the two tiling schemes mentioned, 2.5D enables simpler automated assembly; because no connections exist between adjacent blocks on the same layer, the blocks can be inserted vertically into a layer without concern for the precise orientation of other blocks already present in that layer. This placement requires a relatively simple 1 degree-of-freedom actuator. In contrast, 3D connectivity requires careful assembly planning to avoid creating "holes" in a design that cannot be filled with material because they are surrounded by blocks that have already been placed. This problem extends to cases where only two blocks, touching at their corners have already been placed, and a third block must be placed between them. This third block must be inserted diagonally, and care must be exercised to be sure that no protrusions on any of the materials would interfere with this motion. Designing passive connectors that accommodate this type of motion is a challenge. Tolley describes these issues in more detail (Tolley et al. 2010). The issues with interconnections for 3D tiling can be mitigated by utilizing a connector strategy that retracts, allowing interference-free motion as the materials are being manipulated. Previous work in modular robotics has utilized modules with retractable latches (Jorgensen et al. 2004), however this feature imposes significant mechanical complexity, which usually increases the module size.

For these reasons, we chose to implement Bitblox with a 2.5D tiling scheme. Bitblox utilize a press-fit approach, relying on their metal connectors to provide mechanical and electrical connectivity. Several connected blocks can be seen in Fig. 1, which shows views from the top and bottom. The image shows thruhole pin-and-socket connectors (Mill-max p/n 9407-0-15-01-11-27-10-0), chosen for their simplicity, ability to self-align, and mechanical strength. These contacts integrate a recessed conical alignment geometry near the socket entrance, which guides the pin into the socket if they are slightly misaligned. This approach, when combined with a small amount of compliance in the device that mates two Bitblox, can accommodate off-axis misalignments up to 0.38 mm, a tolerance that is readily achievable with most personal 3D printers. The contacts also incorporate a stepped profile that uses a shoulder to stop the contact when fully mated. This feature provides self-alignment from layer to layer (the Z dimension), allowing a printer with a small amount of compliance to deliberately over-mate the Bitblox when placing them. This approach allows the materials themselves to dictate the overall precision of the assembly. When assembled in this manner, we can estimate the accumulated thickness  $T$  and standard deviation  $\sigma$  from  $N$  layers as shown previously (Hiller and Lipson 2009), where  $\varepsilon$  is the total error tolerance of the object, and  $l$  is the fully-mated length of the connectors, in this case 3.71mm. If we make the approximate, but convenient

$$T = l \times N \quad \sigma = \varepsilon \sqrt{\frac{N}{12}} \quad (1)$$

assumption that the connector length follows a Gaussian distribution and that the tolerance of the connector length is 50um, the expected thickness of 10 layers would be 37.1mm, while the standard deviation would be 45um. As equation 1 shows, while the thickness of an assembly scales linearly with the number of building blocks used, the error in thickness scales with the square root of the number of blocks used; as assemblies grow larger the individual errors of the materials tend to cancel, yielding precise assemblies. Estimating in-plane (X & Y dimensions) error scaling precisely is more complicated, and a proper analysis requires numerical simulations. Previous work (Hiller and Lipson 2009) has shown that the same error-cancellation effect observed in the Z dimension also applies in-plane, and that errors accumulate with the square root of the number of blocks.

Adhesives may be used between layers if permanent mechanical connections are desired, or if higher loads are anticipated. Previous work (Tolley et al. 2008) has employed interfacial electrical interconnects that allow adjacent blocks to connect when brought into contact (forming a butt-joint between adjacent blocks), therefore we explored fabricating small electrical contacts that would support this connection modality. Unfortunately, we found that robust, low resistance electrical connections using this approach require relatively high mating pressures. These high mating pressures place an additional burden on the mechanical latches that hold adjacent blocks together. The lack of a viable interfacial electrical connection scheme partially dictated the 2.5D tiling choice. The end result is a block that is mechanically rotation-invariant and flip-variant.

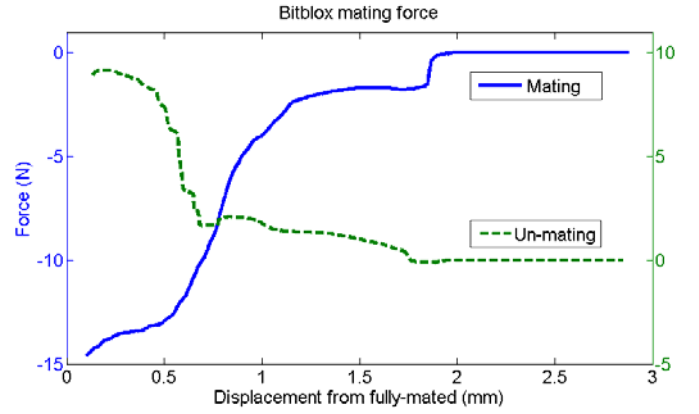


Fig. 2 Bitblox mating (left y-axis) and un-mating force (right y-axis), in Newtons, as a function of the connector separation distance (0 mm is fully-mated). Tensile force is positive; compressive force is negative.

Since Bitblox are intended to be assembled automatically, the connector mating and un-mating force must be known. We used a Bose ElectroForce LM1 testing machine (Bose Corporation; Eden Prairie, Minnesota) to measure the applied force while mating and un-mating the connectors. A typical result is shown in Fig. 2, which depicts results for a test case when all 12 pin-in-socket contacts are being used. This situation requires the maximum force; the required force would be lower if fewer contacts are being used, as would be the case for blocks that do not completely overlap with layers immediately above or below.

### B. Electrical Connectivity

Seeking to minimize size, and constrained by our choice of electrical contact, we chose to accommodate only 2 electrical nets per edge. The blocks have four edges, allowing up to eight nets per block to be routed off-board. Each edge requires three connectors, since we chose to exploit symmetry in order to create a rotation-invariant contact layout: one net is routed to the central contact while the outer two contacts share the second net. Although in principle the blocks could allocate any net to any contact, we chose to reserve the center pin on each edge for the ground reference, while allocating the other available net on each side to various signal routing tasks. This is an arbitrary choice, and may in fact be suboptimal, however it eases manual design of circuits using these blocks. Future versions, when aided by sophisticated design automation software, may employ different signal allocation strategies. We draw parallels between these design choices and those faced by FPGA architecture engineers. The authors of a comprehensive review (Kuon et al. 2008) of FPGA devices describe how early developers experimented with a wide variety of architectural granularity and logic block choices before arriving at the present consensus design. It should be mentioned that even today these choices remain in flux, and significant recent advances (Teifel and Manohar 2004) have been made by questioning long-held FPGA design tenets. Although many of these design choices were based on intuition, some (El Gamal et al. 1989) used comprehensive studies of design reachability by using autorouter tools to automatically test many design variants on a given choice of architecture. We are currently working to develop automated routing tools for Bitblox modules so that similar studies may be carried out. At present we rely on intuition when designing the electrical connectivity of any particular block.

Bitblox have been implemented with several different electrical functions; as a reminder the goal is to create a small number of block types that can be mass-produced and used to assemble more complicated circuits. We have implemented electrical blocks with microcontrollers, field-effect transistors, mechanical momentary switches, batteries, resistors, capacitors, inductors, and diodes. We have also created blocks that purely route or stop signals. Whenever possible, the blocks were given rotational invariance by choosing identical electrical nets for each of the four sides. This eases the routing process, but is not possible for all block types.

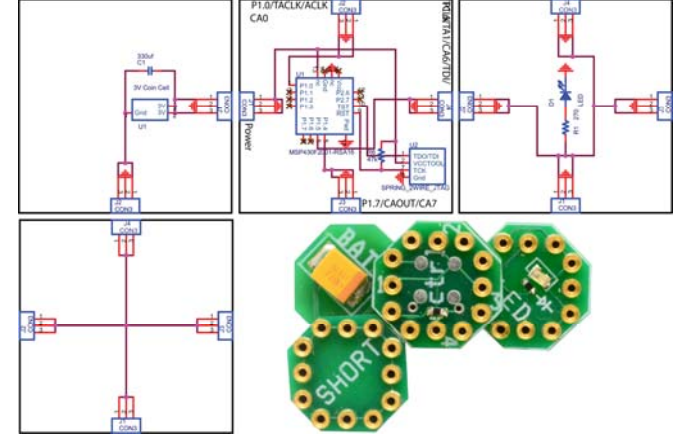


Fig. 4 A simple blinking LED circuit composed of four different block types: (clockwise from lower left) short, battery, microcontroller, LED, and physical circuit.

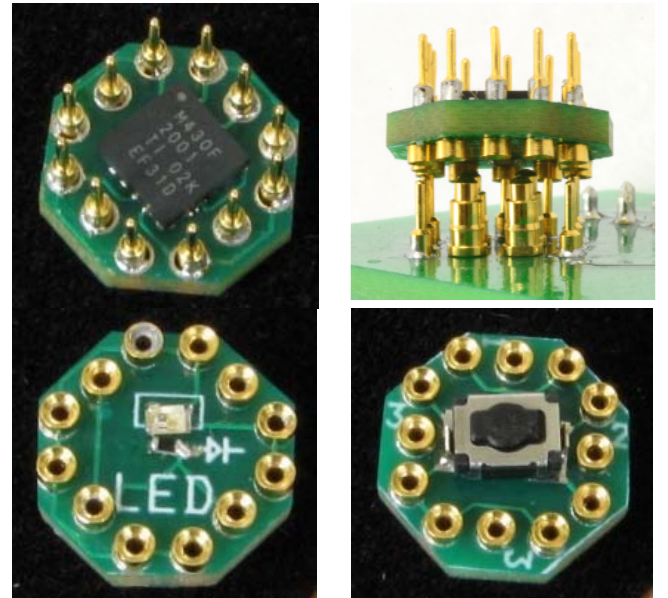


Fig. 3 Four examples of Bitblox with electrical functionality. CW from upper left: microcontroller, microcontroller attached to printhead-programmer with spring-loaded programming, momentary switch, LED. Blocks are 9mm across.

Several blocks are shown in Fig. 3, which also shows the means by which the microcontroller block is programmed. This programmability is a key feature, enabling the behavior of each microcontroller block to be uniquely determined at print-time. When the print head removes the microcontroller block from the material supply area of the printer, four spring-loaded contacts on the print head come into contact with it. These contacts provide power and control lines, allowing the block to be programmed as it is being integrated into the assembly. As illustrated in Fig. 1 and Fig. 4, the blocks interconnect utilizing stacking connectors along their edges. A circuit is designed by arranging schematic blocks, and then replicating the schematic by stacking blocks accordingly. Although the stacking connectors used normally create common nets along all layers, a special vertical isolation block can be used that breaks this connectivity, allowing different nets to exist on different vertical layers. This provides additional design flexibility by allowing circuits to be isolated by layer, much in the same way they are currently isolated on the different layers of a printed circuit board. This approach is almost certainly not the most efficient way of implementing any particular electrical netlist, but it is easier for human designers to develop circuits that are organized this way.

### C. Flexible Elements

The combination of stacking connectors and offset 2.5D tiling creates a very rigid structure, which is normally desirable. However, there must be a means to allow differential movement within the assembly, since actuated machines are part of the desired design space. We addressed this need by creating a hybrid block with rigid plastic outer rails that are connected by a soft rubber cross-bar. This block is shown in Fig. 5, which includes a rendering as well as a photograph of the actual block. We created this block with an Objet Connex500 3D printer. This printer is capable of creating parts from two different materials, and can create complex, interlinked geometries. The hard outer rails (Objet FullCure 720, Elastic Modulus = 2.8GPa,) support three electrical contacts each that are press-fit into pre-printed holes; adhesive (Cyanoacrylate) is used to secure them. The soft cross-bar (Objet Tango+, Elastic Modulus = 0.263 MPa) that connects the four outer rails is woven into the hard material, and includes fine geometry that surrounds the metal contact holes. This approach maximizes contact area between the two materials, and strengthens the assembly. Note that this block does not implement in-plane electrical connectivity. Though electrical isolation may be a benefit for some designs, it is anticipated that electrical connectivity across the flexible block will be desired. We plan to address this issue by designing a thin rigid-flex circuit board that will be laminated with the printed mechanical block before the electrical contacts are inserted. The flex portions of the circuit board will include service loops that will permit relative motion between the rigid outer rails.

### D. Actuation

Actuation at the milli- and micro-scale poses unique challenges to developers of miniaturized robots. Direct-current (DC) motors, a mainstay of academic and commercial robotics practitioners, are in most cases too large for small robotic applications. The smallest commercially available DC motors have stator diameters in the 3-6mm range, and are typically no shorter than 5mm. Though small by absolute standards, these motors are far too large for robotic devices whose maximum dimension may be just a few millimeters. The lack of commercially-available micro-actuators requires roboticists who desire to work at this scale to develop their own. Extremely small electromagnetic (Ahn et al. 1993), electrostatic (Suzuki et al. 1994), and piezoelectric (Flynn et al. 1992) micro-actuators have been developed; Fearing (Fearing 1998) and Dario (Dario et al. 1992) wrote useful reviews that include energy and power density considerations.

We considered several alternative actuation approaches for the Bitblox application, including rotary motors employing

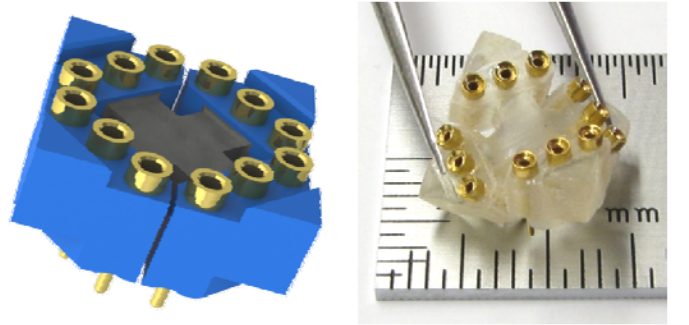


Fig. 5 Flexible block rendering (left); physical implementation showing deformation when stressed (right).

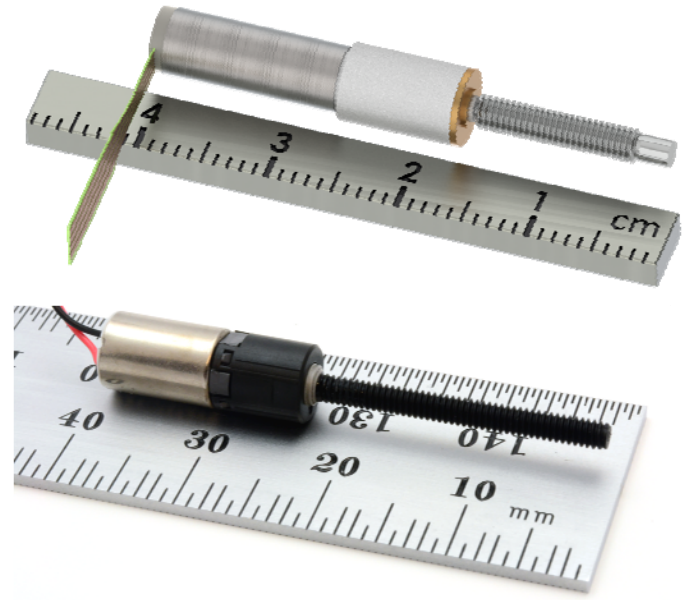


Fig. 6 Commercially available leadscrew actuator from MICROMO (above) and handmade actuator based on 6mm diameter geared hobby motor (below).

electromagnetic or piezoelectric drivers, and linear motors based on electrostatic, shape memory alloy, or thermal expansion phenomena. Each of these approaches imposes tradeoffs on the ultimate design. Although electrostatic and piezoelectric actuators have relatively high force capabilities, they exhibit low stroke, typically requiring additional mechanical transformers to increase the actuator travel. These additional components can add significant complexity to an actuator design. Electromagnetic actuators, in contrast, often exhibit longer stroke and lower force. Their coils can pose a micro-fabrication challenge, and the continuous power dissipation during blocked operation can lead to poor efficiencies. Shape memory alloy (SMA) materials offer a flexible design space, have relatively high blocked-force output and can be relatively easy to fabricate, however they typically exhibit slow dynamic response and convert a relatively small amount of electrical input energy to mechanical work output.

As developers of complex electromechanical systems, roboticists often pursue the strategy of "buy-before-build" (indeed, this is the entire motivation for the Bitblox project!), since this strategy reduces system-development time. We sought out small actuator manufacturers in the hope that an existing product could be integrated into the Bitblox form-factor. As a reminder, Bitblox use a hierarchical mechanical structure based on a minimum size of approximately one cubic centimeter; any appropriate actuator must fit into an integer multiple (a small multiple is desired!) of this volume. Unfortunately, we found few suitable commercial actuators. One product, part number 0515A006B+06A 125:1S2 from MICROMO ([www.micromo.com](http://www.micromo.com); Clearwater, Florida) is illustrated in Fig. 6. It uses a 5.5mm diameter brushless DC motor with a gearbox and leadscrew; the part costs approximately \$290 in quantity 25. Since it is brushless, the motor requires a separate synchronous motor controller. Another commercial actuator, the tiny "Squiggle Motor" (part SQL-RV-1.8), from New Scale Technologies ([www.newscaletech.com](http://www.newscaletech.com); Victor, New York) was also considered. The complexity of the external controllers and the high unit cost of these commercial actuators preclude their use in Bitblox; therefore we sought alternatives.

Faced with the requirement to build our own actuators, and unsure of the best strategy for this application, we chose to explore two different actuator options; one is based on nickel-titanium SMA (Nitinol), and the other employs a geared DC electromagnetic motor. The next sections detail the design choices for each of these actuators and describe their performance in the Bitblox application.

### *I) Actuator Design and Construction*

Although Nitinol is available in many form-factors, drawn-wire is the most widely available, and therefore is frequently used in robotics applications. Practitioners typically load the wire axially. In Nitinol applications that will require multiple cycles, which is common for most actuators, the material strain should be limited to less than 3 or 4 percent (Matthey 2004). This restriction means that if a 2mm stroke is required from an actuator made from an axially loaded Nitinol wire, the wire should be at least 50mm long! This fact often leads designers to employ pulleys or other mechanical force transformers to increase the effective actuator stroke at the expense of applied force. The small volume available in the Bitblox form-factor precludes the use of complex linkages or pulleys, so an alternative design is required. Rather than loading the wire axially, Nitinol can be formed into helical coils, and loaded along the axis of the helix (Kim et al. 2009, Koh and Cho 2012, Onal et al. 2013, Seok et al. pre-press). By varying the pitch of the helix, actuator force can be traded off for stroke, while respecting the 3-4% material strain restriction. We chose a modified version of this approach, illustrated in Fig. 7, which uses a serpentine spring shape. This shape was achieved by holding the Nitinol material with a steel fixture during the heat treating process. The Nitinol was loaded into the cold fixture, pressed into the desired shape, and then the fixture was heated in an oven (SENTRY Xpress 4.0 from Paragon Industries; Mesquite, Texas) for 25 minutes at 900 degrees Fahrenheit, followed by a water quench. Nitinol can be attached to itself and other materials in various ways, including welding, crimping and soldering. We chose to solder the serpentine actuator to the Bitblox because the available space does not permit a reliable crimp connection, and welding to the thin copper traces on the Bitblox circuit board was impractical. Nitinol develops a durable oxide layer that must be removed before the material can be soldered. This layer can be removed via mechanical abrasion or with an etchant; we chose the former. Appropriate flux and solder are also critical to a successful Nitinol solder joint. We used Indalloy Flux #2 and a Tin/Silver solder (97% Sn, 3%Ag),

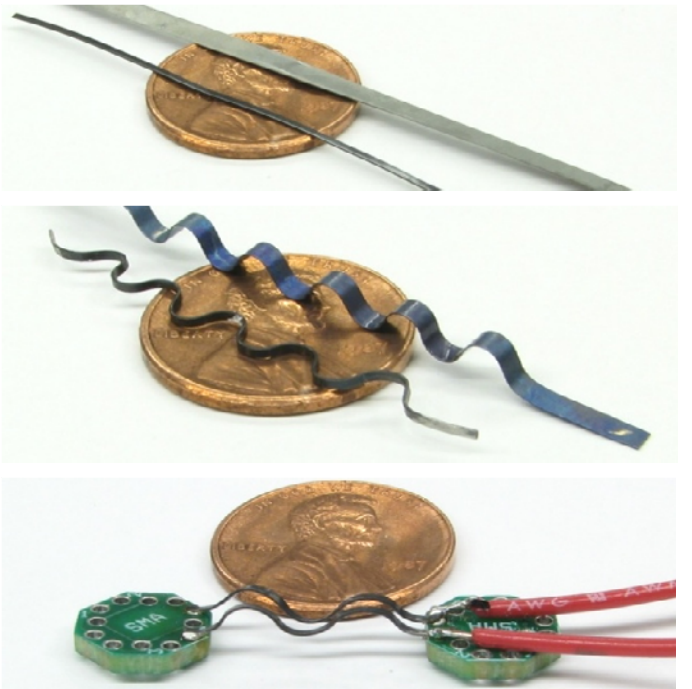


Fig. 7 Nitinol strip material before heat-treatment (top). Serpentine actuators after heat treatment (middle). Simplified SMA Bitblox actuator; connectors and plastic shroud omitted for clarity (bottom).

each from Indium Corporation (Clinton, New York). Finally, rather than using wire with a circular cross-section, we chose to use Nitinol "ribbon" material (part # SM495-FSM0100X0300SO from Nitinol Devices & Components, Inc., Fremont California), which has a rectangular cross-section (0.254 x 0.762 mm), and a transition temperature ( $A_f$ ) of 60 degrees C. Since the metal must cool in order to return to its Martensite phase before the actuator can be cycled, rapid heat transfer is desirable. The larger surface-area-to-volume ratio of a rectangular cross-section decreases the cooling time relative to a circular cross-section with an equivalent area. A rectangular cross-section also makes more effective use of the Nitinol material by applying a more uniform strain profile across the thickness of the material as it is stressed.

Though we were able to build a suitable Nitinol-based actuator, the design left some requirements unfulfilled, as discussed in the Testing and Performance section. We therefore attempted to build a low-cost leadscrew actuator that would be easy to integrate into the Bitblox form factor. Though many very small geared DC motors are commercially available, the vast majority use precision metal parts which push the unit cost above an acceptable level. Fortunately several vendors now sell small (6mm diameter) DC motors attached to plastic planetary gearboxes (part # GM15, \$14 from Solarbotics.com). We added a leadscrew to this motor by machining and tapping the output spindle to accept a 4-40 threaded plastic rod. Several of the fabrication steps are shown in Fig. 8. Once the rod was glued in place, the reassembled motor and gearbox were placed into a 3D-printed plastic shell (fabricated with an Objet Connex 500 printer, using Durus material). Half of the shell is attached to the motor/gearbox body, while the other half is connected to a plastic nut that rides on the threaded shaft. When the shaft rotates, the two plastic halves slide relative to each other.

## 2) Actuator Testing and Performance

Each side of the Nitinol actuator shown in Fig. 7 was clamped in the parallel jaws of the Bose ElectroForce LM1 testing machine and eight different tensile loads, ranging from 0.25 to 3.5 Newtons were applied, forcing the two halves apart. When cold, the Nitinol yielded, allowing the two halves to separate until an equilibrium point based on the effective spring constant was reached. When heated above the transformation temperature (in this case 60 degrees Celsius) the material switched from the softer martensite to the stiffer austenite phase, and the spring contracted forcefully to a new equilibrium position. The upper plot in Fig. 10 depicts the results of these tests. We used a resistive heating approach to raise the material temperature above the transformation temperature during each cycle; each transition from cold to hot and from hot to cold required approximately 9 seconds for the initial response and 22 seconds for a complete phase transformation. Although in principle we could have monitored the actuator temperature with a thermocouple during mechanical testing, we chose instead to characterize the device temperature as a function of supply current ahead of time, since it would be impractical for every Bitblox actuator to integrate a temperature-controlled current feedback driving circuit. The unloaded actuator temperature was measured with a thermocouple (part # 5SC-TT-(K)-30-(36) from OMEGA Engineering Inc.; Stamford, Connecticut), while a power supply (part # E3631A from Agilent Technologies; Santa Clara California) applied a constant current. The applied voltage was also measured, and the results are plotted in Fig. 10. These measurements were taken at room temperature (23 degrees C), the actuators were surrounded by still air, and the system was allowed to reach equilibrium before each data point was recorded. This actuator has a measured overall resistance of 0.3 Ohms. The dimensions of the actuator allow a material resistivity of 1.2 e-6 Ohm-meters to be estimated. Although our measurements predict that an activation current of approximately 1.2 Amps should be sufficient to raise the material above its transformation temperature, we used a higher current (1.75 amps) during mechanical

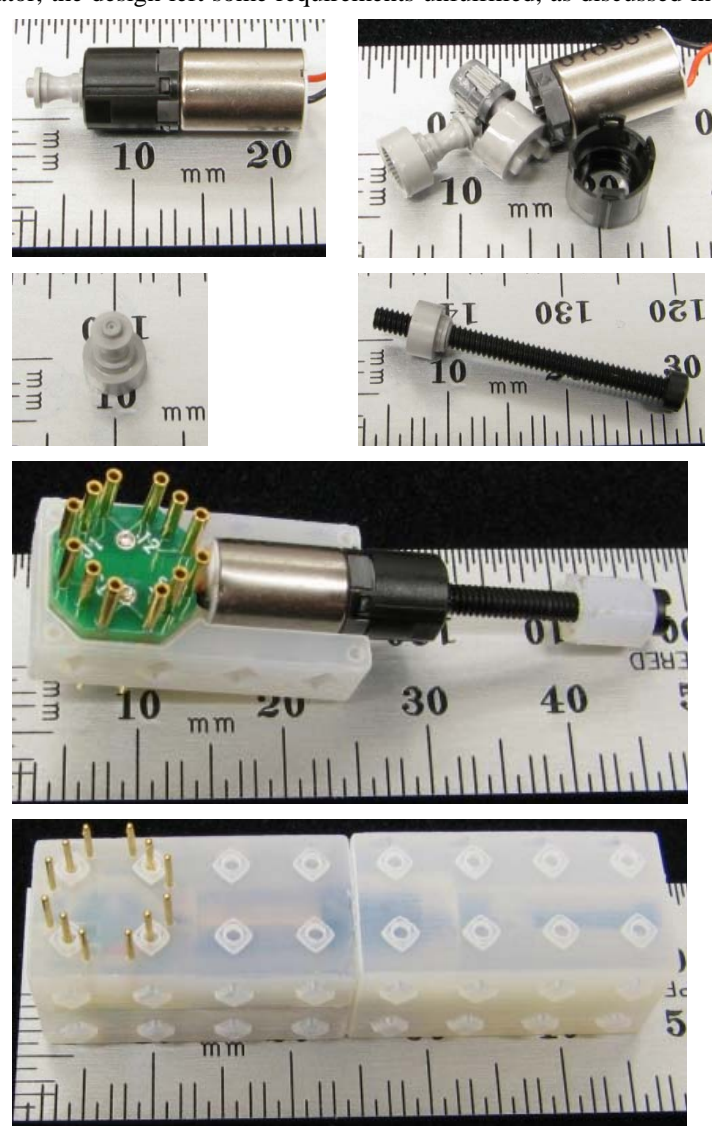


Fig. 8 Leadscrew actuator fabrication. From top left: a commercially available 25:1 gear reduction DC motor; the disassembled gearbox; the output spindle removed; output spindle after drilling and tapping to accept a threaded rod; partially assembled Bitblox actuator; fully assembled Bitblox actuator.

of time, since it would be impractical for every Bitblox actuator to integrate a temperature-controlled current feedback driving circuit. The unloaded actuator temperature was measured with a thermocouple (part # 5SC-TT-(K)-30-(36) from OMEGA Engineering Inc.; Stamford, Connecticut), while a power supply (part # E3631A from Agilent Technologies; Santa Clara California) applied a constant current. The applied voltage was also measured, and the results are plotted in Fig. 10. These measurements were taken at room temperature (23 degrees C), the actuators were surrounded by still air, and the system was allowed to reach equilibrium before each data point was recorded. This actuator has a measured overall resistance of 0.3 Ohms. The dimensions of the actuator allow a material resistivity of 1.2 e-6 Ohm-meters to be estimated. Although our measurements predict that an activation current of approximately 1.2 Amps should be sufficient to raise the material above its transformation temperature, we used a higher current (1.75 amps) during mechanical

testing because it warmed the Nitinol more rapidly, and assured that all parts of the actuator, including those portions closest to the circuit board material which acted as a thermal sink, completed the phase transformation.

We tested the leadscrew actuators by loading them with known masses suspended from the actuated end; the parts were held vertically so that a tensile load was applied axially along the leadscrew. The DC motor was connected to a current-controlled power supply (Keithley SourceMeter 2400) that applied constant current for a fixed amount of time. The starting and ending actuator positions were measured, which allowed an estimate of the average speed to be computed. The actuators have a typical stroke of 8.3mm, with some variation due to assembly differences, and we attempted to use as much of the stroke as possible in

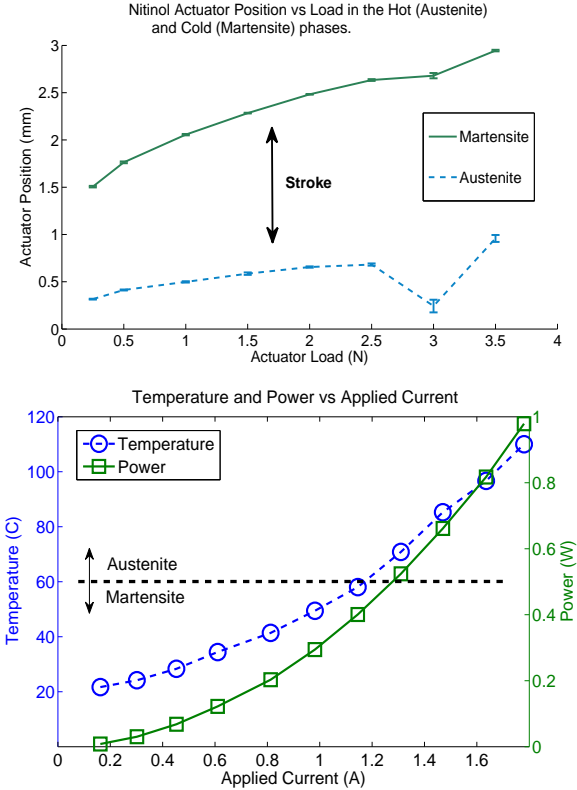


Fig. 10 Plots of force vs displacement in the martensite (detwinned) and austenite phases (top); temperature and power vs current (bottom), for the Nitinol actuator; transition temperature indicated by dashed horizontal line.

each trial. The results for six different loads are shown in Fig. 9. As is evident from Fig. 10 and Fig. 9, both actuators are capable of applying similar amounts of force, although the DC motor-driven leadscrew requires significantly less current. Additionally, the combined gear reduction ratio of the gearbox and leadscrew thread pitch allows the leadscrew actuator to maintain its current position with no power consumption, a significant advantage.

Although not illustrated in the figures, the cycle speed of the leadscrew is also faster than that of the Nitinol version, which is limited by the heat transfer rate into its ambient environment. Though Fig. 9 only shows test results for tensile loads, the DC leadscrew is also capable of applying compressive loads (pushing itself apart), which is not possible with the Nitinol actuator. For these reasons, despite the fact that the Nitinol actuator is relatively easy to construct and enables a somewhat more compact actuator design, we chose to standardize future actuator designs around the DC leadscrew.

#### IV. DESIGNING WITH BITBLOX

Bitblox are envisioned as a general purpose electromechanical design and construction toolkit. Though still early in their development, we attempt to demonstrate the utility of building with digital materials in general, and Bitblox in particular, by using two examples. The first is an electrical-only example, while the second is mechanical only. We have used these separate examples to compare Bitblox against these two traditionally distinct areas of design. However, we would like to reiterate that Bitblox are intended as a general purpose *electromechanical* material, and are designed to merge the electrical and mechanical design-synthesis and fabrication workflows.

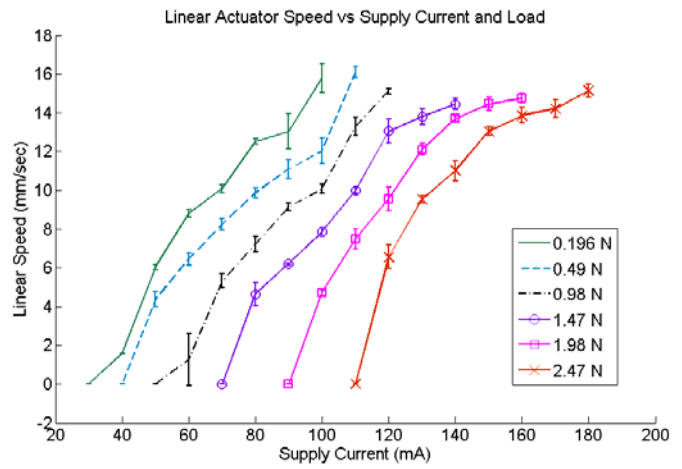


Fig. 9 Bitblox leadscrew actuator Speed vs Force vs Current.

### A. Electrical Systems

The electronics prototyping and design process typically follows the following workflow. First, a problem is identified and specific design goals are set. Next a circuit that meets these criteria is imagined and perhaps sketched out on a piece of paper by hand. The designer then uses schematic-capture software to create the graphical representation of each of the electronic components, and creates their conceptual electrical interconnections, known as the netlist. If device models are available, they can be used with the netlist to simulate the circuit behavior; the most common circuit simulation tool is SPICE or some variant. In the next step the netlist, along with a database that describes all of the mechanical dimensions of the various components is used by the designer to layout the actual copper traces on a circuit board. The resulting CAD files are then sent to a printed circuit board (PCB) manufacturer which ultimately ships a blank PCB back to the designer, who then solders individual components onto the board. Finally, the prototype circuit is available for testing. Each step in this process typically involves a manufacturing lead-time and the workflow requires multiple dimensions of design and fabrication expertise. When a simple circuit needs to physically prototyped the fabrication steps are sometimes omitted; instead a breadboard and short lengths of wire provide reusable interconnects. The advent of low-cost CNC routers that selectively remove copper cladding from circuit-boards has also made producing simple boards in-house a popular option.

Designing and constructing a circuit with Bitblox is akin to assembling a set of children's building blocks. A reasonable inventory of different Bitblox types allows the creation of diverse circuits, and these parts can be recycled for use in other circuits when the prototype is no longer needed. We are developing automated design tools that ease the design of circuits with Bitblox. For example, automated layout software will convert a netlist into a physical plan that describes the location and orientation of each Bitblox part in the design. We have already demonstrated tools that convert the physical plan into toolpath trajectories in order to automate the assembly of complete Bitblox-based designs, as described in the "Printing Designs with Bitblox" section. Previous work (Koza et al. 2005) has demonstrated the use of genetic algorithms in automatically designing passive and active circuits that satisfy a set of pre-established goals. We plan to extend this effort to include evolvable state machines, which map directly onto the programmable microcontroller blocks.

The Bitblox assembly depicted in Fig. 11 implements a 6-channel infra-red remote control that conforms to the standard used by many consumer electronic devices. It has buttons for play, stop, fast-forward, rewind, increase volume and decrease volume. This assembly uses 7 different types of Bitblox, and approximately 130 blocks in total. It required approximately two hours to design and assemble by hand.

### B. Electromechanical Systems

Mechanical system designers utilize a workflow that is separate from but analogous to that used by electrical system designers. Once an objective and a set of specifications that satisfy the objective are defined, the engineer utilizes CAD software to create the specific geometry that satisfies the specification. Next, the design is verified by testing it in a mechanical simulator; any errors are corrected by the designer in an iterative process. Once the design satisfies the specification, a file that describes the mechanical geometry in a standardized format is exported; this file allows a design prototype to be fabricated via traditional methods (e.g.: injection molding, CNC mill), or via newer additive fabrication techniques (e.g.: SLS, FDM). If necessary, mechanical testing is performed to verify that the actual performance matches the prediction produced in simulation.

When using the Bitblox framework, a mechanical designer would follow the initial goal and specification steps by either choosing materials from an existing library and manually determining their positions in an assembly or by using design automation tools to automatically synthesize a design solution. An integrated simulation environment, currently implemented in the open-source VoxCad (Hiller and Lipson 2012b) tool, allows interactive development so a human designer can offer refinements as the design takes shape. The materials in the library need not have been created by the designer; because they use

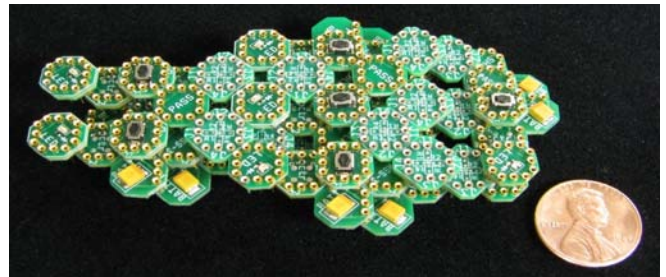


Fig. 11 A five channel (Play/Pause, Stop, Skip Forward, Skip Back, Volume+, Volume-) infrared remote control. This design uses approximately 130 blocks, and relies on seven different block types.

dimensions of design and fabrication expertise. When a simple circuit needs to physically prototyped the fabrication steps are sometimes omitted; instead a breadboard and short lengths of wire provide reusable interconnects. The advent of low-cost CNC routers that selectively remove copper cladding from circuit-boards has also made producing simple boards in-house a popular option.

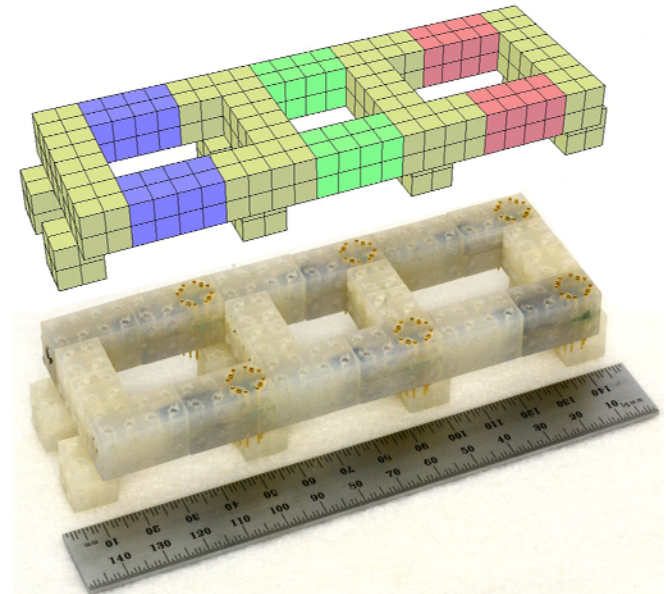


Fig. 12 Simulated (top) and physical (bottom) inchworm robots based on Bitblox. 6DOF robot uses 6 linear actuators to extend each 1/3rd of its body in turn. See the supporting video for a comparison between gaits.

standardized electromechanical interfaces, Bitblox materials designed by one person can be seamlessly used by another. Though the regular lattice structure and fixed electromechanical interfaces used by digital materials restrict the design space, relative to a continuous material, this reduction in design space facilitates design automation. Previous work (Hiller and Lipson 2012a), (Cheney et al. 2013) has shown that complex mechanical designs, which use multiple materials and satisfy specific objectives can be automatically synthesized. When the design is complete, automated assembly tools create the physical part, as described in following sections.

The simple robot shown in Fig. 12 illustrates a proof-of-concept for electromechanical design with Bitblox. This robot uses six of the leadscrew actuators described previously, and sixteen passive blocks. The six actuators are arranged in pairs, with each pair connecting a body segment. In the figure, each of the three actuator pairs is indicated by a different color (red, green, blue). The robot locomotes by moving each section of its body in turn, while the remaining three segments are stationary (see Extension 1). Differential movements between the parallel actuators cause the robot to turn.

## V. PRINTING DESIGNS WITH BITBLOX

One appealing aspect of designing with digital materials is the ability to rapidly create a physical instantiation of a design by “printing” it (depositing the physical materials). We have demonstrated an implementation of this idea using Bitblox and a modified personal 3D printer. Though our implementation is unique, the printer described is not the first machine capable of printing digital materials. Hiller et al designed two machines capable of printing small spherical materials. Their first implementation (Hiller and Lipson 2007) used a parallel print head that could place a 2-D array of spheres simultaneously. Their second implementation (unpublished, personal communication) used several serial print heads that could deposit multiple materials within the same design. Ward (Ward 2010) and Popescu (Popescu 2007) developed printers that could assemble planar materials (GIKs) into 3-dimensional structures. None of these printers or the materials that they use are capable of producing electromechanical devices. The following section describes the Bitblox printer’s development, capabilities and current limitations.

### A. Serial pick-and-place Bitblox assembler based on a personal 3D printer

The Bitblox printer consists of four principle components: the 3-axis stage, the toolhead, the material feed reels, and the path-planning software. Bitblox are designed with an easy-to-assemble 2.5-D connectivity that allows individual blocks to be inserted vertically into a layer with other blocks; as additional blocks are deposited on successive layers the overall assembly takes shape. This straightforward connectivity allows a simple 3-axis machine to position and deposit the different blocks of material. Several personal 3D printers are currently available that use a 3-axis stage as their primary positioning platform; while we chose to use a Fab@Home printer as the basis for the Bitblox printer described, the approach could be adapted to most other personal 3D printers. We modified the Fab@Home design by adding two additional leadscrews to the front of the build tray, which enables the printer to apply sufficient mating forces without any mechanical distortion. We also modified the build tray by laser-cutting an array of holes that match the bottom-side pins on the Bitblox materials. This allows the first layer of each assembly to be unambiguously fixed in the printer’s coordinate system.

The printer’s tool head must be capable of removing a material block from the supply (the feed reels), rotating the block, and then depositing the block into the assembly. While roughly uniform in exterior dimensions, the only true mechanical regularity among materials is the number and position of the pins that connect them. Therefore, the toolhead uses a pin-and-socket design that exploits the un-mating force of the connectors to hold individual material blocks. As the 3-axis tray brings the toolhead into contact with a material block, pins in the toolhead are inserted into the sockets in the material; the unmating force of the connection temporarily bonds the material to the toolhead, allowing it to be manipulated. A rotational degree of freedom in the toolhead allows the material block to be rotated to 0, 90, 180 or 270 degrees relative to the rest of the assembly; for certain materials rotation has an impact on function. Once the material in the toolhead has been placed in its desired location, extractor pins within the toolhead are used to release the connection between the toolhead and the material as the toolhead is pulled away from the assembly.

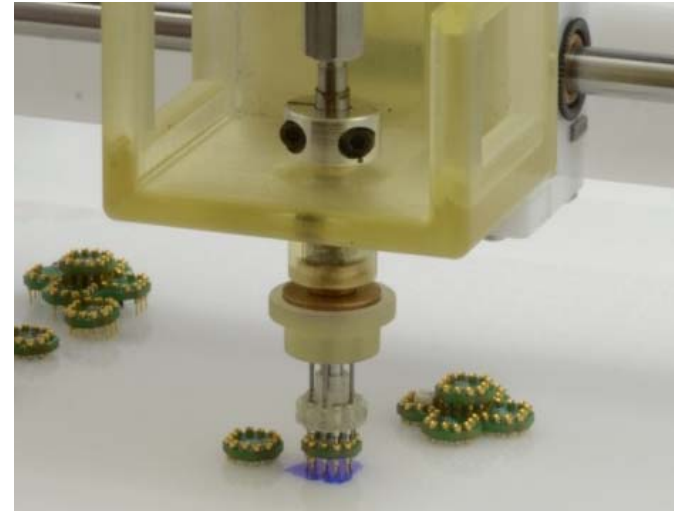


Fig. 13 The Bitblox printer’s toolhead, which uses pin-in-socket connections to manipulate the material blocks.

Much like the ink reservoirs in an inkjet printer, the Bitblox printer requires a reservoir of different material blocks. This is accomplished through the use of a tape-reel approach, in which the materials are pre-loaded into long plastic strips that are rolled up. Each reel contains the same material type; the printer can currently accommodate six different reels of material. The plastic in the reel is formed to retain each individual material in an unambiguous position so the toolhead can remove it. After each material block is removed from the reel, a motor indexes the reel forward so the next material block in the reel is available to the toolhead.

Whether a model is designed manually via VoxCad or automatically with design automation tools, the model descriptor file must be converted into a sequence of moves that describe each material block placement. This conversion algorithm has been implemented with a MATLAB script that accepts a model descriptor file as input and outputs a G-code file. This file is interpreted by the printer's control electronics and describes the complete sequence of motions required to construct the assembly. An example part created by the Bitblox printer is shown in Fig. 14 (see Extension 2). This Bitblox assembly consists of 17 material blocks in total, with 7 different material types. It implements the play and stop functions of a two channel infra-red remote control.

### B. Bitblox assembler scaling

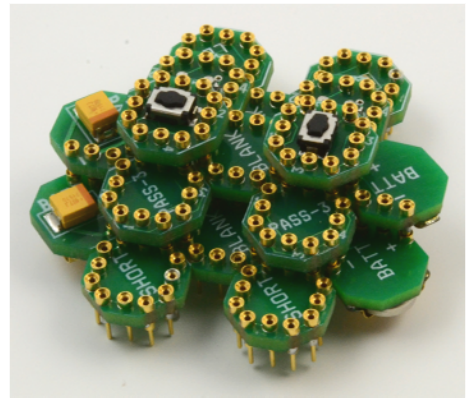
The assembly process we have demonstrated is serial, and therefore the time required to place each individual block is the dominant factor in determining the overall build time. Our current printer requires approximately 10 seconds (depending on the trajectory that the build head follows) to place each block. Through careful tuning of the existing system, this time could potentially be reduced to 2 seconds, allowing assemblies with 1000 blocks to be built in less than 60 minutes. While this may be acceptable for many applications (personal 3D printers can require several hours to produce a design), this printer clearly does not scale to assemblies with more than a few thousand blocks. Faster serial print heads, or several serial print heads used in parallel, as is common in commercial circuit assembly machines, might allow a serial method to produce assemblies with tens of thousands of blocks in a few hours. The Cobra pick-and-place machine (Essemtec USA, Glassboro, NJ) and parallel-linkage manipulators from Bastian Robotics (St. Louis, MO) and (Nabat et al. 2005) are all capable of 2 to 10 placements per second. As the size of available digital materials decreases, assemblies with millions of blocks may become desirable. Parallel assembly processes might provide a means to work at this scale. Building on a previous example (Hiller and Lipson 2007), we have recently demonstrated (Perich et al. n.d.) a print head that can move an entire layer of blocks simultaneously. If each layer contained 1000 rows and 1000 columns of blocks, and it took 30 seconds to place each layer, assemblies with billions of blocks could be fabricated in less than a day.

## VI. CAVEATS, LIMITATIONS AND OPPORTUNITIES

The principles of additive manufacturing listed earlier illustrate the promise of building with digital materials, and thus far we have highlighted the features and benefits of Bitblox. Here, we discuss several limitations of our present implementation, offer potential solutions, and comment on future implementations and applications.

### A. Discrete material size & spacing

The first, perhaps most apparent restriction is the imposition of a regular, lattice-like material arrangement on the designer, which determines the minimum spatial resolution of any particular material. We readily admit that the present Bitblox size, ranging from 370 cubic mm to 5.3 cubic cm, is too large for everyday use but there are a few immediate applications for the current design (electronics prototyping, research into self-designing machines and digital materials). We are concurrently developing smaller 3 cubic mm building blocks, and straightforward methods (Hiller et al. 2011) exist to further scale-down the size of the materials; blocks with similar functionality to those discussed could plausibly occupy 25 cubic micrometers. If actuation is not required, conventional semiconductor fabrication methods could produce even smaller blocks with discrete mixed-signal functionality. A great deal of research effort is currently being expended on producing 3-dimensional circuits using extensions of conventional lithographic methods, but the digital materials framework points toward an obvious alternative: produce simple, verified, high-yield silicon circuits and allow them to interconnect with a regular mechanical interface via soldered or fused junctions. This approach allows circuits with differing process geometries and chemistry to be integrated using many of the same technologies employed by existing packaging methods. Though the overall assembled density of this approach is never likely to surpass conventional integrated circuit fabrication methods, the improvements in yield, reductions in lead time, and increased process compatibility could favor this approach.



Conventional printed circuit board fabrication techniques are well suited to high-volume, low cost applications, but can be inconvenient for low volume uses, including prototyping. Additionally, the dominant form-factor for this method is planar, with circuit components attached to the top and bottom side of a rigid circuit board. Modern cell phone circuits often use several different rigid and flexible circuit boards with intricate, laborious assembly steps in order to pack the desired functionality into the available volume. We envision that future versions of digital material, at appropriate scales, could allow designers greater flexibility in fitting their desired circuits within a certain build envelope. This would be particularly advantageous for low volumes or designs with short lead times; as the consumer electronics industry embraces ever-shortening product cycles, this capability could become particularly desirable. Hybrid approaches might also leverage the best of conventional circuit fabrication techniques and digital materials: a digital materials-based circuit implementing some new desired functionality could be printed and mated with a conventional circuit board supporting legacy functionality via a docking interface.

#### B. Restricted material choices and design space

The vast array of materials available to designers using conventional processes, and the rapidly expanding variety available via analog additive manufacturing, cannot be matched by current digital materials. The choice of allocating a small number of digital material types *a priori* seems to guarantee a reduction in material selection choices, although this can be partially addressed by mixing different digital materials together to produce composite structures. Nevertheless, tradeoffs in aggregate material strength may be inevitable, depending on the bonding methods used during assembly. Though we have advertised it as a useful feature, the strict enforcement of lattice-like interconnections also poses significant design challenges. This concern can be partially addressed by reducing the block size, so that the discrete placement locations become small relative to the intended application, but other issues persist. For example, it is difficult to envision robust actuated continuous-rotation joints that adhere to this framework. Passive rotary joints with one, two or three degrees of freedom might become possible when small block sizes make assemblies with large numbers of blocks practical. A ball and socket geometry would be straightforward for example, although an appropriate material would need to be placed between the two halves of the joint.

#### C. Assembly complexity

Existing analog additive manufacturing techniques scan lasers or print heads across a surface in a fast but essentially linear process. The only parallel process that we are aware of uses DLP projectors to expose photosensitive resin to UV light, producing all the features in a layer simultaneously. The parallel assembly process that we envision for digital materials is more complex than these methods and multiple issues need to be resolved before it can be put into practice. These issues include: fabricating a build head that can selectively pick up one million blocks simultaneously; sorting and aligning entire layers of blocks before the build head picks them up; fusing a layer of blocks after (or during) the placement cycle.

#### D. Increased design complexity and cost

Finally, designing with a digital material imposes additional complexity and cost. The infra-red remote example provided earlier illustrates this point. The remote uses more than 130 blocks, each of which must be assembled ahead of time, and which use 12 connector pins apiece. The material cost of the remote is higher than producing a standalone printed circuit board. Also, the limited number and type of blocks available require additional design steps (and blocks) in order to route signals as desired. For example, the restricted variety of resistor and capacitor blocks requires summing blocks in parallel or series in order to achieve a particular desired composite component value. Some of these challenges can be addressed by software, and this motivates our design automation efforts. Applications involving prototyping or where short lead times exist may justify the use of this process, despite the issues just raised. It seems plausible that the prices of individual blocks of digital material will plummet when their sizes are reduced and when they are mass-produced.

## VII. SUMMARY AND FUTURE WORK

In this work we described the development of a new prototyping and manufacturing ecosystem based on the principles of digital materials and digital manufacturing. We described the limitations of using previous work as a digital material, which motivated the development of a prototype digital material (Bitblox) that implements very simple functionality, employs a regular tiling strategy and uses standardized electromechanical interfaces. These standard interfaces make automated design and construction tractable, and we demonstrated a machine capable of automatically producing complete working electronic assemblies. Work continues on the actuation materials and the printer; we plan to extend the printer to accommodate larger, hierarchical material blocks like the current leadscrew actuator and a battery block. An electrical simulator that can accommodate analog and simple digital circuits is being integrated into the VoxCAD environment that will allow complete electromechanical assemblies to be automatically designed. Experimental studies of design reachability, as a function of voxel electrical connectivity are under way. Finally, to motivate the use of this approach in more complex devices with increased dimensional resolution, much smaller material blocks are being developed.

### VIII. ACKNOWLEDGEMENTS

This work utilized the VoxCAD mechanical simulation environment (<http://www.voxcad.com/>) and we thank its developer, Jon Hiller. Garry Brock helped in measuring the Bitblox connector mating and un-mating force. This work has been supported by the DARPA - Maximum Mobility and Manipulation (M3) Project; Number W911NF-11-1-0093 and by a National Science Foundation Graduate Research Fellowship awarded to R. MacCurdy under Grant No. (DGE-0707428)

### IX. APPENDIX A: INDEX TO MULTIMEDIA EXTENSIONS

Extension	Type	Description
1	Video	Simulated and real 6 degree of freedom “inchworm” robot built with Bitblox.
2	Video	Bitblox assembler producing a 2 channel infra-red television remote control from 13 individual blocks.

### REFERENCES

- Ahn, C., Kim, Y. and Allen, M. (1993). A planar variable reluctance magnetic micromotor with fully integrated stator and coils. *Microelectromechanical Systems, Journal of* **2**(4), 165–173.
- B-Squares (2013). <http://www.b-squares.com/>
- Bug Labs (2013). <http://www.buglabs.net>
- Bulthaup, C. A., Wilhelm, E. J., Hubert, B. N., Ridley, B. A. and Jacobson, J. M. (2001). All-additive fabrication of inorganic logic elements by liquid embossing. *Applied Physics Letters* **79**(10), 1525–1527.
- Cheney, N., MacCurdy, R., Clune, J. and Lipson, H. (2013). Unshackling evolution: Evolving soft robots with multiple materials and a powerful generative encoding. *in ‘Proceedings of the conference on genetic and evolutionary computation (GECCO), 2013’*.
- Cheung, K. C. and Gershenfeld, N. (2013). Reversibly assembled cellular composite materials. *Science* **341**(6151), 1219–1221.
- Cheung, K. C.-W. (2012). Digital cellular solids: reconfigurable composite materials. PhD thesis. Massachusetts Institute of Technology.
- Cohen, D., Lipton, J., Bonassar, L. and Lipson, H. (2010). Additive manufacturing for in situ repair of osteochondral defects. *Biofabrication* **2**(3), 035004. <http://iopscience.iop.org/1758-5090/2/3/035004>
- Cubelets from Modular Robotics (2013). <http://www.modrobotics.com/>
- Dario, P., Valleggi, R., Carrozza, M. C., Montesi, M. C. and Cocco, M. (1992). Microactuators for microrobots: a critical survey. *Journal of Micromechanics and Microengineering* **2**(3), 141. <http://stacks.iop.org/0960-1317/2/i=3/a=005>
- E-Blocks rapid electronic development kits (2013). <http://www.matrixmultimedia.com/eblocks.php>
- El Gamal, A., Greene, J., Reyneri, J., Rogoyski, E., El-Ayat, K. A. and Mohsen, A. (1989). An architecture for electrically configurable gate arrays. *Solid-State Circuits, IEEE Journal of* **24**(2), 394–398.
- Fearing, R. (1998). Powering 3 dimensional microrobots: power density limitations. *in ‘ICRA ’98’*. Vol. 98. nice overview of electrostatic, rotary, piezoelectric, and magnetic actuators for microrobotics.
- Flynn, A., Tavrow, L., Bart, S., Brooks, R., Ehrlich, D., Udayakumar, K. and Cross, L. (1992). Piezoelectric micromotors for microrobots. *Microelectromechanical Systems, Journal of* **1**(1), 44–51.
- Gershenfeld, N. (2005). Bits and atoms. *in ‘IS&T’s NIP 21:International Conference on Digital Printing Technologies,Baltimore, MD’*. p. 2.
- Gershenfeld, N. (2012). How to make almost anything: The digital fabrication revolution. *Foreign Affairs* **91**, 58.
- Gilpin, K., Knaian, A. and Rus, D. (2010). Robot pebbles: One centimeter modules for programmable matter through self-disassembly. *in ‘Robotics and Automation (ICRA), 2010 IEEE International Conference on’*. IEEE. pp. 2485–2492. [http://ieeexplore.ieee.org/xpls/abs\\_all.jsp?arnumber=5509817](http://ieeexplore.ieee.org/xpls/abs_all.jsp?arnumber=5509817)
- Gilpin, K., Kotay, K., Rus, D. and Vasilescu, I. (2008). Miche: Modular shape formation by self-disassembly. *The International Journal of Robotics Research* **27**(3-4), 345–372. <http://ijr.sagepub.com/content/27/3-4/345.short>
- Gilpin, K. and Rus, D. (2010). Modular robot systems. *Robotics & Automation Magazine, IEEE* **17**(3), 38–55. [http://ieeexplore.ieee.org/xpls/abs\\_all.jsp?arnumber=5569030](http://ieeexplore.ieee.org/xpls/abs_all.jsp?arnumber=5569030)
- Gracias, D., Tien, J., Breen, T., Hsu, C. and Whitesides, G. (2000). Forming electrical networks in three dimensions by self-assembly. *Science* **289**(5482), 1170–1172. <http://www.sciencemag.org/content/289/5482/1170.short>
- Griffith, S., Goldwater, D. and Jacobson, J. M. (2005). Self-replication from random parts. *Nature* **437**(7059), 636.
- Grimm, T. (2012). 3d printing merged with printed electronics. <http://www.engineering.com/3DPrinting/3DPrintingArticles/ArticleID/4327/3D-Printing-Merged-with-Printed-Electronics.aspx>
- Hiller, J. and Lipson, H. (2007). Methods of parallel voxel manipulation for 3d digital printing. *in ‘Proceedings of the 18th solid freeform fabrication symposium’*. Vol. 200. p. 211.
- Hiller, J. and Lipson, H. (2009). Design and analysis of digital materials for physical 3d voxel printing. *Rapid Prototyping Journal* **15**(2), 137–149. <http://www.emeraldinsight.com/journals.htm?articleid=1779140&show=abstract>

- Hiller, J. and Lipson, H. (2012a). Automatic design and manufacture of soft robots. *Robotics, IEEE Transactions on* **28**(2), 457–466. [http://ieeexplore.ieee.org/xpls/abs\\_all.jsp?arnumber=6096440](http://ieeexplore.ieee.org/xpls/abs_all.jsp?arnumber=6096440)
- Hiller, J. and Lipson, H. (2012b). Dynamic simulation of soft heterogeneous objects. *arXiv preprint arXiv:1212.2845*.
- Hiller, J., Miller, J. and Lipson, H. (2011). Microbricks for three-dimensional reconfigurable modular microsystems. *Microelectromechanical Systems, Journal of* **20**(5), 1089–1097. [http://ieeexplore.ieee.org/xpls/abs\\_all.jsp?arnumber=5999678](http://ieeexplore.ieee.org/xpls/abs_all.jsp?arnumber=5999678)
- Introducing Illuminato X Machina* (2013). <http://www.illuminatolabs.com>
- Jones, C., Lu, X., Renn, M., Stroder, M. and Shih, W. (2010). Aerosol-jet-printed, high-speed, flexible thin-film transistor made using single-walled carbon nanotube solution. *Microelectronic Engineering* **87**(3), 434–437. <http://www.sciencedirect.com/science/article/pii/S0167931709004560>
- Jorgensen, M. W., Ostergaard, E. H. and Lund, H. H. (2004). Modular atron: Modules for a self-reconfigurable robot. In ‘Intelligent Robots and Systems, 2004.(IROS 2004). Proceedings. 2004 IEEE/RSJ International Conference on’. Vol. 2. IEEE. pp. 2068–2073.
- Ke, Y., Ong, L. L., Shih, W. M. and Yin, P. (2012). Three-dimensional structures self-assembled from dna bricks. *Science* **338**(6111), 1177–1183.
- Kernbach, S., Meister, E., Schlachter, F., Jebens, K., Szymanski, M., Liedke, J., Laneri, D., Winkler, L., Schmickl, T., Thenius, R. et al. (2008). Symbiotic robot organisms: Replicator and symbiont projects. In ‘Proceedings of the 8th Workshop on Performance Metrics for Intelligent Systems’. ACM. pp. 62–69.
- Kim, S., Hawkes, E., Choy, K., Joldaz, M., Foley, J. and Wood, R. (2009). Micro artificial muscle fiber using niti spring for soft robotics. In ‘Intelligent Robots and Systems, 2009. IROS 2009. IEEE/RSJ International Conference on’. IEEE. pp. 2228–2234. [http://ieeexplore.ieee.org/xpls/abs\\_all.jsp?arnumber=5354178](http://ieeexplore.ieee.org/xpls/abs_all.jsp?arnumber=5354178)
- Koh, J.-S. and Cho, K.-J. (2012). Omega-shaped inchworm-inspired crawling robot with large-index-and-pitch (lip) sma spring actuators. *Mechatronics, IEEE/ASME Transactions on* **18**, 419 – 429. [http://ieeexplore.ieee.org/xpls/abs\\_all.jsp?arnumber=6269102](http://ieeexplore.ieee.org/xpls/abs_all.jsp?arnumber=6269102)
- Koza, J. R., Keane, M. A., Streeter, M. J., Mydlowec, W., Yu, J. and Lanza, G. (2005). *Genetic programming IV: Routine human-competitive machine intelligence*. Springer.
- Kuon, I., Tessier, R. and Rose, J. (2008). Fpga architecture: Survey and challenges. *Foundations and Trends in Electronic Design Automation* **2**(2), 135–253. <http://dl.acm.org/citation.cfm?id=1454696>
- LEGO Mindstorm* (2013). <http://www.lego.com/>
- Lipson, H. and Kurman, M. (2013). *Fabricated: The New World of 3D Printing*. John Wiley & Sons.
- Lipson, H. and Pollack, J. (2000). Automatic design and manufacture of robotic life forms. *Nature* **406**, 974–978.
- Lipton, J., MacCurdy, R., Boban, M., Chartrain, N., Withers III, L., Gangjee, N., Nagai, A., Cohen, J., Liu, K. S. J., Qudsi, H., Kaufman, J. and Lipson, H. (2012). Fab@ home model 3: a more robust, cost effective and accessible open hardware fabrication platform. In ‘Proceedings of the Twenty Third Annual International Solid Freeform Fabrication Symposium – An Additive Manufacturing Conference, August 6-8, 2012, Austin, Texas, USA.’.
- Maiwald, M., Werner, C., Zoellmer, V. and Busse, M. (2009). Inktelligent printed strain gauges. *Procedia Chemistry* **1**(1), 907–910. <http://www.sciencedirect.com/science/article/pii/S1876619609002277>
- Makerbot* (2013). <http://www.makerbot.com/>
- Matthey, J. (2004). *Using Nitinol Alloys- Johnson Matthey Engineering Reference*. revision edn. Johnson Matthey. San Jose, California, USA.
- Mironov, V., Boland, T., Trusk, T., Forgacs, G. and Markwald, R. (2003). Organ printing: computer-aided jet-based 3d tissue engineering. *TRENDS in Biotechnology* **21**(4), 157–161. <http://www.sciencedirect.com/science/article/pii/S0167779903000337>
- Nabat, V., de la O RODRIGUEZ, M., Krut, S., Pierrot, F. et al. (2005). Par4: very high speed parallel robot for pick-and-place. In ‘Intelligent Robots and Systems, 2005.(IROS 2005). 2005 IEEE/RSJ International Conference on’. IEEE. pp. 553–558.
- Neubert, J., Cantwell, A. P., Constantin, S., Kalontarov, M., Erickson, D. and Lipson, H. (2010). A robotic module for stochastic fluidic assembly of 3d self-reconfiguring structures. In ‘Robotics and Automation (ICRA), 2010 IEEE International Conference on’. IEEE. pp. 2479–2484.
- Onal, C. D., Wood, R. J. and Rus, D. (2013). An origami-inspired approach to worm robots. *Mechatronics, IEEE/ASME Transactions on* **18**, 430 – 438. [http://ieeexplore.ieee.org/xpls/abs\\_all.jsp?arnumber=6266749](http://ieeexplore.ieee.org/xpls/abs_all.jsp?arnumber=6266749)
- Perich, C., Mackner, A., MacCurdy, R., Steen, P. and Lipson, H. (n.d.). Toward massively parallel manipulation of mm-scale components using electroosmotically controlled drops. (in review).
- Popescu, G. (2007). Digital materials for digital fabrication. Master’s thesis. Massachusetts Institute of Technology. <http://dspace.mit.edu/handle/1721.1/41754>
- RepRap* (2013). [http://www.reprap.org/wiki/Main\\_Page](http://www.reprap.org/wiki/Main_Page)
- Russo, A., Ahn, B., Adams, J., Duoss, E., Bernhard, J. and Lewis, J. (2011). Pen-on-paper flexible electronics. *Advanced materials* **23**(30), 3426–3430. <http://onlinelibrary.wiley.com/doi/10.1002/adma.201101328/full>
- Seelig, G., Soloveichik, D., Zhang, D. Y. and Winfree, E. (2006). Enzyme-free nucleic acid logic circuits. *science* **314**(5805), 1585–1588.
- Seok, S., Onal, C. D., Cho, K., Wood, R. J., Rus, D., Kim, S. et al. (pre-press). Meshworm: A peristaltic soft robot with antagonistic nickel titanium coil actuators. *Mechatronics, IEEE/ASME Transactions on*. [http://ieeexplore.ieee.org/xpls/abs\\_all.jsp?arnumber=6232458](http://ieeexplore.ieee.org/xpls/abs_all.jsp?arnumber=6232458)
- Smolke, C. D. (2009). Building outside of the box: igem and the biobricks foundation. *Nature biotechnology* **27**(12), 1099–1102.
- Srinivasan, U., Liepmann, D. and Howe, R. (2001). Microstructure to substrate self-assembly using capillary forces. *Microelectromechanical Systems, Journal of* **10**(1), 17–24. [http://ieeexplore.ieee.org/xpls/abs\\_all.jsp?arnumber=911087](http://ieeexplore.ieee.org/xpls/abs_all.jsp?arnumber=911087)
- Suzuki, K., Shimoyama, I. and Miura, H. (1994). Insect-model based microrobot with elastic hinges. *Microelectromechanical Systems, Journal of* **3**(1), 4–9.
- Teifel, J. and Manohar, R. (2004). Highly pipelined asynchronous fpgas. In ‘Proceedings of the 2004 ACM/SIGDA 12th international symposium on Field programmable gate arrays’. ACM. pp. 133–142.

- ten Elshof, J. E., Khan, S. U. and Göbel, O. F. (2010). Micrometer and nanometer-scale parallel patterning of ceramic and organic–inorganic hybrid materials. *Journal of the European Ceramic Society* **30**(7), 1555–1577.
- Terfort, A. and Whitesides, G. (1999). Self-assembly of an operating electrical circuit based on shape complementarity and the hydrophobic effect. *Advanced materials* **10**(6), 470–473. [http://onlinelibrary.wiley.com/doi/10.1002/\(SICI\)1521-4095\(199804\)10:6%3C470::AID-ADMA470%3E3.0.CO;2-1/abstract](http://onlinelibrary.wiley.com/doi/10.1002/(SICI)1521-4095(199804)10:6%3C470::AID-ADMA470%3E3.0.CO;2-1/abstract)
- Toffoli, T. and Margolus, N. (1991). Programmable matter: concepts and realization. *Physica D: Nonlinear Phenomena* **47**(1), 263–272. <http://www.sciencedirect.com/science/article/pii/016727899190296L>
- Tolley, M., Baisch, A., Krishnan, M., Erickson, D. and Lipson, H. (2008). Interfacing methods for fluidically-assembled microcomponents. in ‘Micro Electro Mechanical Systems, 2008. MEMS 2008. IEEE 21st International Conference on’. IEEE. pp. 1073–1076. [http://ieeexplore.ieee.org/xpls/abs\\_all.jsp?arnumber=4443845](http://ieeexplore.ieee.org/xpls/abs_all.jsp?arnumber=4443845)
- Tolley, M. T., Kalontarov, M., Neubert, J., Erickson, D. and Lipson, H. (2010). Stochastic modular robotic systems: a study of fluidic assembly strategies. *Robotics, IEEE Transactions on* **26**(3), 518–530.
- Ward, J. (2010). Additive assembly of digital materials. Master’s thesis. Massachusetts Institute of Technology. <http://dspace.mit.edu/handle/1721.1/62084>
- White, P., Kopanski, K. and Lipson, H. (2004). Stochastic self-reconfigurable cellular robotics. in ‘Robotics and Automation, 2004. Proceedings. ICRA’04. 2004 IEEE International Conference on’. Vol. 3. IEEE. pp. 2888–2893. [http://ieeexplore.ieee.org/xpls/abs\\_all.jsp?arnumber=1307499](http://ieeexplore.ieee.org/xpls/abs_all.jsp?arnumber=1307499)
- Yin, P., Choi, H. M., Calvert, C. R. and Pierce, N. A. (2008). Programming biomolecular self-assembly pathways. *Nature* **451**(7176), 318–322.
- Zhao, D., Liu, T., Park, J., Zhang, M., Chen, J. and Wang, B. (2012). Conductivity enhancement of aerosol-jet printed electronics by using silver nanoparticles ink with carbon nanotubes. *Microelectronic Engineering* **96**, 71–75. <http://www.sciencedirect.com/science/article/pii/S0167931712000937>
- Zykov, V., Mytilinaios, E., Adams, B. and Lipson, H. (2005). Self-reproducing machines. *Nature* **435**(7038), 163–164.

(12) INTERNATIONAL APPLICATION PUBLISHED UNDER THE PATENT COOPERATION TREATY (PCT)

(19) World Intellectual Property Organization

International Bureau



(10) International Publication Number

WO 2014/014892 A2

(43) International Publication Date  
23 January 2014 (23.01.2014)(51) International Patent Classification:  
*B65G 54/02* (2006.01)(21) International Application Number:  
PCT/US2013/050650(22) International Filing Date:  
16 July 2013 (16.07.2013)(25) Filing Language:  
English(26) Publication Language:  
English(30) Priority Data:  
61/672,111 16 July 2012 (16.07.2012) US

(71) Applicant: CORNELL UNIVERSITY [US/US]; Cornell Center For Technology, Enterprise &amp; Commercialization, 395 Pine Tree Road, Ithaca, NY 14850 (US).

(72) Inventors: APOORVA, Fnu; 208 West Spencer Street, Apt. 3, Ithaca, NY 14850 (US). MACCURDY, Robert; 1760 Slaterville Road, Ithaca, NY 14850 (US). LIPSON, Hod; 641 Highland Road, Ithaca, NY 14850 (US).

(74) Agents: VALAUSKAS, Charles, C. et al.; Valauskas Corder LLC, 150 South Wacker Drive, Suite 620, Chicago, IL 60606 (US).

(81) Designated States (unless otherwise indicated, for every kind of national protection available): AE, AG, AL, AM, AO, AT, AU, AZ, BA, BB, BG, BH, BN, BR, BW, BY, BZ, CA, CH, CL, CN, CO, CR, CU, CZ, DE, DK, DM, DO, DZ, EC, EE, EG, ES, FI, GB, GD, GE, GH, GM, GT, HN, HR, HU, ID, IL, IN, IS, JP, KE, KG, KN, KP, KR, KZ, LA, LC, LK, LR, LS, LT, LU, LY, MA, MD, ME, MG, MK, MN, MW, MX, MY, MZ, NA, NG, NI, NO, NZ, OM, PA, PE, PG, PH, PL, PT, QA, RO, RS, RU, RW, SC, SD, SE, SG, SK, SL, SM, ST, SV, SY, TH, TJ, TM, TN, TR, TT, TZ, UA, UG, US, UZ, VC, VN, ZA, ZM, ZW.

(84) Designated States (unless otherwise indicated, for every kind of regional protection available): ARIPO (BW, GH, GM, KE, LR, LS, MW, MZ, NA, RW, SD, SL, SZ, TZ, UG, ZM, ZW), Eurasian (AM, AZ, BY, KG, KZ, RU, TJ, TM), European (AL, AT, BE, BG, CH, CY, CZ, DE, DK, EE, ES, FI, FR, GB, GR, HR, HU, IE, IS, IT, LT, LU, LV, MC, MK, MT, NL, NO, PL, PT, RO, RS, SE, SI, SK, SM, TR), OAPI (BF, BJ, CF, CG, CI, CM, GA, GN, GQ, GW, KM, ML, MR, NE, SN, TD, TG).

**Published:**

- without international search report and to be republished upon receipt of that report (Rule 48.2(g))

(54) Title: SYSTEM AND METHODS FOR ELECTROWETTING BASED PICK AND PLACE ASSEMBLY

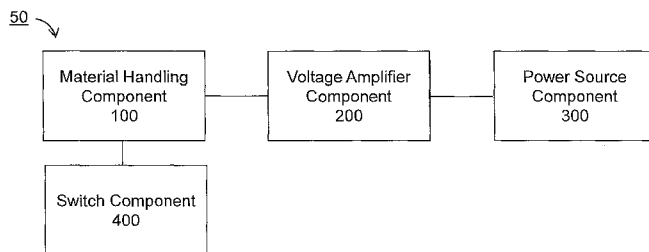


FIG. 1

(57) Abstract: A system based on electrowetting facilitates high-volume assembly of objects including micron sized objects. A material handling component of the system includes an array of electrically controlled nodes that switch their adhesion property based on a voltage supply. The system accurately picks up and places objects including in parallel.

## SYSTEM AND METHODS FOR ELECTROWETTING BASED PICK AND PLACE ASSEMBLY

### PRIORITY CLAIM

5 This Application claims the benefit of U.S. Provisional Patent Application Serial Number 61/672,111 filed July 16, 2012.

### GOVERNMENT FUNDING

The invention described herein was made with government support under grant number W911NF-11-1-0093, awarded by the Defense Advanced Research

10 Projects Agency (DARPA). The United States Government has certain rights in the invention.

### FIELD OF THE INVENTION

The invention relates generally to pick and place system and methods in which objects are picked from one location, transferred to another location, and 15 placed in a precise position. More specifically, the invention relates to system and methods for object manipulation that utilizes electrowetting in order to easily, carefully, and quickly pick and place objects, including micron sized objects, with precision.

### BACKGROUND OF THE INVENTION

20 Automated manufacturing processes often include a mechanism that picks or selects an object and transfers it from one location to another in order for the object to be placed in a precise position.

There have been a number of devices invented in order to move hundreds of small objects. Some look at pick and place robotics to individually grasp and move 25 each piece quickly, while others rely on self-assembly through energy minima. From

suction to magnets to tweezers, numerous products attempt to quickly move large amounts of small objects efficiently and carefully. However, there is a limitation on size. Once objects get too small, for example, around the range of a millimeter and smaller, it becomes more difficult to handle these delicate objects and to quickly 5 arrange the objects in a desired accurate configuration. Furthermore, most inventions use single end effectors to pick up objects – greatly increasing the time to move objects – when two or more objects could be moved in parallel and in any configuration or pattern if properly controlled.

There is a demand for a system and methods that can easily, carefully, and 10 quickly manipulate micron sized objects such as picking and placing objects individually and in parallel as well as in any configuration or pattern. The invention satisfies this demand.

## SUMMARY OF THE INVENTION

The invention is directed to a system and methods that utilizes electrowetting 15 to manipulate one or more objects including micron sized objects. For purposes of this application, a micron sized object is a very small object, for example, an object with a size around, about, or less than one thousandth of a meter (millimeter) or one-millionth of a meter (micrometer).

Electrowetting refers to modification in wetting property of a surface induced 20 by an externally applied electric field. The invention includes a plurality of electrically controlled nodes that switch their adhesion property depending on the voltage supply. Specifically, the electrically controlled nodes display hydrophilic forces to pick-up objects and reverse to hydrophobic forces to place objects.

Nodes comprise an electrode element. In order for the nodes to display 25 hydrophilic forces or hydrophobic forces, the electrode element is coated with a

dielectric element and a hydrophobic element. The micron sized objects to be picked up must be coated with a substance referred to herein as “droplet”. The droplet is of a substance that can be electrically controlled, for example, water.

Specifically, the electrically controlled nodes are hydrophilic while picking the  
5 coated objects and reverse or “switch” to hydrophobic when placing them. It should be noted that by increasing the number of switching nodes per unit area, higher forces can be generated.

In one embodiment, the system comprises a power source component, a voltage amplifier component configured to produce voltage when powered by the  
10 power source component, and a material handling component. The material handling component includes one or more electrically controlled nodes, wherein the one or more electrically controlled nodes comprises an electrode element coated with a dielectric element and a hydrophobic element. The one or more electrically controlled nodes is configured to be hydrophilic when voltage is applied by the  
15 voltage amplifier component in order to pick up the one or more objects and the one or more electrically controlled nodes is configured to be hydrophobic when voltage is discontinued from the voltage amplifier component in order to place the one or more objects. Certain embodiments of the invention may also include a switch component to control nodes individually or in combination.

20 One advantage of the system according to the invention is that objects can be selected and placed with micro scale precision. It is contemplated that the invention may assist three-dimensional (3D) printers as well as be used to pick and place heavy objects.

Another advantage of the invention is that the system according to the  
25 invention accommodates high-volume assembly of micron sized objects since the

system is able to quickly change between a hydrophilic force to pick-up a micron sized object and a hydrophobic force to drop-off micron sized objects.

Another advantage of the invention is that the system exhibits a quick response time.

5 Yet another advantage of the invention is that the system has the ability to control millions of micron sized objects including the ability to control each object independently from another.

10 Yet another advantage of the invention is the system's self-cleaning ability by the virtue of adhesion switching. Specifically, the system is hydrophobic in a ground state, which drives away aqueous remains.

The invention and its attributes and advantages may be further understood and appreciated with reference to the detailed description below of contemplated embodiments, taken in conjunction with the accompanying drawing.

## **DESCRIPTION OF THE DRAWING**

15 The accompanying drawings, which are incorporated in and constitute a part of this specification, illustrate an implementation of the invention and, together with the description, serve to explain the advantages and principles of the invention:

FIG. 1 is a block diagram illustrating the system according to one embodiment of the invention.

20 FIG. 2 illustrates a material handling component of the system according to one embodiment of the invention.

FIG. 3 is a diagram illustrating electrostatically actuated wetting according to one embodiment of the invention.

25 FIG. 4 is a more detailed diagram illustrating electrostatically actuated wetting according to one embodiment of the invention.

FIG. 5 illustrates an object in equilibrium with capillary forces according to one embodiment of the invention.

FIG. 6 is a diagram illustrating the analogy between electrowetting and capacitance-resistance circuit according to one embodiment of the invention.

5 FIG. 7 illustrates a material handling component design according to one embodiment of the invention.

FIG. 8 illustrates multiplexing according to one embodiment of the invention.

## DETAILED DESCRIPTION OF THE INVENTION

FIG. 1 is a block diagram illustrating the system 50 according to one 10 embodiment of the invention. As shown in FIG. 1, the system 50 includes a material handling component 100, a voltage amplifier component 200 and a power source component 300. Certain embodiments of the invention may also include a switch component 400, which may be used to control nodes individually or in combination.

Specifically, the system of the invention includes a material handling 15 component 100, such as a dielectric substrate, comprising one or more electrically controlled nodes 110 as shown in FIG. 2. The one or more electrically controlled nodes 110 comprise an electrode element 120 coated with a dielectric element 130 and a hydrophobic element 140.

FIG. 3 is a diagram illustrating electrostatically actuated wetting according to 20 one embodiment of the invention. A conducting droplet 310 used to coat objects to be picked up and one or more electrically controlled nodes 320 are shown in FIG. 3A. The one or more electrically controlled nodes 320 are hydrophilic when voltage is applied by the voltage amplifier component in order to pick up the one or more objects through the conducting droplet 310 as shown in FIG. 3B. The one or more 25 electrically controlled nodes 320 are hydrophobic when voltage is discontinued from

the voltage amplifier component in order to place the one or more objects through the conducting droplet 310 as shown in FIG. 3C.

FIG. 4 is a more detailed diagram illustrating electrostatically actuated wetting according to one embodiment of the invention. More specifically, an electrical double layer (EDL) enhances the surface tension resulting in the spreading of a droplet 440 across the object as can be seen in FIG. 4B. The term EDL refers to a structure with variation of electric potential near a surface. By coating the electrode element 410 with a dielectric element 420 and a hydrophobic element 430 including droplet 440, not just the actuation power multiplies; it empowers to manipulate a droplet of any conductivity. The development of EDL enhances the surface tension  $\gamma_{SL}$  resulting in the spreading of the droplet. A dielectric element positioned between the electrode element and droplet mimics like an EDL except that the voltage droplet registered across the dielectric can be much higher than across an EDL, which is the key to efficient adhesion switching on a dielectric surface.

A capacitor model of electrowetting suggests:

$$\gamma_{SL} = \gamma_{SL}^0 - \frac{1}{2} \frac{\epsilon_d}{t} V^2$$

where  $\epsilon_d$  is the permittivity of EDL,  $t$  is thickness of EDL and  $\gamma_{SL}^0$  is the solid-liquid surface energy in the absence of an electric field. When combined with the Young's equation of triple junction stability, it gives the modified contact angle:

$$\cos(\theta_{SL}) = \cos(\theta_{SL}^0) + \frac{1}{2} \frac{\epsilon_d}{t \gamma_{LG}^0} V^2$$

A simple free diagram for the picking process is given in FIG. 5 illustrating an object in equilibrium with capillary forces. Specifically, FIG. 5 illustrates an electrode element 510 coated with a dielectric element 520 and a hydrophobic element 530 including a droplet 540 for coating the object 550, which is shown in equilibrium.

Intuitively the meniscus between an object and the material handling component should have a curvature on the sides which would create a lower pressure inside the droplet. This effect dominates rest of the capillary forces if the weight of object is too high; however, this effect is ignored. Other assumptions  
 5 includes the curvature of the picking slot on the material handling component is same as that of the object. Thus, the force analysis boils down to following equation:

$$2\pi R (\gamma_{GL} \cos\theta - \gamma_{DL}) \sin^2\alpha = W_{Tiles}$$

The object is represented by  $V$ , the droplet by  $L$ , the dielectric  $D$ , and the surrounding gas phase by  $G$ . To incorporate the geometry and material property of  
 10 the objects, the above expression is modified to the following form:

$$2\pi R (\gamma_{GL} \cos\theta - \gamma_{DL}) \sin^2\alpha = \frac{4}{3}\pi R^3 \rho_{Tiles} g$$

The wetting angle  $\theta$  is a function of the potential  $V$  maintained across the electrodes. An electrowetting equation is evoked to get the expression dependent on  $V$ .

$$2\pi R \left( \gamma_{GL} \cos\theta_0 + \frac{1}{2} \frac{\epsilon_D}{t\gamma_{LG}^\circ} V^2 - \gamma_{DL} \right) \sin^2\alpha = \frac{4}{3}\pi R^3 \rho_{Tiles} g$$

$$\frac{1}{2} \frac{\epsilon_D}{t\gamma_{LG}^\circ} V^2 \sin^2\alpha = (\gamma_{DL} - \gamma_{GL} \cos\theta_0) \sin^2\alpha + \frac{2}{3} R^2 \rho_{Tiles} g$$

In the above equation,  $\alpha$  is a function of surface tension properties associated with the object material.

$$\sin\alpha = \frac{\sqrt{(\gamma_{VL} - \gamma_{VG})^2 - \gamma_{VL}^2}}{\gamma_{LG}}$$

Effectively, the following equation is obtained in terms of all the known  
 20 physical parameters:

$$\frac{1}{2} \frac{\epsilon_D}{t\gamma_{LG}^o} V^2 \sin^2 \alpha = (\gamma_{DL} - \gamma_{GL} \cos \theta_o) \sin^2 \alpha + \frac{2}{3} R^2 \rho_{Tiles} g$$

$$V = \left[ \frac{2t\gamma_{LG}^2}{\epsilon_D} \frac{((\gamma_{DL} - \gamma_{AL} \cos \theta_o) \sin^2 \alpha + \frac{2}{3} R^2 \rho_g)}{\sqrt{\gamma_{VL}^2 - (\gamma_{VL}^2 - \gamma_{VA}^2)^2}} \right]^{\frac{1}{2}}$$

An advantage of the invention is that the droplets face the object such that the electrodes lie on the same side of the dielectric element.

FIG. 6 is a diagram illustrating the analogy between electrowetting and 5 capacitance-resistance (CR) circuit according to one embodiment of the invention. Specifically, FIG. 6 draws an analogy between a real capacitor-resistance circuit and the classical electrowetting experimental set up. The dielectric element can be thought of as a capacitor and the conducting droplet as a "resistance". Similarly another circuit can be thought of with two capacitors and a resistance in between.

10 FIG. 7 illustrates a material handling component design according to one embodiment of the invention. Not only are the two electrodes are on same side, it also has faster switching time. One embodiment of the material handling component comprises of a capacitor  $C$  and a resistance  $R$ , giving a switching time  $\tau \sim CR$ . In another embodiment, the material handling component has two capacitors  $C$  and a 15 resistor  $R$  with net capacitance  $\frac{C}{2}$  and hence switching time  $\tau \sim \frac{CR}{2}$ . This assumes that droplet size is same and ignores the fact that capacitor also depends on the area of two capacitor plates.

FIG. 8 illustrates multiplexing according to one embodiment of the invention. A droplet once actuated to hydrophilic nature remains hydrophilic even if the system 20 is switched off. This means, for example, that 1000 x 1000 objects can be independently controlled by 2000 switches. This allows for massive parallelization, albeit with accommodating circuitry.

A unique behavior is observed with the invention. The wetting property till was retained until a short circuit occurred. This observation is critical to massive parallelization of picking and placing objects. The “retention till shorted” can be exploited to multiplex the actuation. For example, manipulating an array of  $n \times n$  nodes independently of each other may include  $2n^2$  wires coming of the material handling component whose switching is controlled by  $n^2$  switch components. This type of wiring is necessary only if a continuous supply of power is required to retain the objects at their position. Because a pulse is sufficient to trigger the picking, a scheme as shown in FIG. 8 can be employed. This requires just  $2n$  switch components and can be further reduced to  $4\log(n)$  switch components by deploying a particular multiplexing method.

The described embodiments are to be considered in all respects only as illustrative and not restrictive, and the scope of the invention is not limited to the foregoing description. Those of skill in the art may recognize changes, substitutions, adaptations and other modifications that may nonetheless come within the scope of the invention and range of the invention.

**CLAIMS**

1. A system comprising the use of electrowetting to manipulate one or more objects, the system comprising:

a power source component;

5 a voltage amplifier component configured to produce voltage when powered by the power source component;

a material handling component including one or more electrically controlled nodes, wherein the one or more electrically controlled nodes comprises an electrode element coated with a dielectric element and a hydrophobic element, the one or 10 more electrically controlled nodes configured to be hydrophilic when voltage is applied by the voltage amplifier component in order to pick up the one or more objects and the one or more electrically controlled nodes configured to be hydrophobic when voltage is discontinued from the voltage amplifier component in order to place the one or more objects.

15

2. The system comprising the use of electrowetting to manipulate one or more objects according to claim 1 further comprising a switch component to control the electrode element.

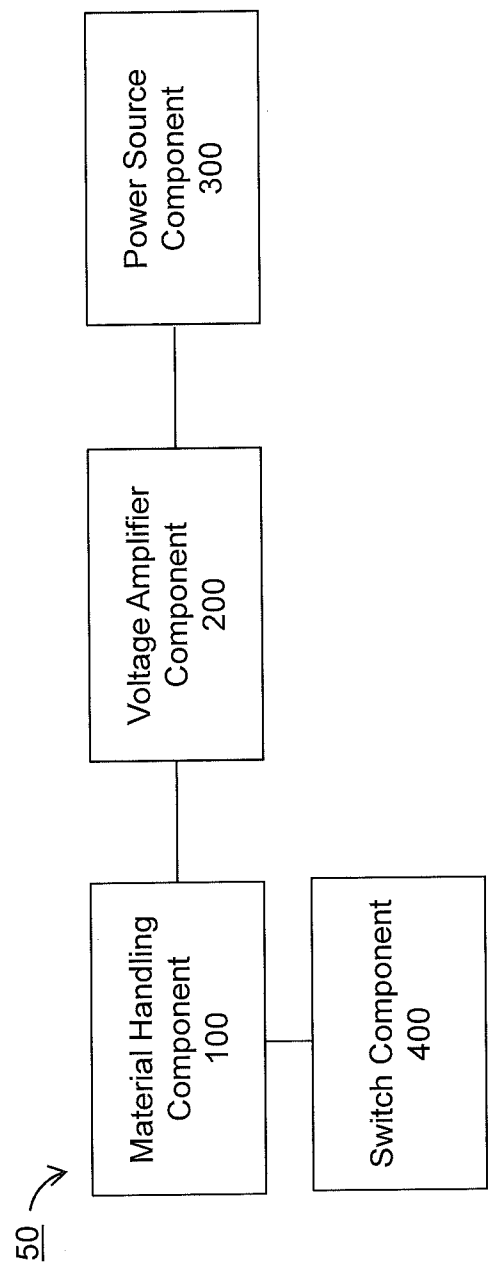


FIG. 1

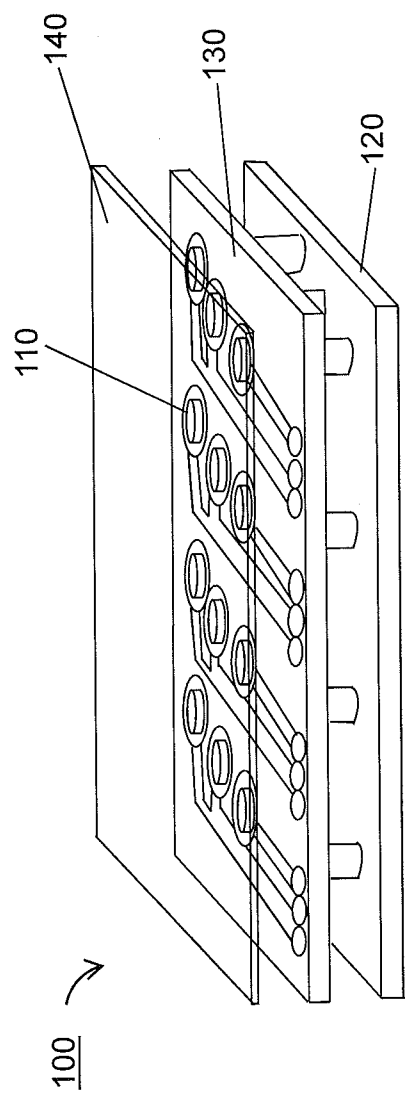


FIG. 2

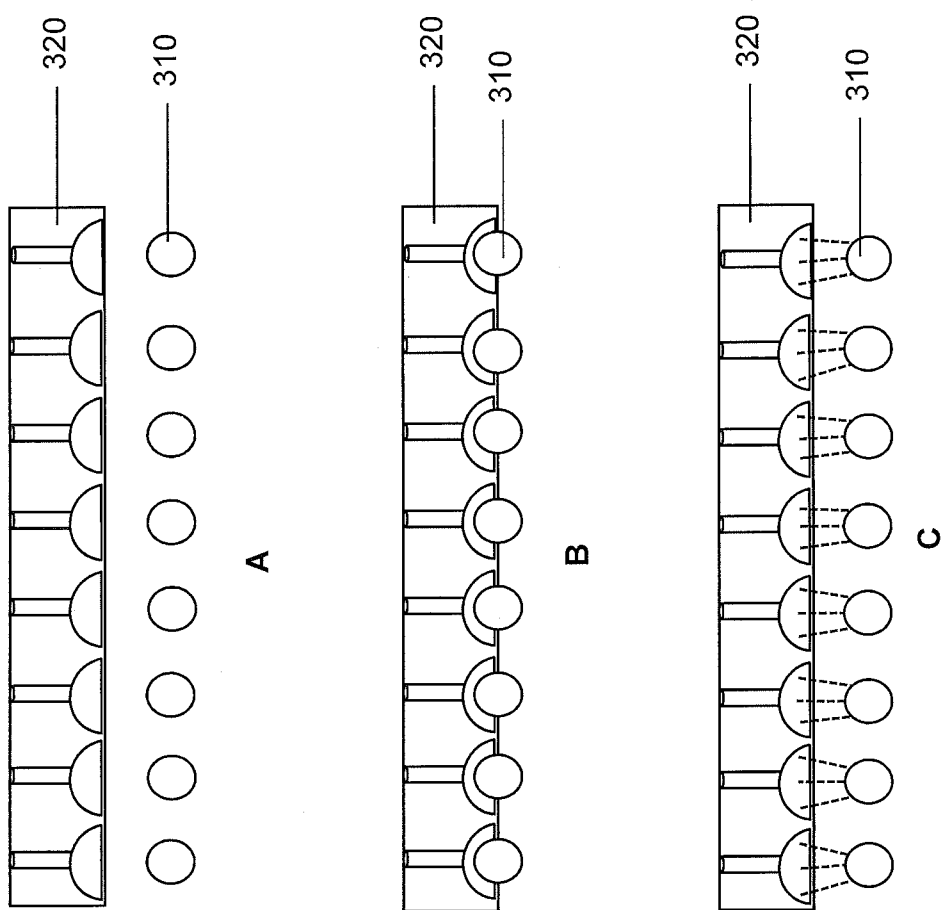
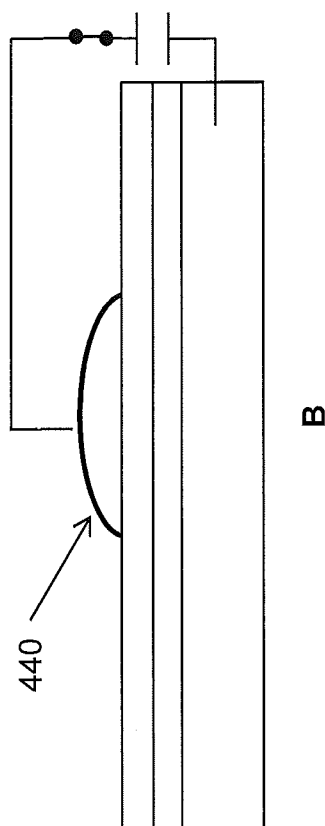
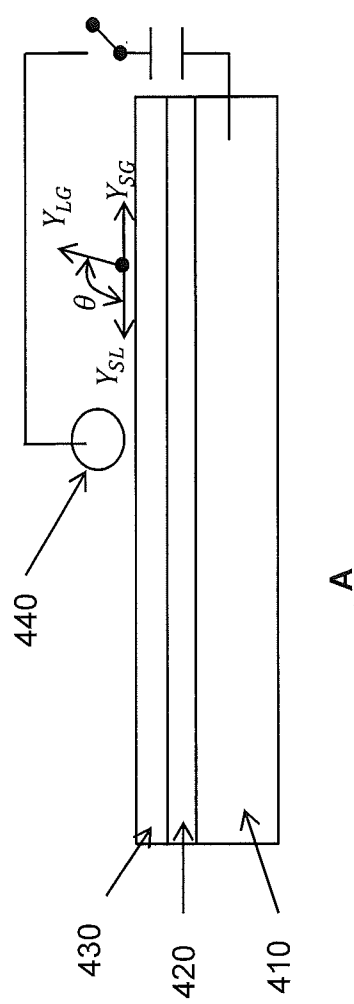


FIG. 3

3/7



B



A

FIG. 4

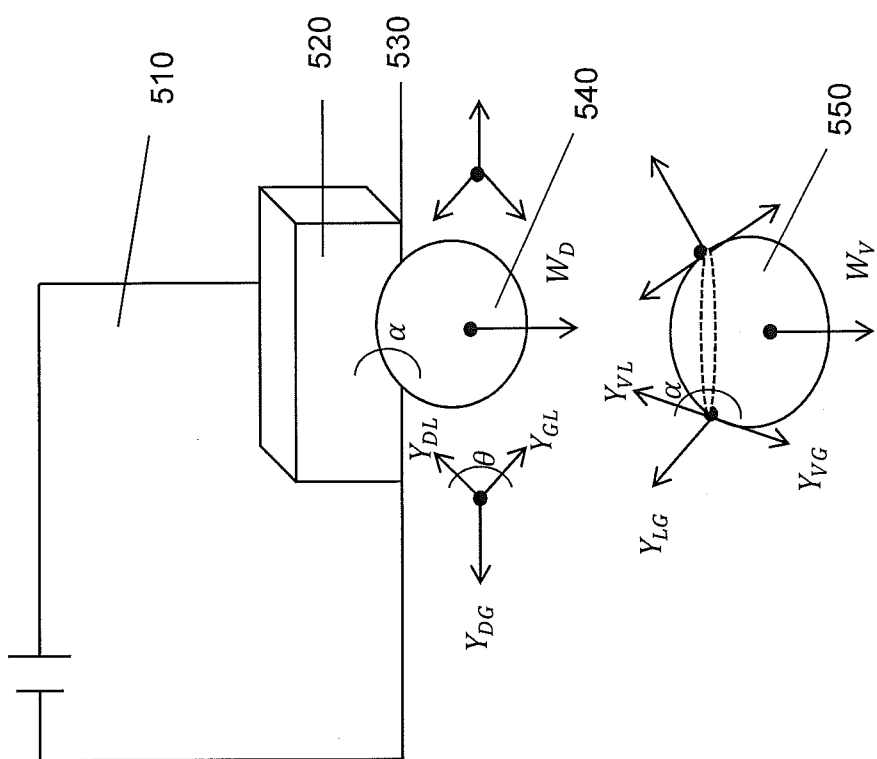


FIG. 5

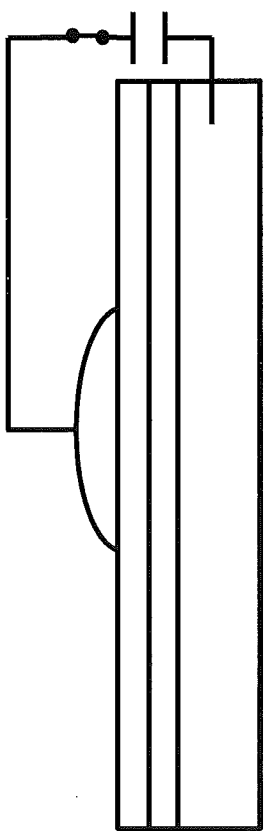
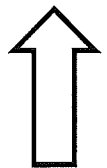
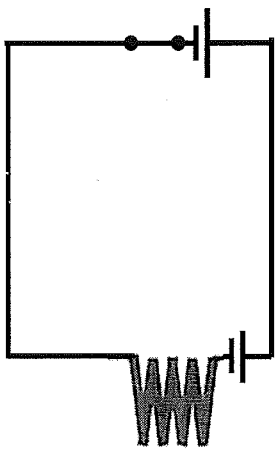


FIG. 6

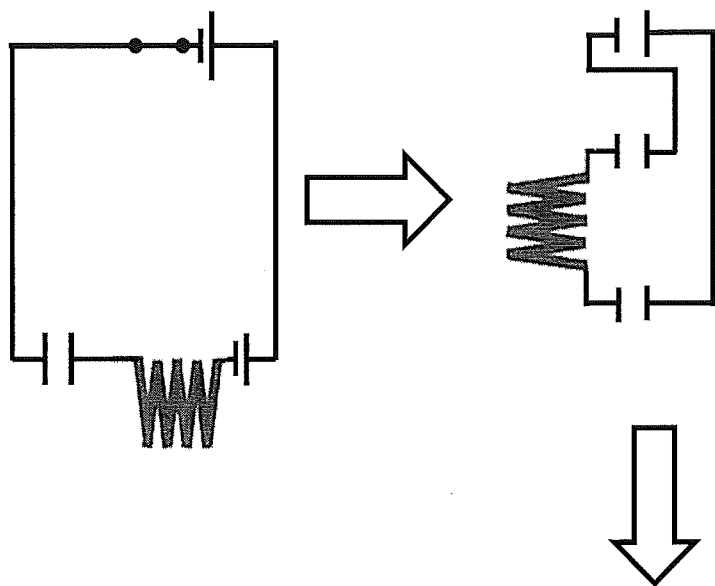
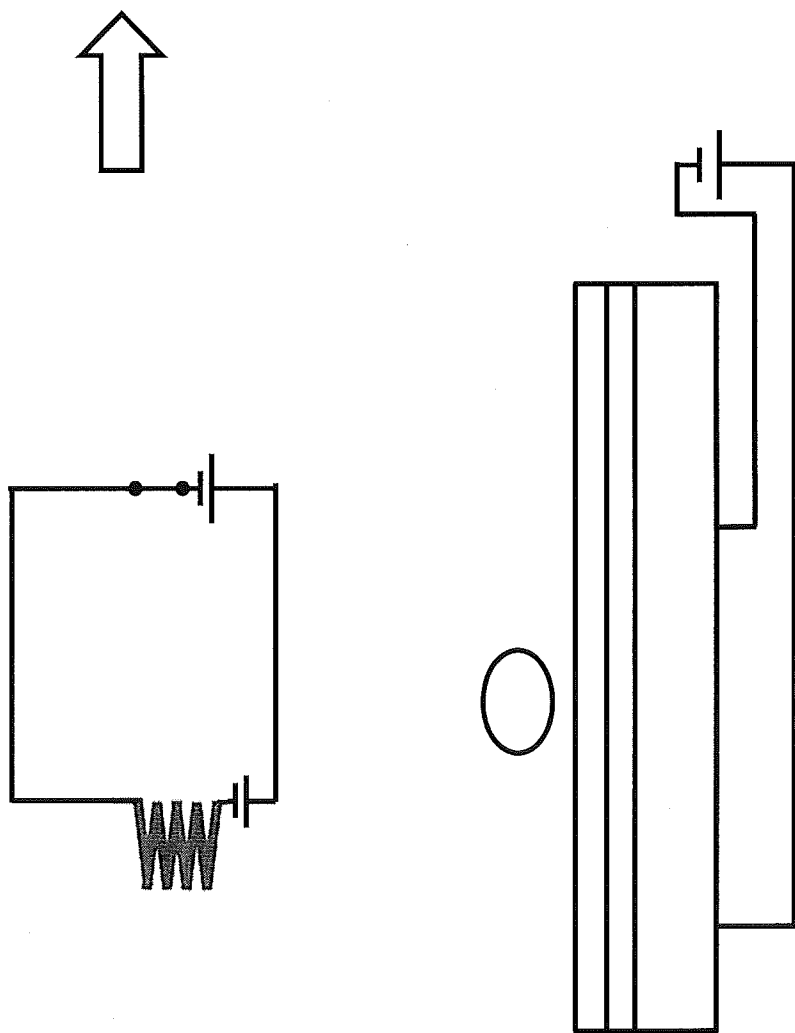


FIG. 7



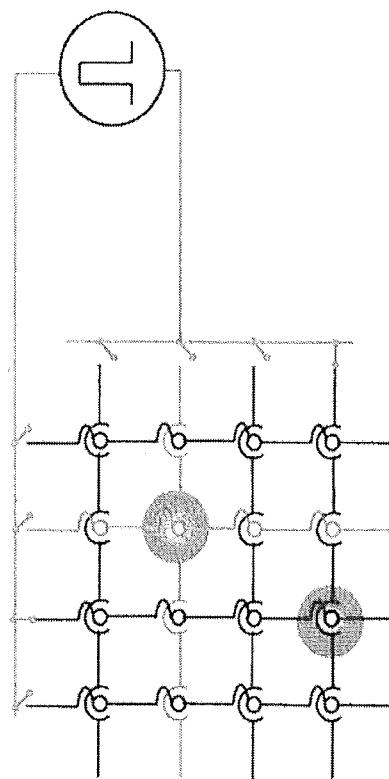


FIG. 8

